Development and Study of an Electron Cyclotron Resonance Waveguide Plasma Cathode for Electric Propulsion Applications

by

Brandon Robert Weatherford

A dissertation submitted in partial fulfillment
of the requirements for the degree of
Doctor of Philosophy
(Nuclear Engineering and Radiological Sciences)
in The University of Michigan
2011

Doctoral Committee:

Associate Professor John Foster, Chair
Professor Alec Gallimore
Professor Ronald Gilgenbach
Professor Mark Kushner
Hani Kamhawi, NASA
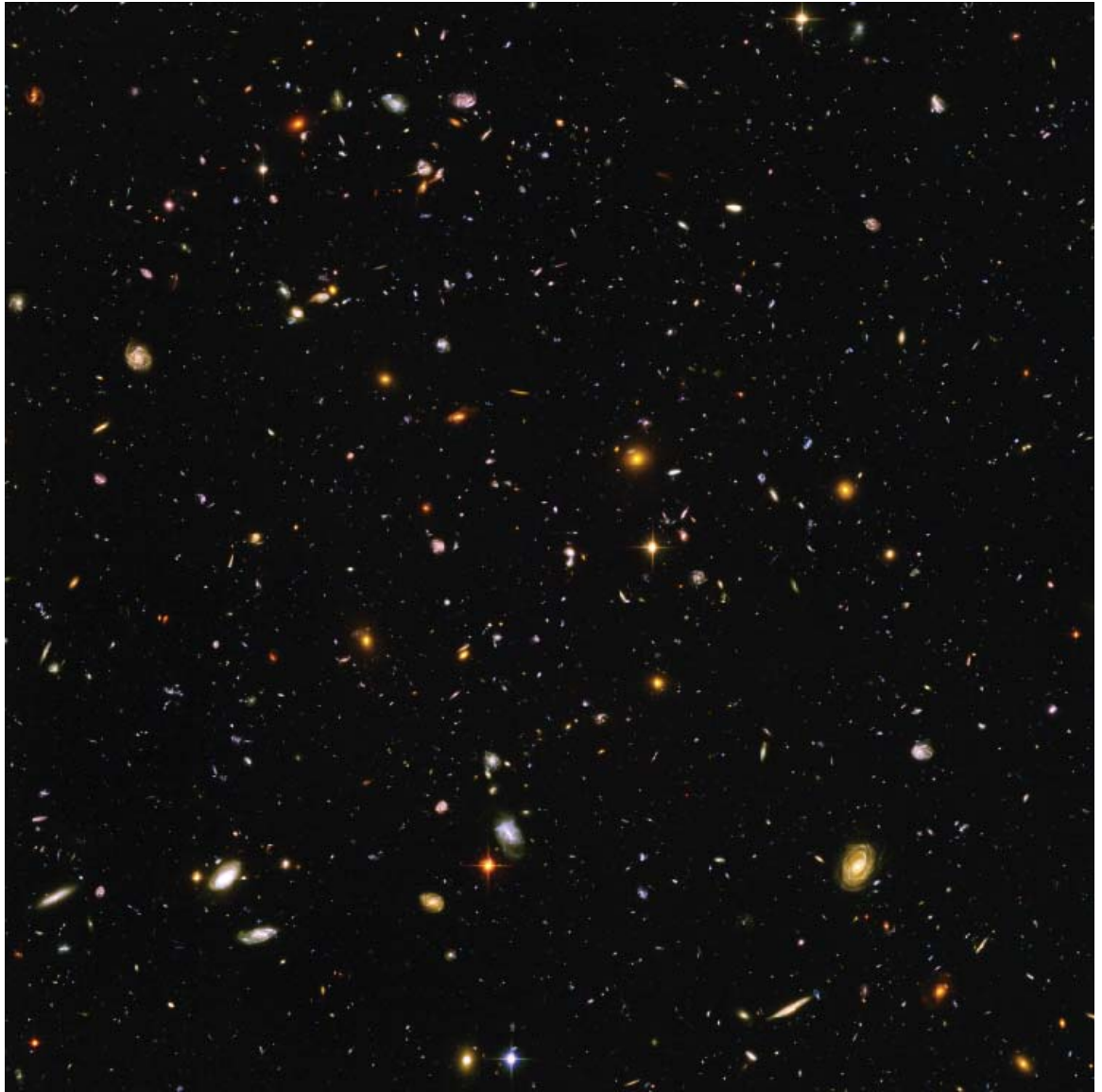
"Those worlds in space are as countless as all the grains of sand on all the beaches of the earth." - Carl Sagan

For my friends and family, who are everything to me.

ACKNOWLEDGEMENTS

There are dozens of people in my personal and professional life that I cannot thank enough for their guidance and support during my time in graduate school. Without each one of them, this thesis would not have been possible.

My advisor, Prof. John Foster, has been an outstanding mentor and friend over the past five years. I consider myself lucky to have been his first graduate student. I have learned an extraordinary amount from him over the years (from plasma physics to vacuum leak fighting to obscure sci-fi movies on cable TV) and it has really been a pleasure to help him establish his lab. Dr. Foster is a great teacher and scientist, and most of all he a great person. I look forward to working and keeping in touch with him for many years to come.

Dr. Hani Kamhawi from NASA Glenn Research Center deserves special mention for his mentoring during my GSRP fellowship. Over the course of three years, I spent several weeks working alongside him in Cleveland, and truly enjoyed it. Even though Dr. Kamhawi kept quite busy with his work, he was always available when I needed something and had great advice. I had a great time working with him and am grateful for everything he's done, even though he loves to harass me about my favorite football team. Dr. Edward Barnat at Sandia National Labs was another great mentor during the seven months that I spent at his lab in Albuquerque. Dr. Barnat has a wealth of knowledge, and I am still amazed at his experimental know-how. He is a great guy to work with and to learn from, and I am excited to continue with that in the future. I would like to thank Dr. Alec Gallimore, Dr. Ron Gilgenbach, and Dr. Mark Kushner

for serving on my dissertation committee, and for their helpful suggestions during the course of my studies. I would also like to thank Dr. Y.Y. Lau for his participation in my oral preliminary examination. I am proud to have a group of such respected researchers involved with my graduate work.

I was truly lucky to end up with such a wonderful group of labmates. Over the years, they have transformed from co-workers into some of my closest friends. We have had too many great times together to recall, and my experience in grad school would not have been the same without them. Aimee Hubble, Ben Yee, Brad Sommers, Eric Gillman, and Paul Cummings deserve special thanks for all of their support as we went through each phase of the graduate student growing pains together. I also want to thank the rest of the wonderful friends that I've made in graduate school, undergrad, and high school - you know who you are, and I love all of you.

I could not have asked for a better family, and they are the people that really deserve the credit for anything that I've been able to accomplish. Andrew, Erik, Dana, Brianne, Dad and Lara, and Mom and Barclay have always given me the drive to keep going when things got tough. Words cannot describe how much you all mean to me. Thank you for all that you have done.

TABLE OF CONTENTS

LIST OF FIGURES

Figure

ABSTRACT

Development and Study of an Electron Cyclotron Resonance Waveguide Plasma
Cathode for Electric Propulsion Applications

by

Brandon R. Weatherford

Chair: John E. Foster

In electrostatic ion thrusters and Hall thrusters, electron sources are used for propellant ionization and neutralization of the thruster beam. Thermionic emitter-based sources are commonly used, but they possess inherent lifetime limitations due to emitter depletion, poisoning, and sputtering of the emitter surface. For long duration electric propulsion (EP) driven missions or semi-permanent plasma contactor installations, these emitters have become primary limiting components on thruster life. There are two goals to this work: first, to develop and demonstrate the feasibility of an emitterless plasma cathode for EP; and second, to study the underlying physics of emitterless cathodes. The waveguide plasma cathode uses traveling 2.45 GHz microwaves in a cylindrical waveguide geometry, with permanent magnets, to generate an electron cyclotron resonance (ECR) discharge. Electron current is extracted from this source plasma through a downstream aperture. This device delivered up to 4.2 amperes of electron current, at low power (90 W/A) and high gas utilization.

The device was tested with argon, krypton, and xenon. Probe diagnostics were used to measure axial profiles of electron density, electron temperature, and plasma

potential, inside the device and in the external plume. These measurements show that some trace plume ionization is necessary for substantial current extraction. Plasma potential in the plume tracks with a biased anode, and a weak electric field in the plume transports current across the anode-cathode gap. Internal plasma conditions are also discussed. The plasma density in the extraction aperture increased by orders of magnitude, relative to the source discharge density, during electron current extraction. This is attributed to the formation of a dense plasma structure at the aperture. Laser collision-induced fluorescence (LCIF) was used to create two-dimensional images of plasma density and effective electron temperature at the aperture. The structure had a high density core, surrounded by a layer of high energy electrons accelerated by a double layer. Probe diagnostics verified the existence of a potential gradient between the aperture and bulk plasma. The aperture plasma acts as an effective loss area for electrons, and may be a common feature of plasma cathodes that should be included in models of these devices.

CHAPTER I

Introduction

This research focuses on the study and development of a microwave plasma cathode, as a proof of concept long-lived electron source for space applications. Though the primary application of interest is electric propulsion, the device could also be used for charge control (*e.g.* on the International Space Station). In this chapter, an overview of electric propulsion systems and plasma contactor units is presented, along with a brief summary of the most commonly used electron sources – thermionic emitters. Limitations of thermionic emitters are are discussed along with the consequences of these limitations on space applications, leading to the motivation for this work.

1.1 Electric Propulsion Overview

Electric propulsion (EP) can be defined as the use of electrical energy to produce thrust for spacecraft. While EP is in general a lesser-known variety of space propulsion, it has emerged as a reliable, mature technology. The key advantage of EP lies in the separation of the propellant from the energy source, in contrast with chemical systems where energy is released from chemical bonds in the propellant itself. By simply accelerating the propellant with electrical energy, one can increase the exhaust velocity to many tens of thousands of meters per second. Owing to
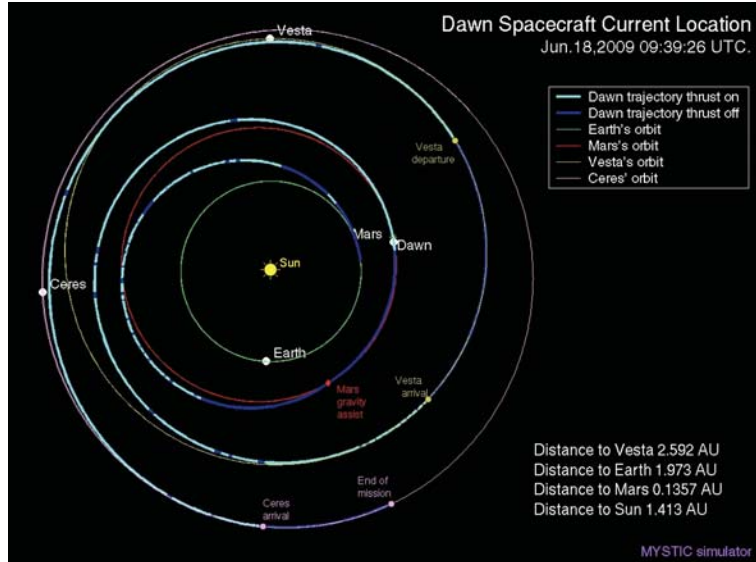
Figure 1.1: Trajectory of the Dawn spacecraft, displaying the throttling capability of ion thrusters. Figure from [20].

the capability of high exhaust velocities, flexibility in mission planning using EP is unmatched in chemical propulsion systems. A prime example of this flexibility is the Dawn mission, launched in 2007, which utilizes three electrostatic ion thrusters developed for NASA's Deep Space 1 mission.[20] The Dawn spacecraft is an EP-driven explorer that will rendezvous with the two largest bodies in the asteroid belt, Vesta and Ceres. The thrusters aboard Dawn will be used for a cruise phase from Earth to Mars gravity assist, and again from Mars gravity assist to Vesta. Then, Dawn will be captured at Vesta, and transfer to a science-enabling orbit around that body. After ten months of science operations at Vesta, the thrusters will again be used to escape Vesta, cruise to Ceres, and transfer again to a science orbit. The mission will conclude with five months of science operations at Ceres.[9, 10] As shown in Figure 1.1, this complicated trajectory of the Dawn spacecraft requires several phases of propulsion and coasting, for which EP is exceptionally suited.

The advantage of EP over chemical propulsion systems lies in the difference in attainable exhaust velocities. This can been seen through the examination of the rocket equation. Here, the ratio of deliverable payload mass, m_f, to the total initial

mass of a spacecraft, m_i, is given by,

$$\frac{m_f}{m_i} = \exp\left(-\frac{\Delta v}{u_e}\right) \qquad \text{Rocket Equation} \qquad (1.1)$$

where u_e is the propellant exhaust velocity and Δv is the total change in velocity needed to carry out a given mission. Each maneuver (orbit transfer, escape, etc.) requires a specific total Δv, and the amount of propellant required for a mission grows exponentially with Δv. Because EP systems can generate exhaust velocities at least 10 times greater than chemical, the propellant mass required for a given Δv can be dramatically reduced using EP. In general, exhaust velocity is not specified for rocket systems; rather, the specific impulse is used. Specific impulse is roughly proportional to the exhaust velocity, and is defined as the ratio of thrust to the weight of the ejected propellant per unit time.

Because of its enabling capabilities, EP remains an active field of research. One key area of research is the extension of engine life.[36, 28, 30, 18] Lifetime is an important concern since EP thrusters are inherently low thrust. This means that to achieve a given Δv, the engine must operate for much longer time periods than chemical rockets. This work focuses on extending engine life using a novel cathode replacement technology.

1.2   Electron Sources in EP Devices

In the most common electric propulsion systems, such as electrostatic ion thrusters and Hall effect thrusters, the electron source is an essential component. Electron sources perform two major functions: ionization of the propellant gas and charge control. The gridded ion thruster is a mature EP technology that has recently been demonstrated in space on the Deep Space 1 and Dawn missions. A simple schematic of
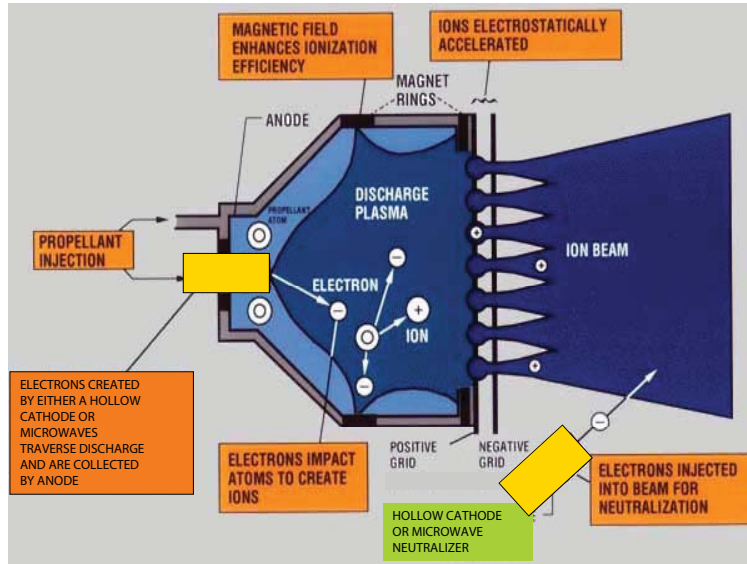
Figure 1.2: Schematic of an electrostatic ion thruster. Graphic from [56].

an ion thruster is shown in Figure 1.2. Propellant is fed into the discharge chamber which contains an electron source (typically a hollow cathode assembly) known as the discharge cathode. The discharge cathode is biased negatively relative to the chamber walls, which function as the anode. As electrons are accelerated by the applied electric field and confined by the magnetic field (established by permanent magnets), they ionize the propellant, resulting in the chamber filling with plasma. On the downstream end of the thruster, a series of aligned, biased grids is used to extract ions from the plasma and accelerate the ions to high velocity, forming an ion beam. This produces thrust typically on the order of tens of milliNewtons. The grid nearest the discharge chamber, known as the "screen" grid, is biased positively relative to the space (reference) potential. This raises the internal plasma potential to facilitate ion extraction and acceleration. The second grid is biased negatively to establish a focusing electric field and to prevent electron backstreaming into the thruster.

If a spacecraft is electrically isolated from the ambient space plasma, as ions are extracted from the thruster, the spacecraft will charge negatively. This negative charging will tend to attract the accelerated ions back toward the spacecraft, and

HALL ACCELERATOR

ELECTROMAGNETS USED TO
ESTABLISH MAGNETIC FIELDS

OUTER
MAGNETIC
POLE

INNER
MAGNETIC
POLE

ELECTRON
SOURCE

E

B

PROPELLANT
INJECTION

ELECTRONS
TRAPPED IN
CROSSED FIELDS

ELECTRONS IMPACT
ATOMS TO CREATE
IONS

IONS
ELECTROSTATICALLY
ACCELERATED
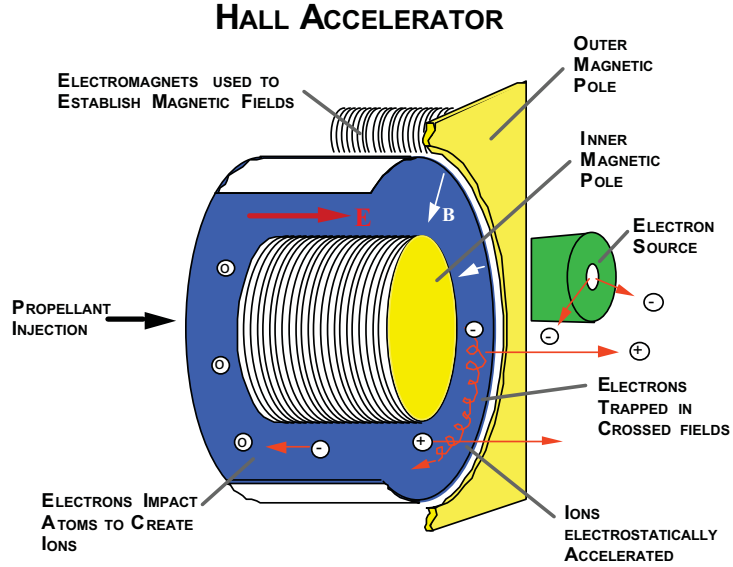
Figure 1.3: Schematic of a Hall effect thruster. Graphic from [57].

will eventually prevent thruster operation. To mitigate the charging effect, a second electron source known as a "neutralizer" is mounted externally, which emits electrons into the thruster beam. With the neutralizer, current continuity is maintained at a lower spacecraft voltage relative to the ambient space plasma, allowing the thruster to maintain efficient operation. For a point of reference, the full-power operating condition of NASA's Evolutionary Xenon Thruster (NEXT) is 3.52 amperes of thruster beam current.[30, 65]

Similarly, electron sources are needed in Hall effect thrusters, again for both propellant ionization and beam neutralization. In the Hall thruster, the effective discharge "chamber" is an annular shaped channel, shown in Figure 1.3. A radial magnetic field is established across the channel by two electromagnets. Propellant is fed from the upstream, at the anode. A single electron source is mounted just outside of the thruster and biased negatively with respect to the anode. As electrons travel toward the anode, their flow to the anode is is impeded by the radial magnetic field lines. This buildup of negative space charge in the channel establishes an axial electric field, which has two main consequences. For one, electrons in the

channel orbit in the azimuthal direction through $\mathbf{E} \times \mathbf{B}$ drift, and the oribiting electrons ionize the propellant through collisions. Additionally, the axial electric field is an accelerating mechanism for ions, which are expelled from the thruster. As opposed to the electrostatic ion thruster, the same electron source that is used for propellant ionization also neutralizes the thruster beam. The HiVHAC currently under development at NASA Glenn Research Center (GRC) requires up to 5 amperes of neutralizer current.[38]

1.3   Electron Sources for Spacecraft Charge Mitigation

A related application for electron sources on spacecraft is the mitigation of charge buildup on a floating structure immersed in the ambient space plasma. Charging is undesirable in that it can lead to arcing, which can damage solar arrays and electronics. For this reason, charge control of the International Space Station (ISS) is a critical issue. As the ISS orbits the Earth, it is exposed to the ambient plasma in the ionosphere.

By virtue of being a floating structure in a plasma, the ISS will float to a negative voltage relative to the surrounding plasma by a few times the effective electron temperature:

$$V_f = -k_{\mathrm{B}} T_e \ln \left(\frac{M}{2\pi m} \right)^{1/2} \tag{1.2}$$

where V_f is the floating potential, k_{B} is the Boltzmann constant, T_e is the electron temperature, M is the ion mass, and m is the electron mass. Electron temperatures at the ISS altitude are typically less than 0.5 eV, so this effect alone is not particularly hazardous. The 140-160 volt ISS solar arrays, on the other hand, operate at a high voltage relative to the ambient space potential, which can lead to arcing. [58]
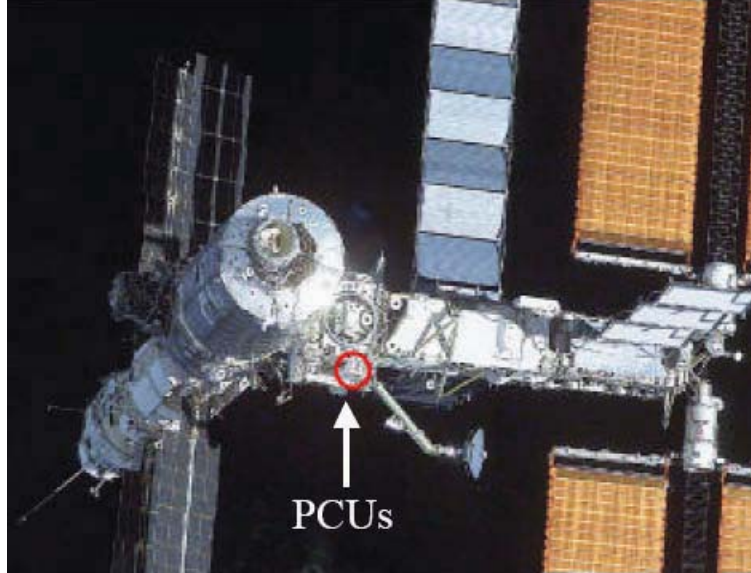
Figure 1.4: Location of plasma contactor units on the International Space Station. Photograph from [40].

To prevent arcing on the ISS, plasma contactor units (PCUs) were developed, which establish a low-impedance plasma bridge between the structure and surrounding plasma. This eventually grounds the negative potential to the ambient space potential, thereby eliminating the potential difference. The PCU is comprised of a HCA, power electronics unit, and expellant management unit. The design specficiations for the ISS PCU include a clamping voltage of ± 20 V, deliverable electron current up to 10 A, and 18,000 hours of operating lifetime. [40] HCA-based plasma contactors are currently installed on the ISS, as shown in Figure 1.4.

1.4   Thermionic Emitters and Associated Limitations

Thermionic electron emitters such as hot filaments and coated oxide cathodes have been used in early ion thruster designs. [50, 41] Thermionic emission is the basis for HCA operation, and is the process by which electrons are released from a heated metal surface. Here, the population of electrons in the Fermi distribution with energy greater than the work function of the material escape from the surface. The electron

current density emitted from a surface is related to the temperature and work function by the Richardson-Dushmann equation:

$$J_0 = \frac{4\pi m e k_{\mathrm{B}}^2}{h^3} T^2 \exp\left(-e\Phi/k_{\mathrm{B}}T\right) \tag{1.3}$$

where e is the elementary charge, T is the material temperature, h is Planck's constant, and Φ is the work function of the material. An increased operating temperature therefore corresponds to higher current densities. Because work functions are on the order of a few eV, the cathode must operate at high temperatures; $\sim 1000°C$ or higher. Refractory metals must therefore be used in hot cathode construction. Under an applied electric field, the emitted current can be increased via the Schottky effect. The applied field suppresses the quantum-mechanical potential barrier at the material surface, amplifying the emitted current according to Equation (1.4):

$$J_e = J_0 \exp\left(\frac{e^{3/2}E^{1/2}}{(4\pi\epsilon_0)^{1/2}\,k_{\mathrm{B}}T}\right) \tag{1.4}$$

where E is the applied electric field and ϵ_0 is the permittivity of free space.

The oxide cathode was developed to increase the deliverable current density of thermionic emitters by lowering the work function. Or conversely, for a given current density, the oxide cathode is able to operate at a lower temperature, improving the emitter lifetime by reducing the vaporization rate. Oxide cathodes are often made by coating the emitter in a triple-carbonate material consisting of barium, strontium, and calcium oxides, as shown in Figure 1.5. While the work function of the bulk emitter material remains the same, the oxide layer lowers the work function at the surface significantly. However, because the sustainability of the coating is also dependent on the operating temperature and emitted current, the selection of work function
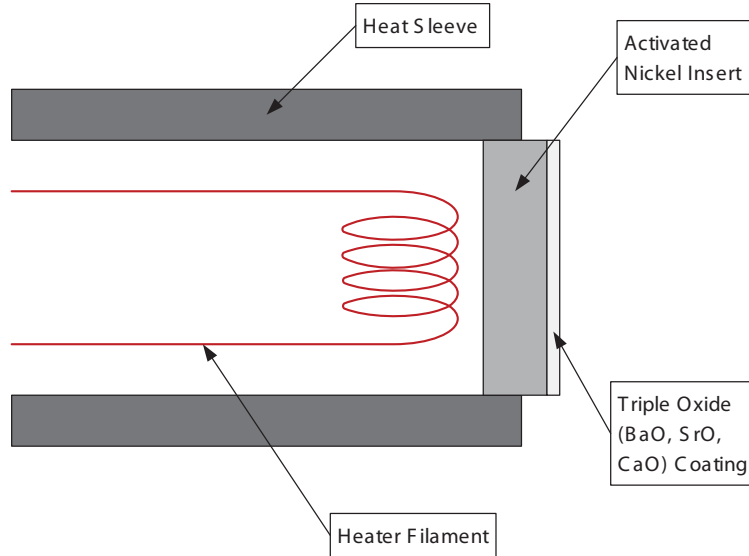
Figure 1.5: Schematic of an oxide cathode with heater. Schematic based on [72].

and operating temperature depends on the application and service lifetime. Common tungsten emitters coated with triple carbonate have work functions around 2 eV (as opposed to 4.5 eV for pure tungsten) and operating temperatures in the range of 1100 to 1300 K. [31]

Dispenser cathodes are a form of oxide cathode that address, at least to a degree, the limited lifetime of coated emitters. In coated oxide cathodes, the oxide coating evaporates away over time, particularly at high temperatures. In addition, triple carbonate coatings are very sensitive to contamination by common compounds like water vapor, oxygen, and carbon dioxide. If exposed to any contaminants, the cathode surface is poisoned, increasing the surface work function, and suppressing emission at nominal operating temperatures. The dispenser cathode employs porous tungsten as the bulk material. In a reservoir cathode, a reservoir of barium carbonate is situated directly beneath the tungsten. Barium gradually diffuses through the tungsten to the surface, replenishing the low work function layer as it is lost from the surface. In the impregnated dispenser cathode, barium is injected within the pores of the tungsten emitter, thereby mitigating the need for a reservoir. A reservoir dispenser cathode is
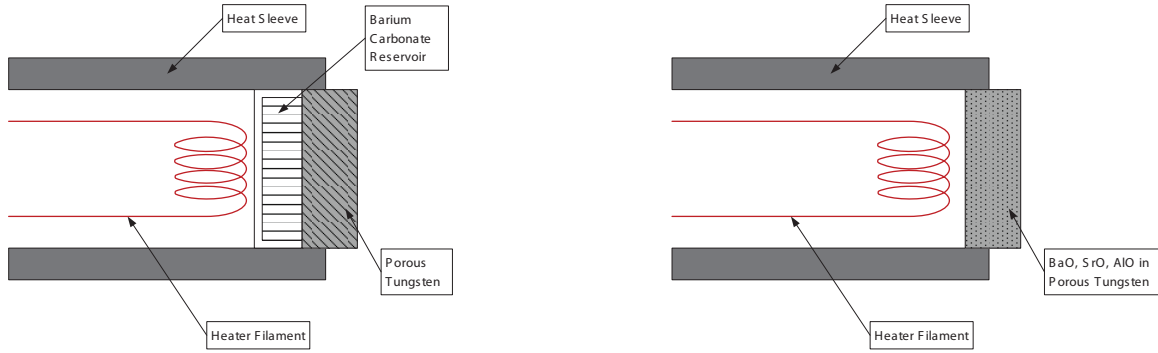
Figure 1.6: Schematics of *a*) a reservoir dispenser cathode and *b*) an impregnated dispenser cathode. Schematics based on [72].

shown alongside of an impregnated dispenser cathode in Figure 1.6.[72]

The thermionic emitter is the established electron source of choice for many applications. However, oxide cathodes have inherent lifetime limitations such as the aforementioned poisoning and vaporization of emissive material. The cathode surface can also be sputtered by incident ions. Cathode lifetime is a priority in EP systems, since the cathode may be required to operate for tens of thousands of hours in long duration missions. Therefore, thermionic electron sources can sometimes be of limited utility in EP. To achieve the current densities needed for thruster beam neutralization with service lifetimes, several plasma-based electron sources have been developed. One is the hollow cathode assembly (HCA), which uses thermionic emission to generate a dense plasma, from which electron current is extracted. Emitterless plasma cathodes based on helicon, RF, and microwave plasma discharges have also been studied. The microwave plasma cathode presented this dissertation is another novel plasma cathode approach. The next chapter describes the HCA in more detail, and summarizes the wide spectrum of plasma cathodes in the literature to date.

CHAPTER II

Plasma Cathodes in the Literature

2.1 Plasma Cathode – An Overview

A plasma cathode is a device in which electron current is extracted from a plasma discharge. A variety of ionization mechanisms can be used to generate the discharge, including direct current (DC), radio frequency (RF), and microwave heating. Plasma cathodes have several advantages over thermionic emitters in certain applications. Plasma cathodes can be operated in pulsed mode and generally have a shorter start-up time than purely thermionic sources. The lifetime of a plasma cathode is not limited by emitter degradation, emitter depletion, or poisoning associated with thermionic devices. This latter point has made plasma cathodes quite attractive for long duration space applications, and several variations of plasma cathode have been studied for this reason.

A plasma cathode consists of two major components, as illustrated in Figure 2.1: 1) the discharge chamber, and 2) the electron extraction circuit. Plasma is produced in the discharge chamber, which is usually terminated with an aperture to increase neutral confinement within the chamber. The use of an aperture also limits the electron extraction area to a fraction of the internal wall surface area. As presented in more detail in Chapter 3, a large ratio of chamber wall area to extraction aperture area is a necessary condition for efficient electron extraction from a quasineutral plasma.
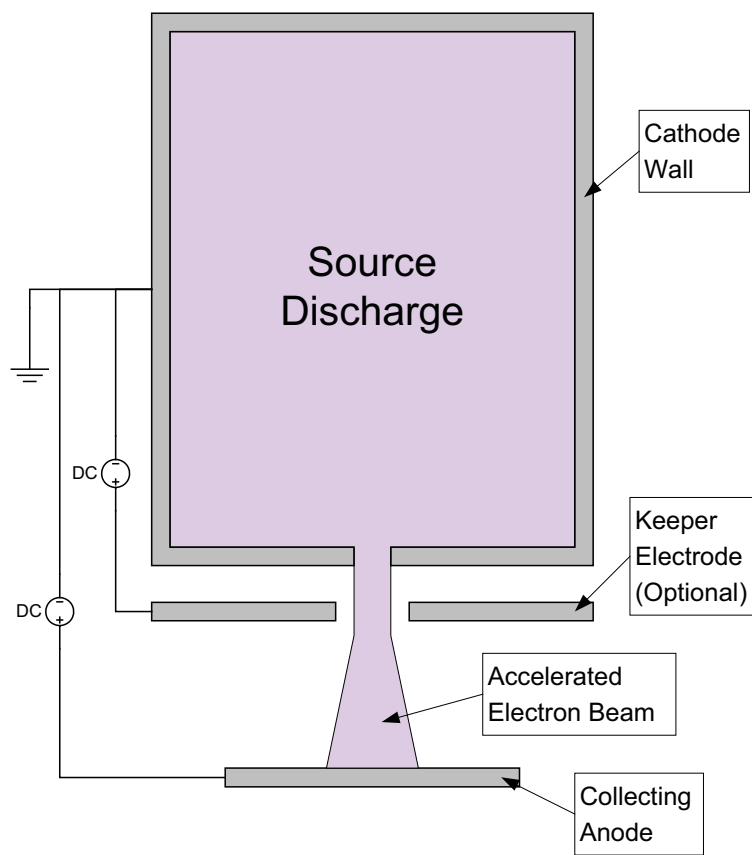
Figure 2.1: Schematic of a basic plasma cathode setup.

The extraction circuit consists of one or a series of external electrodes which are biased positively relative to the discharge chamber potential, to extract and accelerate electrons out of the device. In some cases, a "keeper" electrode is used to establish the extraction electric field at the aperture. The extraction anodes can be biased with either DC or pulsed power supplies, depending on the application.

2.2   Hollow Cathode Assembly

By far, the most well-established electron source in modern EP systems is the HCA. Originally developed in the 1960's, [62] the HCA combines some of the advantages of thermionic emitters with those associated with plasma cathodes. Because of its high power efficiency and legacy, the HCA has been employed as a discharge and neutralizer cathode on the vast majority of EP-driven missions.

A schematic of a typical HCA is shown in Figure 2.2. The cathode consists of a hollow tube with an aperture at the exit plane. The key component of the HCA is an annular thermionic emitter insert impregnated with work function-lowering material. The insert is situated at the downstream end of the cathode tube. A heater coil is wrapped around the cathode tube near the insert, and heats the insert so the surface of the insert emits electrons thermionically. A feed gas, typically high purity xenon, is injected from the upstream end of the tube, and flows past the insert and through the aperture. The emitted electrons from the insert ionize the feed gas as they flow through the cathode orifice. A dense plasma is formed within the orifice, mitigating space charge buildup and allowing a large amount of current to be extracted from the HCA. As electron current is extracted, ions in the hollow cathode are accelerated into the insert by the ion sheath at the surface, which gives rise to self-heating – eliminating the need for an external heater during HCA operation.

HCAs are exceptionally efficient electron sources from a power consumption standpoint. In plasma cathodes, the total power consumed is a combination of
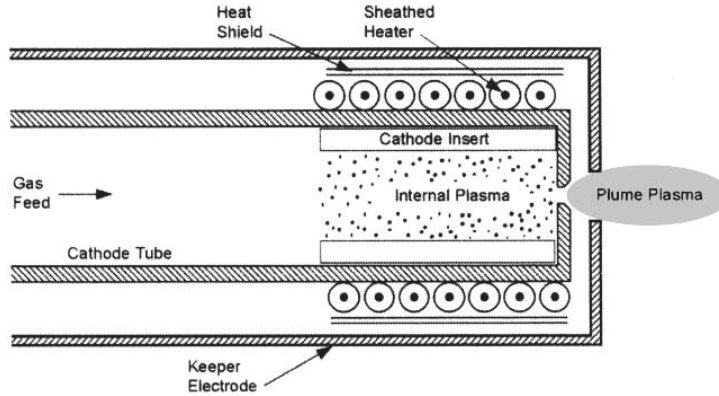
Figure 2.2: Schematic of a typical hollow cathode assembly with keeper electrode. Image from [25].

heating/discharge power, beam extraction power, and power consumed by ancillary components like electromagnets. HCAs have demonstrated tens to hundreds of amperes of extracted electron current while in self-heating mode, where the only power consumed is by current flowing to the keeper anode and/or external collector (*e.g.* ion beam).

Generally, high current levels are not required for neutralization of thruster beams. For example, the full power operating condition for the NASA's Evolutionary Xenon Thruster (NEXT) ion thruster requires 3.52 A of beam current and 3.00 A of keeper current, at a beam voltage of 10 V and keeper voltage of 11 V.[29] This translates to a total power consumption of just 10 W/A, which is an order of magnitude lower than can be achieved with emitterless plasma cathodes. The HCA is also a compact device, often less than 10 mm in diameter, which is another advantage of the HCA in EP applications. An example of the size of the HCA relative to an actual thruster is shown in Figure 2.3.

The HCA does have some drawbacks relative to emitterless plasma cathodes. The main consideration when using HCAs for EP systems is the potentially limited lifetime. For long-duration missions to the outer planets and beyond, or applications on semi-permanent structures like the ISS, HCA lifetime is a constraint. For example,

Figure 2.3: Photograph of HCA mounted with the NASA-103M.XL (HiVHAC) prototype thruster. Image from [38].

NASA's previously proposed Jupiter Icy Moons Orbiter (JIMO) mission to Europa, Ganymede, and Callisto was expected to require thruster and neutralizer lifetimes on the order of six to ten years. [56] However, the HCA has only recently been demonstrated in a 30,352 hour long-duration life test, with significant degradation of the HCA keeper electrode, although the emissive insert remained in operable condition. [64]

There are a handful of potential failure mechanisms for HCAs that have been identified. These include sputter erosion of the keeper electrode and cathode orifice, as well as depletion of the emissive material within the emissive insert, and poisoning of the emissive insert via surface reactions with trace contaminants in the feed gas. Electrode erosion has been a persistent problem in past HCA designs, but has largely been eliminated with the introduction of graphite as the keeper electrode material on the cathode for NEXT.[30] Emitter poisoning can be avoided through costly handling procedures and the use of extremely high purity (99.9995 percent pure) xenon feed gas.[26] Even if all other failure mechanisms are avoided, emitter impregnate depletion persists as an inherent limitation on the life of the HCA.

Conventional hollow cathodes use tungsten impregnated with a triple oxide mixture (BaO, SrO, and CaO) as the work function lowering material. In order to address the depletion-related lifetime constraints associated with impregnated oxide dispenser HCAs, alternative HCA designs have been investigated. An example of a LaB_6 based hollow cathode developed at JPL for ion and Hall thrusters is shown in Figure 2.4. The design is similar to that of conventional HCAs but the emitter is made of sintered LaB_6 stock that is machined into its annular shape. The advantage of LaB_6 over barium impregnated cathodes arises from the fact that the bulk LaB_6 is the emissive material itself, so the insert is immune to the poisoning and depletion failure modes. LaB_6 has a higher work function (2.67 eV) than barium-impregnated tungsten (2.06 eV), so the LaB_6 cathode must operate at a higher temperature

16
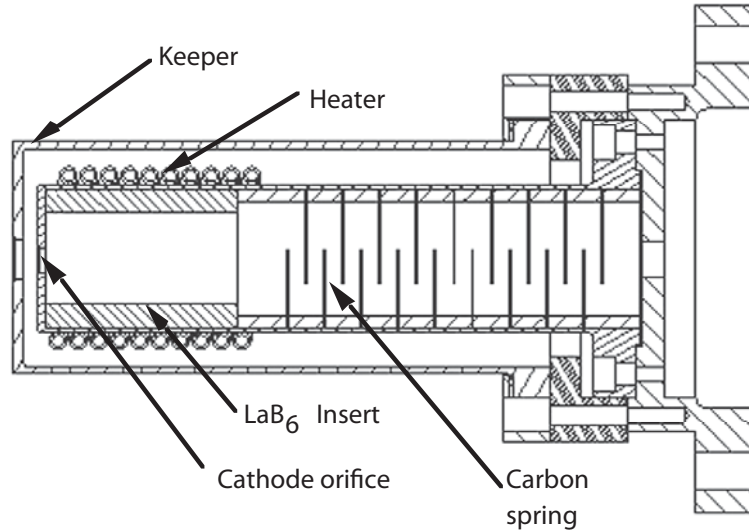
Figure 2.4: Schematic of the LaB6 hollow cathode, developed at JPL. Graphic adapted from [26].

than conventional cathodes. Because of the elevated operating temperature around 1600 °C, the use of LaB_6 places additonal constraints on the materials in contact with the insert. The JPL cathode demonstrated a total emitted current of up to 100 A, at typical discharge voltages around 25 V and xenon flow rates of 9 sccm. LaB_6 cathodes have been employed in Russian Hall thruster systems since 1972, mainly for satellite stationkeeping.[2] The potential lifetime of the LaB_6 cathode has been estimated at tens of thousands of hours, making it a potentially attractive alternative for long duration exploratory missions.

2.3 Electron Cyclotron Resonance Plasma

Another method of extending the lifetime of electron sources for EP systems has been to eliminate the emitter altogether, exploiting the plasma cathode approach. A variety of ionization mechanisms have been used for the source discharge, but the most established emitterless cathodes have featured ECR heating. ECR heating involves the resonant absorption of microwaves, propagating along static magnetic field lines, at the condition where the microwave frequency, f, equals the electron

cyclotron frequency. The electron cyclotron frequency, ω_{ce}, is given by,

$$\omega_{ce} = \frac{eB}{m},\tag{2.1}$$

where e is the elementary charge, B is the static magnetic field strength, and m is the electron mass. Microwaves in a plasma with a propagation vector parallel to the magnetic field can exist as either right hand circularly polarized (RHCP) or left hand circularly polarized (LHCP) waves. The RHCP wave has an electric field vector that rotates in the right-hand sense around the magnetic field line. Because electrons also orbit in the right-hand sense, at the resonance condition, electrons experience a constant acceleration by the electric field. Accelerated electrons collide with the feed gas atoms, sustaining a discharge through electron impact ionization. A more detailed treatment of the theory behind ECR heating is presented in Chapter 3.

2.3.1 Hayabusa – ECR Neutralizer

The state of the art of emitterless plasma cathode for EP applications is the neutralizer for the μ10 microwave ion thrusters on the Hayabusa exploratory spacecraft. Launched on May 9, 2003, Hayabusa successfully navigated to the asteroid Itokawa and touched down on the surface in September 2005, acquiring a sample of the astroid material. The spacecraft returned to Earth in March 2010, concluding the first demonstrated mission powered exclusively by microwave ion thrusters and neutralizers.[53]

A schematic of the μ10 neutralizer is shown in Figure 2.5. Xenon gas is fed into the neutralizer chamber at flow rates of 0.5 to 2 sccm, resulting in an internal pressure from 5 to 10 mTorr. The neutralizer uses 4.2 GHz microwaves to produce the discharge in a chamber with an inner diameter of 1.8 cm. The ECR heating zone is established by a ring of samarium cobalt permanent magnets, and microwaves were coupled into the resonant heating zone by an L-shaped antenna. The neutralizer

body was biased negatively relative to the thruster body, and electrons were drawn from the ECR discharge through an aperture on the downstream end.

Plasma densities on the order of 10^{12} cm^{-3} were measured at the ECR heating zone. This is a significantly overdense plasma for a 4.2 GHz source, roughly a factor of 10 higher than the ordinary wave cutoff density n_c, given by,

$$n_c = \frac{4\pi^2 f^2 m \epsilon_0}{e^2} \tag{2.2}$$

where ϵ_0 is the permittivity of free space. The production of overdense plasma is facilitated by the strong degree of confinement of electrons in the ECR heating zone. However, this comes at a cost, as the diffusion of electrons from the heating zone to the aperture is hindered by the strong magnetic field. The μ10 neutralizer was demonstrated at 0.5 sccm gas flow to deliver 140 mA of beam current, with 8 W of absorbed microwave power and a discharge voltage of -48 volts relative to the space potential of the ion beam. Taking the total power consumption as the sum of microwave power and beam extraction power, the electron production cost of the device is 105 W/A. The drastic difference between the ECR plasma cathode power requirements and those of the HCA demonstrates the main drawback of emitterless plasma cathodes: they are much less energy efficient than emitter-based sources. Nonetheless, for applications where lifetime is important, emitterless plasma cathodes may be the best choice. It should be noted that these electron sources are not truly "electrodeless," as they are often called, but instead are "emitterless," because the plasma cathode body itself is a positively biased electrode (relative to the thruster plume) that collects ion current from the source plasma.

Although the μ10 neutralizer was able to successfully complete the Hayabusa mission, this specific type of design may not be suitable for longer duration missions. During the development life tests of the μ10 neutralizer, it was observed that the launching antenna was continuously eroded by ion sputtering from the dense ECR
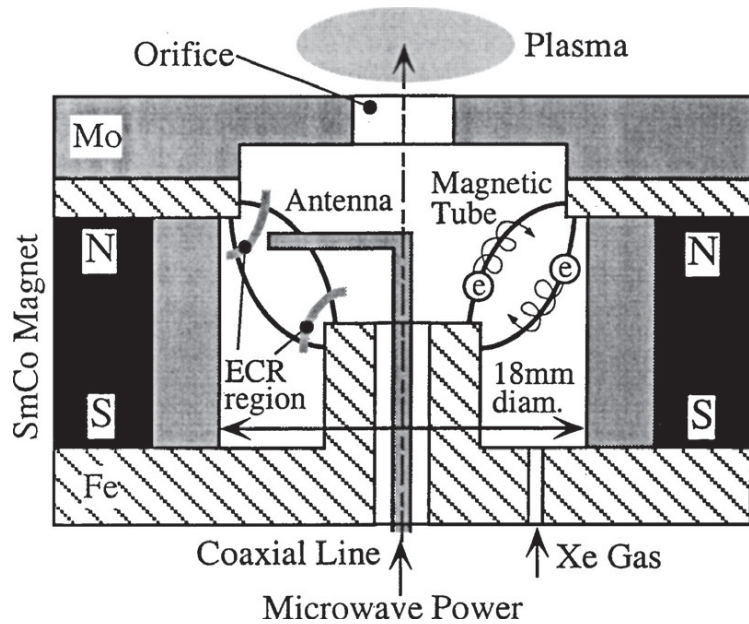
Figure 2.5: Schematic of the 4.2 GHz μ10 neutralizer on the Hayabusa spacecraft. Figure from [19].

discharge. After 5200 hours of operation, the antenna had eroded from a diameter of 1.5 mm to 0.9 mm at the tip and 1.3 mm at the root.[42] During the Hayabusa mission, two neutralizers had failed over time, and a third experienced degraded performance. The spacecraft employed an array of four thruster/neutralizer pairs, and the mission had to be completed through the use of one neutralizer with a separate thruster unit.[53]

2.3.2 Other ECR Plasma Cathodes

Other varieties of ECR plasma cathodes have been investigated as well. At NASA GRC, a coaxial-feed ECR plasma cathode was considered as a possible neutralizer source for the High Power Electric Propulsion (HiPEP) thruster. The initial design was similar to that of the μ10 neutralizer, but excited at a lower frequency, 2.45 GHz. Extraction through a circular aperture and a slot in the side of the source were both tested. The maximum extractable current from this source was measured at 2.45 A, at a flow rate of 3.5 sccm, microwave power of 125 W, and extraction bias of 70 V.[39]
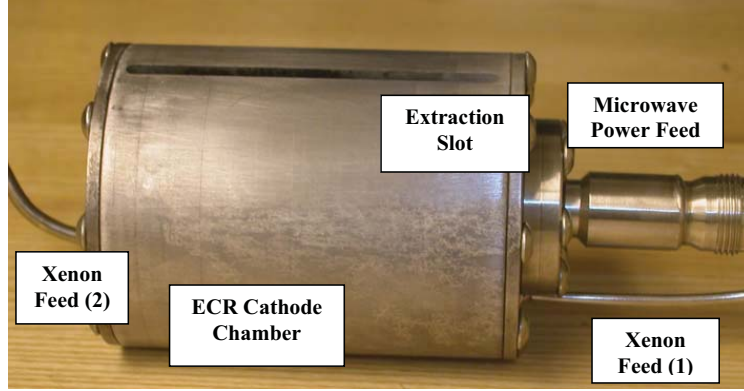
Figure 2.6: Photograph of the NASA 2.45 GHz ECR plasma cathode device. Figure from [39].

One ECR cathode developed at the University of Michigan (U-M) consisted of a "grill" loaded with an array of permanent magnets, which was used to set up a large area of ECR heating zones.[35] The ECR zones were established by five rows of samarium cobalt magnets, with five magnets in each row, and the source was typically operated with the magnet rows in attraction with neighboring rows, as shown in Figure 2.7. Microwaves were launched, through a lucite window, via a microwave horn which transitioned from WR-284 rectangular waveguide to a cross-section of 16.7 cm by 24.1 cm. The microwave electric field was oriented perpendicular to the grill "ribs", and the microwaves propagated through the slots in the grill to the ECR zones. Mild steel pole pieces were designed to push the resonance zones downstream from the grill (at about 1 cm downstream) and mitigate the absorption of microwaves on the upstream side of the magnets. Double Langmuir probes were used to measure a plasma density of 5×10^{10} cm^{-3}, which is just under the cutoff density for 2.45 GHz microwaves (7×10^{10} cm^{-3}). A graphite electrode was used to measure the extractable electron current from the source. Extracted currents up to 0.7 A were observed at 200 W of microwave power and an extraction bias of 40 V, for a total production cost of 320 W/A. The main limitation on extractable electron current was assumed to be the collection area for ions at the grill surface, which must be sufficient to balance
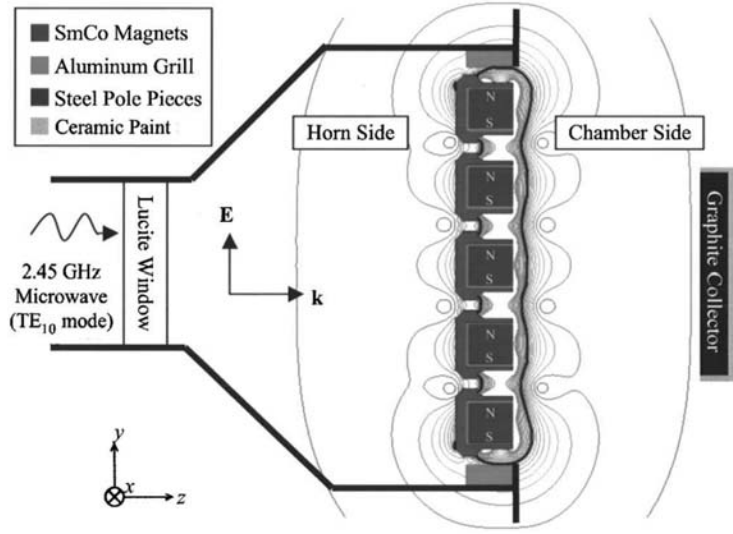
Figure 2.7: Schematic and magnetic field profile of the large area grill ECR plasma cathode. Figure from [35].

the electron current lost to the downstream anode.

2.4 Microwave Resonant Cavity Plasma

Another microwave plasma cathode in the literature was based on a plasma discharge in a microwave resonant cavity.[16] This source, which operated at 5.8 GHz, is shown in Figure 2.8. In the resonant cavity discharge, no static magnetic field is required; the discharge is heated directly via a strong microwave frequency electric field within the cavity. The TM_{011} resonant cavity mode was the basis for this design, with dimensions chosen according to,

$$f = \frac{1}{2\pi\sqrt{\mu_0\epsilon_0}}\sqrt{(2.405/r)^2 + (\pi/l)^2} \tag{2.3}$$

where μ_0 is the permeability of free space, r is the cavity radius, and l is the cavity length. The plasma cathode source chamber was a cylindrical section of waveguide, 4 cm in diameter. An alumina pressure window was mounted 10.2 cm upstream from the extraction aperture in order to separate the microwave launching antenna from
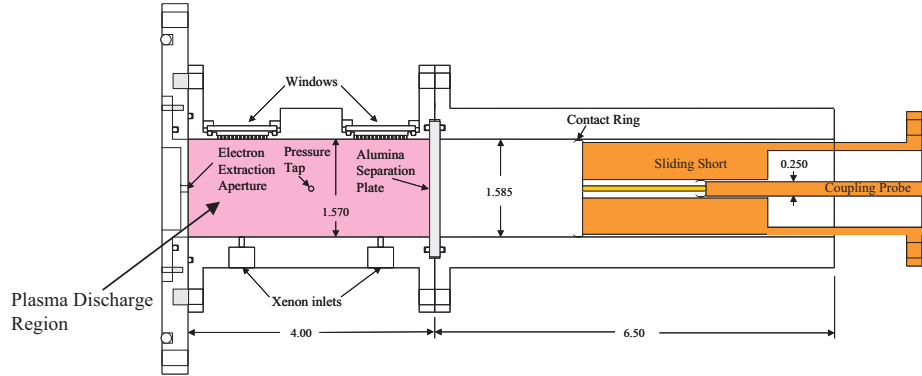
Figure 2.8: Schematic of the resonant cavity microwave plasma cathode. Figure adapted from [14].

the high density plasma, thereby avoiding the antenna sputtering limitation of the μ10 neutralizer. The source ran on xenon feed gas at pressures of 70 to 100 mTorr. The launching antenna was mounted on a sliding short upstream from the pressure window, and the short was used for load matching. Electron current was extracted through a downstream aperture by a keeper electrode in tandem with a downstream collection anode. Electron currents up to 2.1 A were extracted from this device, at absorbed microwave powers of 60 W and the extraction anode biased at 50 V. Additionally, the keeper electrode collected a constant 0.1 A, with a bias in the range of 40 to 50 V. An advantage of this resonant cavity design is the ability to establish a discharge away from the launching antenna without the use of magnetic fields that may hinder electron extraction from the device. However, since the incoming microwaves would propagate in the ordinary mode, the internal plasma density is limited by the cutoff density. At 5.8 GHz, this corresponds to 4.2×10^{11} cm^{-3} being the upper limit on the internal plasma density.

2.5   Inductively Coupled Plasma

A plasma cathode using an inductively coupled plasma (ICP) source discharge was developed by Godyak, *et.al.*[22] The discharge chamber was a 100 mm long

cylinder, 75 mm in diameter; the discharge was heated by an internal 25 mm diameter RF antenna energized at 2 MHz. The downstream extraction tube was 15 mm in diameter, and extractable electron current was measured using a movable electrode 2.5 cm in diameter. The plasma cathode was operated at a flow rate of 10 sccm, and at this flow rate the internal pressure was varied between 0.1 and 10 mTorr. Total extractable currents up to 1.4 A were achieved, and because the ratio of the area of the chamber walls to the electron loss area was less than $(\sqrt{M_i/2\pi m})$, the extracted current was limited by the ion loss area. Partial (RF only) power consumption values up to 33 W/A were documented, indicating a high degree of power absorption in the ICP discharge. Total efficiencies (RF plus beam extraction power) were documented at 80 W/A.[60]

2.6   Helicon Plasma

A much higher current plasma cathode was developed at the University of Wisconsin, which relies on a high density helicon discharge. The source, shown in Figure 2.9, may be suitable for very high power thruster systems in which tens of amperes of neutralizer current may be required. The helicon plasma cathode, known as the NES, is based on the principle of "non-ambipolar flow," in which virtually all ions are lost to one boundary of the plasma while all electrons are lost to the extraction aperture. The NES consists of a 6.0 cm inner diameter by 21 cm long graphite cylinder, centered in a 7.5 cm diameter by 25 cm long quartz tube. This was surrounded by a single turn of a water-cooled antenna that was used to excite the helicon mode at 13.56 MHz. The graphite sleeve has six axial slots which allow for inductive coupling to the internal plasma while suppressing plasma potential fluctuations that arise from capacitive coupling. The graphite cylinder is biased negatively with respect to an external electron extraction ring and collecting anode, both grounded. Global nonambipolar flow is established in the NES because the

electron current extracted through the aperture is balanced by ion current to the graphite sleeve. The ratio of the sleeve area to the aperture area in the NES was designed to establish this condition, assuming a uniform plasma density inside the device. When the cathode sleeve was biased at -40 V, emissive probe measurements detected the presence of an electron sheath at the extraction aperture. All electrons incident on this electron sheath would then be lost to the external anode. When the graphite sleeve is biased to a large negative value, the majority of bulk electrons are electrostatically prevented from reaching the sleeve by a high voltage sheath at the sleeve. The dominant electron loss area then becomes the electron sheath at the extraction ring, while ions are readily lost to the graphite sleeve. This is the condition of global nonambipolar flow, the theory of which is described in more detail in Chapter 3.

The NES delivered 30 A of electron current on 2 sccm of xenon feed gas and RF power of 1300 W under a -40 V bias.[48] On 15 sccm of argon, 15 A was extracted at an RF power of 1200 W and extraction bias of 40 V.[47] The NES, while efficient in the high-power regime, was tested with electromagnets in order to establish the nearly ideal magnetic field needed to sustain helicon discharges. This does provide an additional power requirement which somewhat counteracts the high efficiencies that were documented. Preliminary results of NES operation with permanent magnets in place of the electromagnets demonstrated an extractable current of up to 15 A on argon, but required the extraction ring and anode to be biased separately, so this may not be a simple problem to address.[27] However, for high current applications, and perhaps with further optimization of the magnetic field, the NES may be a promising alternative to the HCA.
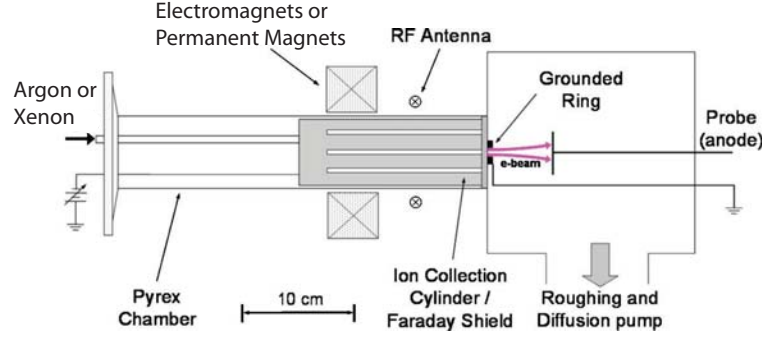
Figure 2.9: 3-D schematic image of the Nonambipolar Electron Source (NES). Figure from [48].

2.7 Design Principles from the Literature

The aforementioned plasma cathode studies provide useful insights regarding plasma cathode design. Based on the state of the art electrodeless plasma cathode, Hayabusa's μ10 neutralizer, one key lifetime limitation of these devices is sputtering erosion of components in contact with the source discharge. As shown by that device and the magnetic grill-based ECR plasma cathode, it is necessary to balance the increase in plasma density achieved by strong magnetic confinement in ECR sources with the ability to detach electrons from that magnetic field. Ion losses to the cathode walls, limited by the Bohm current, must be substantial enough to balance electron losses from the plasma cathode, or the extractable current will be limited, as seen in the ECR grill source and the ICP plasma cathode. However, when these losses are approximately balanced, efficient electron extraction can be achieved, as demonstrated by the NES. The ECR plasma cathode described in this dissertation was developed to combine these design rules of thumb.

CHAPTER III

Theory

A number of fundamental processes govern the operation of the plasma cathode. First is the ionization mechanism for the source discharge, which supplies the electrons to be extracted. For the plasma cathode described herein, ECR heating is the primary ionization mechanism. Another important aspect is the transport of electrons to the extraction aperture of the device and the corresponding motion of positive ions to the plasma cathode walls. At each of these boundaries, sheaths develop which either enhance or hinder electron or ion losses. Of particular interest is the extraction and acceleration of electrons from a free plasma boundary at the extraction aperture. The theory behind each of these relevant processes is summarized in this chapter.

3.1 Electron Cyclotron Resonance Discharges

3.1.1 Wave Propagation in Plasmas

Because of the discrepancy in mass between electrons and ions in a plasma, microwave frequency perturbations in a plasma will strongly affect the motion of the electrons while leaving ions relatively undisturbed. Under the influence of an electric field, the acceleration of ions is less than the electron acceleration by a factor of $\sqrt{m_e/M_i}$, where m_e is the electron mass and M_i is the ion mass. Over a microwave cycle, the displacement of electrons is therefore much larger than that of the ions.

In a model of microwave propagation in plasma, the interaction of electrons with the microwave electric field are considered, while the ions are assumed to remain motionless over the relevant timescale.

3.1.2 Ordinary Waves

The simplest propagation mode for electromagnetic waves in a plasma is that of the ordinary wave (O-wave). Here, it is assumed that the plasma is unmagnetized, and because the O-wave is a transverse wave, the wave electric field vector $\mathbf{E_1}$, wave magnetic field vector $\mathbf{B_1}$, and propagation vector $\mathbf{k_1}$ are mutually perpendicular. Let the wave propagation be in the $\hat{z}$ direction, the electric field along $\hat{x}$, and magnetic field along $\hat{y}$. If we assume that all quantities have a $\exp\left(i\left(kz - \omega t\right)\right)$ dependence, then a linearized form of Faraday's law,

$$\nabla \times \mathbf{E} = -\frac{\partial \mathbf{B}}{\partial t} \tag{3.1}$$

can be written as,

$$ikE\hat{y} = i\omega B\hat{y} \tag{3.2}$$

and similarly, Ampere's law,

$$\nabla \times \mathbf{B} = \mu_0 \mathbf{J} + \frac{1}{c^2}\frac{\partial \mathbf{E}}{\partial t} \tag{3.3}$$

can be written as,

$$-ikB\hat{x} = \mu_0 J_1 \hat{x} - \frac{1}{c^2}i\omega E\hat{x} \tag{3.4}$$

where $J_1 = env_1$ is the electron current density in response to the microwave fields, v_1 is the perturbed electron velocity and c is the speed of light. The velocity perturbation

is related to the electric field via the linearized momentum equation,

$$i\omega v_1 = \frac{e}{m_e} E_1. \tag{3.5}$$

Equations (3.1 – 3.5) can be combined to solve for the dispersion relation for the O-wave,

$$\omega^2 = \omega_{pe}^2 + k^2 c^2. \tag{3.6}$$

where ω_{pe} is the plasma frequency, defined as:

$$\omega_{pe}^2 = \frac{ne^2}{m\epsilon_0}. \tag{3.7}$$

Wave propagation can only occur for the case when the wavenumber is real-valued, which occurs when:

$$\omega > \omega_{pe}, \tag{3.8}$$

or in terms of plasma densities, the plasma density n must be less than the critical density n_c defined in terms of the microwave frequency:

$$n_c = \frac{4\pi^2 f^2 m_e \epsilon_0}{e^2} \tag{3.9}$$

The frequency associated with n_c is known as the cutoff frequency. When the plasma density exceeds the cutoff value, the majority of incident microwave energy will be reflected, while some will decay in an evanescent fashion, with an e-folding length equivalent to the plasma skin depth. The presence of an upper density limit for microwave propagation presents an obstacle to some microwave-heated plasma cathode designs. In the case of resonant cavity sources that operate based on surface wave heating, the cutoff density can be responsible for limiting the extractable electron

current from the device.

3.1.3 Other Electromagnetic Plasma Waves

A similar treatment can be applied to waves traveling along a static magnetic field, taking into account two polarization components, E_{1x} and E_{1y}, with corresponding magnetic field quantities B_{1x} and B_{1y}. The solution of the momentum equation, Ampere's Law, and Faraday's law for this configuration gives two dispersion relations,

$$\frac{k^2 c^2}{\omega^2} = 1 - \frac{\omega_{pe}^2}{\omega\left(\omega + \omega_{ce}\right)} \tag{3.10}$$

and,

$$\frac{k^2 c^2}{\omega^2} = 1 - \frac{\omega_{pe}^2}{\omega\left(\omega - \omega_{ce}\right)}, \tag{3.11}$$

where ω_{ce} is the electron cyclotron frequency, given by,

$$\omega_{ce} = \frac{eB}{m_e}, \tag{3.12}$$

where B is the static magnetic field strength. The dispersion relations given by Equations (3.10) and (3.11) designate the LHCP and RHCP waves, respectively. Waves in a medium are cut off from propagation when the index of refraction, $N = kc/\omega$, is equal to zero, and resonantly absorbed when N increases without bound. For the RHCP wave, a resonant condition occurs for $\omega = \omega_{ce}$, that is, when the frequency of the wave matches the orbit frequency of electrons in the magnetic field. The reason for this can be shown schematically in Figure 3.1. The electric field vector rotates in the right-hand sense around the magnetic field line at the angular frequency ω. When the ECR condition is met, electrons can orbit in phase with the electric field and continuously absorb energy from the microwave electric field. This heating mechanism is exploited in ECR plasma cathodes.
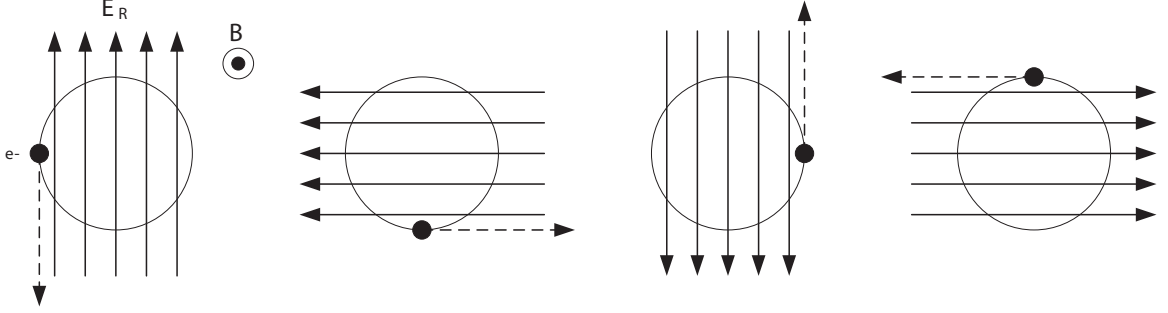
Figure 3.1: A cartoon of ECR heating, showing the orientation of the RHCP wave electric field and electron motion at phases in multiples of $\pi/2$. Figure based on [44].

The RHCP wave experiences a cutoff at the right hand cutoff frequency, ω_R,

$$\omega_R = \frac{\omega_{ce} + \sqrt{\omega_{ce}^2 + 4\omega_{pe}^2}}{2}.$$
(3.13)

The resonant absorption of microwaves at the electron cyclotron resonance conditions requires that the wave be launched in the direction of a decreasing magnetic field. This unimpeded absorption is illustrated on the Clemmow–Mullaly–Allis (CMA) diagram, as shown in Figure 3.2. Here, the quantity $\omega_{ce}\omega_{ci}/\omega^2$ is plotted against the quantity ω_p^2/ω^2. In this sense, the diagram (which includes ion dynamics) shows increasing magnetic field along the vertical axis, increasing plasma density along the horizontal axis, and in general, the upper right corner corresponds to lower frequency oscillations. The right hand cutoff is shown as the dashed line while the electron cyclotron resonance is the solid line. In the regime of $\omega > \omega_{ce}$ and $\omega > \omega_{pe}$, the right hand cutoff is consistently on the side of lower magnetic field than the resonance, so if one moves from a low field to high field configuration on the CMA diagram, the cutoff is encountered before the resonance. The spacing between the cutoff and resonance, and therefore the effect on the incoming wave, depends on the plasma density. When launched from the low-field side, some fraction of the incident microwave will be reflected, while some can tunnel through to the resonance in an evanescent fashion. However, when the wave is launched from the high-field side, the

$\frac{\omega_{ce}\,\omega_{ci}}{\omega^2}$

$\omega = \omega_{ci}$

$\frac{m_+}{m_-}$

$u_l = 0$

Increasing B

$u_0 = \infty$

v_{ph} c $\mathbf{B}_0$

$u_x = 0$

$\omega = \omega_{pe}$

$\omega = \omega_{ce}$

$\frac{m_-}{m_+}$

$u_R = 0$

$u_l = u_x = \infty$

$u_r = \infty$

1   Increasing n $\frac{\omega_p^2}{\omega^2}$
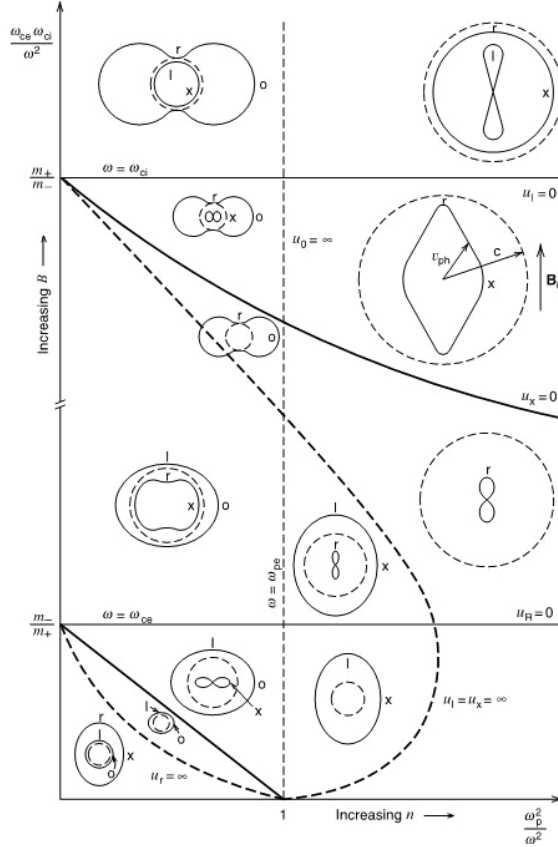
Figure 3.2: The CMA diagram. Resonances are shown as solid lines and cutoffs as dashed lines. Figure from [1].

resonance is encountered before the cutoff and the wave is completely absorbed.[45]

3.1.4 Waveguide Modes

In order to separate the launching antenna from the plasma, it is necessary to understand the microwave propagation in the plasma cathode chamber. Microwaves are often steered through sections of waveguide, which form a complete conducting boundary around the direction of propagation. The wave travels along the waveguide via the alternating current and corresponding electric fields induced in the waveguide walls by the wave.

Microwave propagation can take place in either transverse electric (TE) or transverse magnetic (TM) modes, which can be determined by solving the wave

equation with conducting boundaries corresponding to the waveguide walls. The solution gives a semi-infinite series of TE and TM modes, depending on the waveguide dimensions and material within the waveguide, and are commonly denoted by eigenvalues n and m. There is a minimum frequency that can propagate along a waveguide for a given dimension. For TE modes in cylindrical waveguide, the series of cutoff frequencies is given by,

$$f_{c,nm} = \frac{p'_{nm}}{2\pi a\sqrt{\mu\epsilon}} \tag{3.14}$$

where $f_{c,nm}$ is the cutoff frequency, a is the waveguide radius, μ and ϵ are the permeability and permittivity, respectively, of the material in the waveguide, p'_{nm} is the mth root of J'_n, and J'_n is the derivative of the nth Bessel function of the first kind. Conversely, for a given frequency, a minimum waveguide radius can be determined according to,

$$a_{c,nm} = \frac{p'_{nm}}{2\pi f\sqrt{\mu\epsilon}} \tag{3.15}$$

where $a_{c,nm}$ is the cutoff radius for mode TE_{nm}. The cutoff radii for the TM modes are given by,

$$a_{c,nm} = \frac{p_{nm}}{2\pi f\sqrt{\mu\epsilon}} \tag{3.16}$$

where p_{nm} is the mth root of J_n and J_n is the nth Bessel function of the first kind.

Mode competition between allowed TE and TM modes in a waveguide can cause undesirable changes in the electromagnetic field patterns in the waveguide, which can in turn affect coupling and plasma uniformity. Mode competition can be addressed in two ways. Resistive elements or slots can be placed in regions of the waveguide wall to hinder the flow of the current patterns that drive unwanted modes. Depending on the wave frequency, one can also limit the propagation of higher order modes by
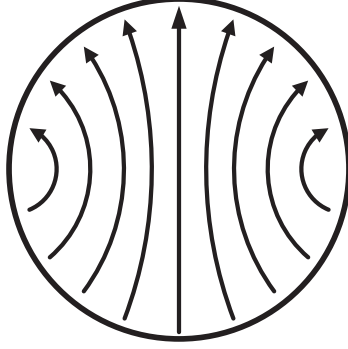
Figure 3.3: Electric field pattern in the circular TE_{11} mode.

using a waveguide radius below the cutoff of the undesired modes. In a cylindrical waveguide, the smallest cutoff radius corresponds to the circular TE_{11} mode, and the next largest radius corresponds to the TM_{01} mode. By choosing the waveguide radius between these two cutoffs, propagation in the TE_{11} mode alone can be assured. The electric field pattern of the TE_{11} mode is shown in Figure 3.3. The field vectors are oriented perpendicular to the waveguide axis and terminate perpendicular to the waveguide wall. The electric field magnitude is peaked on axis and has a null at the wall, in the direction perpendicular to the polarization.[59]

The effective propagation wavelength of electromagnetic radiation in a waveguide differs from that in free space. The waveguide wave number, k_z is calculated from the free space wave number $k_0 = 2\pi f/c$ and the cutoff wave number k_c, according to,

$$k_z = \sqrt{k_0^2 - k_c^2}. \tag{3.17}$$

The "guide" wavelength along the direction of propagation is then given by $\lambda_g = 2\pi/k_z$. The cutoff wave number depends on the waveguide radius as well, and for the circular TE_{11} mode, is found from $k_c = 1.841/a$.

3.1.5 ECR Heating Models

The source of electrons in the U-M plasma cathode is an ECR discharge produced within the waveguide. ECR heating can be briefly described as the resonant absorption by electrons of energy in RHCP waves in a plasma. While modeling of ECR heating is still an area of active research, some theoretical studies have been undertaken to predict the relationship between absorbed power, pressure, field strength, and plasma density. An analytical one-dimensional calculation by Lieberman estimates the power requirements for collisionless ECR heating in a non-uniform magnetic field.[45] One can expand the electron cyclotron frequency in a region near the resonance zone according to,

$$\omega_{ce}(z') = \omega(1 + \alpha z')$$ (3.18)

where $z' = z - z_{\text{res}}$ is the distance from the resonance location and $\alpha = (1/\omega_{ce})(\partial \omega_{ce}/\partial z')_{\text{res}}$. By using the collisionless complex momentum equation including the ECR electric field and averaging over the initial phase difference between electron motion and the electric field, the average energy gained as a single electron traverses the resonance zone W_{ecr} can be found:

$$W_{\text{ecr}} = \frac{\pi e^2 E_r^2}{m\omega|\alpha|v_{\text{res}}}$$ (3.19)

where E_r is the electric field strength at resonance and v_{res} is the parallel speed of the electron through the resonance zone. The electron flux incident on the resonance zone is nv_{res}. Multiplying the energy gain per electron (Equation 3.19) by the incident flux gives the total power absorbed per unit area, S_{ecr}:

$$S_{\text{ecr}} = \frac{\pi n e^2 E_r^2}{m\omega|\alpha|}.$$ (3.20)

For this calculation, the absorbed power in collisionless ECR heating is proportional to the plasma density and the square of the electric field at resonance. Similar calculations have been carried out that take into account the effect of electron collisions on ECR heating, but these are not typically applicable in ECR discharges where the electron residence time in the resonance zone is often much shorter than the mean collision time.

3.2 Charged Particle Transport

In low-temperature plasmas, particle transport over the length of the discharge is dominated by collisions with neutrals if the pressure is sufficiently high. The mean free path for electron-neutral collisions, λ_e, is:

$$\lambda_e = \frac{1}{\sigma_{el} n_g} \tag{3.21}$$

where, σ_{el} is the elastic scattering cross section and n_g is the neutral gas density. The ion-neutral mean free path is similarly defined using the ion-neutral scattering cross-section. If the mean free path for a species is shorter than the discharge dimensions, then the species will undergo collisions before reaching the plasma boundary. In that case, collisional processes must be considered in the macroscopic transport of the species in the discharge.

3.2.1 Mobility

In an unmagnetized plasma, the effect of collisions can be introduced in the momentum equation via a collision term in the two-fluid model:

$$mn \left[\frac{d\mathbf{v}}{dt} + \mathbf{v} \cdot \nabla \mathbf{v} \right] = qn\mathbf{E} - \nabla P - mn\nu_m \mathbf{v} \tag{3.22}$$

where q is the fluid element charge, $\mathbf{v}$ is the bulk velocity of the species, $P = nk_B T$

is the pressure associated with the species, and ν_m is the collision frequency for momentum transfer. In steady state, Equation (3.22) reduces to,

$$qn\mathbf{E} - \nabla P - mn\nu_m\mathbf{v} = 0. \tag{3.23}$$

and with the definition of particle flux $\Gamma = n\mathbf{v}$,

$$\Gamma = \mu n\mathbf{E} - D\nabla n \tag{3.24}$$

where we define the particle mobility μ as,

$$\mu = \frac{q}{m\nu_m} \tag{3.25}$$

and the particle diffusion coefficient D as,

$$D = \frac{k_B T}{m\nu_m} \tag{3.26}$$

The particle mobility is a quantity that relates the bulk flow of a species to the applied electric field, taking into account the microscopic effects of collisions with other species.

3.2.2 Diffusion

Even in the absence of an applied electric field, a single species of particles will tend to diffuse away from regions of high concentration, via collisions, according to:

$$\frac{\partial n}{\partial t} - D\nabla^2 n = G - L \tag{3.27}$$

where G and L are terms representing production and loss rates, respectively. However, in a quasineutral plasma, the diffusion rates are influenced by the interaction between electrons and ions. To maintain quasineutrality, the flux of electrons entering

or leaving a volume must equal that of the ions:

$$\mu_i n \mathbf{E} - D_i \nabla n = \mu_e n \mathbf{E} - D_e \nabla n, \tag{3.28}$$

where subscripts i and e denote the relevant quantities for ions and electrons. Initially, electrons diffuse away from a region at a faster rate than the ions. This charge separation gives rise to the formation of an ambipolar electric field:

$$\mathbf{E} = \frac{(D_i - D_e)\nabla n}{(\mu_i + \mu_e)n}. \tag{3.29}$$

This field slows the outward flux of electrons, and a balance is reached wherein the electrons and ions diffuse at the same rate. If the electron and ion fluxes are equal, $\Gamma = \Gamma_e = \Gamma_i$, and the common flux can be written as $\Gamma = D_a \nabla n$, with the ambipolar diffusion coefficient D_a defined as,

$$D_a = \frac{\mu_i D_e + \mu_e D_i}{\mu_i + \mu_e} \tag{3.30}$$

Ambipolar diffusion is the dominant transport mechanism for ions and electrons in a quasineutral plasma. For common laboratory discharges, Equation (3.30) can be simplified further by the assumptions $\mu_e \gg \mu_i$ and $T_e \gg T_i$. This leads to an ambipolar diffusion coefficient with a value of $D_a = D_i T_e / T_i$, implying that both species diffuse at an intermediate rate, between the single-species ion and electron diffusion rates.

3.2.3   Plasma Confinement

The presence of a magnetic field further complicates particle transport. Parallel to the magnetic field lines, diffusion takes place at the same rate as in unmagnetized plasmas. For motion perpendicular to the field, however, the transport of electrons across field lines is suppressed significantly when the electron Larmor radius, $mv_\perp / eB$,

is much smaller than the physical dimensions of the discharge. Transport across field lines follows from a two-fluid analysis including the magnetic force term ($q\mathbf{v} \times \mathbf{B}$). Transport is then described by the incorporation of the Hall parameter (ω_c/ν_m) in the perpendicular mobility and diffusion coefficients, $\mu_\perp$ and $D_\perp$:

$$\mu_\perp = \frac{\mu}{1 + (\omega_c/\nu_m)^2} \tag{3.31}$$

and,

$$D_\perp = \frac{D}{1 + (\omega_c/\nu_m)^2} \tag{3.32}$$

For high magnetic fields, the Hall parameter $\omega_{ce}/\nu_m \gg 1$, implying that magnetic effects dominate collisional effects. In this limit, the diffusion coefficient and mobility of electrons across field lines scale inversely with the square of the magnetic field strength. If it is assumed that the plasma solely diffuses perpendicular to magnetic field lines, transport is governed by magnetized ambipolar diffusion:

$$D_{\perp a} = \frac{\mu_i D_{\perp e} + \mu_e D_{\perp i}}{\mu_i + \mu_e}, \tag{3.33}$$

which can again be simplified by the assumption that $\mu_e \gg \mu_i$, giving $D_{\perp a} \approx D_{\perp i}$. In practice, ambipolar diffusion in a magnetic field is more complex because electrons readily diffuse along field lines. The ambipolar electric field established by the charge separation between electrons and ions diffusing across field lines is shielded out by electrons rapidly flowing along the field lines. In this case, rather than solving for a balance of electron and ion fluxes ($\mathbf{\Gamma}_e = \mathbf{\Gamma}_i$), continuity must by satisfied by equating the divergences: $\nabla \cdot \mathbf{\Gamma_e} = \nabla \cdot \mathbf{\Gamma_i}$.

Often it is experimentally observed that cross-field diffusion occurs faster than is predicted classically. In this case, it is proposed that instabilities can facilitate anomalous diffusion across field lines, giving rise to the Bohm diffusion coefficient: [8]

$$D_{\text{Bohm}} = \frac{k_B T_e}{16B}. \tag{3.34}$$

3.3 Sheaths

Sheaths are regions of non-neutral charge density which usually appear at the boundaries of plasmas. As a result, nonzero electric fields arise in the sheath, which act on electrons and ions that enter the sheath. The structure of the sheath depends on the relative loss rates of the charged particles at the boundary. There are a variety of sheath types, as described below.

3.3.1 Ion Sheaths and Presheaths

The most simple sheath is that established by a plasma in contact with a conducting surface at a potential Φ. Because the particles in the plasmas rearrange in response to an electric field, a quasineutral plasma will tend to shield out applied potentials. Assume a cold plasma with constant ion density $n_i = n_0$ and an electron density that has a Boltzmann distribution $n_e = n_o \exp(e\Phi/k_B T_e)$. Poisson's equation then gives for a simple planar geometry,

$$\frac{d^2\Phi}{dx^2} = \frac{en_0}{\epsilon_0} \left(\exp(e\Phi/k_B T_e) - 1 \right). \tag{3.35}$$

Assuming that $e\Phi \ll k_B T_e$, one can linearize the result to find,

$$\frac{d^2\Phi}{dx^2} = \frac{en_0\Phi}{\epsilon_0 k_B T_e} \tag{3.36}$$

and therefore,

$$\Phi(x) = \Phi_0 \exp(-|x|/\lambda_D) \tag{3.37}$$

where λ_D is the Debye length, defined as,

$$\lambda_D = \left(\frac{\epsilon_0 k_B T_e}{e n_0} \right). \tag{3.38}$$

Equation 3.38 gives, to first order, the length scale over which a potential is shielded out in a plasma. It arises through a balance of the electron temperature and applied potential Φ, and it decreases as the number of available particles for shielding out the potential n_0 is increased.

Without linearizing Poisson's equation, and taking into account conservation of ion energy and ion continuity, the sheath potential is governed by:

$$\frac{d^2\Phi}{dx^2} = \frac{e n_s}{\epsilon_0} \left[\exp(e\Phi/k_B T_e) - \left(1 - \frac{e\Phi}{W_i} \right)^{-1/2} \right] \tag{3.39}$$

where n_s is the quasineutral plasma density at the sheath boundary and W_i is the incident ion energy at the sheath edge. For the electric field arising from Equation (3.39) to have a real solution, the ion speed at the sheath edge u_s must satisfy the Bohm criterion,

$$u_s \geq u_B = \sqrt{\frac{k_B T_e}{M_i}}. \tag{3.40}$$

Because the ions must enter the sheath at the Bohm speed, there must be an accelerating electric field in the bulk plasma to accelerate the ions from $T_i \approx 0$ to the Bohm speed u_B. This is achieved through a presheath potential drop, much smaller in magnitude than the sheath potential itself, but acting over a distance of several Debye lengths. The plasma potential in the bulk plasma with respect to the potential at the sheath/presheath interface is $\Phi_p - \Phi_s = k_B T_e/2e$.

3.3.2 High Voltage (Space Charge-Limited) Sheaths

When the sheath potential difference is much larger than the electron temperature in eV, then it can be assumed that the sheath itself is completely devoid of negative space charge. Again using conservation of ion energy in the sheath, the continuity equation, and Poisson's equation, we find for a planar geometry,

$$\frac{d^2\Phi}{dx^2} = -\frac{J_0}{\epsilon_0}\sqrt{\frac{2e\Phi}{M_i}} \tag{3.41}$$

where J_0 is the ion current density. Integrating and choosing $\Phi = 0$ and $E = 0$ at $x = 0$, and defining the potential $\Phi = -V_0$ at the sheath edge, gives the Child-Langmuir Law for space charge limited sheaths:

$$J_0 = \frac{4\epsilon_0}{9}\sqrt{\frac{2e}{M_i}}\frac{V_0^{3/2}}{s^2} \tag{3.42}$$

Equation (3.42) presents a limitation on the magnitude of current that can be transported through a sheath of thickness s under a voltage V_0. This becomes relevant when estimating the ion current lost to the walls of discharges with a plasma potential several times the electron temperature. The Child-Langmuir law also holds true when calculating the amount of electron current that can be transported across a vacuum gap, with the electrode spacing d replacing the sheath thickness s. The limitation on current transport arises from the effect of space charge on the applied potential. The space charge suppresses the electric field at the emission surface. A balance is established between this shielding effect and the applied potential, determining the space charge limited current.

3.3.3 Double Layer Sheaths

Double layer sheaths are those which arise from two adjacent regions of electron and ion space charge, resulting in a potential gradient of varying curvature. They
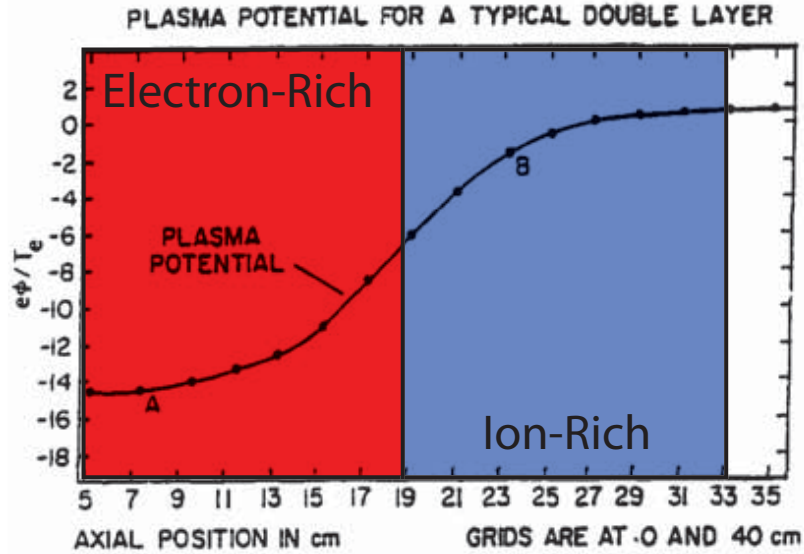
Figure 3.4: Example of a double layer potential profile. Image adapted from [33] to show electron- and ion-rich regions.

have been observed in several configurations, including at the surface of positively biased anodes immersed in plasma [4, 5, 70], in expanding magnetic fields [21], at the interface between plasma contactor plumes and the ambient space plasma [73], and at the exit plane of plasma electron sources. [48] An example of a double layer potential profile is shown in Figure 3.4

Double layer sheaths can be established by the relatively fast depletion of electrons from a region, which then leaves an ion-rich region in its place. This is usually facilitated by asymmetric boundary conditions at two different plasma boundaries. Double layers can exist far from any plasma boundary, but are thought to be coupled to the boundary through a presheath.[34] In order for the double layer solution to be stable, the Bohm criterion must still be satisfied for incident ions; therefore, ions must still be accelerated to the Bohm speed by a presheath. Presheaths can span length scales on the order of the plasma device dimensions, so double layers can exist nearly anywhere in a plasma discharge.[33] The experimental results in Chapter 7 show that double layer sheaths may play an important role in the extraction of electrons from the source discharge at the plasma cathode aperture.

43
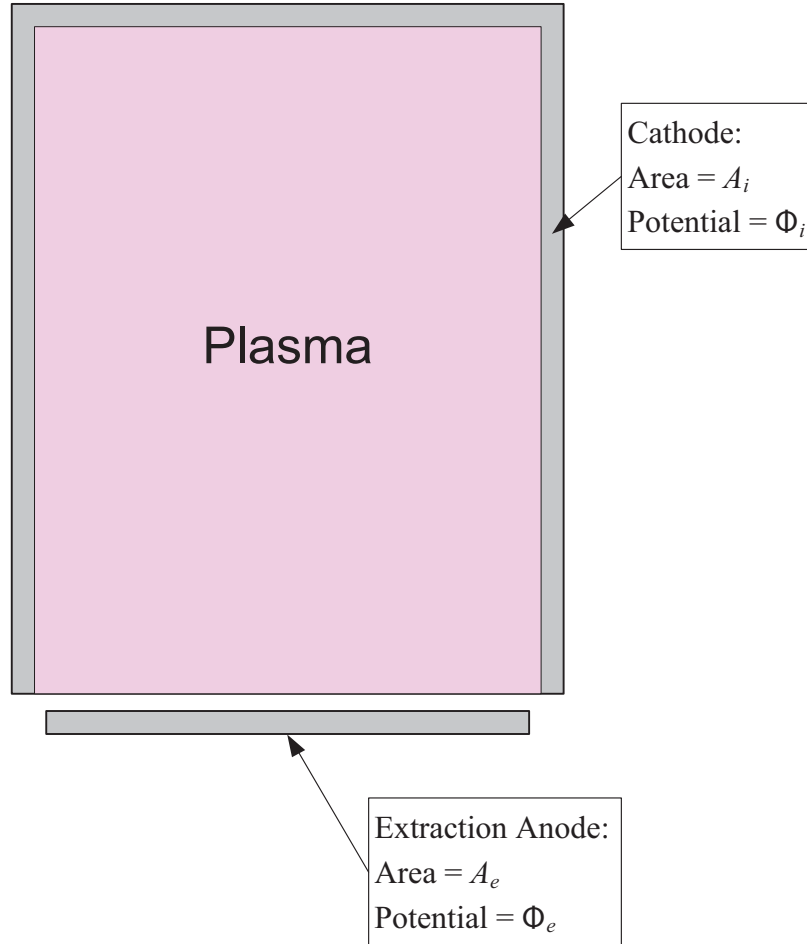
Figure 3.5: Schematic of plasma bounded by two conductors.

3.4   Electron Extraction from Plasma

Electron extraction from a plasma depends on the global plasma parameters as well as the geometry of the extraction circuit. A general theory of plasma cathode operation has been described by Oks, summarized here. [54]

Assume that plasma is bounded by a surface consisting of two parts, as illustrated in Figure 3.5. The first part is a cylindrical conductor, completely surrounding the plasma with the exception of one end of the cylinder. This conductor, referred to as the cathode, has a potential Φ_i and total area A_i. The second boundary is conducting disc called the "extraction anode", at the open end of the cylinder, with potential Φ_e and area A_e. Ions are lost to the surfaces at equal current densities given by the

Bohm current. Therefore, the ion current lost to the cathode wall, $I_{i,i}$ is,

$$I_{i,i} = J_i A_i = 0.61en\sqrt{\frac{k_B T_e}{M_i}}A_i \qquad (3.43)$$

where J_i is the Bohm current density. Similarly, the ion current lost to the extraction anode $I_{i,e}$ is given by,

$$I_{i,e} = J_i A_e = 0.61en\sqrt{\frac{k_B T_e}{M_i}}A_e \qquad (3.44)$$

Note that the ion loss rate is independent of the anode or cathode potentials. For electrons, the picture is slightly different, because an electron is only lost when it has enough energy to overcome the sheath potential barrier. The electron current lost to the cathode $I_{e,i}$ is given by,

$$I_{e,i} = J_{e,i} A_i = J_{e,\text{sat}} \exp[-e(\Phi_p - \Phi_i)/k_B T_e]A_i \qquad (3.45)$$

where $J_{e,\text{sat}} = 0.25en\sqrt{8k_B T_e/\pi m}$, Φ_p is the plasma potential, and Φ_i is the cathode wall potential. Similarly, the electron current lost to the anode $I_{e,e}$ is,

$$I_{e,e} = J_{e,e} A_e = J_{e,\text{sat}} \exp[-e(\Phi_p - \Phi_e)/k_B T_e]A_e. \qquad (3.46)$$

If both electrodes are at the same potential, then electron and ion losses are uniform and balanced at every surface. When the electrodes are at different potentials, then the plasma responds in order to globally conserve current losses. If the anode is biased positively relative to the cathode, the ion losses to both surfaces remain the same as in the unbiased case. The total electron loss rate remains equal to the ion loss rate, so $I_{i,i} + I_{i,e} = I_{e,i} + I_{e,e}$. At the condition where $\Phi_e > \Phi_i$, conservation of current along with Equations (3.45) and (3.46) dictate that the fraction of electron current lost to the anode increases and the fraction of electrons lost to the cathode

decreases. In order for this to occur, the global plasma potential necessarily increases to increase the cathode sheath potential and suppress the number of electrons that can overcome the cathode sheath.

The maximum current density that can be extracted is limited by the electron saturation current $J_{e,\text{sat}}$, which is approached as $\Phi_e \to \Phi_p$. Although the plasma potential increases with applied bias, it is possible for the collector potential to increase at a faster rate than Φ_p. Once the maximum current density is extracted, electrons can then be accelerated in the regime where $\Phi_e > \Phi_p$.

Because the extractable current is limited by the ion current to the cathode walls, plasma cathodes should be designed so that $A_e \ll A_i$. This usually leads to plasma cathodes in which electrons are extracted from an aperture which is much smaller than the cathode wall area. The use of an aperture adds a second benefit to the cathode design, in that it reduces the gas consumption rate at a given internal operating pressure, which is an important consideration in EP applications.

Oks suggests that the dimensions of the extraction aperture relative to the internal plasma properties should be considered.[55] The aperture radius r_e relative to the sheath width s determines the location of the plasma boundary at the aperture, placing another constraint on the extractable current. Three limiting cases are shown in Figure 3.6. When $r_e \ll s$, the quasineutral plasma boundary is separated from the aperture plate by a thick sheath and electrons must overcome a potential barrier to be lost through the aperture, similar to electrons lost to the cathode wall. In the opposite case, $r_e \gg s$, the sheath is quite thin and the quasineutral plasma expands through the aperture and into the gap. This allows for the maximum extractable current, equal to the thermal electron current density through the aperture. In this case the perturbation of the plasma potential by the applied bias is substantial, so this regime may not be the best for applications in which the extracted electron energy is important. The intermediate case, where $r_e \approx s$, the potential barrier is nearly zero

(a) $r_e \ll s$	(b) $r_e \approx s$	(c) $r_e \gg s$
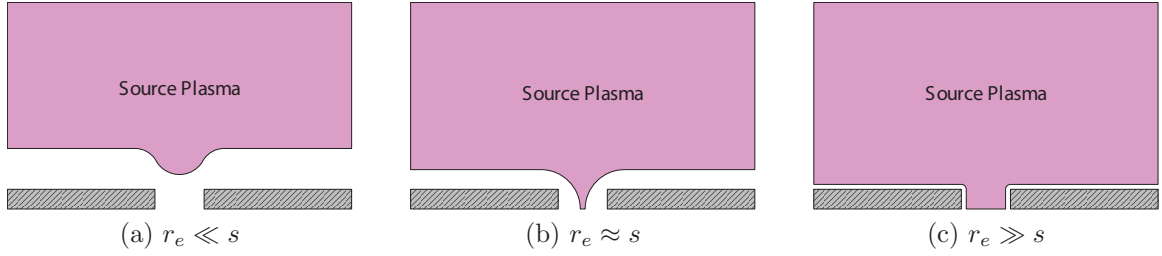
Figure 3.6: Variation in plasma boundary location as a function of aperture size and sheath thickness.

at the aperture exit, allowing for a combination of electron current extraction and controllable electron energies. The illustrations in Figure 3.6 assume that the electric field in the anode-cathode gap do not penetrate through the aperture. In practice, the superposition of the applied electric field with the boundary sheath can influence the shape of the emitting plasma boundary. At high voltage in particular, rarification of the local plasma density near the aperture can occur via the applied electric field, resulting in a concave plasma boundary in that region.

3.4.1 Global Nonambipolar Flow and Electron Sheaths

The theory of plasma cathode operation was expanded upon by Baalrud, Hershkowitz, and Longmier, by introducing the concept of global nonambipolar flow.[4] Simply stated, nonambipolar flow occurs in a condition when all electrons are lost to one boundary of the plasma while all ions are lost to the other boundary. This condition was studied with the use of a planar electrode inserted in a plasma and biased positively relative to the chamber walls. In the analogy of the plasma cathode, the inserted electrode would be denoted A_e and the walls A_i. The nonambipolar flow regime corresponds to the condition when the maximum electron current is extracted, and is exactly balanced by the total ion Bohm current to the cathode walls. It is suggested that for nonambipolar flow to occur, the ratio of electron loss area to ion loss area must fall within a specific range, and the sheath structure at the electrode

will vary depending on this ratio of areas.

If it is assumed that the anode bias is much larger than the electron temperature, then ions are lost to both boundaries at the Bohm current, and electrons are lost to both boundaries by overcoming the ion sheath potential. Using global current conservation, the condition for a monotonic ion sheath (*e.g.* purely negative curvature) at the extraction anode becomes:

$$\frac{A_e}{A_i} \geq \left(\frac{0.6}{\mu} - 1\right)^{-1} \approx 1.7\mu \tag{3.47}$$

where $\mu = \sqrt{2.3m/M_i}$. Monotonic electron sheaths can also be observed when ions are lost only to the walls (at the Bohm current) and electrons are lost to both boundaries. The criterion for this regime is

$$\frac{A_e}{A_i} < \mu. \tag{3.48}$$

For the regime between these two extremes,

$$\mu < A_e/A_i < 1.7\mu, \tag{3.49}$$

a double layer sheath forms at the anode in order to balance total current losses. Again in this regime, the plasma potential is much less than the anode bias and no ions are lost to the anode. However, the double sheath establishes a condition where the bulk plasma potential remains much greater than $k_B T_e$, so no electrons are lost to the walls; this is the global nonambipolar regime. Another feature of this condition is that the plasma potential "locks" to a value a few Volts negative of the anode bias, somewhat analogous to what is predicted by the Oks plasma cathode model.[4] Baalrud and Hershkowitz performed emissive probe measurements to map out the spatially varying plasma potentials in an argon plasma, in each of these three configurations, by changing the extraction anode area. As seen in Figure 3.7, all three

48
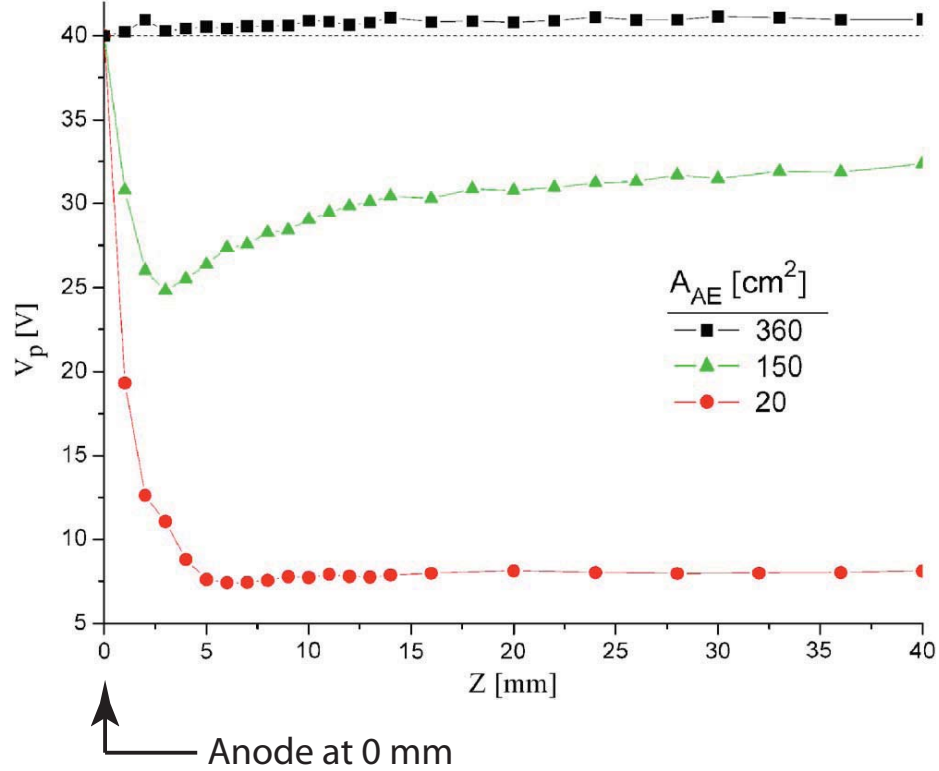
Figure 3.7: Measured potential profiles associated with a monotonic ion sheath (black squares), double layer sheath (green triangles), and monotonic electron sheath (red circles). Plot adapted from [4].

sheath types were detected at the anode, corresponding to the correct area ratios.[4]

The nonambipolar flow model was used in the design of the Nonambipolar Electron Source described in Chapter 2, in which the areas of the extraction orifice and internal collection cylinder were chosen to satisfy Equation (3.49). This approach led to an efficient electron source capable of delivering tens of Amperes of electron current.[48]

The models of the mechanism behind electron extraction from a plasma provide a useful starting point in designing and characterizing a new type of plasma cathode. The global balance of electron and ion currents needs to be considered when choosing the plasma cathode dimensions, and when aiming for a given target current, this constrains the size of the device. However, as will be presented in Chapter 7, the electron extraction mechanism may not be as simple as it seems. While the data in this thesis confirms some of the predicted features of plasma cathodes (like plasma

potential locking), it appears that electron extraction can perturb more than just the plasma potential. The act of extracting large electron current can drive density gradients and induce an "effective" electron loss area from the bulk plasma, which exceeds that of the extraction aperture. This effective loss area is realized through a double layer sheath that forms between the aperture and the bulk plasma. The double layer can expand away from the aperture, increasing the loss area for electrons, and consequently increasing the extracted electron current. The data raise some interesting questions about plasma cathode operation that may need to be included in these models in the future.

CHAPTER IV

Experimental Design

This chapter presents an overview of the design process behind the U-M waveguide plasma cathode, along with a description of the facilities and the plasma diagnostics used in this study. In particular, the first version of the device is described along with the results and lessons learned. The final proof-of-concept plasma cathode design is then described, the performance of which is benchmarked in Chapter 6, and is studied in more detail in Chapter 7.

4.1   Ridged Waveguide Design

Two waveguide plasma cathode designs are presented in this study. The first design arose from previous work on the "grill"-style ECR plasma cathode at U-M, originally studied by Hidaka *et. al* and described in Chapter 2 (Figure 2.7).[35] Experiments using this initial design provided valuable insight for the next iteration of the plasma cathode. One of the findings of that previous work was that the extractable electron current was likely limited by the available collection area for ion current at the grill surface. To study this possibility, a waveguide-style plasma cathode was designed with a large cathode surface area while using a similar magnetic configuration as the "grill" source.

The first constraint on the plasma cathode dimensions was determined from the

51

microwave propagation in circular waveguides, outlined in Chapter 3. Foremost, the radius of the waveguide needed to be larger than the cutoff radius for 2.45 GHz microwaves in the desired mode. To ensure that the electric field pattern would be predictable and avoid mode switching, the waveguide dimensions were chosen to allow the lowest-order, circular TE_{11} mode to propagate while cutting off higher order modes. The baseline inner radius of the waveguide was chosen at 38 mm, just above the cutoff radius of 36 mm for the TE_{11} mode, but below the 47 mm cutoff for the circular TM_{11} mode.

The next design step was the magnetic circuit layout. Because the circular TE_{11} mode is peaked on axis, the ECR heating zone was designed to overlap with the axis in the region of peak electric field, to maximize absorption of the incident microwave energy by the plasma. The ECR heating zone was established by samarium cobalt block magnets (1.4 cm $\times$ 1.6 cm $\times$ 4.5 cm, and magnetized along the thinnest dimension.) The "grill" source used similar magnets oriented in attraction with one another across the gaps in the grill. Plasma heating was presumably achieved through ECR and upper hybrid heating (where $\mathbf{k} \perp \mathbf{B_0}$).

The magnetic field strength corresponding to the ECR condition at 2.45 GHz is 875 Gauss. To achieve this field on axis, the magnets would have to be placed much closer together than the outer dimensions of the waveguide. The Ansoft Maxwell 2D magnetostatic solver was used to determine the required spacing of the magnets. The waveguide pattern was modified to accommodate the magnets by using a "ridged" waveguide design. The ridges allowed for two bar magnets each to be placed in slots on the atmosphere side of the waveguide. In addition to establishing a strong magnetic field on axis, the magnets could then be moved and re-arranged outside the vacuum, and they were protected from potential heating damage. The magnetic field pattern given by Maxwell 2D with the magnets in attraction is shown in Figure 4.1. Here, the field is only plotted inside the waveguide; the walls are made of copper and the

(a) Contour plot, with $B = 875$ Gauss in bright green.

(b) Legend

(c) Vector plot, with $B = 875$ Gauss in bright green. Vector length does not scale with field strength.
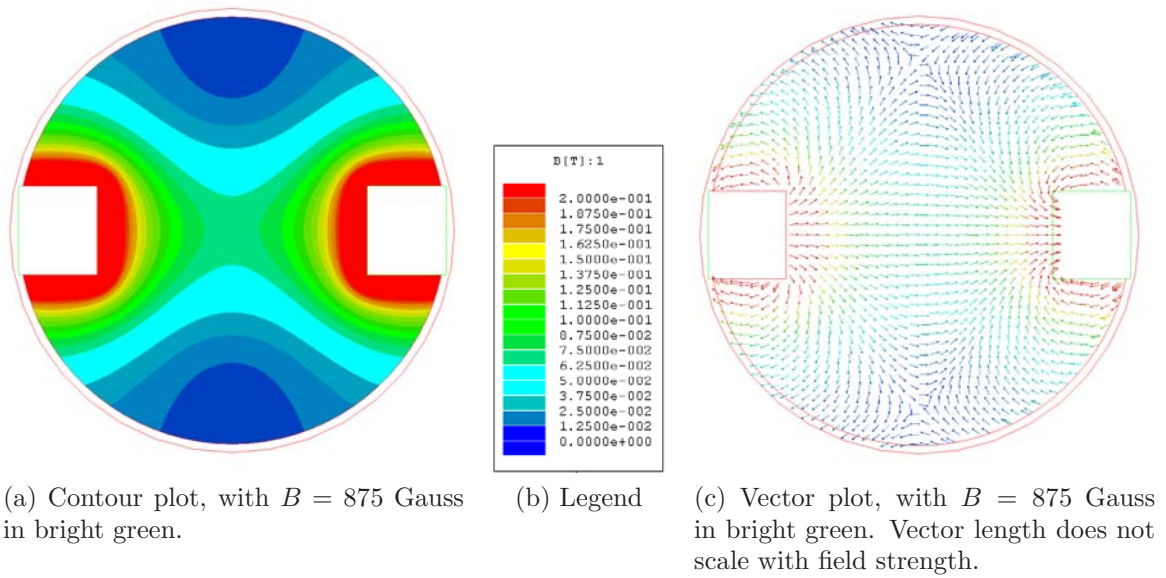
Figure 4.1: Magnetic field profile for ridged waveguide plasma cathode, magnets in attraction.

SmCo block magnets are shown outlined in green.

The magnetic field strength corresponding to the ECR zone is clearly on the centerline, and wraps around the edges of the magnet slots further away from the axis. Between the magnet slots, the field vectors are horizontal and therefore perpendicular to the propagation vector (into the page). The design also allows the magnets to be placed in repulsion, which would form a cusped field structure. The magnetic field contours and a vector field plot for the magnets in repulsion are shown in Figure 4.2. Here, the 875 Gauss heating zone is closer to the surface of the magnets than in Figure 4.1. This configuration produces a null magnetic field on centerline, which could enhance electron transport to the exit plane of the device. This configuration lacks the magnetic confinement of the previous configuration. In this case, electrons can freely diffuse along field lines from the heating zone to a large wall surface area.

Once the magnet placement was established, the Ansoft HFSS 3D electromagnetic solver was used to calculate the vacuum microwave field profile. The launching waveguide circuit (coax adapter, tuner, etc.) were to be installed with the electric

(a) Contour plot, with $B = 875$ Gauss in bright green.

(b) Legend

(c) Vector plot, with $B = 875$ Gauss in bright green. Vector length does not scale with field strength.
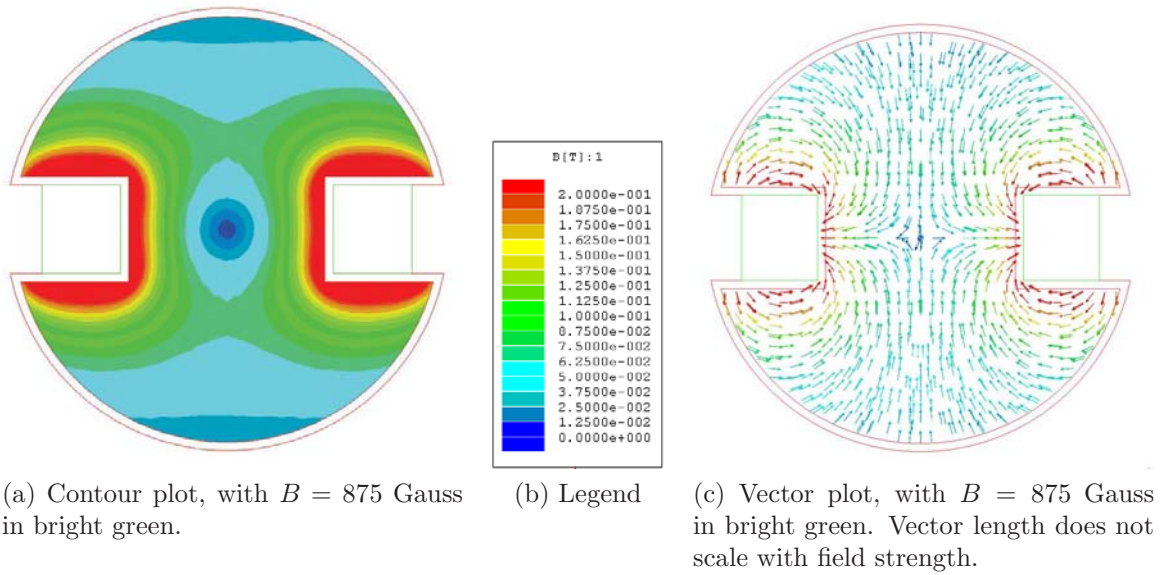
Figure 4.2: Magnetic field profile for ridged waveguide plasma cathode, magnets in repulsion.

field oriented in the vertical direction in the previous plots: the relevant electric field polarization is the vertical plane, *i.e.*, perpendicular to the plane containing the magnet slots. For either ECR or upper hybrid heating to take place, the the electric field must be perpendicular to the magnetic field. In Figure 4.3a, a contour plot of the (vacuum) peak electric field strength, in the vertical polarization, is shown with the addition of the magnet-containing ridges. This plot was taken from a plane perpendicular to the waveguide axis, through the center of the magnet-containing ridges. An incident power of 1 W was assumed at the upstream port. The field strength in the vertical polarization was an order of magnitude less than that in the horizontal polarization after the ridges were added to the purely cylindrical waveguide. To increase the field strength in the vertical polarization, sharp field-enhancing edges were introduced to the top and bottom surfaces. The peak field strength after the addition of the field-enhancing edges is shown in Figures 4.3c and 4.3d.

The vertically polarized field strength is clearly enhanced by the additional edges, which should increase the likelihood of ECR breakdown occurring between the magnet
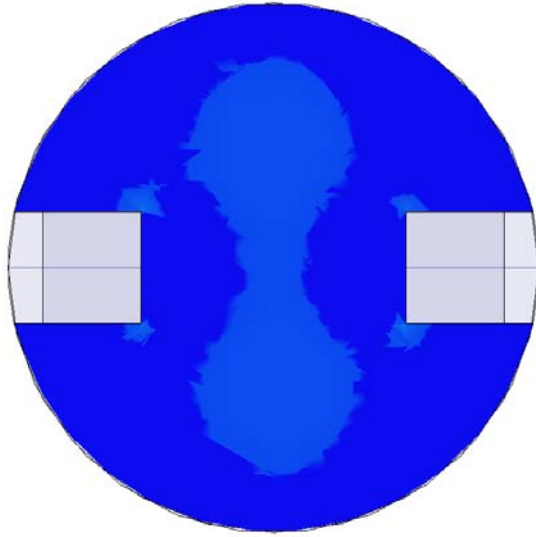
(a) No edges.
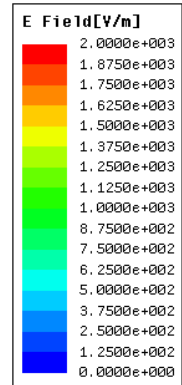
(b) Legend.
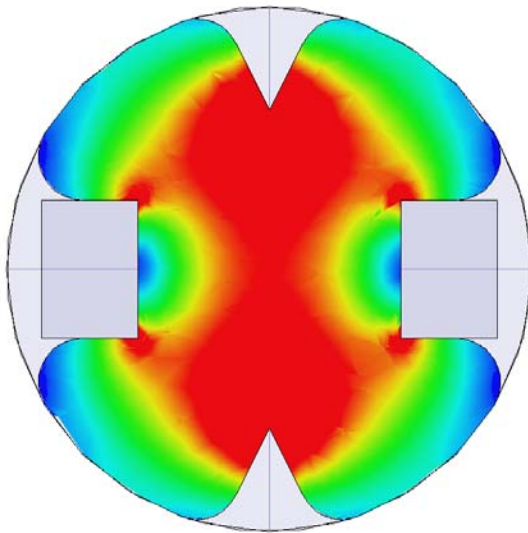
(c) With edges, E-field contour plot.
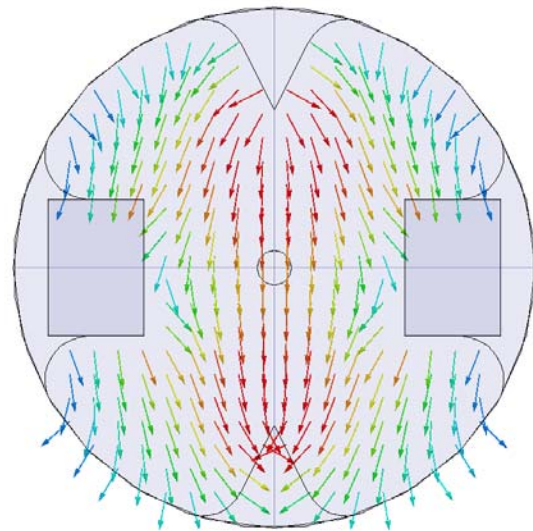
(d) With edges, E-field vector plot.

Figure 4.3: Comparison of electric field profiles, with and without field-enhancing edges.
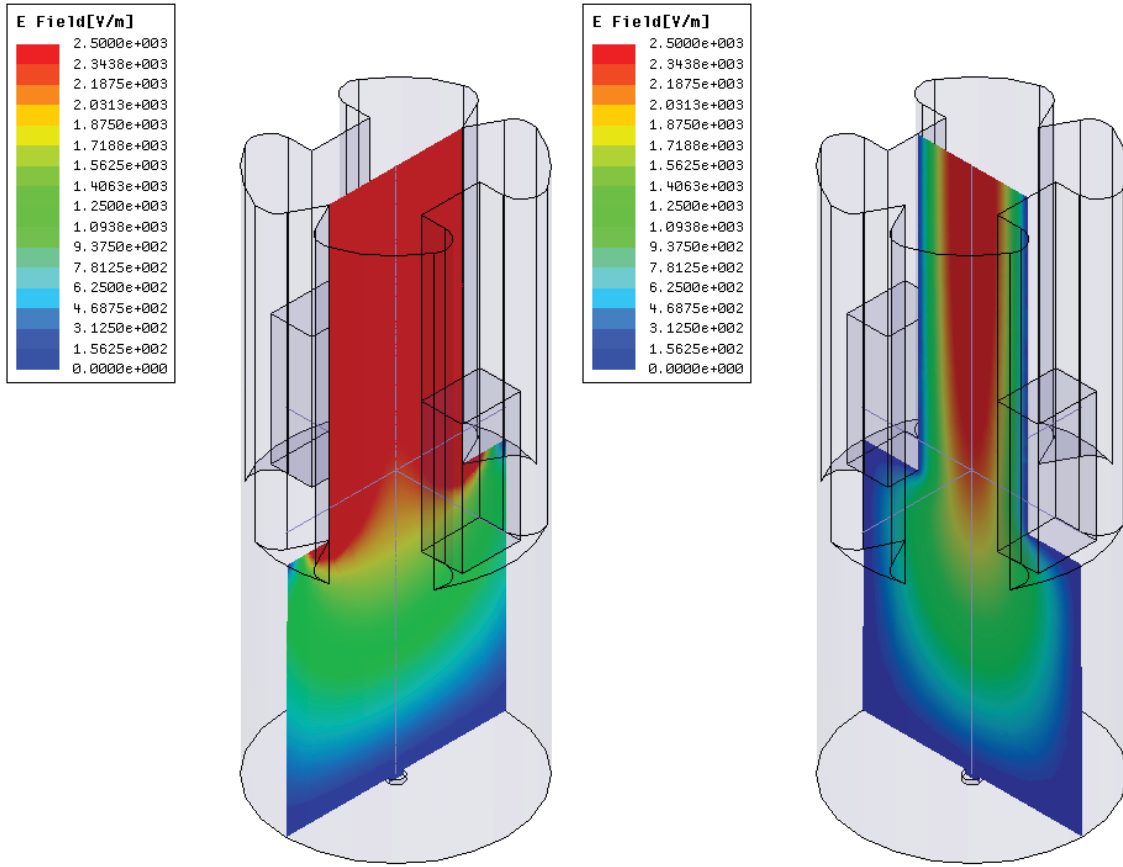
(a) E-field contour plot, in plane between edges (b) E-field contour plot, in plane between magnets

Figure 4.4: Axial electric field profiles with field-enhancing edges.

ridges. To determine the desired length of the waveguide structure, the axial profile of the electric field was calculated in a similar fashion. At the far end of the structure, a 0.15 cm thick conducting endplate was installed with an orifice on centerline, 0.5 cm in diameter. With no plasma present, the endplate acts as a microwave short, and the electric field at the plate is zero. The field will then increase further from the endplate up to 1/4 of a guide wavelength from the endplate. The HFSS results in the axial direction are shown in Figures 4.4a and 4.4b.

The length of the waveguide downstream of the magnet ridges was adjusted until the electric field in the ECR zone was maximized. As shown in the axial profiles,
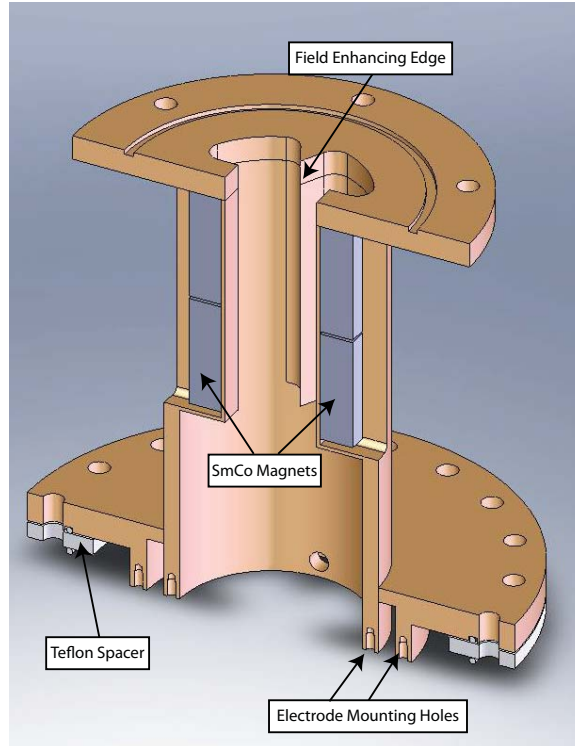
Figure 4.5: Illustration of the ridged waveguide plasma cathode setup.

there is a region of gradual increase in electric field between the endplate and the field-enhancing edges, as expected. The magnetic and electric field modeling resulted in the waveguide design shown in Figure 4.5. The structure had a nominal inner radius of 38 mm and length 182 mm. The spacing between the inner faces of the magnet-holding ridges was 38 mm, and the wall thickness of the ridges was 1.5 mm. The field-enhancing edges penetrated 15 mm inward from the inner waveguide wall, and had a point angle of 53 degrees. Both the magnet ridges and field-enhancing edges were 100 mm long, starting from the upstream end of the device.

The downstream end of the device allowed for mounting endplates and electrodes as needed. The flange which mated the source to the chamber had an O-ring groove, which sealed against a Teflon (or aluminum) washer that in turn sealed against the vacuum chamber flange with another O-ring. This arrangement provided the option of electrical isolation between the plasma cathode and chamber. The upstream end

of the source was sealed by a quartz pressure window.

4.2 Experimental Setup

Testing and characterization of the electron source were carried out at the Plasma Science and Technology Laboratory (PSTL) and NASA GRC. Differences in the hardware setup at these locations warrant some discussion of the facilities and accompanying equipment.

4.2.1 U-M Testing Facility

During the initial design phase of the study, the source benchmarking was carried out in a stainless steel vacuum chamber at PSTL. The main vacuum chamber has an inner diameter of 45 cm and a length of 62 cm. The waveguide plasma cathode was mounted on a custom-built top flange for the facility and exhausted into the chamber. Mounted to a flange on the side of the chamber (through a 20 cm to 15 cm ConFlat reducer) was a Pfeiffer-Balzers TPU-170 turbomolecular pump (with a pumping speed of 170 L/s on air), which was used to evacuate the facility. The turbopump was backed by a Pfeiffer L-80 rotary vane pump, which was connected to the turbopump by a flexible hose. A second flex hose was also installed between the roughing pump and the chamber body, and could be isolated by a valve near the chamber after roughing. The background pressure achieved in this facility was typically around 2×10^{-5} Torr after pumping for one hour. A schematic of the U-M vacuum facility with pumping scheme is shown in Figure 4.6.

Argon gas was fed into the plasma cathode via 6.4 mm diameter stainless steel tubing. The flow rate was controlled by a VACOA MV-25 leak valve and measured using an Omega FMA 1802 flow meter with a range of 0-10 sccm on N_2. The pressure in the vacuum chamber was monitored using a Lesker KJL-6000 thermocouple gauge and a G100F ion gauge, connected to a KJL-4500 ion gauge controller.
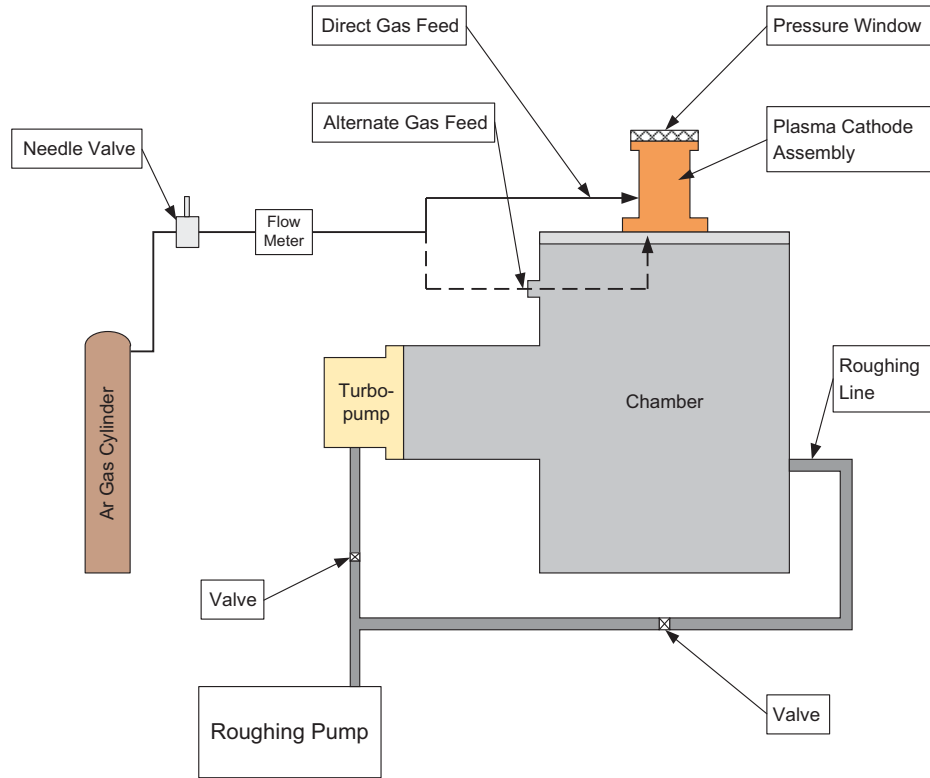
Figure 4.6: Block diagram of U-M vacuum facility and pumping scheme.

In all tests at the U-M facility, the microwave source was a 2.45 GHz magnetron from National Electronics which can deliver up to 2 kW of power. The magnetron head was mounted directly to a three-port circulator which redirects reflected power to a water load. The downstream port of the circulator was connected to a 60 dB two-way directional coupler, which was used to monitor forward and reflected microwave power with HP 435B analog power meters and HP 8481A sensor heads. All waveguide components were WR340 rectangular waveguide. The directional coupler was connected to a three-stub tuner for load matching, which was then connected to a WR340-to-Type N coaxial adapter. A photograph of this section of the microwave circuit is shown in Figure 4.7.

A Tensolite WHU 18-1818 high power microwave cable was used to couple microwaves into the waveguide plasma cathode assembly. For the first ("ridged waveguide") design, the cable was connected to a Type N-to-circular waveguide

59
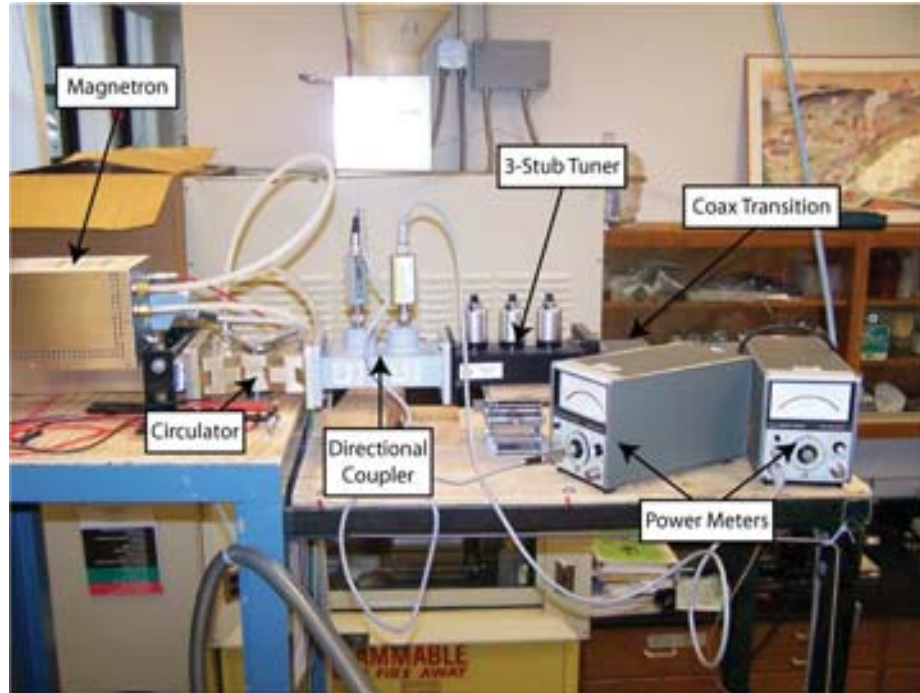
Figure 4.7: Photograph of the microwave power circuit at the U-M vacuum facility.

adapter made in-house. The cable, waveguide adapter, and ridged waveguide plasma cathode are shown along with the U-M vacuum facility in Figure 4.8. When testing the final design, a WR340-to-circular waveguide transition was used in place of the in-house adapter, as shown in Figures 4.9 and 4.10.

4.2.2 NASA GRC Facility

The vacuum facility at NASA GRC, referred to as VF-56, was used for further benchmarking and study of the cylindrical waveguide plasma cathode. A photograph of the plasma cathode assembly mounted on VF-56 is included in Figure 4.11 along with a block diagram of the pumping scheme for VF-56 in Figure 4.12. The stainless steel chamber is 1 meter in diameter and 1 meter long, attached to a roughing pump via the bottom flange. After roughing, the chamber is evacuated by a cryopump with a pumping speed of 15000 L/s on air. The pumps and isolation valves are controlled remotely via a PC interface. The ultimate pressure in this facility was typically on
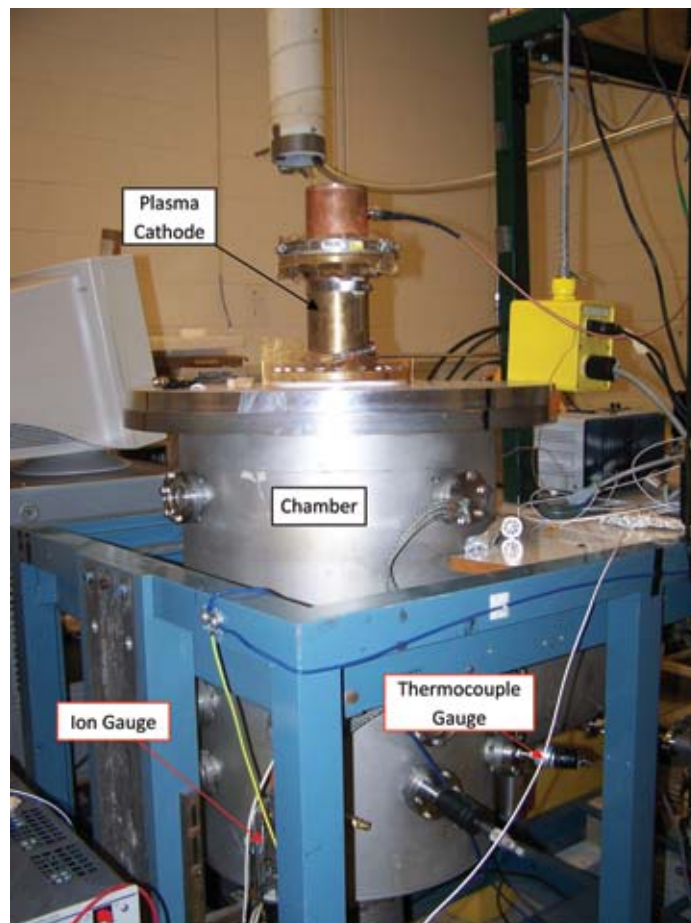
Figure 4.8: Photograph of the U-M vacuum facility with waveguide plasma cathode.
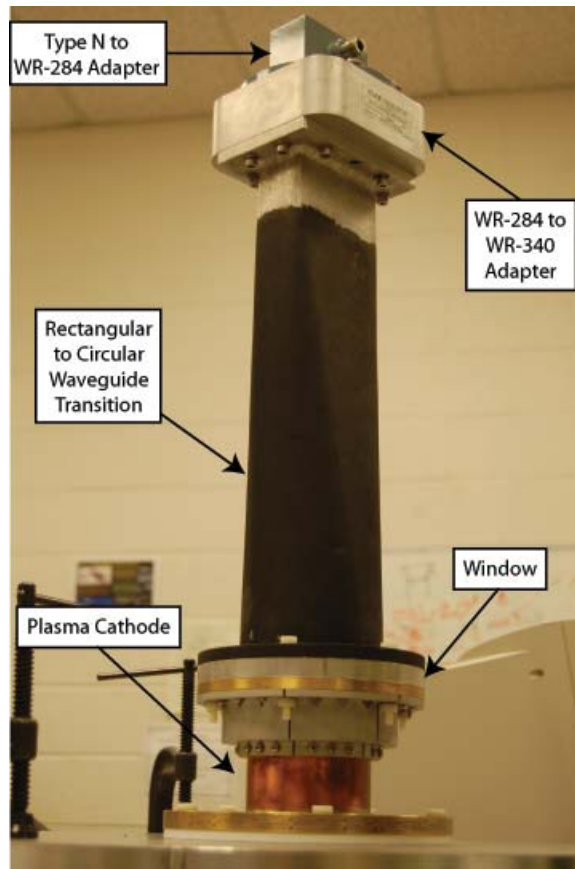
Figure 4.9: Photograph of the microwave launching setup with waveguide plasma cathode at the U-M vacuum facility.
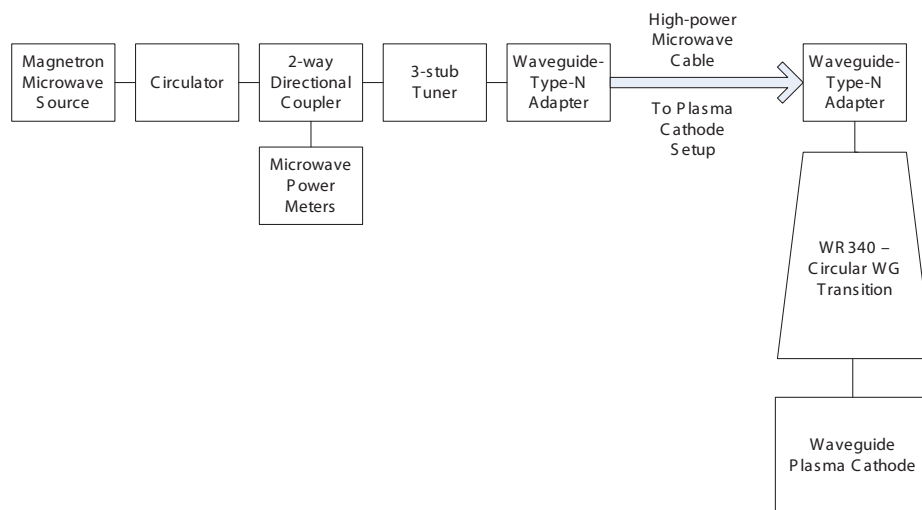
Figure 4.10: Block diagram of microwave power setup at the U-M vacuum facility.
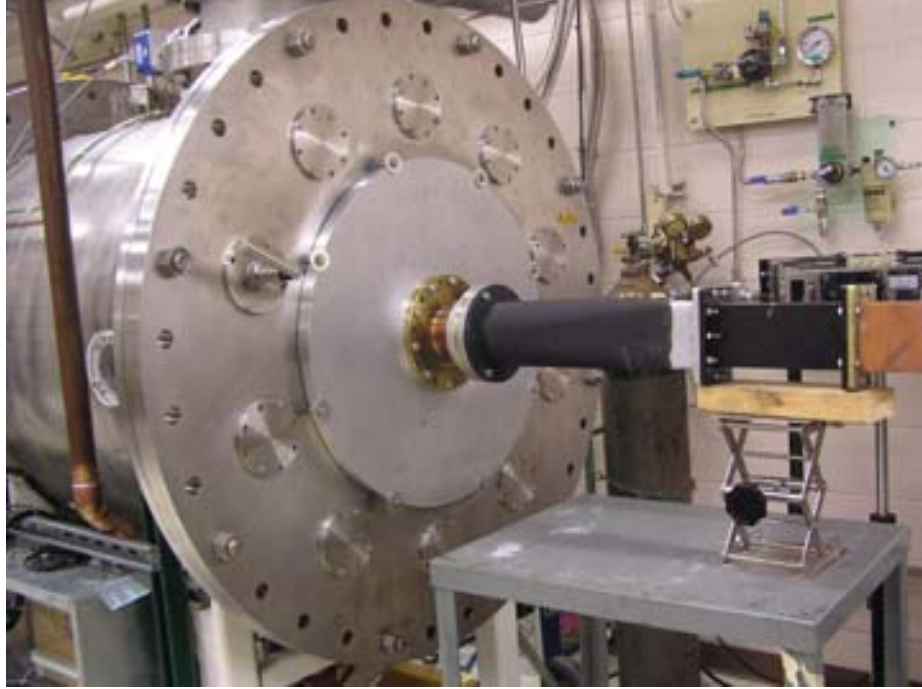
Figure 4.11: Photograph of the NASA GRC vacuum facility 56 (VF-56) with waveguide plasma cathode.

the order of 5×10^{-7} Torr. The plasma cathode was operated on argon, krypton, and xenon gases at VF-56. The mass flow controllers used were calibrated for xenon, and the ionization gauge was calibrated for N_2; these were corrected for the gas type being used in each test.

The microwave power system was similar to that used at U-M (Figure 4.10). A Sairem 2.45 GHz, 300 W microwave generator with a Type N output was used. Directly attached to the output was a Valvo VFU 1045C water-cooled microwave isolator, which was mounted to a Type-N 50 dB, two-way directional coupler from ATM Microwave. The microwave power was measured with two Agilent E4418B power meters and Agilent 8481A sensor heads. The downstream end of the directional coupler was connected directly to a coax-to-WR340 waveguide adapter. This adapter was mounted to the WR340 3-stub tuner from U-M and the WR340-to-circular waveguide transition. The transition was mounted to the plasma cathode assembly on the upstream end of the pressure window.
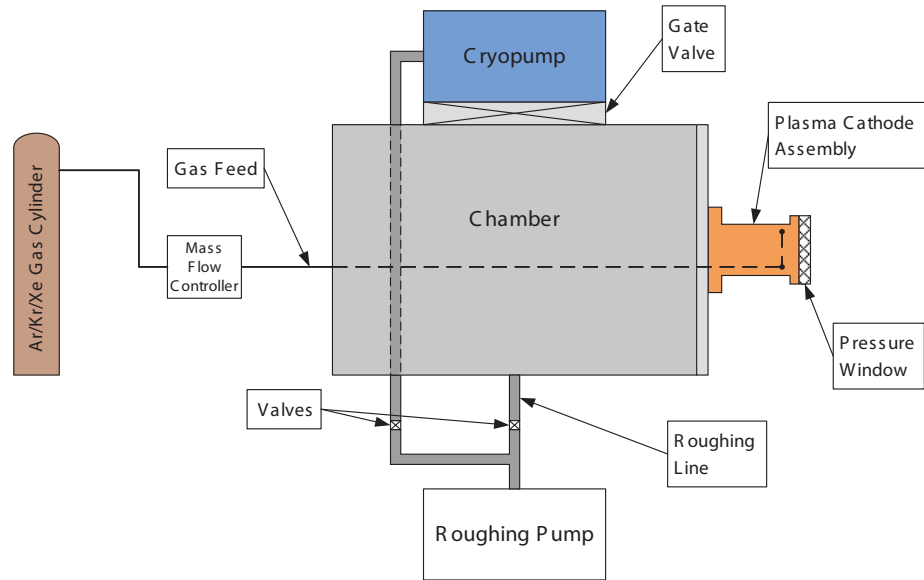
Figure 4.12: Block diagram of VF-56 pumping scheme.

4.2.3 Diagnostics at U-M and NASA

The first diagnostic used in studying the waveguide plasma cathode designs was a simple extraction electrode. For the initial ridged waveguide tests, this electrode was a circular disc of 1010 steel sheet, 5.6 cm in diameter ≈ 1 mm thick. For tests of the final (cylindrical) device design, a molybdenum electrode 12 cm in diameter and 1 mm thick was used. The electrode was biased positively with respect to the plasma cathode body with a DC power supply, as shown in Figure 4.13. In the vast majority of tests, the plasma cathode was grounded to the vacuum facility. However, with the use of the Teflon washer between the plasma cathode and chamber, along with DC breaks in the gas feed line and upstream waveguide, the cathode body and electrode could be left floating if desired.

4.2.3.1 Langmuir Probe Theory

A single Langmuir probe was used to study the plasma characteristics of the source. A generic current-voltage characteristic of a Langmuir probe is shown in Figure 4.14. The analysis of the current profile depends on the size of the probe
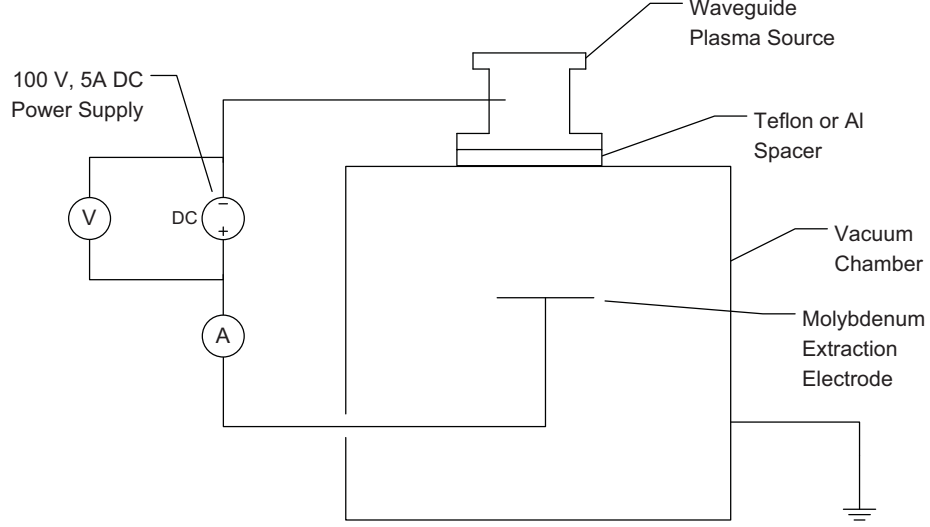
Figure 4.13: Illustration of extraction electrode circuit used for benchmarking extractable current.

relative to the Debye length λ_D.[32] For cylindrical Langmuir probes, if $r_p \gg \lambda_D$, where r_p is the probe radius, the sheath is very thin at the probe surface and the probe can be treated as a planar collection surface with area A_p. In the opposite case where $r_p < \lambda_D$, the probe trace must be analyzed to compensate for orbital motion of ions about the collector.[51] Additionally, at large magnetic field strengths, if the Larmor radius for electrons r_e is much smaller than the probe dimensions, then electron flux is magnetized and flow to the probe is no longer isotropic.[11]

In the analysis of Langmuir probe traces, it is assumed that the electron population is Maxwellian in nature. The probe current I_p as a function of probe voltage V is given by,[63]

$$I_p = -I_{i,\mathrm{sat}} + I_{e,\mathrm{sat}} \exp[-e(\Phi_p - V)/k_B T_e] \tag{4.1}$$

where Φ_p is the plasma potential, $I_{i,\mathrm{sat}}$ is magnitude of the ion saturation current,

$$I_{i,\mathrm{sat}} = 0.61 en \sqrt{\frac{k_B T_e}{M_i}} A_p, \tag{4.2}$$
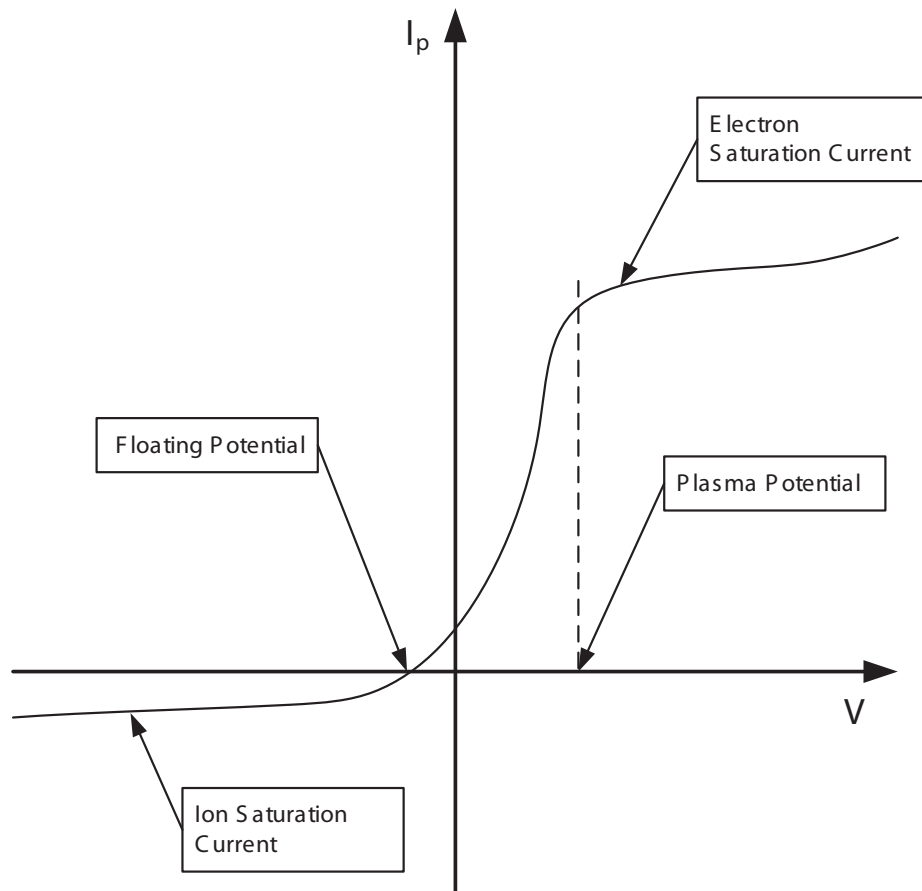
Figure 4.14: Example of a Langmuir probe current-voltage characteristic.

and $I_{e,\text{sat}}$ is the magnitude of the electron saturation current,

$$I_{e,\text{sat}} = \frac{1}{4}en\sqrt{\frac{8k_BT_e}{\pi m}}A_p. \tag{4.3}$$

The ion current to the probe is limited by the Bohm current at the sheath edge, and the factor of $0.61 \times n_0$ is the ion density at the sheath edge, which is rarefied via acceleration through the presheath.[8] In the thin-sheath case, the ion current is independent of the probe voltage, so for a large negative probe bias the electron current term practically vanishes. The probe current then equals the ion saturation current, which can be used to determine the density by,

$$n = I_{i,\text{sat}}/(0.61e\sqrt{\frac{k_BT_e}{M_i}}). \tag{4.4}$$

The determination of plasma density from the ion saturation current requires that the electron temperature be known. The uncertainty in the absolute plasma density as determined from the ion saturation current is often assumed to be within a factor of two to four due to geometric effects and perturbation of the surrounding plasma. The relative uncertainty between measurements can be lower, with a given probe and at comparable plasma conditions, and this uncertainty was reported by the probe analysis software as 10 to 20 percent for the data in this work.

When the probe bias is increased to the point where the total probe current is zero, equal amounts of electron and ion current are collected by the probe, corresponding to the floating potential Φ_f: the potential that an electrically isolated object would float to when immersed in a plasma. From Equation (4.1), the electron and ion saturation currents, floating potential, plasma potential, and electron temperature are all interrelated by,

$$I_{e,\text{sat}} = I_{i,\text{sat}}\exp\left[\frac{e(\Phi_p - \Phi_f)}{k_BT_e}\right] \tag{4.5}$$

67

At intermediate voltages, the electron component of the probe current varies exponentially with the probe bias. The electrons collected by the probe must have enough energy to overcome the probe sheath potential. As the probe voltage is varied in this electron retardation region, the probe sheath acts as a discriminator and the shape of the I-V characteristic yields information on the electron energy distribution function (EEDF). For a Maxwellian electron population, one can combine Equations (4.1) and (4.5) and find for $V < \Phi_p$,

$$I_p = I_{i,\text{sat}}[\exp\left(\frac{e(V - \Phi_f)}{k_B T_e}\right) - 1] \tag{4.6}$$

which can be rewritten as,

$$\ln(I_p + I_{i,\text{sat}}) = \frac{e(V - \Phi_f)}{k_B T_e} + \ln(I_{i,\text{sat}}). \tag{4.7}$$

Equation (4.7) provides a means of determining the electron temperature from the I-V characteristic in the electron retardation region. When the natural logarithm of that summed current is plotted against the bias voltage, the slope of the curve in the retardation region is $e/k_B T_e$, thereby allowing for the determination of T_e. For all probe traces in this work, the slope of the retardation region was accurately determined with an R^2 value of at least 0.9, and it is reasonable to assume a conservative uncertainty in the electron temperature of ± 0.2 to 0.3 eV.

For non-Maxwellian plasmas, the analysis is not so simple, and the concept of a "temperature" is not strictly meaningful. However, the electron retardation region can still give insight into the non-Maxwellian EEDF. The EEDF, $g(E)$, is defined as,

$$g(E) = 2\pi \left(\frac{2e}{m_e}\right)^{3/2} \sqrt{E} f[v(E)] \tag{4.8}$$

where E is the electron energy and $f[v(E)]$ is the electron velocity distribution. The EEDF can be found from the second derivative of the electron retardation region

by,[17, 45]

$$g(V) = \frac{2m_e}{e^2 A}\sqrt{\frac{2eV}{m_e}}\frac{d^2 I_p}{dV^2}. \tag{4.9}$$

While in theory this is possible, in practice, the determination of the EEDF from probe traces can be difficult. Probe characteristics must be differentiated twice to find the EEDF, and each differentiation amplifies the noise in the measurement. The second derivative of the probe trace is also used to determine the plasma potential. In the electron retardation region, the I-V characteristic has an upward curvature until a "knee" is reached at the plasma potential, corresponding to the voltage where $d^2 I_p/dV^2 = 0$. At probe voltages above the plasma potential, the full electron saturation current is collected, but in practice the probe current can continue to increase due to sheath expansion. Because of this, the electron saturation current is not usually well-defined, and thus not as accurate of a measure of plasma density as ion saturation current. The plasma potentials reported in this work were clearly indicated by the second derivative method, and uncertainties in these measurements are likely within ±1 or 2 Volts.

4.2.3.2 Probe Configurations

Several Langmuir probe configurations were used in this study, and will be described in context with the corresponding results. One large segment of the plasma cathode study was carried out at NASA GRC, using a planar Langmuir probe on a one-dimensional translation stage to generate spatial profiles of plasma density, electron temperature, plasma potential, and in some cases, EEDFs. The probe was used to study the visible plume that emanates from the plasma cathode orifice during current extraction, as well as the "source" plasma properties inside the waveguide plasma cathode itself. A schematic of the experimental setup for these tests is shown in Figure 4.15.
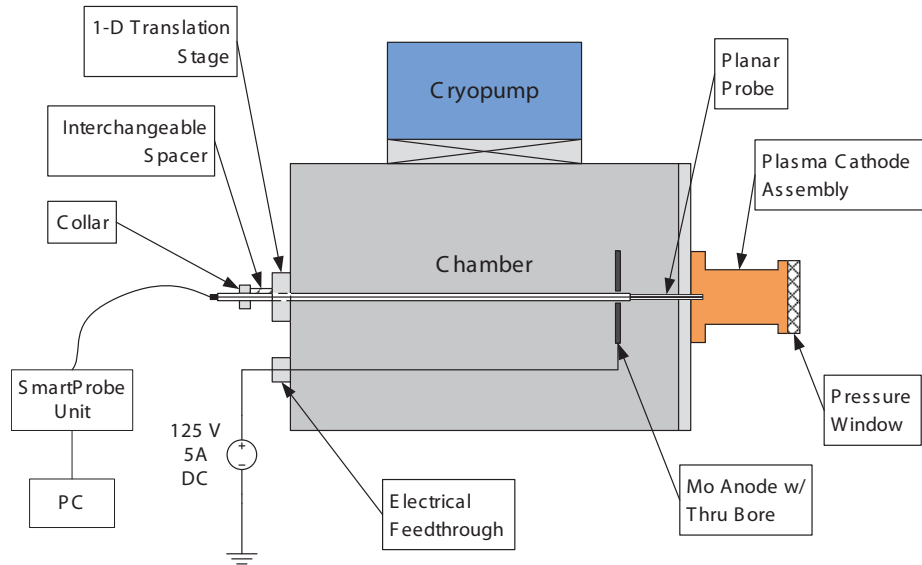
Figure 4.15: Illustration of Langmuir probe mounted on axial translation stage at VF-56.

The 12 cm diameter molybdenum extraction electrode was mounted 14 cm downstream from the plasma cathode, and had a 1.2 cm diameter hole drilled through the center to allow for the probe to pass through. The probe itself was a 3.2 mm diameter tungsten planar surface, slightly recessed (~ 0.5 mm) from the end of a piece of alumina tubing, 3.5 mm in diameter. The alumina and probe were cemented into a section of 6.35 mm OD stainless steel tubing, 58 cm long, so that the probe body extended ~ 15 cm from the end of the tubing. The total length of the translation stage and probe assembly was 120 cm, which allowed the full range of motion from the extraction electrode to the cathode aperture and inside the plasma cathode tested at NASA GRC. The translation stage was naturally pulled inward when the chamber was under vacuum, and could be positioned within ~ 1 mm with the use of an external collar clamp and interchangeable spacers between the collar and feedthrough body.

4.3 Testing of Ridged Waveguide Device

Though the ridged waveguide device shown in Figure 4.5 is not the main focus of this thesis, it was the starting point for the final waveguide plasma cathode design. A brief summary of the performance and lessons learned from this design is presented here.

Once the ridged waveguide device was built, the design was benchmarked. The body was grounded to the chamber, and initially the 5.6 cm diameter extraction electrode was mounted at the exit plane of the source. The SmCo magnets were placed in the two slots in seven configurations, shown in Figure 4.16. Cases 1 through 3 involved one magnet in each slot, placed in attraction, but in different positions relative to the pressure window (at the top of the images). Cases 4 and 5 are similar, but with the magnets placed in repulsion. In cases 6 and 7, two magnets were used, with the magnets in repulsion in case 6 and in attraction in case 7.

The first study of the ridged waveguide design was intended to determine the required magnetic field geometry for the maximum extractable electron current from the discharge. In each configuration, the absorbed (forward minus reflected) microwave power level was fixed at 60 W, and the electrode bias was fixed at +40 V. The gas flow rate was varied from 0 to 15 sccm of argon, corresponding to pressures up to 0.92 mTorr. For each configuration, the maximum extractable electron current was recorded along with the corresponding flow rate. During testing, the microwave cables were heated to $\sim$ 50 degrees C during operation. This heating, which accounts for a small fraction of the absorbed power, was neglected in this work. The results of all of these tests are compiled in Table 1.

Depending on whether the magnets were in attraction or repulsion, the plasma cathode behaved quite differently. In cases 1, 2, 3, and 7, the discharge self-started at low power levels of 25-30 W absorbed. Typically the peak electron current was extracted at flow rates of 1.5 to 4 sccm, the discharge appeared stable, and the

71

(a) "Case 1"

(b) "Case 2"

(c) "Case 3"

(d) "Case 4"

(e) "Case 5"

(f) "Case 6"

(g) "Case 7"
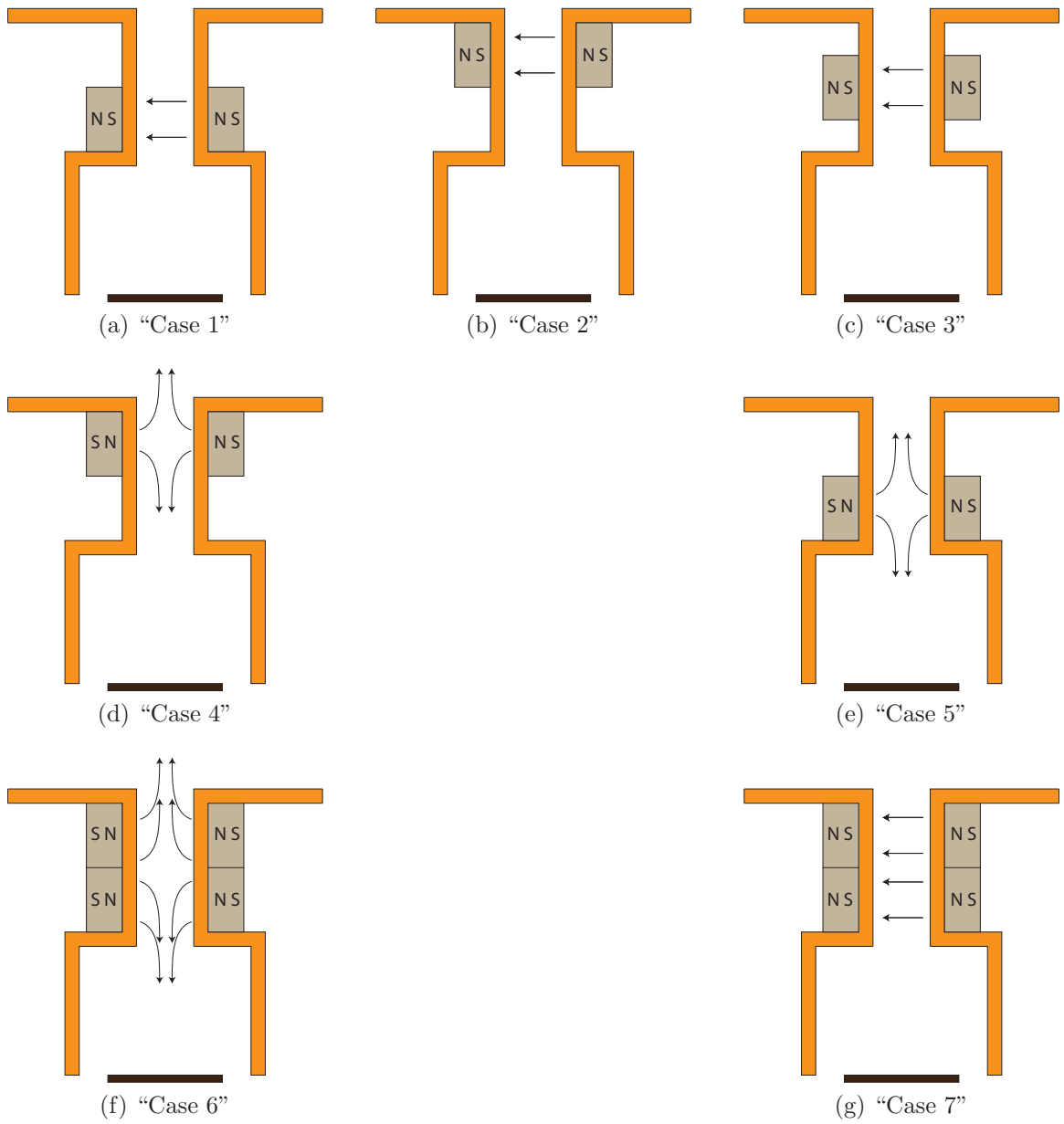
Figure 4.16: List of tested magnet configurations with ridged waveguide design.

electron current measurements were repeatable. The extractable currents in these configuration were on the order of tens of milliamperes, which is far too small to be acceptable for most thruster neutralizer applications.

When the magnets were placed in repulsion, however, the device performed much differently. Self-starting could not be accomplished, and breakdown could only be achieved with additional magnets placed around the periphery of the device. The original assumption was that with the magnets in repulsion, ECR heating may have been enhanced by the predominantly axial component of the magnetic field. The magnetic field also affects the transport of electrons from the heating zone to the exit plane. While the horizontal magnetic field in cases 1,2,3, and 6 provided a high degree of confinement in the heating zone and a stable discharge, electrons in those cases must diffuse perpendicular to a magnetic field on the order of several hundred Gauss to be extracted. With the axially-oriented repulsive magnetic field, electrons would be able to freely diffuse along the field lines to escape. However, it appeared that the radial component of the magnetic field (Figure 4.2) may have been responsible for the instability of these configurations.

The repelling magnets were able to deliver electron currents a factor of two to three higher (131 mA, case 4) than in the cases with attracting magnets, but the discharge was unstable and could only be operated at high flow rates ($\geq$ 15 sccm argon). Regardless of whether the magnets were in repulsion or attraction, the extractable current was significantly larger when the magnets were placed near the pressure window, and the additional magnetic field produced by magnets on the downstream side hindered performance. Because efficient ECR heating requires that the incident microwaves be launched from high to low magnetic field regions, the positioning of the magnets near the window is expected to be the ideal setup. Some plasma erosion of the field enhancing edges was observed during these tests, resulting in some depressions in the edges less than $\sim$ 0.5 mm deep. Based these results, it

Case #	Slot Configuration	Max Electron Current [mA]	Flow Rate @ Max e-Current [sccm]	Max Ion Current [mA]	Flow Rate @ Max I+ Current [sccm]
1	1 magnet each, bottom of slots, attraction	44.4	3.8	1.5	1.5
2	1 magnet each, top of slots, attraction	75.6	2.0	1.5	1.3
3	1 magnet each, centered in slots, attraction	48.6	3.4	1.1	1.5
4	1 magnet each, top of slots, repulsion	131.0	15.8	0.7	3.9
5	1 magnet each, bottom of slots, repulsion	No Discharge			
6	2 magnets each, repulsion	38.4	15.8	0.8	3.6
7	2 magnets each, attraction	57.3	1.3	2.0	1.3

Figure 4.17: Summary of results with ridged waveguide design.

was decided that a better design would establish an axial magnetic field near the upstream window (to enhance ECR heating and transport downstream) while also symmetrically confining electrons in the ECR heating zone (to provide stability and high plasma density). This was the basis for the cylindrical waveguide plasma cathode design that is the main focus of this thesis.

4.4 Cylindrical Waveguide Design

A schematic depiction of the revised plasma cathode is shown in Figure 4.18. Similar to the ridged design, 2.45 GHz microwaves are launched from the upstream end of the source through a quartz pressure window. An ECR discharge is formed in the resonant heating zone, which is established by an external permanent magnet ring.
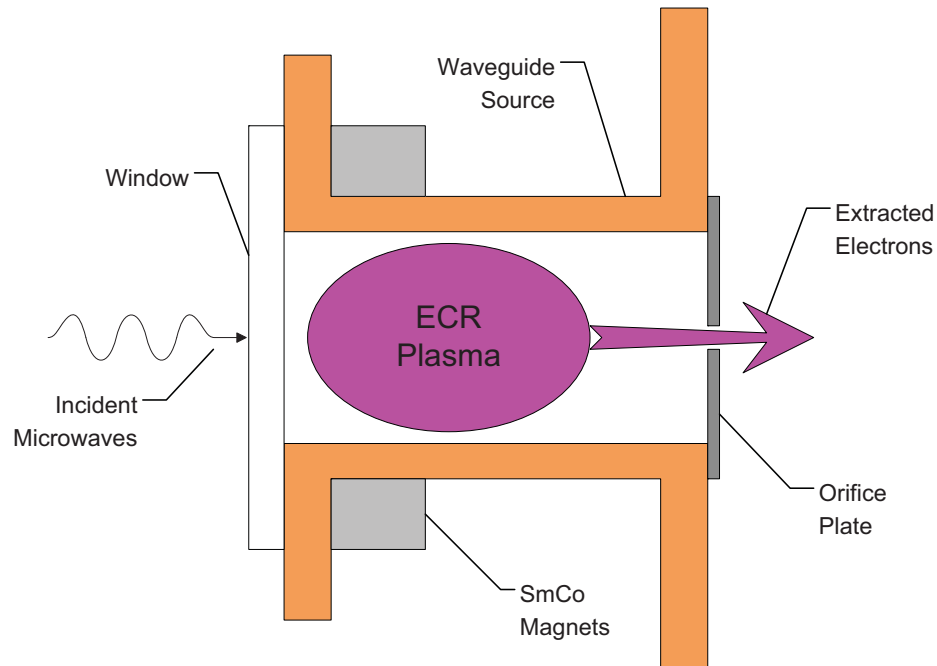
Figure 4.18: Schematic of cylindrical waveguide plasma cathode concept.

4.4.1 Magnetic Circuit

Maxwell 2D was used to calculate the ideal magnet configuration for the source. As with the ridged waveguide setup, the magnetic circuit was designed so that the 875 Gauss magnetic field occurred on the axis of the waveguide, where the electric field was strongest. The magnets were also placed as close as possible to the upstream pressure window to minimize microwave reflection and to incorporate the insight gleaned from the ridged waveguide source. Figure 4.19 shows the cylindrically symmetrical magnetic field profile that was chosen. The model assumes two solid rings of grade 26 samarium cobalt (from Magnet Sales & Manufacturing, Inc.), the same material and cross-sectional dimensions as the magnets used in the previous design. The magnets are oriented upward, establishing an 875 Gauss, axial magnetic field on the centerline of the waveguide. The axial field profile allows electrons to freely diffuse from the heating zone to the exit plane of the source. Electrons can also travel along the magnetic field to the window, but are not collected at the window surface. The

(a) Contour plot, with $B = 875$ Gauss in bright green.

(b) Legend

(c) Vector plot, with $B = 875$ Gauss in bright green. Vector length and spacing do not scale with field strength.
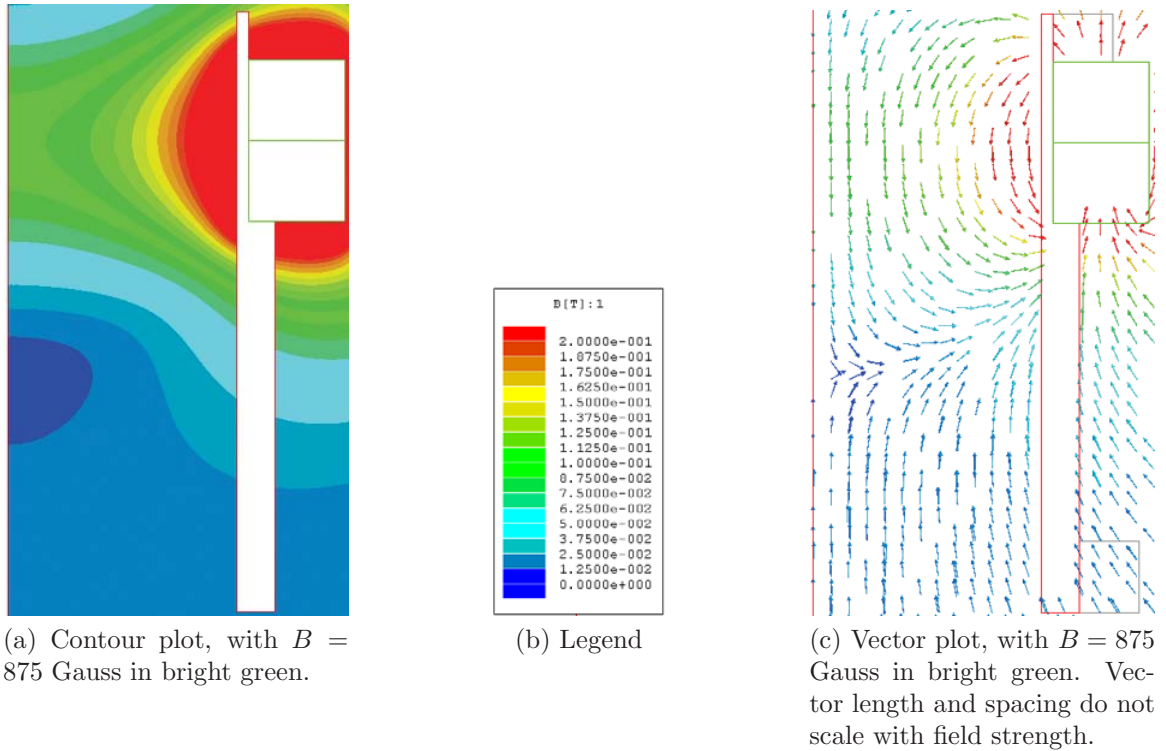
Figure 4.19: Magnetic circuit in cylindrical waveguide plasma cathode design.

waveguide walls are assumed to be copper, with a nominal thickness of 6.4 mm. To get the magnet rings close enough to centerline to meet this condition, the waveguide walls are thinner in regions where the magnets are located; here, the wall thickness is 2 mm and the inner radius of the waveguide is 38 mm.

In the physical embodiment of this design, the magnets used were not actually solid rings. Instead, they were machined from the large SmCo magnets used in the grill and ridged waveguide designs. After machining, the magnets had dimensions of 1.4 cm × 1.6 cm × 2.1 cm, magnetized along the shortest dimension. Twenty-four magnets were machined, and stacked on top of one another in pairs. The 12 magnet pairs were then closely arranged around the neck of the waveguide.

A null is found in the magnetic field on axis and roughly 6 cm from the pressure window. This occurs due to the competition of the near and far-field solutions of the axially oriented magnet ring. In the center of the magnet ring, the magnetic field

points in the opposite direction of the ring magnetization. That is, with the magnet ring oriented upward as in Figure 4.19c, the field on centerline points downward. Far downstream from the magnets, the entire ring appears as a single magnetic dipole; in this region, the field is oriented in the same direction as the magnets (upward in Figure 4.19c). The strong ECR heating zone is formed in the near-field region.

4.4.2 Microwave Circuit

The microwave circuit for the cylindrical device was designed using the same methodology as in the ridged waveguide design. The radius of the waveguide was chosen to just exceed the cutoff radius for the circular TE_{11} mode but not that of any higher order modes. Because the guide wavelength increases as the waveguide radius approaches the cutoff radius, the axial position of the peak electric field relative to the plasma cathode endplate also depends on the waveguide radius. In the plasma cathode, the internal surface area for ion collection should be made as large as possible, which implies that it should have a high aspect ratio. This is achieved by choosing a radius (38 mm) close to the cutoff radius (36 mm). The maximum electric field is expected at a distance of $\lambda_g/4$ from the endplate, where λ_g is the guide wavelength. For a radius of 38 mm, this corresponds to a distance of 9.3 cm from the endplate, which should be the minimum length of the plasma cathode that includes the peak electric field in the device. A total plasma cathode length of 10 cm was chosen to ensure that this condition was met. These dimensions were chosen assuming vacuum conditions within the waveguide in order to ensure breakdown of the feed gas. With plasma inside the device, the cutoff radius and guide wavelength are expected to slightly increase, which is the reason for the inner dimensions (3.8 cm and 10 cm) that are slightly larger than the calculated values (3.6 cm and 9.3 cm). A plot of the relative intensities of the magnetic field and vacuum electric field, as a function of distance from the pressure window, is shown in Figure 4.20.
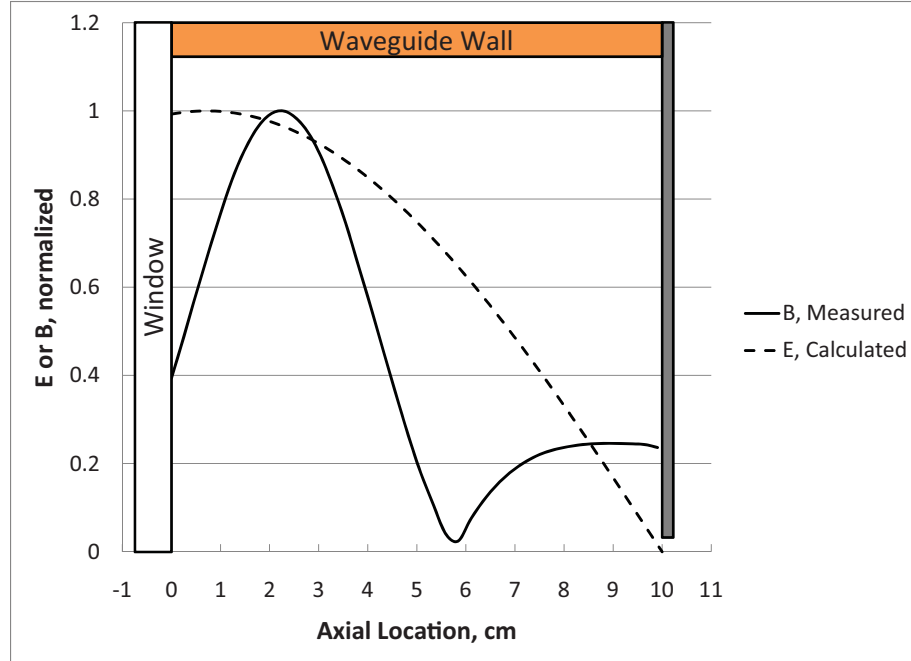
Figure 4.20: Illustration of microwave electric field (before breakdown) and static magnetic field overlap.

4.4.3 Mechanical Design

By combining the magnetic and microwave field calculations, the cylindrical waveguide plasma cathode design was finalized. The completed embodiment is shown in Figure 4.21. A groove was machined in the outer wall of the waveguide to move the ring of magnets closer to the axis. The groove could hold 12 pairs of SmCo magnets, which were bolted to the waveguide body and upper flange in pairs, by six aluminum clamps. The upper flange was designed to mate with the quartz pressure window, pressure window clamp, and circular waveguide transition while also providing a means for attaching the magnet clamps. The bottom flange was of the same design as that on the ridged waveguide – a 15 cm ConFlat bolt pattern, with an O-ring groove. The bottom O-ring sealed against a washer, which was sealed against by the vacuum facility cover and a second O-ring. The bottom flange had the same blind bolt hole pattern in the bottom as the previous design, for attaching interchangeable orifice endplates and other diagnostics. Gas was fed into the source through a ring

78
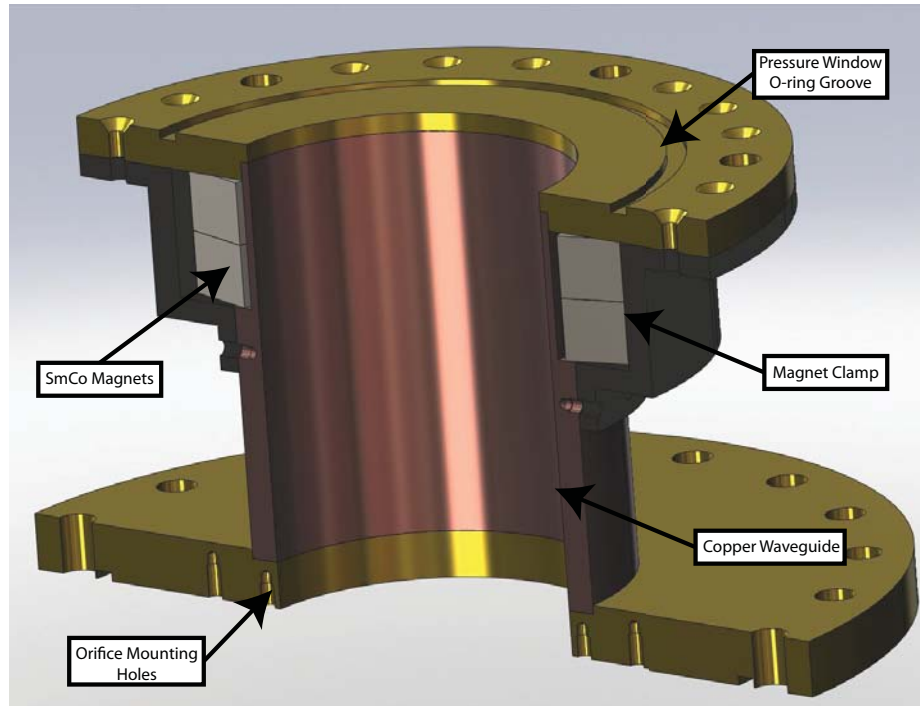
Figure 4.21: Schematic of cylindrical waveguide plasma cathode final design.

plenum made of 3.2 mm OD stainless steel tubing, with 8 evenly spaced holes roughly 1 mm in diameter. The ring plenum was mounted ~ 6 mm downstream of the pressure window. The plenum holes were directed toward the vacuum window.

CHAPTER V

Device Performance

The cylindrical waveguide plasma cathode design was fabricated and tested. Initial testing was carried out at the vacuum facility at PSTL, including an initial optimization of the extraction aperture and performance characteristics on argon feed gas. Also, Langmuir probes in fixed locations were used to study the plasma properties during operation. Afterward, the device was moved to the higher pumping speed facility at NASA GRC, and more broadly characterized on argon, krypton, and xenon feed gases as well. This chapter summarizes the initial testing and performance of the proof-of-concept waveguide plasma cathode.

5.1 Initial Testing

5.1.1 Open-ended Source

For the initial tests at U-M, the source was mounted on the PSTL vacuum facility as explained in Chapter 4. The source was electrically isolated from the vacuum chamber by using a Teflon washer, a DC block in the waveguide assembly (just upstream of the rectangular-circular waveguide transition) and a ceramic DC break in the gas feed line. The extraction electrode, positioned 1.9 cm downstream of the exit plane, was biased to +100 V relative to the plasma cathode body. The argon flow rate was varied from 3 to 9 sccm, and the extracted current was measured at
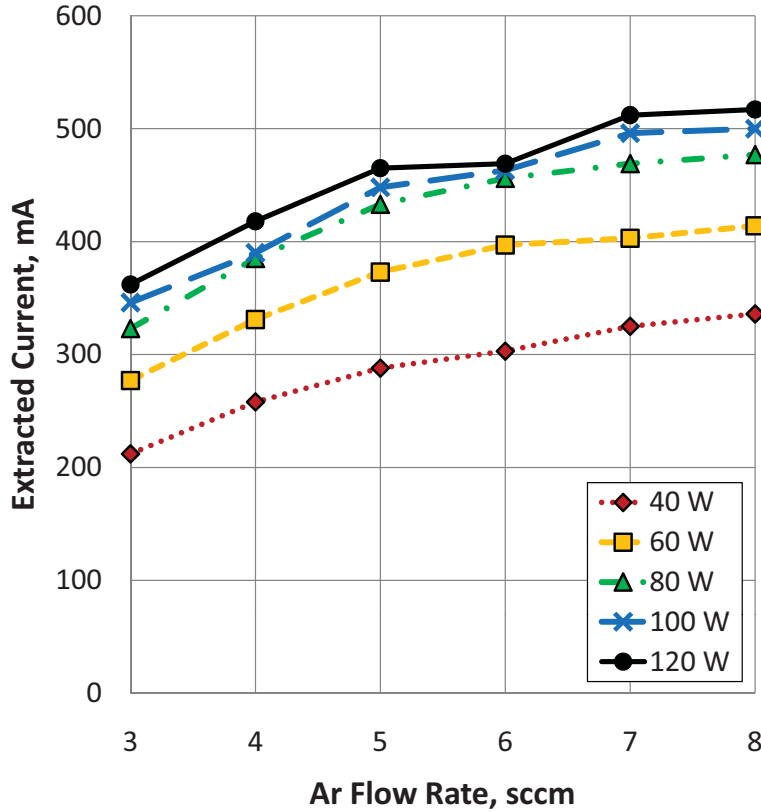
Figure 5.1: Dependence of extracted current on flow rate and microwave power, at 100 V bias.

absorbed (total minus reflected) microwave power levels ranging from 40 to 120 W. Testing was limited to this range of flow rates and microwave power levels to keep the experiments in the context of a realistic electron source for EP systems – the neutralizer for the 440 W, 13 cm Xenon Ion Propulsion System (XIPS) thruster runs on 0.5 sccm of xenon, while the neutralizer for NEXT uses 4 sccm of xenon and 6.83 kW.[7, 29] Variations in extracted current with bias voltage are shown in Figure 5.1.

In all cases, the ECR discharge was self-starting and stable, with or without the 100 V bias applied. The current extraction tests with the open source were already a significant improvement on the ridged waveguide design, reaching a peak electron current of 517 mA at 8 sccm and 120 W of microwave power. At 3 sccm and 60 W of microwave power, the ridged waveguide source delivered 32 mA of current, while

the cylindrical device delivered 220 mA. At all power levels, the current increased monotonically with increasing gas flow, suggesting that even better performance could be achieved at higher internal pressures. Because the exit of the plasma source was open to the vacuum chamber without any constricting aperture, the pressure inside the source was assumed to be near the background chamber pressure – 0.21 to 0.64 mTorr over this range of flow rates. The reduced rate of current increase with additional microwave power suggested that the deliverable current was limited by insufficient neutral pressure inside the source.

The Teflon washer was then replaced with an aluminum washer, and the source was mounted to the chamber with steel (instead of nylon) bolts. Additionally, the DC block was removed from the waveguide circuit. The plasma cathode was grounded to the vacuum facility and extracted current was measured over the same matrix of operating conditions. This was done to determine whether the inclusion of the chamber walls in the circuit would significantly influence the performance of the source. If the plasma cathode is grounded, the chamber walls would act as an additional effective cathode area. This is only a concern if the electron extraction from the source is limited by ion current at the cathode wall, and if the ion current collected by the chamber is comparable to that collected at the plasma cathode walls. The extracted current from the grounded source was plotted against the extracted current from the floating source at the same conditions. The results are shown in Figure 5.2 over the range of flow rates from 3 to 8 sccm, microwave power of 40 to 120 W, and an extraction bias of 100 V. There is some scatter in the data, which could result from the grounding of the plasma cathode or the modification of the microwave circuit. However, the data did not show any substantial difference between the magnitude of extracted current in the two configurations, so further benchmarking tests were carried out with the source grounded to the chamber. This had the added benefit of reducing microwave leakage and the likelihood of vacuum leakage associated with
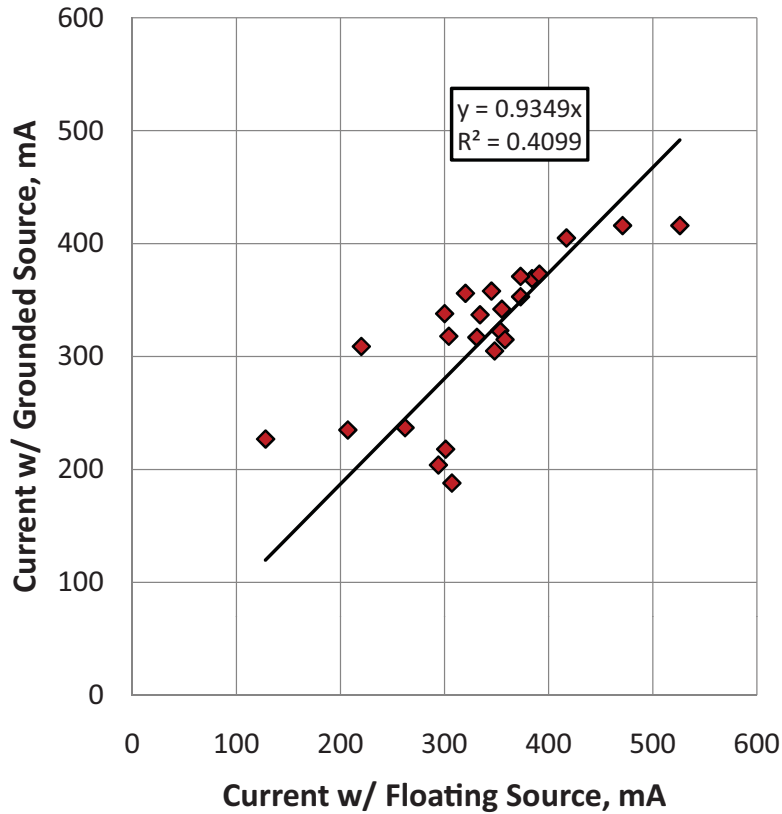
Figure 5.2: Extracted current on argon with floating source vs. grounded source. using the Teflon washer.

5.1.2 Extraction Orifice Optimization

From the open-ended plasma cathode performance, it was decided that an extraction aperture should be mounted at the exit plane of the source to increase the internal pressure. Endplates for the plasma cathode were fabricated, each of them ~ 1.5 mm thick. Four different aperture diameters were tested, with diameters of 19, 13, 6.4, and 4.0 mm, respectively. The molybdenum electrode was mounted 14 cm downstream from the endplate, and biased at a fixed voltage of +80 V. Again, the absorbed microwave power was varied from 40 to 120 W, and the extracted current was measured. For a fixed argon flow rate of 5 sccm, as shown in Figure 5.3, the source response to orifice size suggested that increasing the internal pressure by reducing the
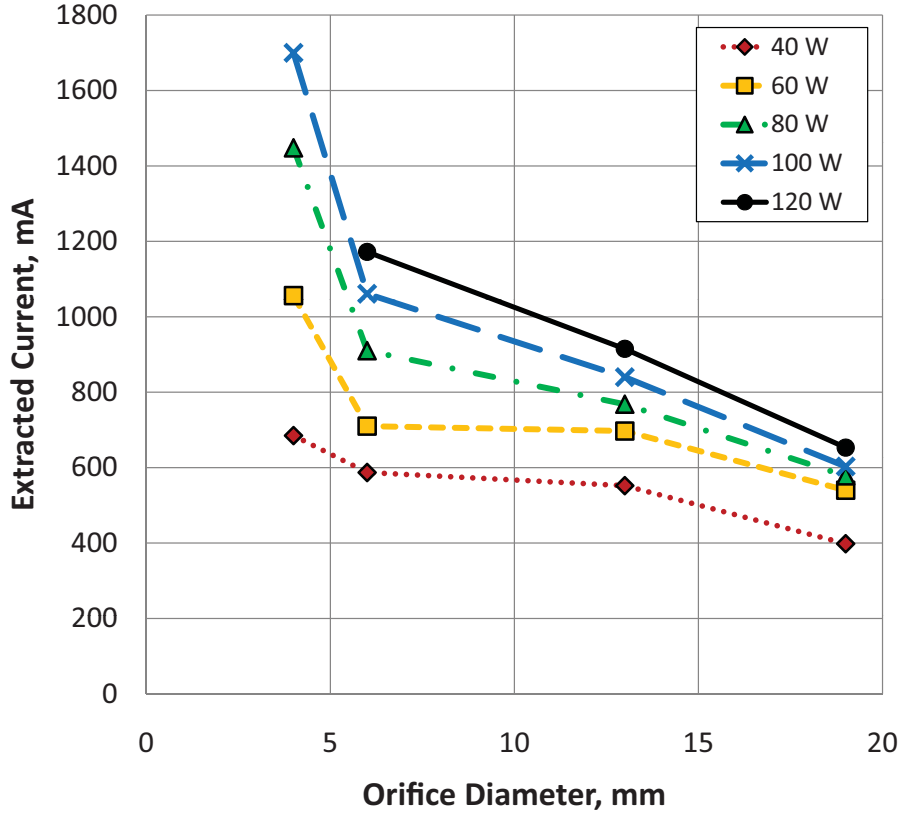
Figure 5.3: Extractable current vs. orifice diameter, at 80 V bias and 5 sccm.

aperture size was the pathway to higher extractable currents. This trend was observed over a flow rate range of 3 to 8 sccm.

The ideal aperture size for global nonambipolar flow to take place is determined from the ratio of the internal wall area to the aperture area. The ideal ratio between the areas is calculated from,

$$\frac{A_i}{A_e} = \sqrt{\frac{2M_i}{\pi m}}, \tag{5.1}$$

where A_i is the wall area and A_e is the aperture area.[47] For argon, this ratio is 215, giving an aperture diameter of 13 mm for this design. However, as seen in Figure 5.4, the extractable current continued to increase with flow rate with this aperture size. There are a couple of reasons for this disagreement. Although such an aperture size may be necessary for nonambipolar electron extraction, a smaller aperture increases
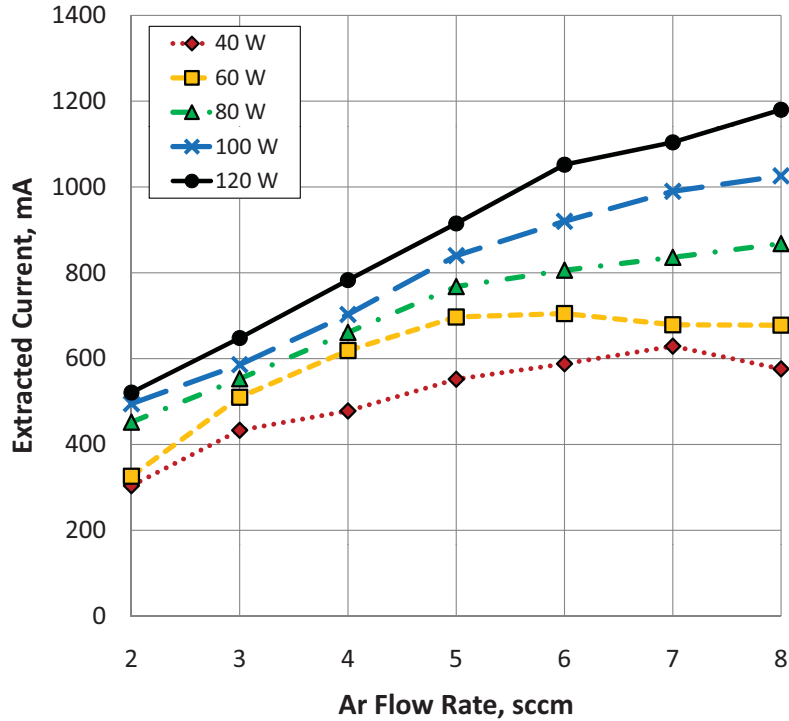
Figure 5.4: Extracted current profiles with 13 mm aperture.

the the internal plasma production rate by increasing the pressure. Additionally, the collection surface is not necessarily the physical area of the aperture; instead, the boundary may be concave upstream of the aperture. When a thicker 4 mm aperture (13 mm long) was used, no current could be extracted from the source in the desired voltage range, so the thin 4 mm aperture was chosen as the best case scenario for future tests.

5.2   Performance on Argon

5.2.1   Extracted Current Benchmark – 4 mm Aperture

Using a 100 Volt, 5 Ampere DC power supply, the source was tested using a 4 mm aperture. It was noticed that when the extraction anode was biased positively and
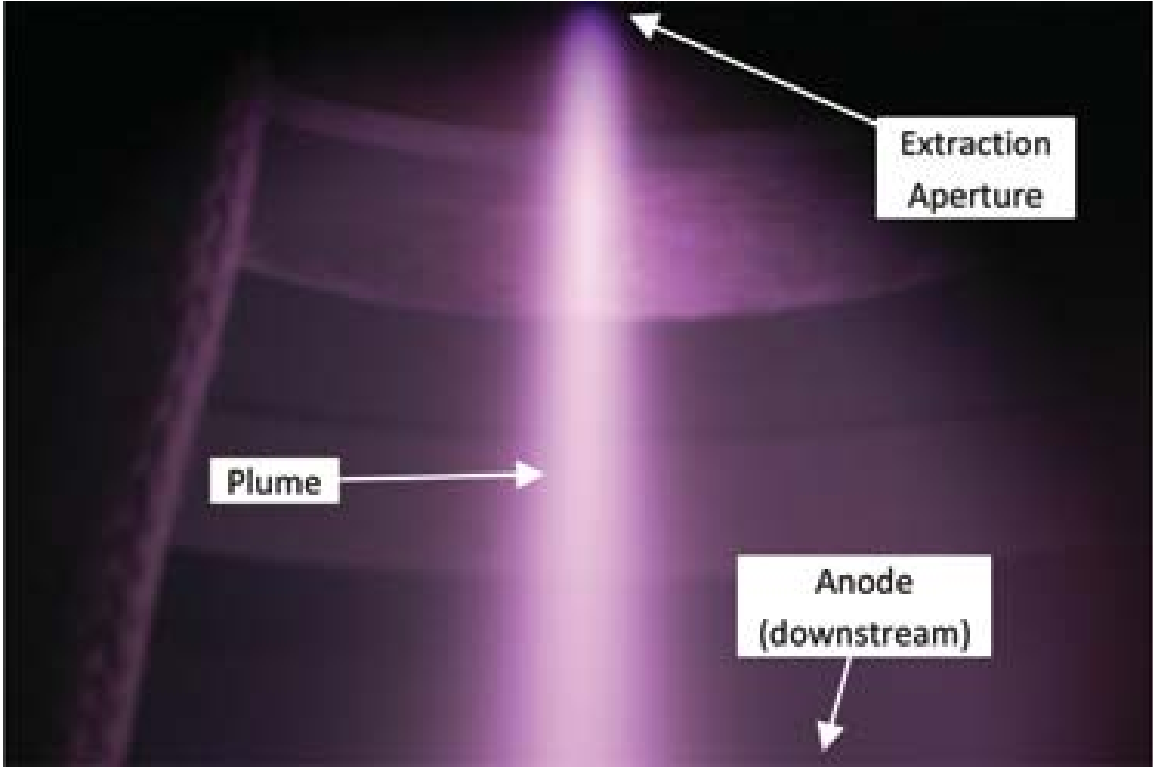
Figure 5.5: Visible plume from ECR plasma cathode, 4 mm aperture, 80 V.

electron current was collected, a bright plume was observed between the aperture and external anode. The plume at an operating condition of 80 V and 6 sccm is shown in Figure 5.5. The collimated, bright plume is evidence of collisional excitation of the background gas by the extracted electron beam. The observed emission across the 14 cm gap cannot be explained by relaxation of neutral atoms expanding away from the plume. The mean neutral speed is roughly 400 m/s, while the radiative relaxation time is on the order of tens of nanoseconds, so neutrals can only travel fractions of a millimeter before emitting. It appears that instead, the emission is a result of accelerated electrons leaving the plasma cathode and exciting background gas which is also flowing through the aperture.

The extractable current with the 4 mm aperture was measured as a function of flow rate and absorbed microwave power, at extraction voltages of 60, 80, and 100 V, as shown in Figure 5.6. The peak current in this range of operating conditions was

4.24 Amperes, achieved at 6 sccm, 120 W of microwave power, and a bias of 100 V.

The extracted current measurements suggest general trends in both the plasma production within the device and the electron extraction from the source. At all voltages, increasing the microwave power generally resulted in a corresponding increase in the extractable current, and in most cases this trend was roughly linear. This suggests that electron production in the plasma cathode is linearly dependent on the input power, consistent with electropositive plasma models.[45] The extracted current generally increased with flow rate at low pressures, implying that as additional neutral atoms are supplied to the source, they are ionized and the density increases in turn.

This behavior changes when the applied bias is increased, however. At high voltages, the extractable current saturates, particularly at the upper end of the flow rate range (with internal pressures of 60 to 70 mTorr). For example, under a bias of 80 V, the current saturates around 2 Amperes at flow rates above 5 sccm. Increasing the extraction bias to 100 V roughly doubles the maximum current, to a value around 4 Amperes. In addition, at 100 V and high flow rates (above 6 sccm), the microwave power circuit could not be matched to the load in a way that could supply 100 or 120 W of microwave power; as the forward power was increased, the reflected power increased by the same amount. In total, the benchmarking data initially suggested that for high enough internal pressures and microwave power levels, the extractable current is largely determined by the extracted voltage. This makes some intuitive sense, since the performance of the plasma cathode is expected to be a convolution of the plasma production within the source and the mechanism for electron extraction. The behavior at high voltages suggests that the two mechanisms may not be entirely disconnected. That is, the applied DC bias is likely to influence the electron extraction from the aperture, but it may also provide a degree of current "amplification" through additional ionization within the source. High energy electrons are also more likely to
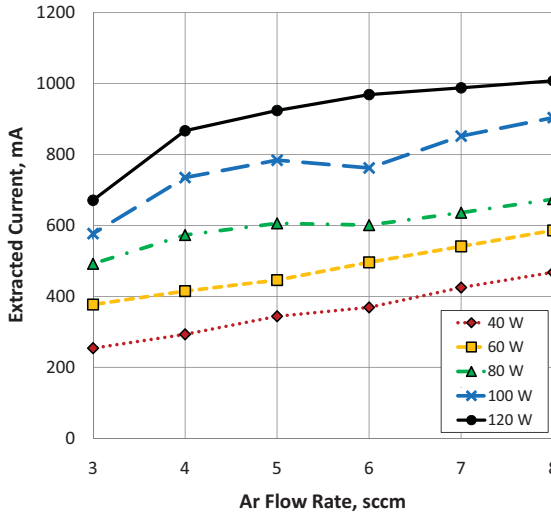
(a) 60 V Bias.
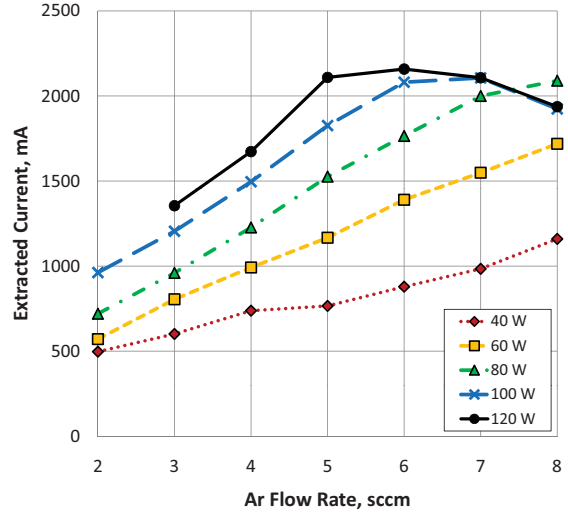
(b) 80 V Bias.
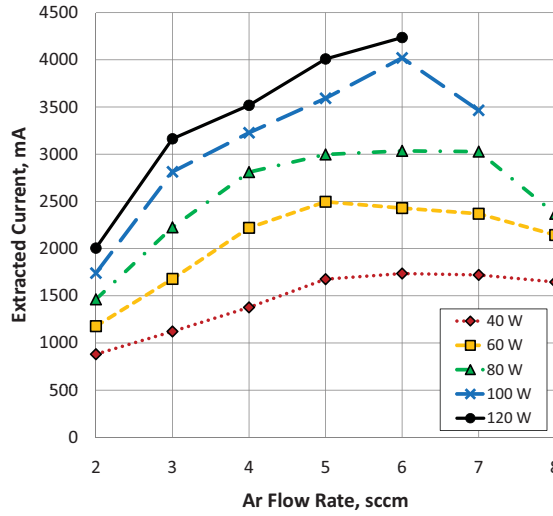
(c) 100 V Bias.

Figure 5.6: Extractable current vs. microwave power and flow rate, on argon at U-M facility.

produce some ionization external to the source, shielding out any space charge buildup that would tend to limit the current transported across the gap. This information eventually led to a more detailed study of the internal source plasma and external plume, as well as the electron extraction mechanism, which are presented in Chapters 6 and 7, respectively.

It should be noted that a coating was often observed on the quartz pressure window after operating the source above ~ 60 V for an extended period of time. This is a result of high energy ions impacting the internal walls of the plasma cathode. In one test, after operating for ~ 1 hour at 100 V, it was suspected that the window coating had suppressed microwave absorption in the plasma, when the extracted current decreased over the course of minutes at fixed conditions. As a precautionary measure, the window was cleaned during experiments using cerium oxide power. The sputtering coating of the window introduces a possible failure mode for the waveguide plasma cathode, which may be need to be addressed in a prototype model. This study focuses on the feasibility of the waveguide plasma cathode approach from the standpoint of deliverable current and the underlying plasma physics, and the window coating problem is left to future development studies.

5.2.2 Power and Gas Efficiency

Two figures of merit are often used to quantify the performance of thrusters and plasma cathodes: the electron production cost and the gas utilization factor.[24] The electron production cost is defined as the ratio of total input power to extracted current, where the total power is the absorbed (forward minus reflected) microwave power and the beam extraction power (current $\times$ anode bias). The electron production costs calculated from the argon benchmarking tests is shown as a function of flow rate in Figure 5.7. At all microwave power levels, the production cost decreases monotonically with flow rate, up to 6 sccm. This is reasonable since the ionization
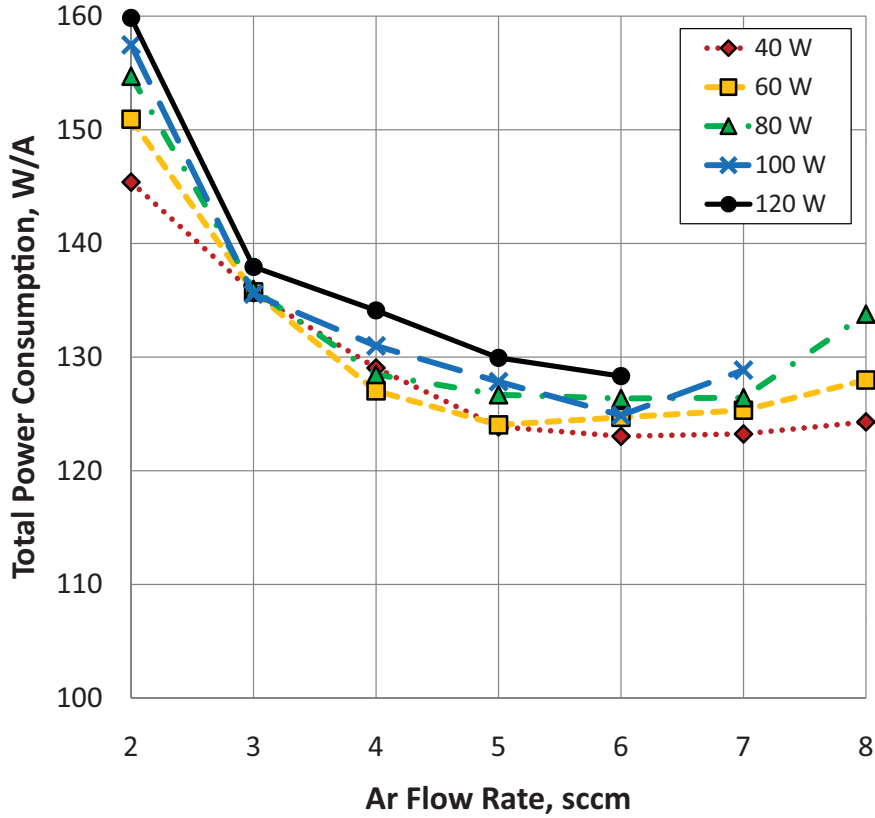
Figure 5.7: Electron production cost, on argon at 100 V bias.

rate is proportional to the internal neutral and electron densities; in this regime, as the internal plasma density is increased, the extracted current increases as well. At higher flow rates, the production cost levels off and current extraction may be limited by the extraction voltage rather than the internal density. As additional microwave power is absorbed by the plasma, that power is effectively wasted and the production cost increases. This also corresponds to the behavior seen in Figure 5.6 at high flow rates.

The gas utilization factor is defined as the ratio of the emission current to the gas flow rate measured in equivalent Amperes. This parameter gives a measure of how many electrons are extracted from the device per neutral gas atom fed into the device. In other words, the gas utilization is roughly the number of times a neutral atom is recycled within the source before being lost through the aperture. The dependence
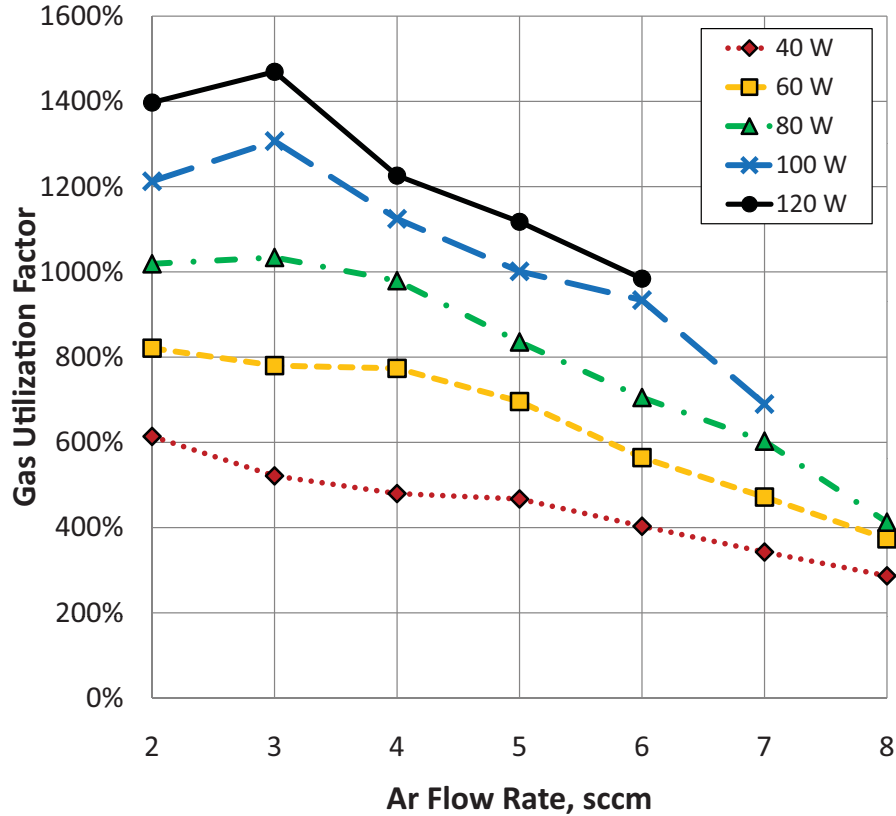
Figure 5.8: Gas utilization factor, on argon at 100 V bias.

of the gas utilization factor on the flow rate is shown in Figure 5.8, taken at a bias of 100 V. The utilization is at its maximum at the lowest flow rates, where the current is likely limited by internal ionization rate. As the flow rate is increased, the utilization converges to a value around 300 percent, regardless of input microwave power. This behavior again suggests that at high flow rates, the current is limited by the extraction bias rather than the supply of neutral gas to the device.

5.2.3   Internal Pressure Variations with Power & Flow

A measure of the internal pressure was eventually necessary for a more quantitative study of the source plasma behavior. While the internal pressure was initially estimated using the aperture conductance and flow rate, experimental verification of those calculations would solidify those results. After the current extraction tests
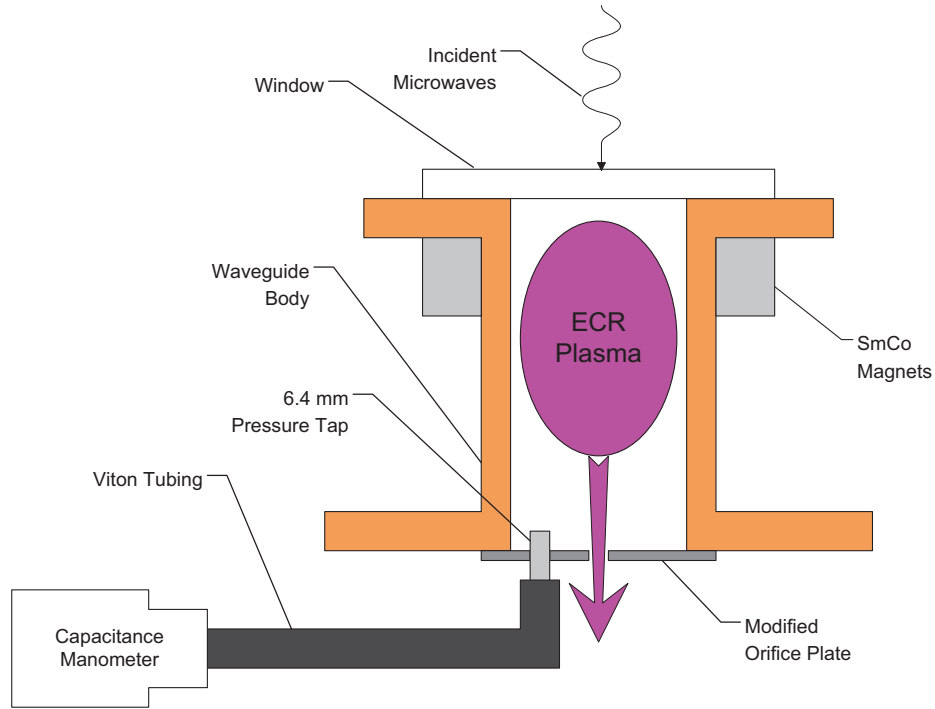
Figure 5.9: Schematic of setup for internal pressure measurements.

on argon, a second endplate was built with a pressure tap, which was connected to a gas feedthrough on the exhaust chamber by a section of flexible tubing. A capacitance manometer with a range of 1 Torr was connected to the gas feedthrough, as shown in Figure 5.9.

The internal pressure was measured as a function of flow rate, with no applied bias and no microwave discharge. Over the same range of flow rates, the microwave discharge was initiated at absorbed power levels from 40 to 120 W. No change in the internal pressure was detected due to the microwave power alone, so the neutral gas was not heated significantly by the ECR plasma. At each power level, the extraction electrode was biased at 60, 80, and 100 V, and after two minutes (when the pressure measurement stabilized), the pressure was recorded. In this case, the applied bias did have a small but noticeable impact on the internal pressure. Generally, the pressure varied from 20 to 60 mTorr in the flow rate range of 2 to 8 sccm, as shown in Figure 5.10 for the case of 120 W microwave power. At all voltages, the pressure scaled
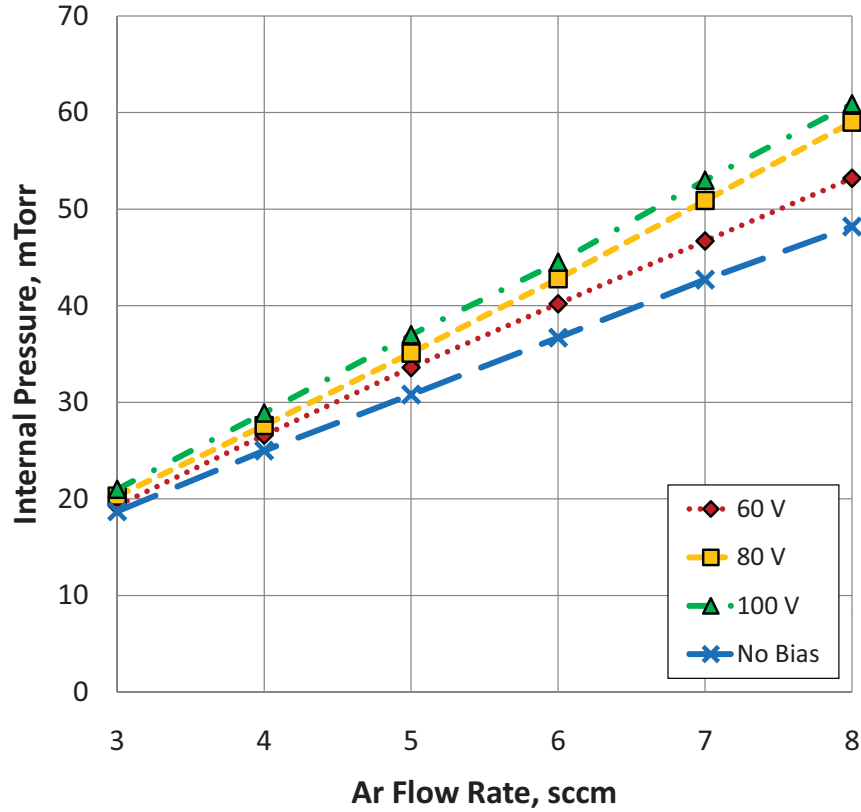
Figure 5.10: Internal pressure vs. flow rate and applied bias, at 120 W.

linearly with flow rate, as expected. The difference in pressure between the biased and unbiased cases was most pronounced for the upper extremes of the power and voltage range. At the 120 W, 100 V case, the pressure during current extraction reached 62 mTorr, an increase of nearly 30 percent from the unbiased case (48 mTorr). This may be due to additional heating of the gas during current extraction or the "plasma plug" effect that is observed when a dense plasma is formed near flow constriction such as an orifice.

5.2.4 Initial Langmuir Probe Measurements

A Langmuir probe was used to study the possibility of electron multiplication in the external plume shown in Figure 5.5. Ionization in the plume amplifies the total collected current. A cylindrical probe, 0.51 mm in diameter and 3.0 mm long,

Incident
Microwaves

Window

Waveguide
Body

ECR
Plasma

SmCo
Magnets

Probe "C"

1.0 cm

1.1 cm

0.5 cm

Probe "B"

4.3 cm
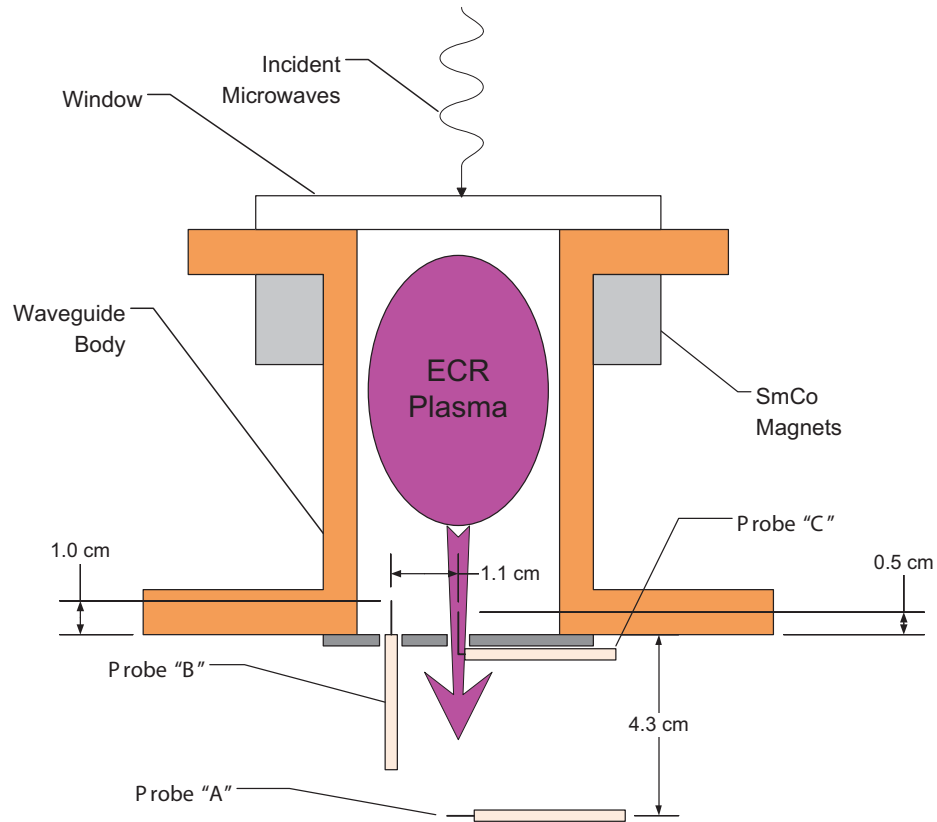
Probe "A"

Figure 5.11: Schematic illustrating fixed probe locations.

was used in this test along with the SmartProbe automated Langmuir probe analysis software from Scientific Systems. The exposed probe tip was mounted so that it was centered in the visible plume, 4.3 cm downstream from the extraction aperture, and is shown as "Probe A" in Figure 5.11. The ion density in the plume was measured as a function of applied bias, and the results are shown in Figure 5.12.

As seen from the probe data, the plasma density in the plume increased monotonically as the bias voltage was increased, and the extracted current tracked along with it. This in itself does not suggest that electrons produced from external ionization contribute directly to the extracted current, however. If it is assumed that electrons leaving the plasma cathode aperture are accelerated to an energy proportional to the applied bias, then the plasma density at a fixed location as a function of bias can be used to check whether plume ionization acts as a secondary
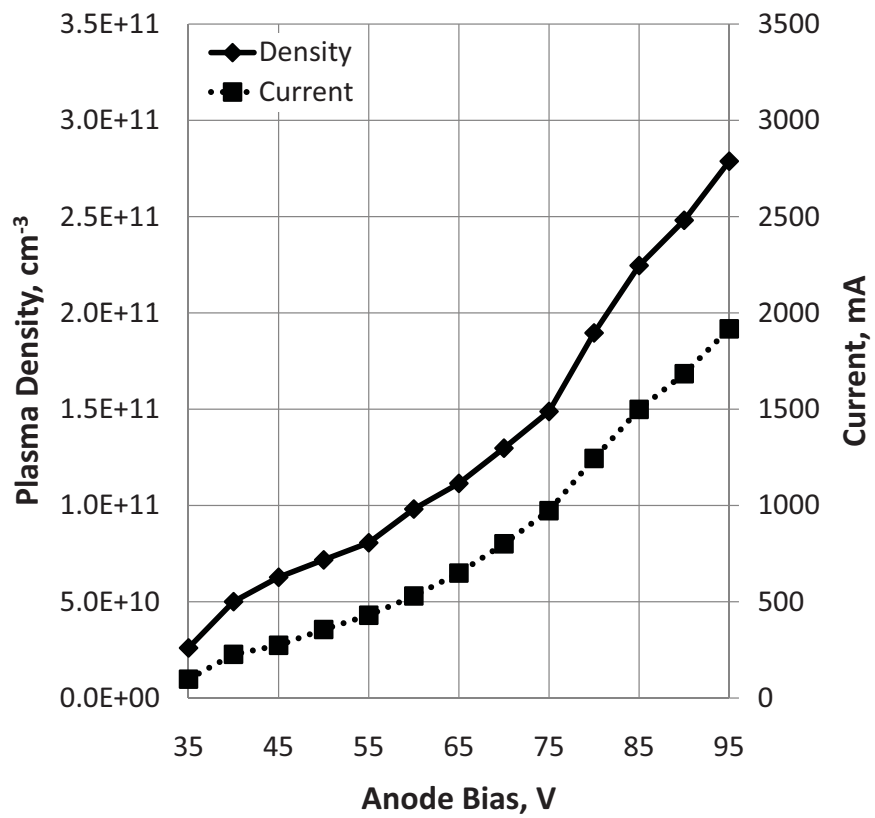
Figure 5.12: Ion density from fixed Langmuir probe in the plume, at 60 W and 6 sccm.

electron source at high voltages. If flux is conserved between the extraction aperture and the downstream probe, then the plasma density at the probe should scale linearly with $I/\sqrt{V}$, where I is the extracted current and V is the anode bias. The density at the probe is plotted against this ratio in Figure 5.13. As the voltage is varied, the plasma density at the probe is clearly explained by this scaling, so the plume does not act as a significant source or sink of electrons. If plume ionization were amplifying the measured current, Figure 5.13 would deviate from this linear relationship. The density measured in the plume is large enough to account for the full extractable current at the anode surface. These findings suggest that the plume may be similar to the positive column in glow discharges, wherein the plume overall is quasineutral, and current is transported across the column by a relatively small electric field. This possibility is addressed in more detail by the axial Langmuir probe maps in the plume, described in Chapter 6.

Another region of interest is that inside the plasma cathode, at the exit plane of the source. A Langmuir probe, 0.51 mm in diameter and 6 mm long, was installed 1.1 cm from the center of the orifice, and oriented axially. The probe tip was 1.0 cm from the endplate (Probe "B" in Figure 5.11). These measurements were taken to quantify the plasma properties within the source downstream of the ECR zone. With an anode bias of 80 V, probe traces were taken over a range of flow rates from 3 to 8 sccm and microwave power levels from 40 to 100 W. The plasma density and electron temperatures from these measurements are shown in Figure 5.14.

The internal probe measurements give a plasma density that is significantly overdense over the range of operating conditions. While the cutoff density in the plasma cathode (at 2.45 GHz) is 7.4×10^{10} cm^{-3}, densities up to 3.8×10^{11} cm^{-3} were measured at the probe. The electron temperature varied in the range of 2 to 4 eV, with lower temperatures at higher internal pressures, as increasing collision frequency is responsible for electron cooling. The densities and temperatures of the
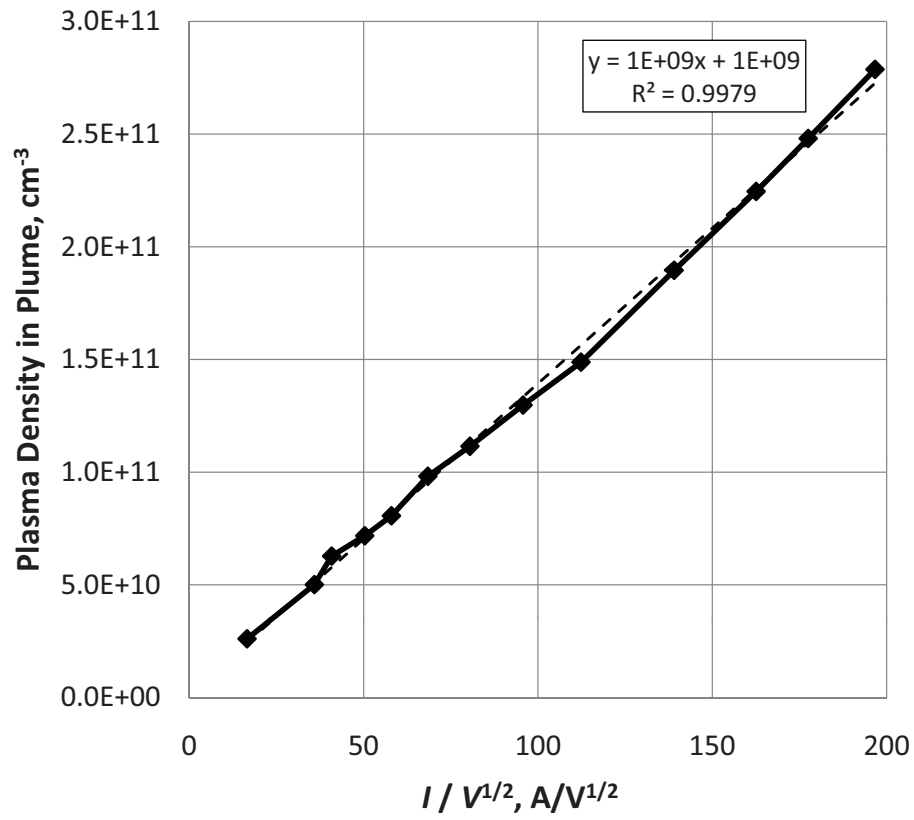
Figure 5.13: Demonstration of flux conservation with varying voltage, on argon.

(a) Plasma Density.

(b) Electron Temperature.
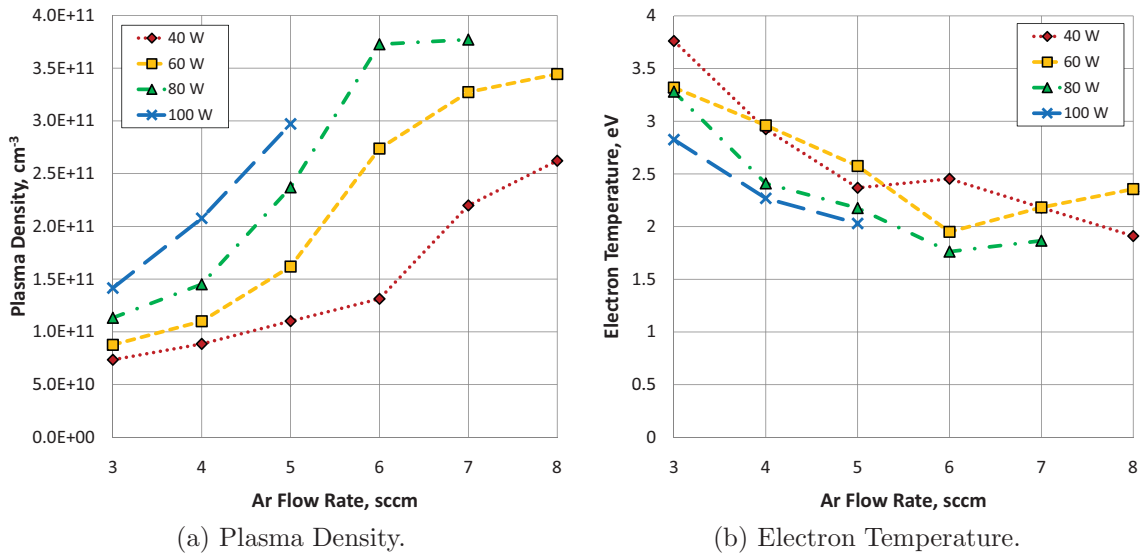
Figure 5.14: Plasma density and electron temperature, internal probe, 80 V bias.

bulk plasma were used to calculate the maximum extractable current from the 4 mm aperture, using the Maxwellian electron saturation current density (J_{sat} from Equation (3.46)). The calculated current is plotted against the actual measured current at each operating condition, as shown in Figure 5.15. There is a marked difference between the measured and extractable current, though the two values are linearly related overall. The measured current was a factor of 8 larger than the calculated current. Possible reasons for the discrepancy include a radial non-uniformity in plasma density within the source as well as additional ionization in the region near the extraction aperture. As mentioned previously, the plasma boundary at the aperture can become convex via rarefaction of the extracted electrons in that region. The calculated current in Figure 5.15 assumes a circular loss area equal to the aperture area. If a hemispherical boundary is assumed instead, then the loss area increases by a factor of two, bringing the measured and calculated values closer to one another.

Another Langmuir probe was installed in the orifice region itself, shown as Probe "C" in Figure 5.11. The probe was 0.28 mm in diameter, 9.5 mm long, and oriented on centerline. The probe was mounted so that 5 mm of the probe tip was situated downstream of the aperture endplate, with the remainder inside the source. The plasma measurements taken with this probe represent spatially averaged plasma properties in this orifice region. I-V characteristics were taken at variable microwave power levels, with and without an 80 V extraction bias. The measured plasma density is shown in Figure 5.16.

Without an applied bias, the density varies in the range of 4.5×10^9 to 8.8×10^9 cm^{-3}, well below the cutoff density. With an 80 V bias, the density increases by nearly two order of magnitude. It is apparent that the DC electric field is important not only for electron extraction, but it may also influence the plasma density at the aperture. This could be achieved by either by enhancing electron transport along the
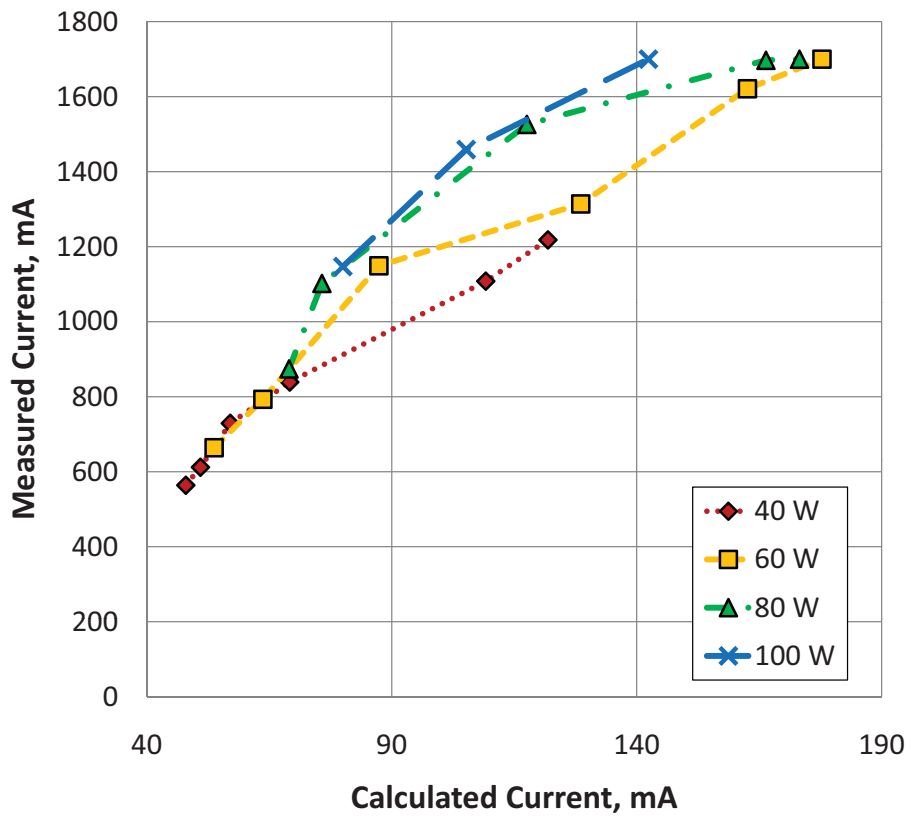
Figure 5.15: Measured current vs. calculated current, on argon with 80 V bias.
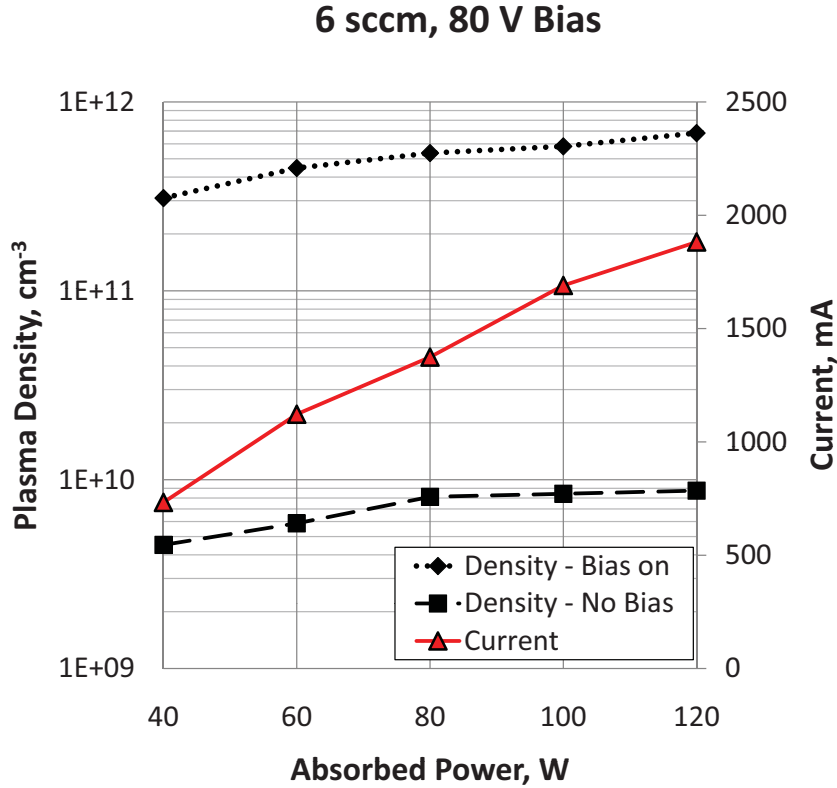
6 sccm, 80 V Bias

Figure 5.16: Plasma density in extraction aperture, on 6 sccm argon, with and without 80 V bias.

static magnetic field lined from the ECR zone to the aperture, or it may be directly responsible for additional ionization in the aperture. A detailed study of the region upstream of plasma cathode apertures was performed later to clarify this behavior, and is presented in Chapter 7.

The plasma densities at the three aforementioned probe locations (Figure 5.11) are plotted together in Figure 5.17 at 6 sccm and with an 80 V bias. Again, with no applied bias, the plasma densities in all three locations were quite low - on the order of 10^9 cm^{-3} inside the source, and undetectable in the plume region. With the 80 V bias, the plasma is clearly non-uniform. The region inside the source but away from the aperture contained plasma densities above 10^{11} cm^{-3}, suggesting that overdense plasma production was taking place in the ECR zone. The density in the orifice was higher than in the bulk, but trended with the bulk density. The plume plasma density
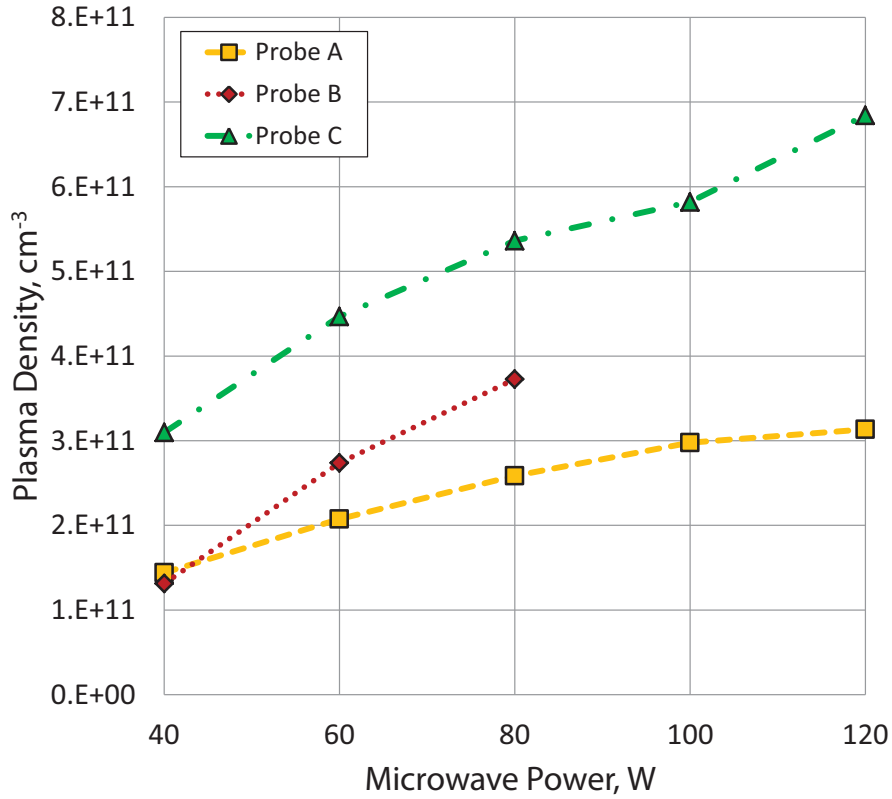
Figure 5.17: Comparison between ion densities at three locations, at 6 sccm and 80 V: Plume, orifice, and in the bulk of the source.

was consistently lower than the density in the other two locations, presumably due to expansion of the plume outside the plasma cathode. The trends in plasma density support the notion that the applied bias influences the plasma density in the orifice, which is not assumed in basic plasma cathode models.

5.2.5 Dependence on Background Pressure

Because the Langmuir probe data showed large ion densities in the plume (on the order of 10^{11} cm^{-3}), tests were conducted in a facility with higher pumping speeds and lower background pressure to study the effect of the background pressure on extractable current. One possible effect of a higher background pressure is ionization in the plume, which could directly multiply the electron current measured at the

anode, giving an inaccurate assessment of the actual extracted current. Plume ionization can also mitigate space charge buildup in the gap and allow high currents to be transported to the anode. A second argon gas feed was connected directly to the vacuum chamber to control the background pressure. The anode remained 14 cm from the extraction aperture, and the plasma cathode was run with the same procedure as in earlier tests. The resulting plots of extractable current vs. argon flow rate are shown in Figure 5.18, with a bias of 60 V.

The extractable current displayed a clear dependence on background pressure. The high current levels seen at the higher background pressure facility were not observed at the lower background pressures. The extractable current increased with background pressure at all source flow rates. The leveling off of extractable current at high flow rates and microwave power was observed in both facilities, suggesting that the current saturation effect may depend primarily on the conditions in the plasma source itself. To further clarify the background pressure dependence, the source conditions were fixed at 6 sccm and 60 W, and the background pressure was varied. This was done for two extraction voltages: 60 V and 80 V. The data was combined with benchmarking data from U-M at the same flow rate and microwave power, at 60, 80, and 100 V. The combined results are shown in Figure 5.19, with VF-56 denoted as "Facility 1" and the U-M chamber denoted as "Facility 2." At chamber pressures below $\sim 5 \times 10^{-5}$ Torr, the plume could not be initiated at 60 or 80 V.

As the background pressure is increased, additional ionization takes place in the plume, and the current increases linearly. Once the pressure reaches a critical value, the current becomes nearly independent of pressure, at all three voltages. During background pressure studies at U-M, it was assumed that plume effects were negligible because all measurements were taken above the critical pressure. At 60 V, the critical pressure is 1.7×10^{-4} Torr; at 80 V, it is 2.6×10^{-4} Torr. The ratio
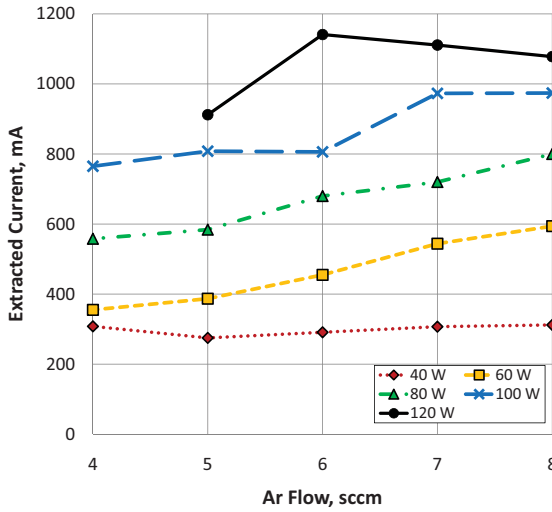
(a) 9.6×10^{-5} Torr.
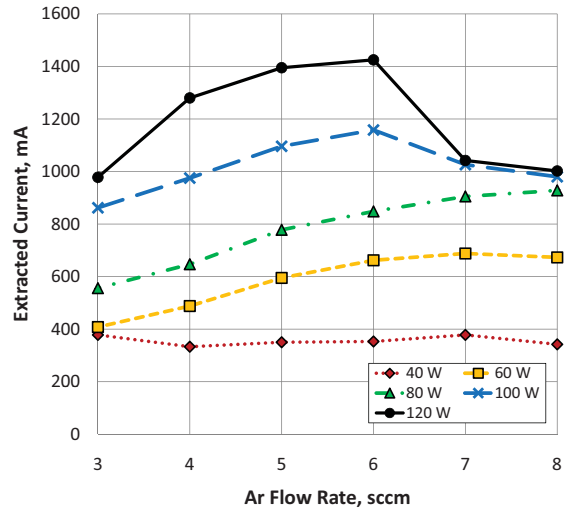
(b) 3.8×10^{-4} Torr.
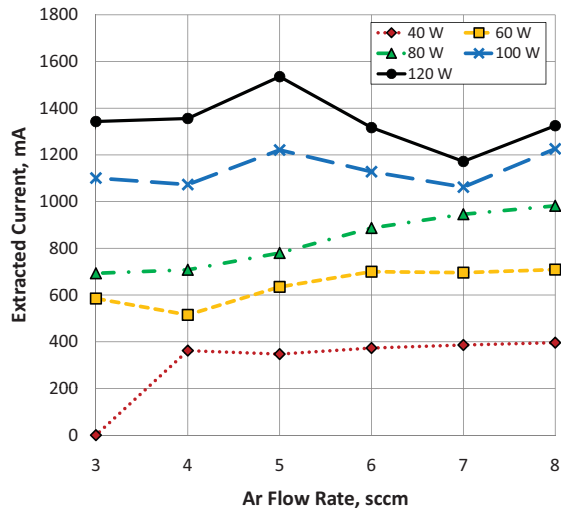
(c) 5.5×10^{-4} Torr.

Figure 5.18: Extracted current on argon vs flow rate, at variable background pressures.
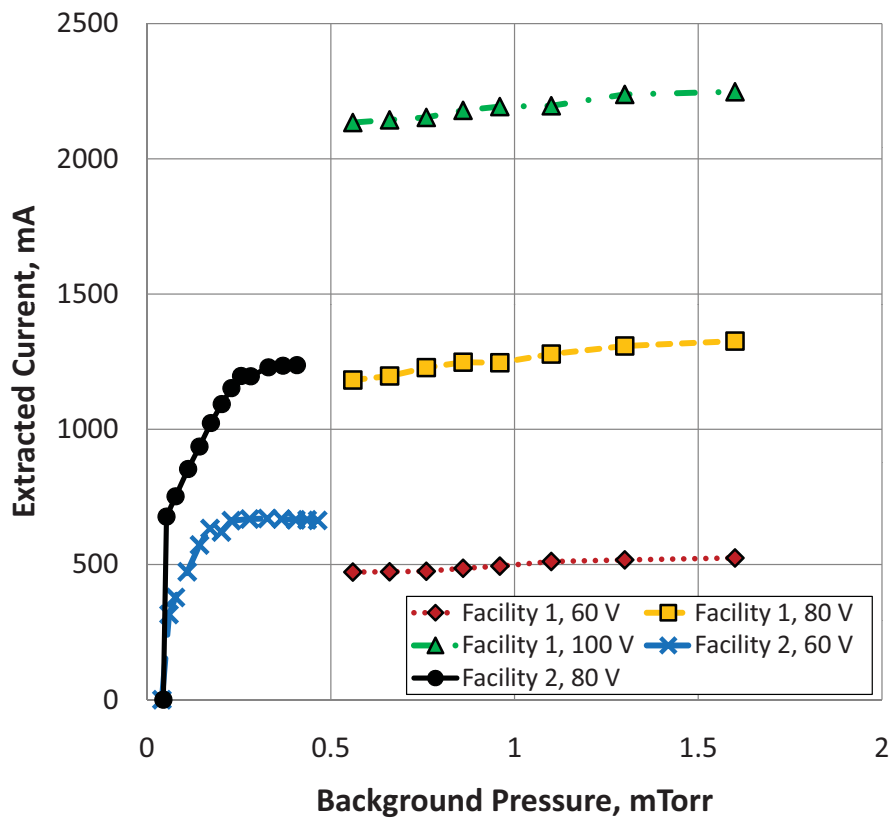
Figure 5.19: Extracted current vs. background pressure, on argon at fixed discharge conditions.

between the two critical pressures (0.7) corresponds to the ratio between the voltages. The background pressure trends provide some insight into the necessary conditions for plume formation. Below the critical pressure, the ionization rate in the plume is insufficient; as electrons are extracted through the aperture, negative space charge builds up in the 14 cm gap, which limits the extractable current. As the pressure is increased, additional plume ionization neutralizes the space charge, and the current limit is increased. Above the critical pressure for a given voltage, the plume ionization is sufficient to neutralize the space charge in the gap, and all electrons leaving the aperture can be transported across the gap.

If ionization in the plume were contributing directly to the measured current, that is, if electrons born in the plume were a large fraction of the measured electron current, then the current should continue to increase above the critical pressure. A slight increase in current is observed above the critical pressure, but is more subtle than at sub-critical pressures. This is likely due to the direct contribution from plume ionization just described. At a background pressure of 0.5 mTorr, the minimum ionization pathlength for argon is roughly 1.5 m, much larger than the gap. As a first-order estimate (calculated from: $1-\exp(-0.14 \text{ m}/1.5 \text{ m})$), only 9 percent of extracted electrons from the aperture are expected to undergo ionization collisions within the gap. The background pressure data suggests that in the given electrode configuration, a minimum degree of plume ionization is needed to maximize the extractable current via space charge neutralization.

5.3 Performance on Krypton

In actual electric propulsion systems, argon is not typically used for the feed gas because of its relatively high ionization energy (15.75 eV) and storability. During the initial development of the plasma cathode, argon was used due to its relatively low cost. However, it was expected that better performance could be achieved with

krypton and xenon feed gases, with ionization potentials of 14.0 eV and 12.1 eV, respectively. Krypton testing was performed at VF-56. The external plume could be established at an anode bias as low as 40 V, with no additional background flow. That is, the background pressure solely from the krypton flow through the plasma cathode was sufficient to establish the plume.

As the gas conductance of the aperture scales with $M_i^{-1/2}$, the internal pressure was calculated from the argon pressure measurements (Figure 5.10). The krypton flow rate was varied from 3 to 10 sccm, and by these calculations, the internal pressure varied from 27 to 88 mTorr with no applied bias, somewhat higher than with argon. The background pressure varied from 2.6×10^{-5} to 7.9×10^{-5} Torr over this range. The extracted current as a function of flow rate, microwave power, and bias is shown in Figure 5.20. Again, with flow and voltage held constant, there is a linear relationship between microwave power and extractable current. The more striking feature of the plots in Figure 5.20 is the emergence of a clearly defined peak current, which occurs at a single flow rate for each anode bias. In most cases, this "peak" flow rate is the same regardless of microwave power level. As the bias is increased, the peak extracted current shifts to lower flow rates, and the dependence on flow becomes more peaked as the microwave power is increased. This agrees with the current trends in the earlier argon benchmarks, where at high microwave power, the extracted current peaked and then fell off with flow rate. This peaked behavior is likely to be due to behavior within the source, rather than in the plume. With quasineutral plume filling the anode-cathode gap, the current conducted across the gap is expected to scale with E/N. The background pressures are quite low in this case, so as the voltage is increased, the flow rate for peak current would increase as well. However, this is the opposite behavior from what is seen in Figure 5.20, so the peak flow rate is not determined by the plume conductivity. More likely, the DC bias dictates the internal pressure at which electrons can be extracted through the aperture most efficiently, or
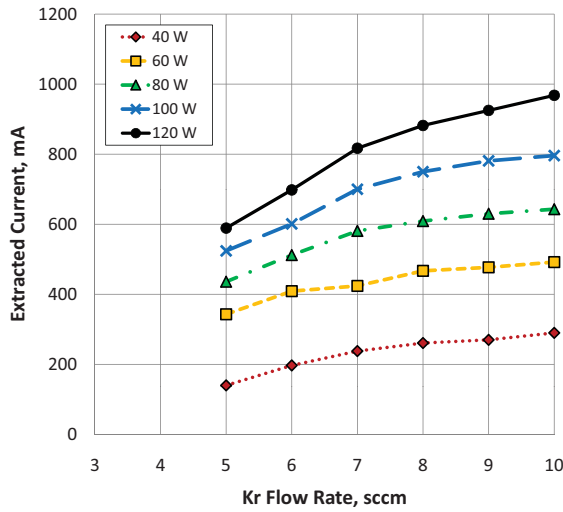
(a) 40 V Bias.
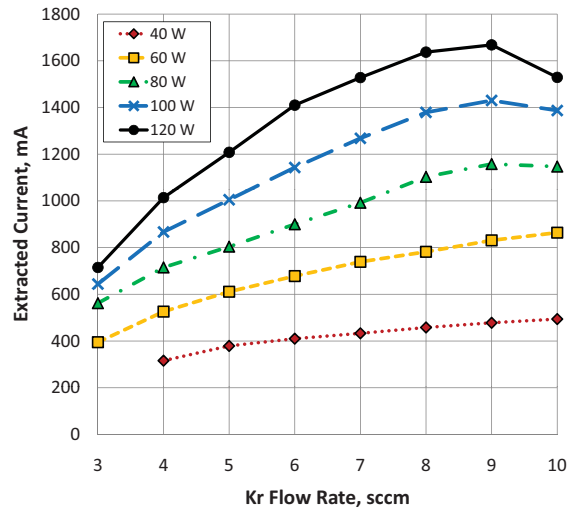
(b) 50 V Bias.
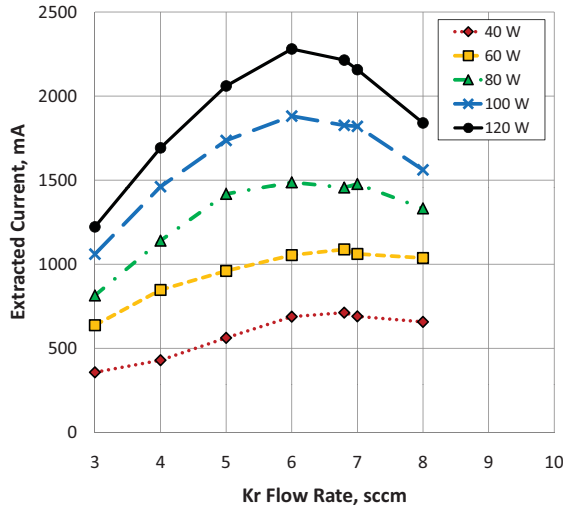
(c) 60 V Bias.
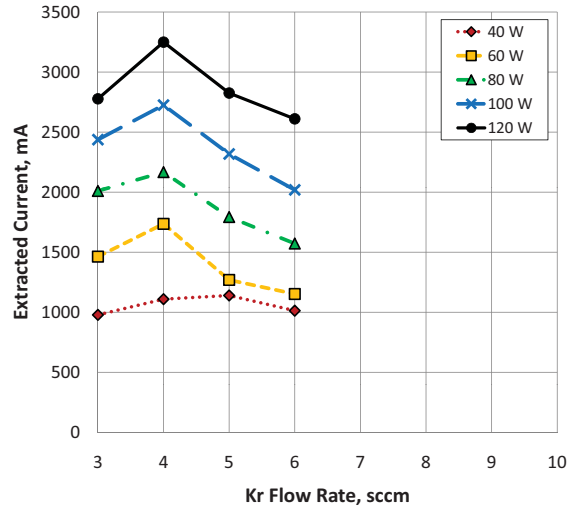
(d) 80 V Bias.

Figure 5.20: Plasma cathode performance on krypton.

drives ionization inside the source as electrons stream from the ECR heating zone.

5.4 Performance on Xenon

5.4.1 Current Extraction

A similar series of current extraction tests was performed with xenon feed gas as well. As with krypton, the plume could be initiated without any background flow, and in general the plume was stable at lower flow rates than on krypton. The plume was sustained at an anode bias as low as 30 V, and was run at flow rates from 1.5 to 6 sccm. The internal xenon neutral pressure varied from 16 to 77 mTorr over this flow rate; the background pressure varied from 1.2×10^{-5} to 3.8×10^{-5} Torr. The results of the current extraction tests are shown in Figure 5.21 for the 30, 40, and 50 Volt cases; the 60, 80, and 100 Volt cases are in Figure 5.22. The trends in extracted current are again similar to the other feed gases. The peaked trends in current are present, along with the shift to lower flow rates with increasing bias. The current again becomes more peaked, (i.e., more sensitive to flow) as the microwave power and bias are increased. At a bias of 100 Volts, a peak current of 4.2 Amperes was extracted, at 120 W of microwave power. This is comparable to the currents achieved on argon, but at a third of the required gas flow.

5.4.2 Power and Gas Efficiencies

As expected from the ionization potentials of the two gases, there was a marked increase in the power and gas efficiencies of the plasma cathode when run on xenon as opposed to argon. For comparison to the performance on argon, the electron production cost is plotted against xenon flow rate and microwave power for an extraction bias of 80 V in Figure 5.23. The electron production cost appears to be more sensitive to flow rate when operating on xenon, though in both cases there

108

(a) 30 V Bias.
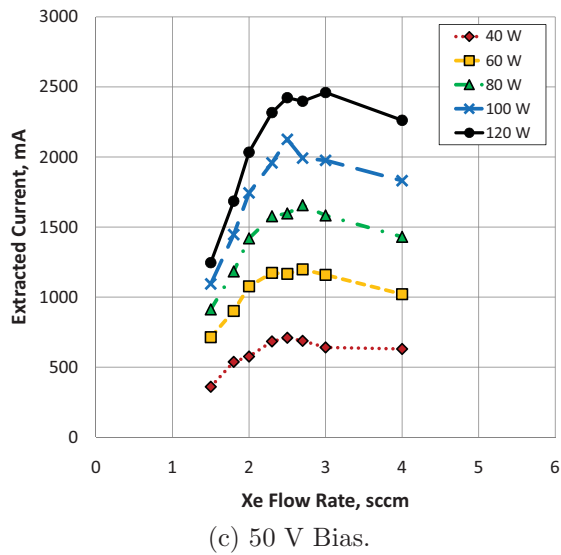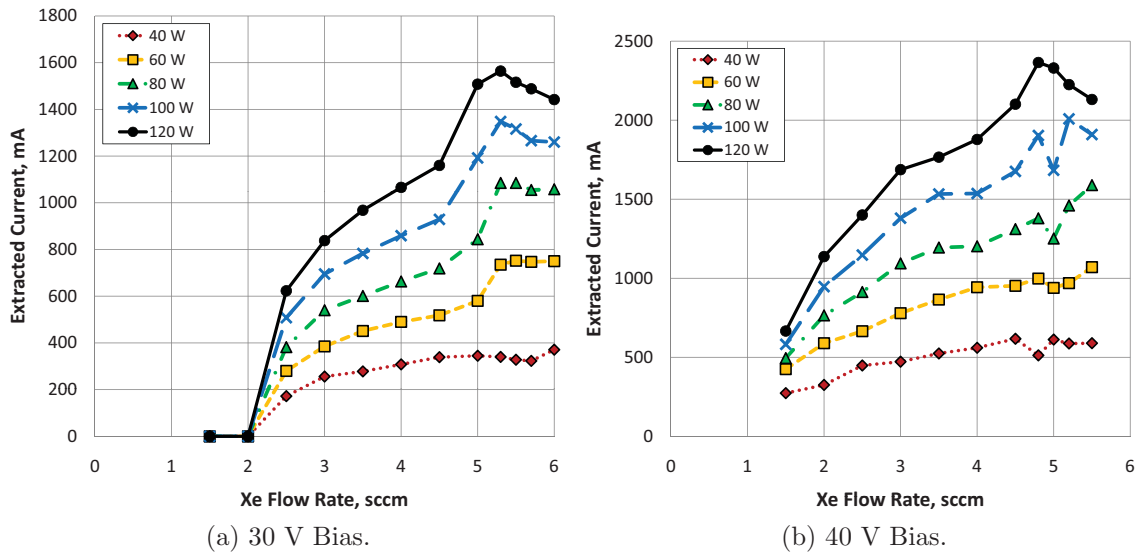
(b) 40 V Bias.

(c) 50 V Bias.

Figure 5.21: Plasma cathode performance on xenon.
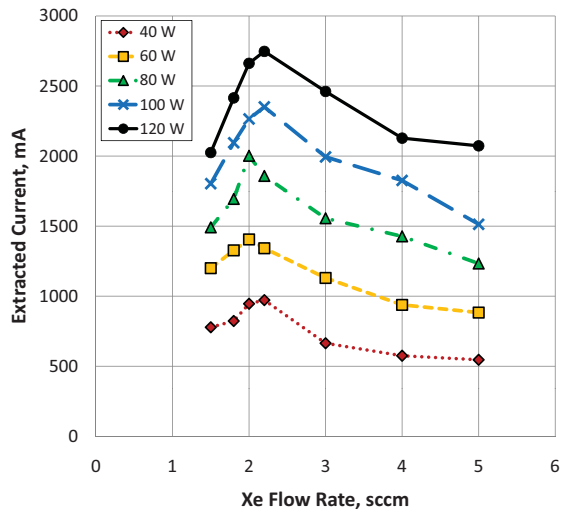
(a) 60 V Bias.
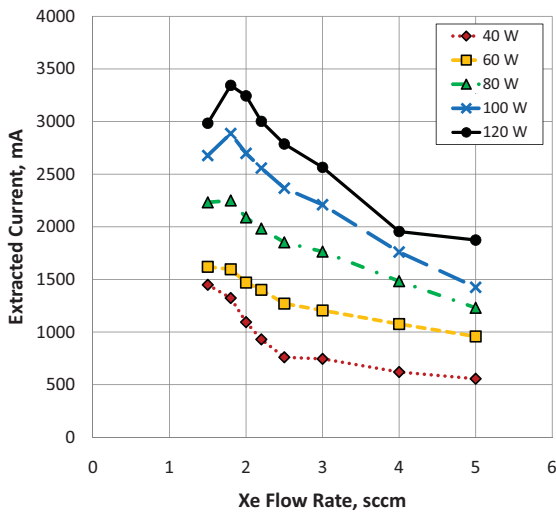
(b) 80 V Bias.
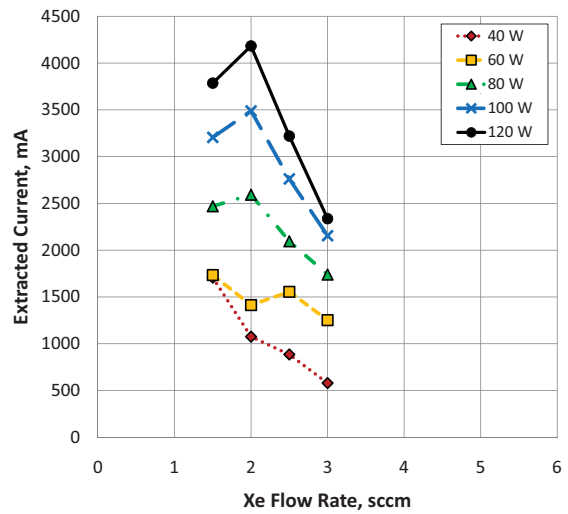
(c) 100 V Bias.

Figure 5.22: Plasma cathode performance on xenon.
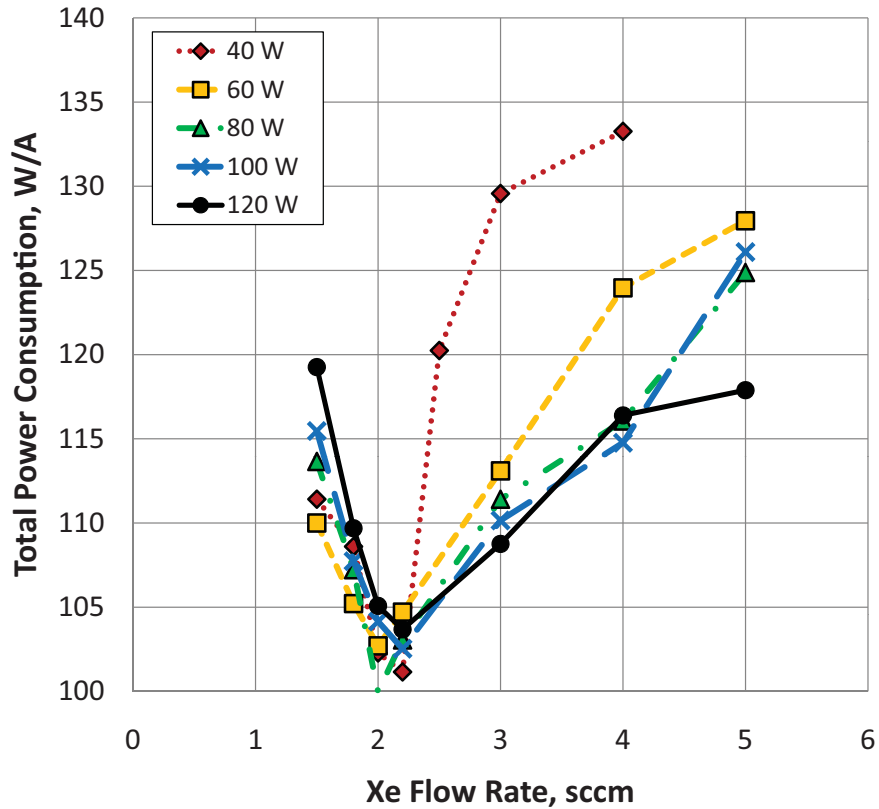
Figure 5.23: Total power consumption vs. flow rate, on xenon.

is a clear optimum pressure for a fixed anode bias. Below the optimum flow rate, the dependence on microwave power is weaker than at higher flows. This low flow range can be interpreted as a region where current may be limited by internal plasma density. If the microwave power is increased, the internal density does as well, and the extracted current follows. At the high-pressure side of the optimum, there is more dispersion between the microwave power levels. It may be that, as in the case with argon, the current is limited by a combination of internal density and the efficiency of the electron extraction. Here, increasing the contribution of ECR heating to the plasma density reduces the total power consumption, but the current is not limited entirely by microwave power. If that were the case, the electron production cost would be relatively independent of power, if a linear relationship between the power and internal plasma density is assumed.
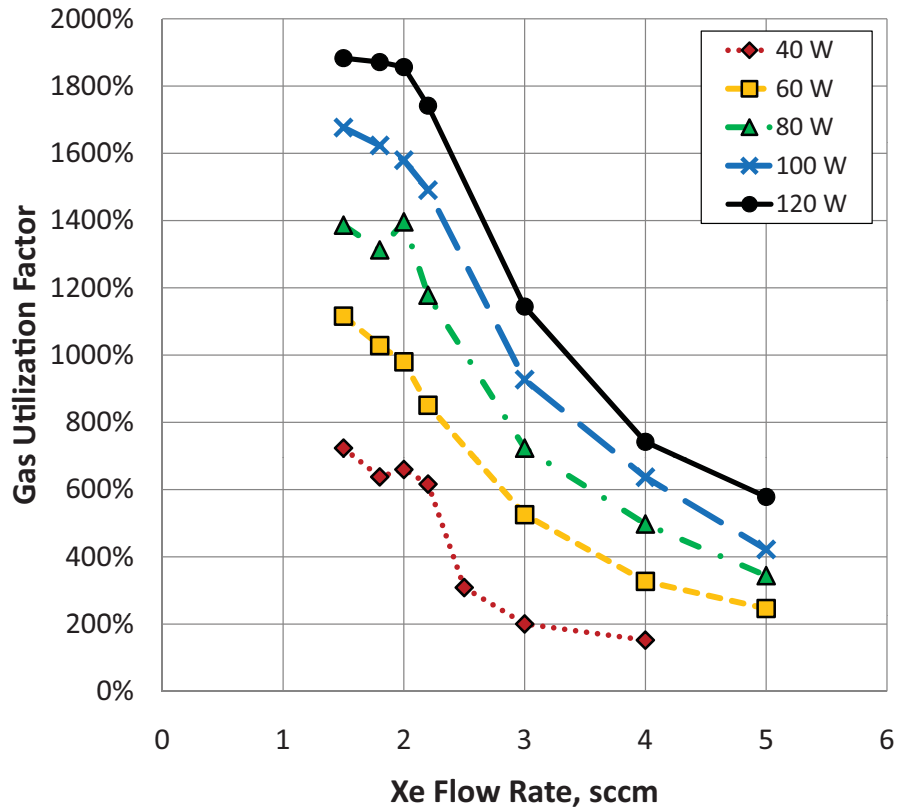
Figure 5.24: Gas utilization vs. flow rate, on xenon.

The gas utilization factor on xenon is shown in Figure 5.24 at the same conditions. On xenon, the utilization is relatively independent of the flow below the optimum value. This agrees with the trends in power consumption, in that the discharge may be power-limited in this case. Over all flow rates, as microwave power is increased, the utilization follows in a linear fashion. At flow rates below the optimum, the gas is utilized to its maximum regardless of the internal pressure, because the current is limited by the microwave power. At higher flow rates, the gas is utilized less effectively. Here, the current will still increase with the internal plasma density, but if electrons are not readily extracted from the plasma, the utilization suffers as a result.

The electron production cost was plotted against the gas utilization to clarify the range of operating conditions that were achieved on xenon. The plot, shown in

Figure 5.25 includes all data points from the xenon tests. There is a clear tradeoff in the power and gas efficiencies demonstrated with the plasma cathode. At 30 V, the device is inefficient with respect to both metrics, where it is likely that even if high density plasma is produced within the source, it is not efficiently extracted through the aperture. At 50 V and above, the trends in the metrics are reasonable. For a given internal plasma density, more current can be extracted as the bias is increased, and the gas utilization increases in kind. However, a higher fraction of the total power consumed goes into the DC "beam power" ($I \times V$) and the electron production cost increases to reflect that. Figure 5.25 differs significantly from trends seen in electrostatic ion thrusters, wherein the power loss increases asymptotically as the utilization approaches 100 percent.[24] Once an ion is extracted from a thruster it is lost, and at best it can deliver one ion per injected neutral. In the plasma cathode, ions can be recycled multiple times via surface recombination, with one electron extracted per cycle. The efficiency of the plasma cathode is predominantly limited by the beam extraction power rather than the internal discharge losses. As a result, gas utilization of several thousand percent can be achieved at high voltages. For efficient operation with respect to both power and gas consumption the ideal condition is at the "knee" in (Figure 5.25), where at 40 V, a power consumption as low as 91 W/A is achieved at a gas utilization of 690 percent; delivering 2.4 A of electron current.

5.5 Dependence on Bias

The trends in extracted current are compared to the Child-Langmuir scaling for space charge-limited emission in Figure 5.26 for each of the three gases. In each plot, the dependent variable is $I^{2/3}$ where I is the extracted current, plotted against the anode bias V. The space charge limited current should scale as $V^{3/2}/s^2$, where s is the thickness of the extraction sheath; in the space charge limited regime, the plots
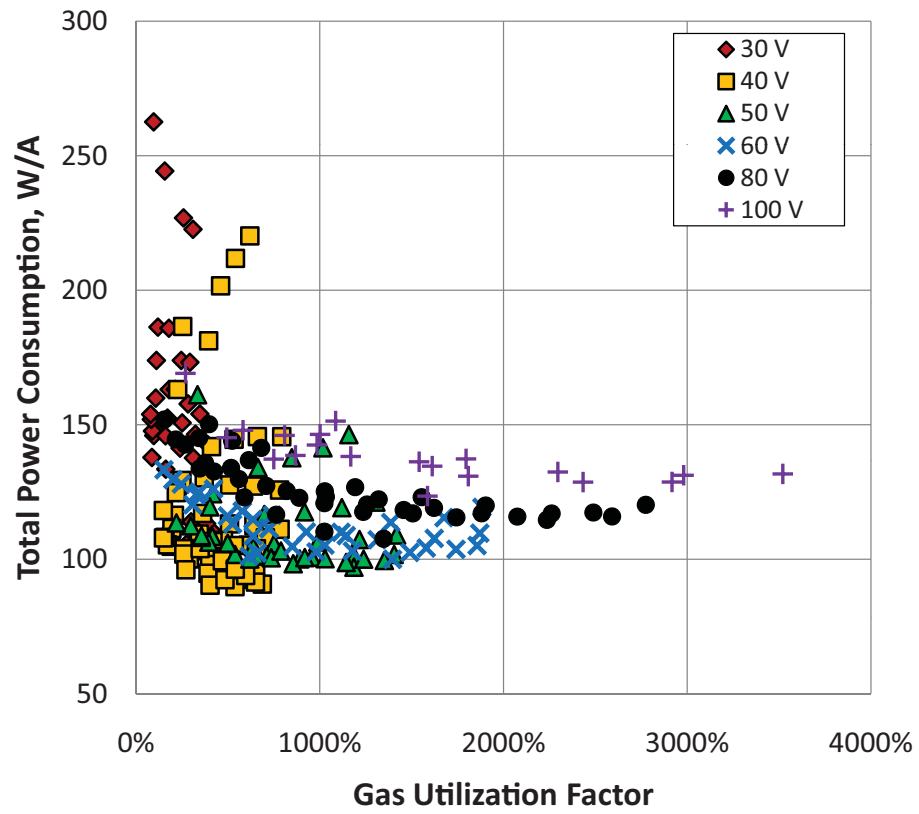
Figure 5.25: Total power consumption vs. gas utilization, on xenon.

should therefore be linear. On argon, the plasma cathode was run at 6 sccm and 60 W of microwave power while the bias was varied from 40 to 100 V. The results are superimposed with a linear trendline, showing that on argon at these conditions, the current is space charge limited.

The plots for xenon and krypton are shown at 6 sccm and 3 sccm, respectively. On these two gases, the linear dependence is seen at low voltages, indicating space charge limited emission. On xenon, the extracted current deviates from the Child-Langmuir scaling above 50 V, and at higher voltages the extracted current is roughly independent of the anode bias. This indicates competition between processes in the plasma cathode system. At low voltage, the internal plasma density is not the limiting factor on extracted current; instead, the limit is the electron flux that can be traverse the high voltage extraction sheath. At high voltage, the "ceiling" on the extractable current increases linearly with microwave power. This linear dependence on the power shows that the current is limited by the internal plasma density. In this regime, the bias is sufficiently high to extract the available electrons. However the internal density is likely too low to balance the extracted electron current with an equal amount of ion current to the internal walls of the device.

5.6   Comparison with Literature

The first objective of this research was to develop a viable concept of an antenna-less ECR plasma cathode for electric propulsion systems. The deliverable current on all three feed gases suggested that this type of design can support the neutralization of several thruster systems. Currents up to 4.2 Amperes were extracted on both argon and xenon, which exceeds the nominal beam current of the NSTAR (1.8 Amperes) [10], NEXT (3.52 Amperes) [29], and 25 cm XIPS (3.01 Amperes) [71] DC ion thrusters. The waveguide plasma cathode also delivered more current than the state of the art μ_{10} microwave plasma cathode (100 mA), though μ_{10} was designed
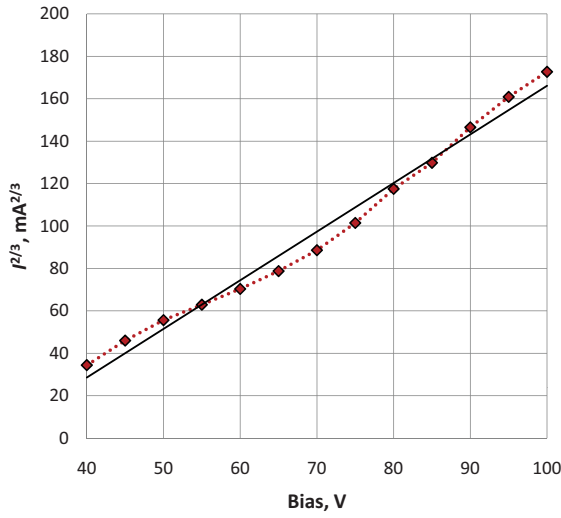
(a) Argon at 6 sccm, 60 W.
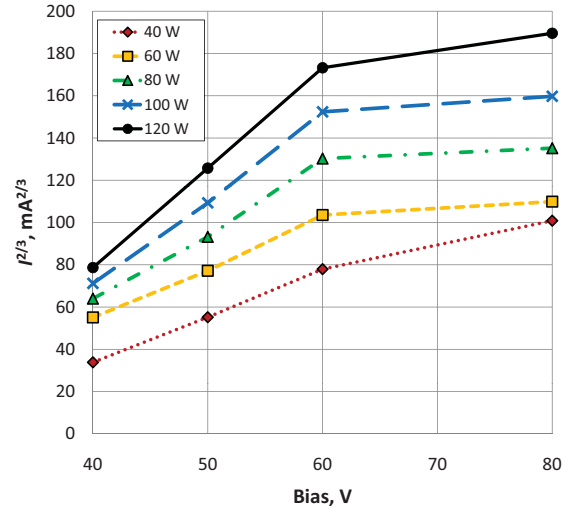
(b) Krypton at 6 sccm.
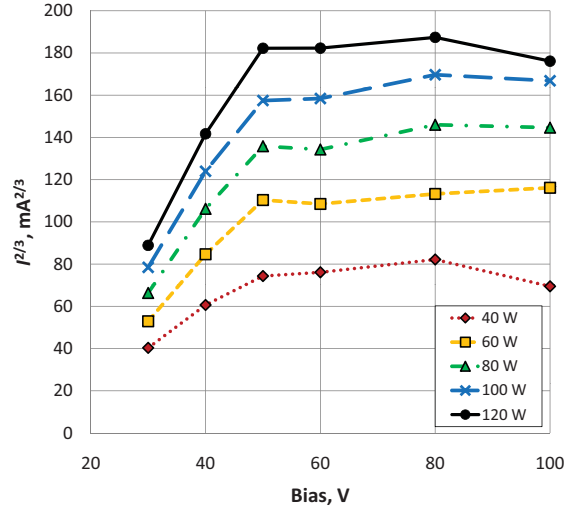
(c) Xenon at 3 sccm.

Figure 5.26: Current$^{2/3}$ vs. applied bias.

	Max. Electron Current	Min. Total Power Consumption	Max. Gas Utilization
Extracted Current [mA]	**4183**	2008	3786
Xe Flow Rate [sccm]	2.0	5.2	1.5
Absorbed Power [W]	120	100	120
Extraction Voltage [V]	100	40	100
Total Power Consumption [W/A]	128.7	**89.8**	131.7
Argon Gas Utilization [%]	2917	539	**3520**

Figure 5.27: Summary of best-case performance conditions of the waveguide plasma cathode.

as a low-power mission. The deliverable current and power efficiency of the device are below that of a HCA, but it operates at comparable flow rates. In this respect, this technology may be applicable to those high power missions where engine life is the most important metric; for thruster systems on the order of 10 kilowatts or more, the waveguide plasma cathode would consume but a small fraction of the total thruster power. A table which summarizes the operating conditions for maximum current, minimum power consumption, and maximum gas utilization is included in Figure 5.27.

The performance of the U-M waveguide plasma cathode is compared with similar devices in the literature in Figure 5.28. In all cases, total power consumption was defined as the absorbed "heating power" (microwave or RF, forward minus reflected) plus the "beam power" (extracted current times cathode bias), normalized to the extracted current. The "best case" performance was chosen for each device, with the exception of the μ_{10} engine, which uses the nominal values for the actual flight. All devices were based on microwave discharges, with the exception of Wisconsin 2008, which was the NES helicon plasma cathode. Additional power sinks such as electromagnets were not included in the power consumption calculations. The three points that are shown for the U-M source are those listed in Figure 5.27.
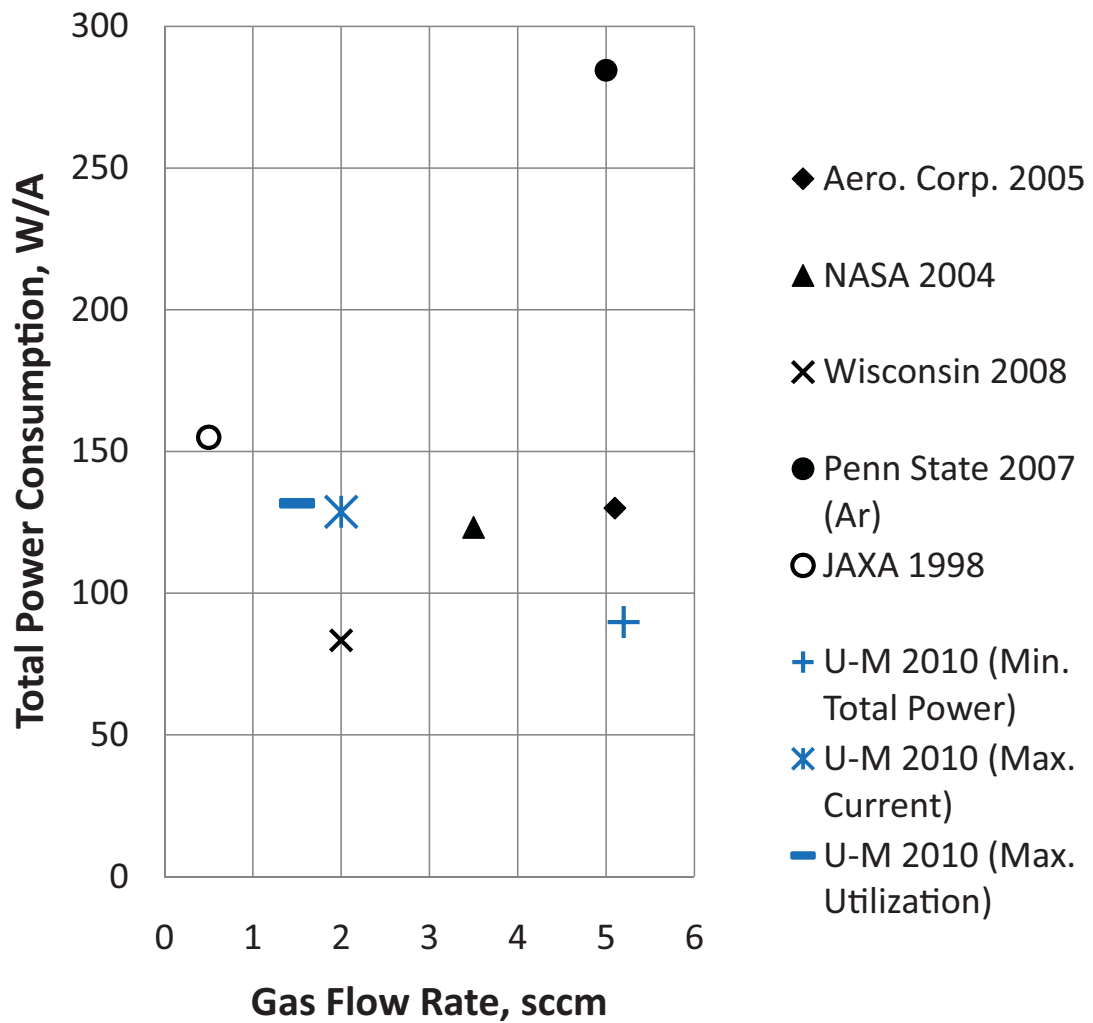
Figure 5.28: Comparison between best operating conditions for U-M source and other results in the literature.

5.7 Summary of Performance Tests

The initial benchmarking tests at U-M and NASA GRC demonstrated the feasibility of the waveguide plasma cathode concept for long-term EP missions. The device was not optimized to the prototype stage, but was able to deliver electron current in excess of the requirements for several flight-qualified thrusters. These experiments raised some questions about the physics of the device. With argon gas, a minimum background pressure was required in order to conduct significant amounts of current across the gap. The data suggested that this may be due to a minimum amount of trace ionization needed to mitigate space charge buildup in the gap. On argon, the required pressure was supplied by flowing background gas into the vacuum facility. On krypton and xenon, however, the plume was established with only the background pressure arising from gas flow through the plasma cathode itself.

The extracted current was not a simple function of neutral gas pressure, microwave power, and extraction bias. Instead, the experiments showed that there may be separate regimes where deliverable current is dominated by one factor over another, i.e., source plasma density versus electron extraction efficiency. Probe measurements suggested that the act of extraction electrons from the aperture via an applied electric field dramatically increased the plasma density in the aperture. This is not assumed in the literature on plasma cathodes, where the plasma potential, but not plasma density, is influenced by electron loss from the source. The two following chapters outline probe-based and optical experiments that were performed to investigate the plasma cathode physics in more detail.

CHAPTER VI

Spatial Mapping of Plasma Characteristics

While the performance data incorporating the extractable current as a function of operating conditions were useful in determining the feasibility of the ECR plasma cathode for space applications, they are of limited utility in quantifying trends in plasma properties within the device which in turn yield more fundamental insight into the operation of the device. The translatable planar Langmuir probe described in Chapter 4 was used to quantitatively study the plume and internal "source" plasma over the range of conditions used in the benchmarking tests. This chapter presents the results of the probe measurements and summarizes the implications for understanding plasma cathode behavior.

6.1   Langmuir Probe Mapping - External Plume

The Langmuir probe was first used to create axial maps of plasma density, plasma potential, and effective electron temperature in the external plume during current extraction. As described in Chapter 4 (Figure 4.15), the probe was centered in the plume and initially positioned just upstream of the extraction anode (13.5 cm from the aperture), through a hole in the center of the anode. A Langmuir probe trace was acquired and analyzed using the automated SmartProbe system. To obtain spatially resolved data, the probe position was translated in steps of 0.6 cm, with a probe

trace was taken at each position. The closest attainable approach to the aperture was limited by the physical obstruction of the probe probe body, which eventually extinguished the plume. The anode current was recorded at each position as well, to assess the effect of the probe body on current transport. While the plume was established, the current in most cases was remained within 10 percent of that when the probe was fully retracted from the plume, until the plume was extinguished. A typical Langmuir probe trace acquired in the plume is shown in Figure 6.1. The I-V characteristic is plotted as the natural logarithm of the probe current against the probe bias. For all cases, the plasma potential was determined from the rounded "knee" in the curve. This was done using the intersecting slope method, wherein the electron saturation and electron retarding region near the floating potential are linearly extrapolated. The intersection of the two linear fits provides an estimate of the plasma potential. At the far negative voltage end of the plot, the logarithm of the absolute value of ion current is shown.

6.1.1 Plasma Density

Plasma density profiles were recorded on xenon gas at flow rates of 2, 4, and 6 sccm. The profiles, shown in Figure 6.2, show two distinct regions of the plume. There is a sharp exponential decay in plasma density within the first ~ 4 cm of the aperture, followed by a more gradual exponential decay over the next 10 cm. The immediate dropoff in density is due to the beam expansion in the radial direction as it exits the aperture, as well as rarefaction of the beam as it is accelerated by the small electric field in the plume. The region near the anode where the plasma is more axially uniform is likely due to the weak, relatively flat drift field in this region.

From Figure 6.2, the region near the aperture decays with an e-folding length of roughly 1 cm; this is generally the case regardless of microwave power, bias, or flow rate. Similarly, in the downstream region, the exponential decay length is roughly 7 to
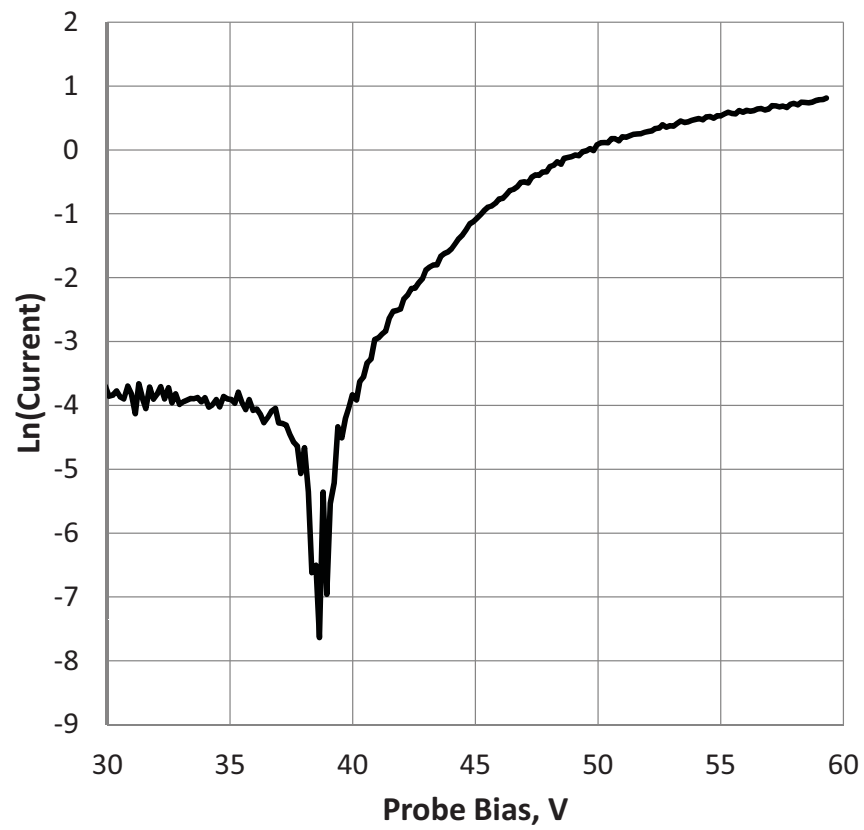
Figure 6.1: Sample Langmuir probe trace taken in the xenon plume, 7.8 cm from the aperture, at 6 sccm, 120 W, and 60 V.

10 cm. The peak densities seen in the xenon plume, at 6 mm from the aperture, were up to 7×10^{11} cm^{-3}, which is an order of magnitude above what would be expected based on the microwave cutoff density in the plasma cathode. As the microwave power was increased from 60 W to 120 W, the plasma density at the anode increased correspondingly in a linear fashion. At a xenon flow rate of 2 sccm, as shown in Figure 6.3, the linear trend with microwave power remains, but the peak measured densities are 30 percent lower than in the 6 sccm case. The increase in downstream density with flow rate is due to an increase in the internal "source" plasma density at the aperture with the internal pressure. At the lower flow rate, the downstream density has a stronger dependence on anode bias, varying from 0.3 to 1.5×10^{10} cm^{-3} over the range of 40 to 80 V, while at 6 sccm, that range is only 0.6 to 1.0×10^{10} cm^{-3}. This extra sensitivity of the downstream density to anode bias at low flow rates may in part explain the shift in peak extractable current to lower flow rates as the applied bias is increased.

The axial density profiles in the plume are shown in Figure 6.4 for krypton. Three sets of these profiles were recorded. The first was taken with the microwave power and flow rate fixed, with an axial sweep taken at anode voltages of 50, 60, and 80 V. Next, the bias and flow were held constant, and the dependence on microwave power was studied over the range of 60 to 120 W. The third set of profiles was taken at fixed voltage and microwave power, with the flow rate varied from 4 to 8 sccm.

Again with krypton, the two distinct regions with different density gradients are observed. While the data in the beam expansion region is not sufficient for determining trends in that region, the plasma density profiles in the region of 6 to 14 cm can be discussed. (Data points are missing near the aperture, because the plume was extinguished there. For this data set, the probe started near the aperture and was retracted, instead of first establishing the plume and then moving toward the aperture.) The exponential decay lengths of the density profiles are nearly
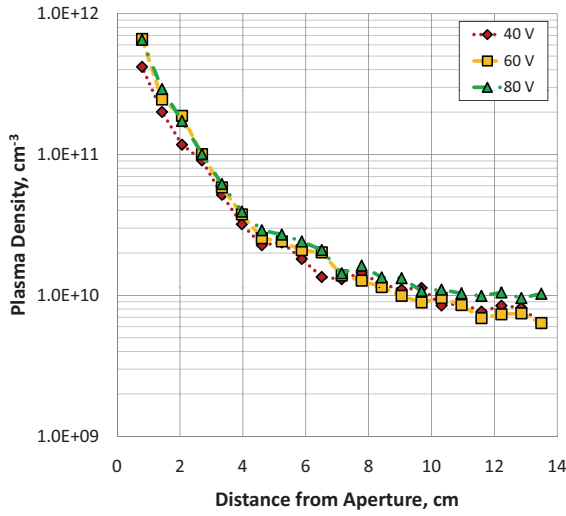
(a) Variable Bias, 60 W, 6 sccm.
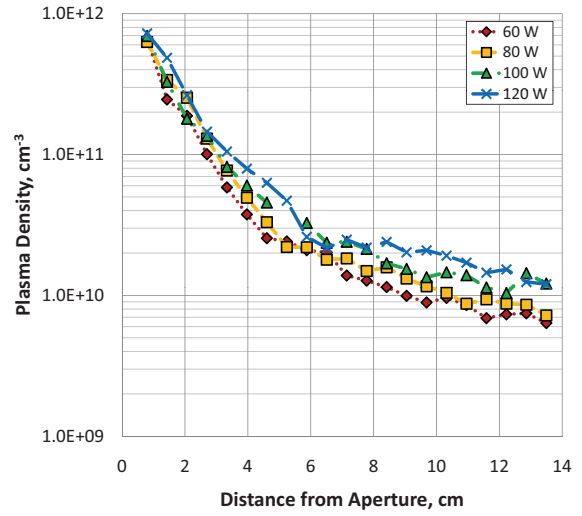
(b) Variable Power, 60 V, 6 sccm.
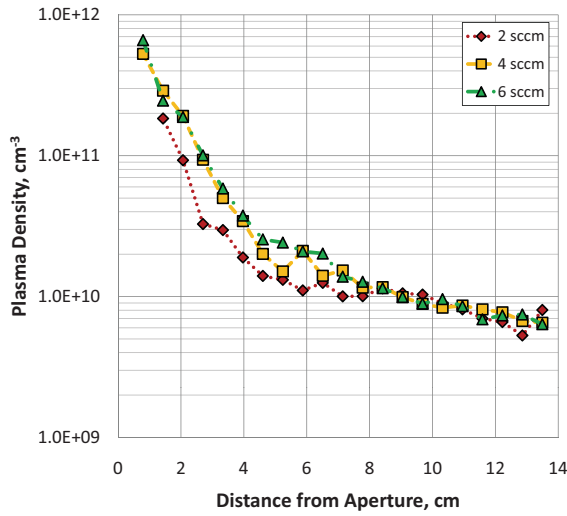
(c) Variable Flow, 60 W, 60 V.

Figure 6.2: Plasma density along xenon plume vs. microwave power, flow rate, and anode bias. Anode located at 14 cm.

(a) Variable Bias, 60 W, 2 sccm. (b) Variable Power, 60 V, 2 sccm.
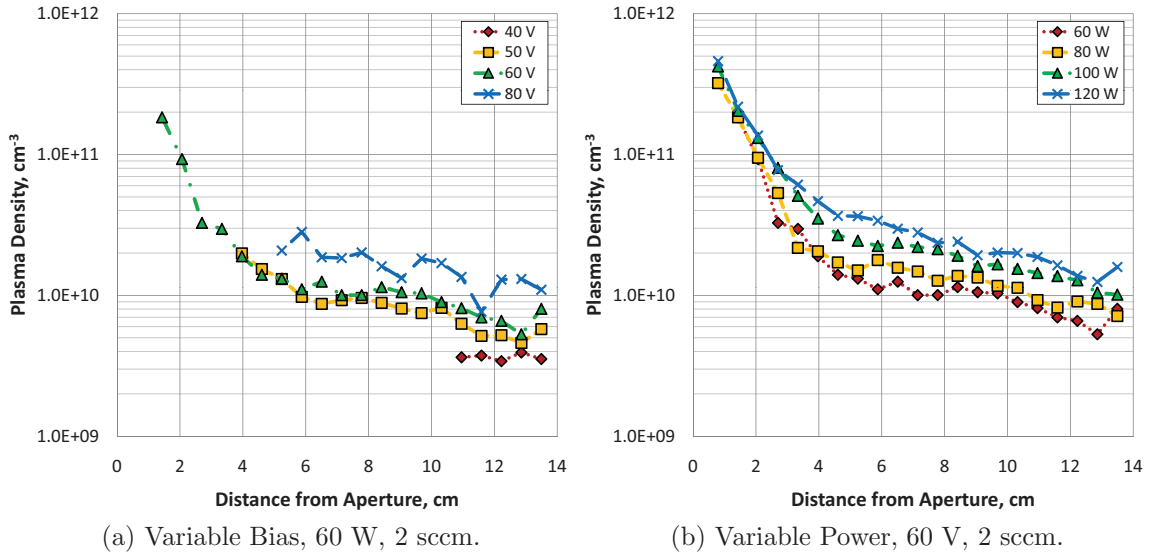
Figure 6.3: Plasma density along xenon plume, at 2 sccm flow rate. Anode located at 14 cm.

independent of applied bias and microwave power in this region, as determined by exponential fits to the data. At 6 sccm and 60 W, the e-folding length is roughly 6 cm in the 60 and 80 V cases, and 8 cm in the 50 V case. In the case of fixed bias at 60 V, the e-folding length is similar when the microwave power is varied between 80 and 120 W, though the density at the anode increases linearly with power. The background chamber pressure of 5.6×10^{-5} Torr at these conditions gives an electron-neutral mean free path on the order of 1 meter; however, the neutral pressure is likely higher on axis, in the region near plasma cathode aperture. When the flow rate is reduced to 4 sccm, the decay length increases to roughly 12 cm, supporting the suggestion that neutral density flow from the aperture contributes to the local neutral pressure in the gap. The lower pressure at 4 sccm increases the mean free path in the gap, making the density profile more uniform, *i.e.,* the decay length increases.

The argon density profiles in Figure 6.5 show similar behavior in the downstream region, though the plume was extinguished when the probe was placed closer than 2 cm from the aperture. For all probe maps that were recorded with argon,

(a) Variable Bias, 60 W, 6 sccm.

(b) Variable Power, 60 V, 6 sccm.
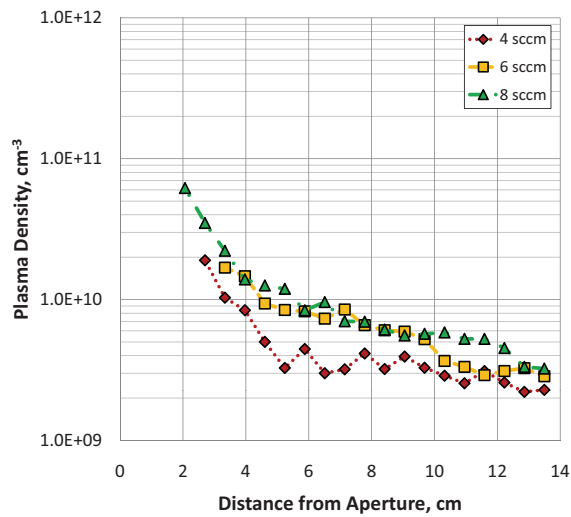
(c) Variable Flow, 60 W, 60 V.

Figure 6.4: Plasma density along krypton plume vs. microwave power, flow rate, and anode bias. Anode located at 14 cm.

126

a background gas flow was established to maintain the plasma plume, with a background pressure of 2.3×10^{-4} Torr. This was done to ensure that the neutral pressure in the plume was above the threshold value described in Chapter 4. The linear dependence of downstream plasma density on microwave power again holds true, as does the independence of the decay length in the region of 2 to 4 sccm from the aperture. In this region, the e-folding length varied between 2.3 and 3 cm for all probe sweeps, while the downstream e-folding length was in the range of 12 to 15 cm.

6.1.2 Plasma Potential

The axial profiles of plasma potential provide additional insight into the properties of the plume. The series of plasma potential measurements in the xenon plume corresponding to the density maps in the previous section are shown in Figure 6.6. At the flow rate of 6 sccm, the plasma potential is nearly uniform along the plume, and tracks with the anode bias, as is seen in the positive column of glow discharges.[45] At all voltages, the potential at the downstream end of the plume tracks along with the anode bias, but at a potential that is 12 Volts negative of the anode potential. This corresponds to the ionization potential of xenon, and indicates the existence of an electron sheath at the anode surface. There is a small electric field along the length of the plume, as the potential increases by a few volts between the aperture and anode surface. Linear fits to the potential profiles in Figure 6.6a give plume electric fields of .05 V/cm at 40 V, 0.10 V/cm at 60 V, and 0.17 V/cm at 80 V. While these fields are small, it will be shown later that they can account for the transport of large electron currents from the aperture to the anode. There is no significant dependence of the plume potential on the microwave power; however, the electric field increased from a value of 0.10 V/cm at 60 W to 0.15 V/cm at 120 W.

The dependence of the potential profile on flow is perhaps more interesting. The chamber background pressure varied from 1.6 to 3.8×10^{-5} Torr over the range of flow

(a) Variable Bias, 60 W, 6 sccm.
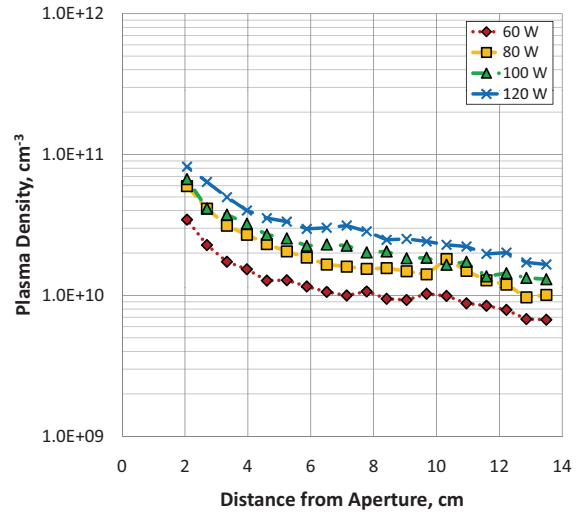
(b) Variable Power, 60 V, 6 sccm.
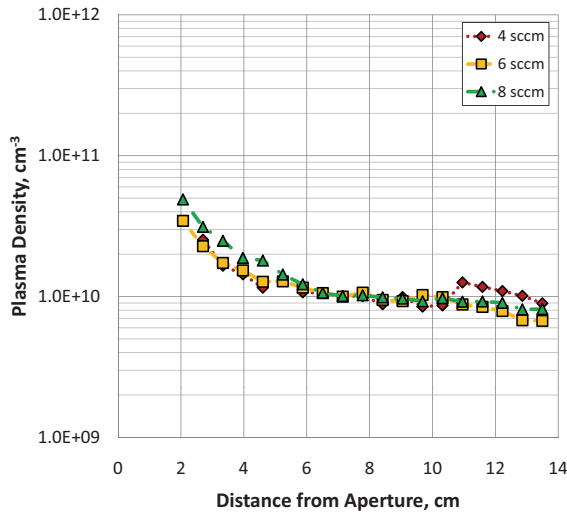
(c) Variable Flow, 60 W, 60 V.

Figure 6.5: Plasma density along argon plume vs. microwave power, flow rate, and anode bias. Anode located at 14 cm.
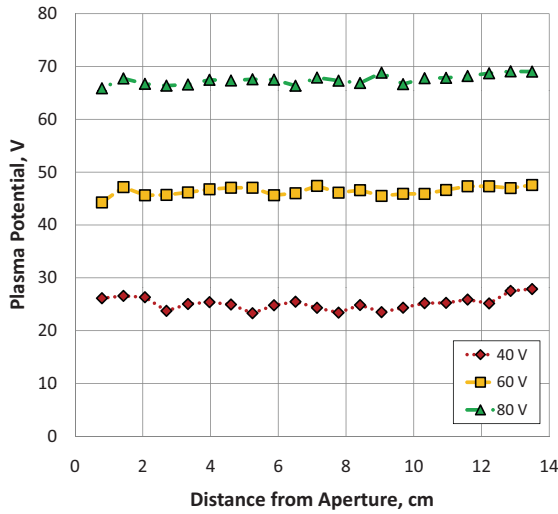
(a) Variable Bias, 60 W, 6 sccm.
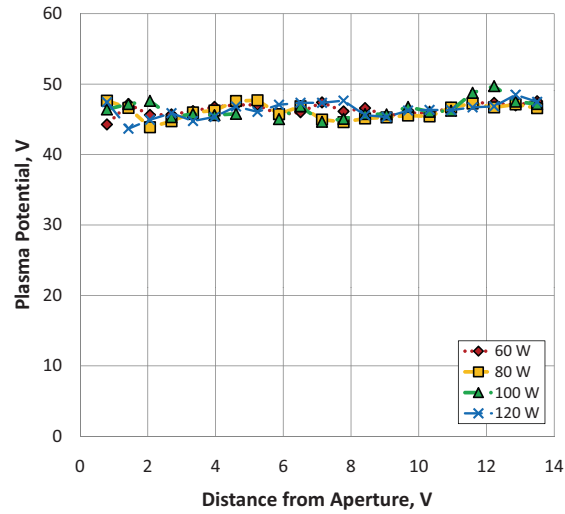
(b) Variable Power, 60 V, 6 sccm.
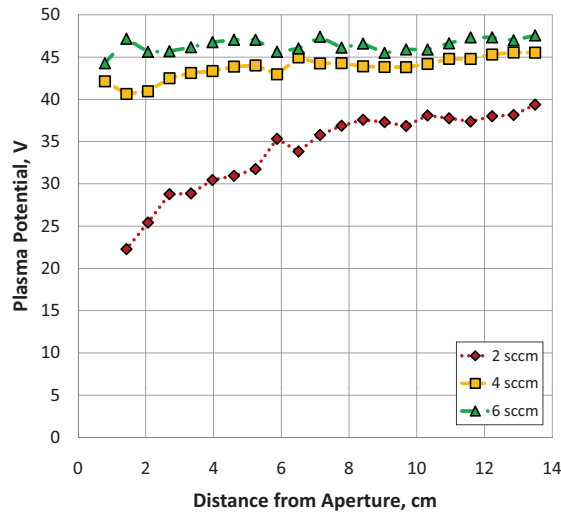
(c) Variable Flow, 60 W, 60 V.

Figure 6.6: Plasma potential along xenon plume vs. microwave power, flow rate, and anode bias. Anode located at 14 cm.
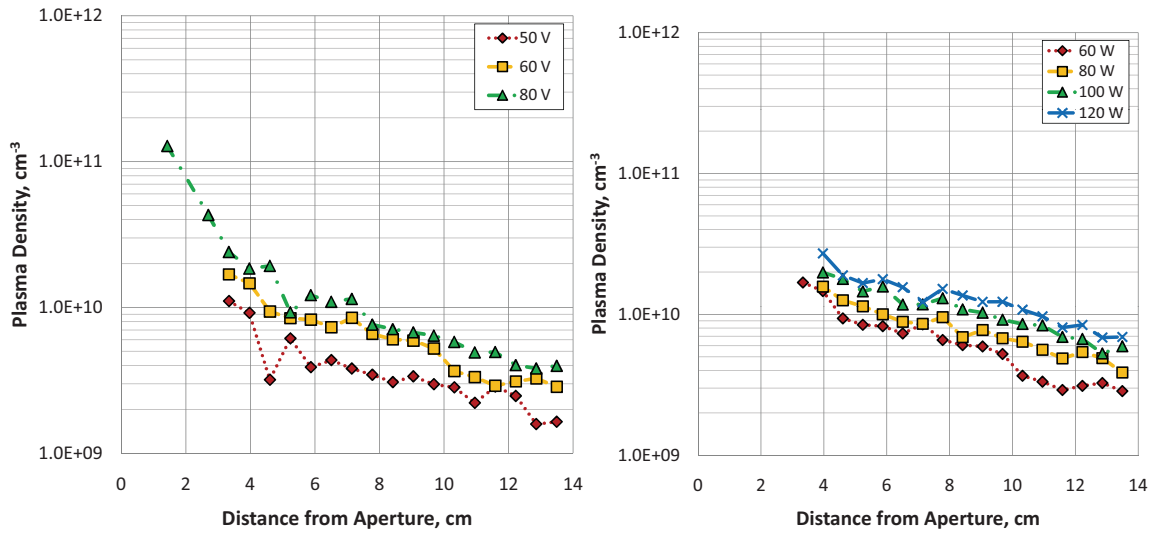
(a) Variable Bias, 60 W, 2 sccm.

(b) Variable Power, 60 V, 2 sccm.
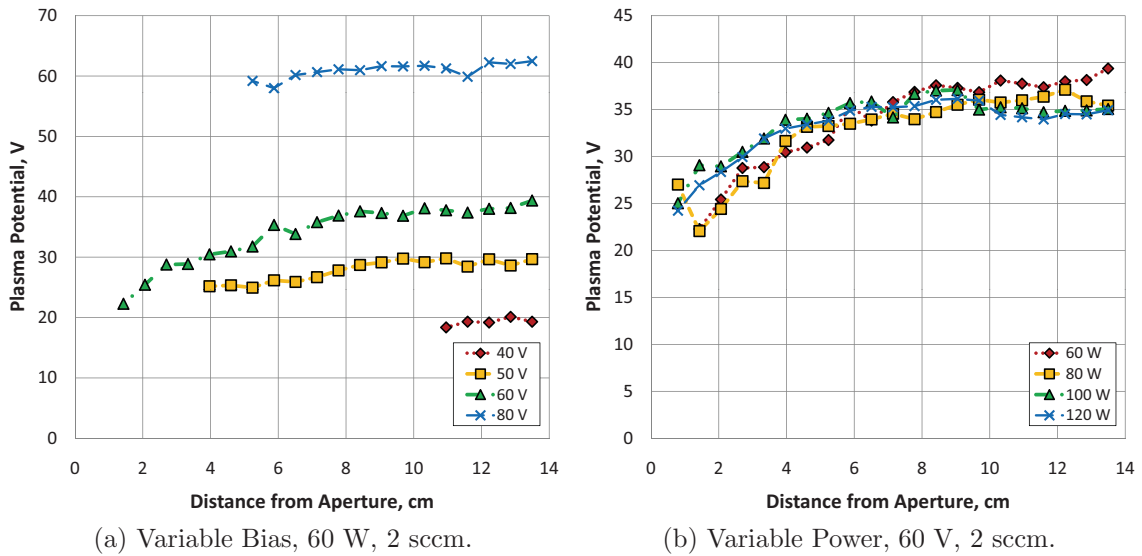
Figure 6.7: Plasma potential along xenon plume, at 2 sccm flow rate. Anode located at 14 cm.

rates shown. The gas flow rate significantly affected the shape of the potential profile. In the traces shown in Figure 6.6c, as the flow rate is decreased from 6 to 2 sccm the potential profile becomes less uniform and the potential drop across the plume increases. The nearly flat potential profile at high flow indicates a sufficient amount of external ionization to neutralize space charge in the gap. A small electric field is maintained in this case to transport current along the plume. With a lower flow rate, however, the external ionization is insufficient. The electric field in this case, between 1.4 and 5.8 cm, is 3.1 V/cm. In addition, the potential drop between the anode and plume increases. These trends are illustrated further by the plots in Figure 6.7. The potential of the plume is independent of the microwave power level to within a few volts, but again, the electric field decreases as the microwave power is increased. This is perhaps because additional microwave power generates more available electrons at the aperture which can then produce more ionization in the gap, partially shielding out the field.

Similar profiles are seen in the krypton and argon plumes, shown in Figures 6.8

and 6.9. The plume potentials near the anode track roughly 20 V below the anode bias in all cases. As the microwave power is increased, the plume potential at the anode remains constant to within ~ 5 V for both gases. The electric field is small across the gap, under 0.5 V/cm in all cases. On krypton, the dependence on flow is similar to that on xenon, with the anode potential drop increasing as the flow is reduced. On argon, however, the profiles are more independent on flow. In this respect, the difference between the gases arises from the fact that the xenon and krypton plumes were "self-fueling," i.e., the neutrals in the plume originate from gas flow through the plasma cathode aperture. For the argon plume, the additional background flow necessarily reduced the dependence of plume neutral pressure on the flow through the source.

6.1.3   Electron Temperature

Electron temperature measurements in the plume are not useful, since the plasma in this region is non-Maxwellian in nature. The electron energy distribution is instead influenced in part by the DC electric field. This manifests itself in the Langmuir probe traces (per Figure 6.1) as a rounded electron retardation region without a clearly defined linear region. A typical electron energy probability function (EEPF) taken in the plume is shown in Figure 6.10. The EEPF is defined as,

$$g_p(V) = V^{-1/2}g(V), \qquad (6.1)$$

where V is the electron energy and $g(V)$ is the electron energy distribution function defined in Chapter 4. One advantage of using the EEPF is that $\ln(g_p(V))$ decreases linearly with V, for Maxwellian plasmas. The EEPF in the plume shows some non-Maxwellian characteristics. The peak in the EEPF occurs at 3 eV rather than zero, suggesting a shifted distribution to higher electron energies, and a high energy shoulder is seen at 6 to 7 eV. An "effective" electron temperature can be assigned to
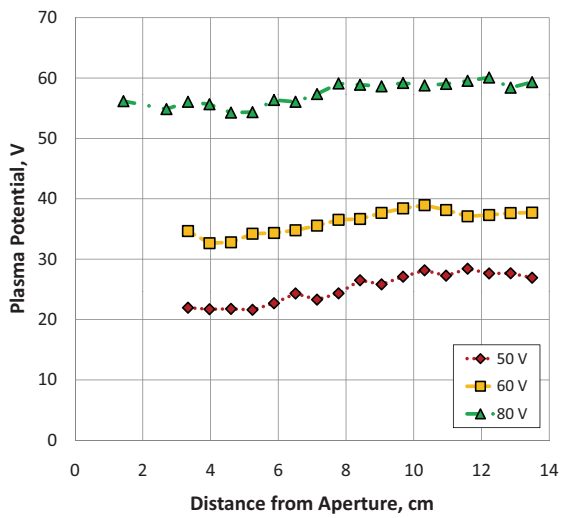
(a) Variable Bias, 60 W, 6 sccm.
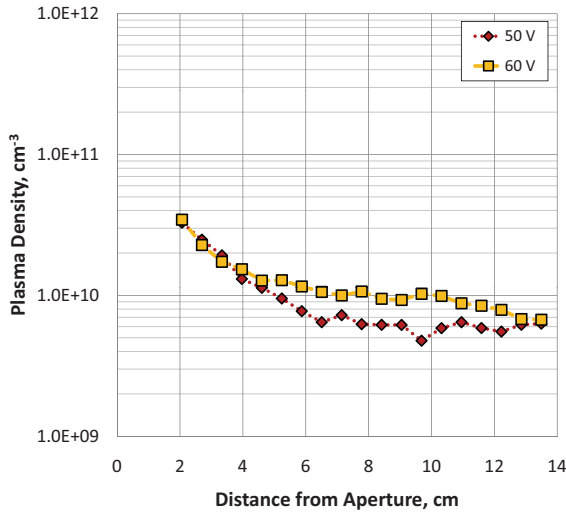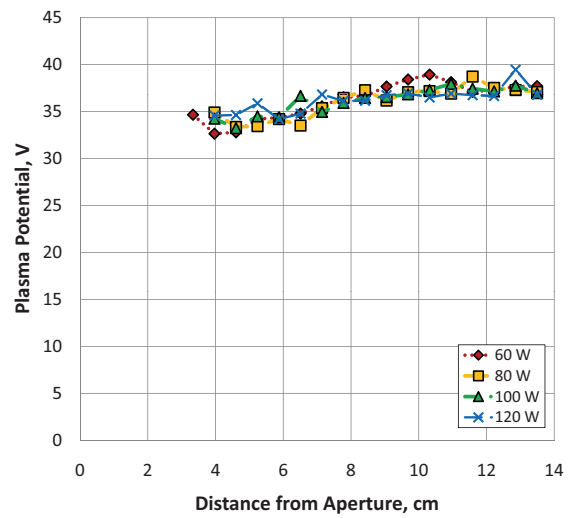

(b) Variable Power, 60 V, 6 sccm.
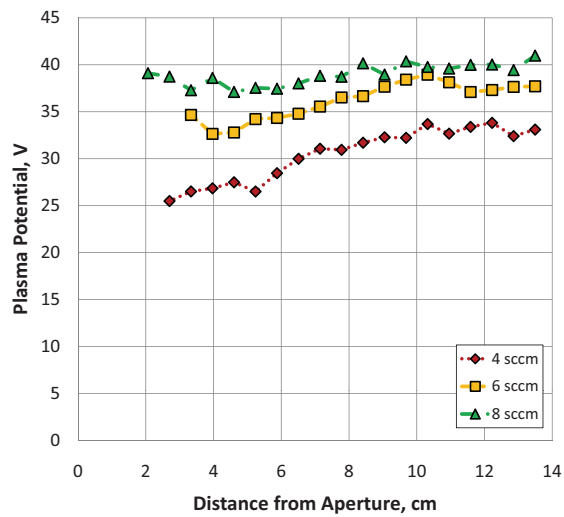
(c) Variable Flow, 60 W, 60 V.

Figure 6.8: Plasma potential along krypton plume vs. microwave power, flow rate, and anode bias. Anode located at 14 cm.
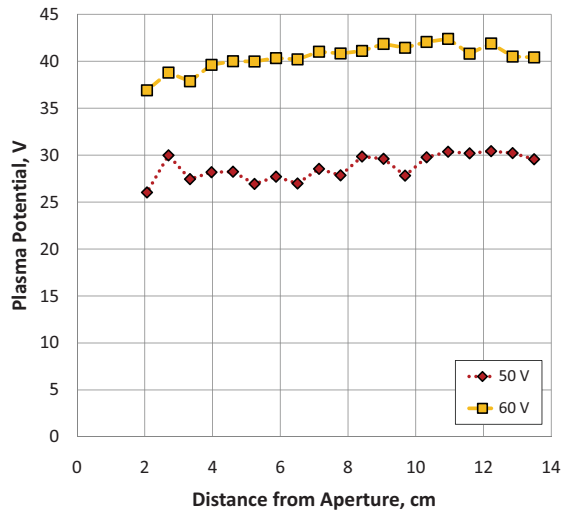
(a) Variable Bias, 60 W, 6 sccm.
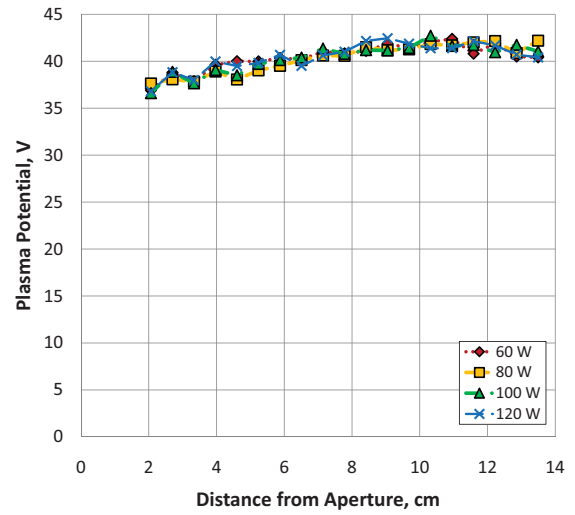
(b) Variable Power, 60 V, 6 sccm.
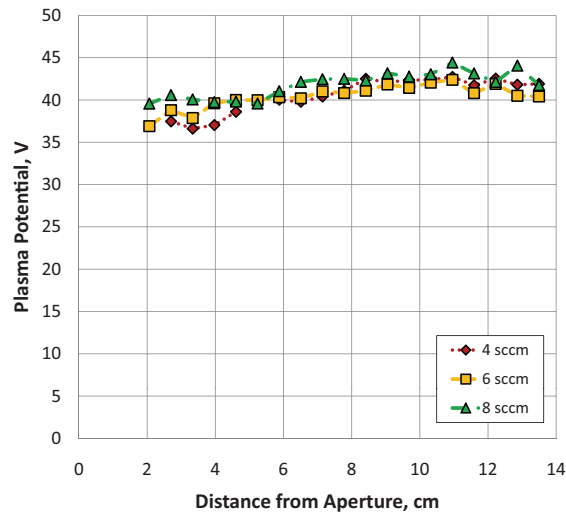
(c) Variable Flow, 60 W, 60 V.

Figure 6.9: Plasma potential along argon plume vs. microwave power, flow rate, and anode bias. Anode located at 14 cm.
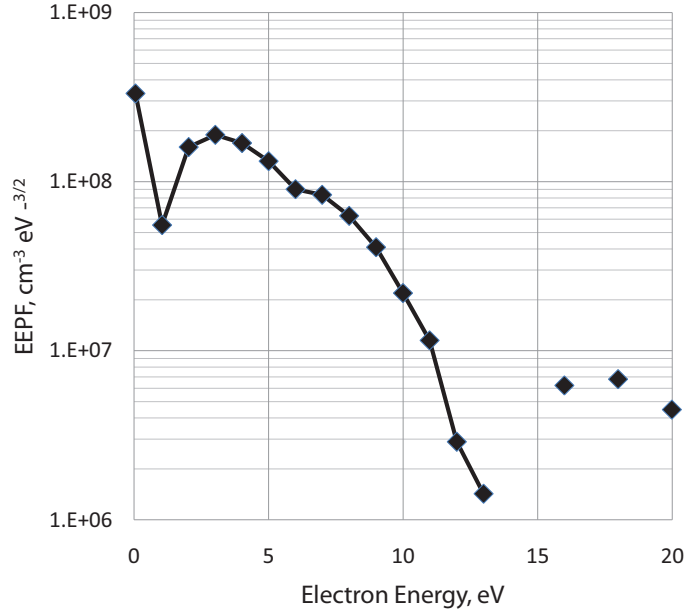
Figure 6.10: EEPF measured in the Kr plume, 7.8 cm from the aperture, at 6 sccm, 60 W, and 60 V.

non-Maxwellian plasmas, which is defined as $T_{eff} = 2 < V > /3$, where $< V >$ is the mean electron energy. The estimated "effective" electron temperatures in the krypton plume are shown in Figure 6.11. While the EEDF is non-Maxwellian in the plume, there does not appear to be any systematic change in the effective temperature along the length of the plume. This agrees with the plasma potential profiles that suggest electrons are only slightly accelerated along the length of the plume.

6.2 Langmuir Probe Mapping - Source Plasma

The Langmuir probe was also used to map out the axial distribution of plasma properties within the plasma cathode itself. Again, the ECR discharge was initiated and load matched with the waveguide tuner. With the probe inserted through the extraction aperture, the plume could not be established for these measurements. Thus, during the interior probe measurements no current was extracted. Because the presence of the probe reduced the effective loss area, and therefore the conductance of

(a) Variable Bias, 60 W, 6 sccm.

(b) Variable Power, 60 V, 6 sccm.
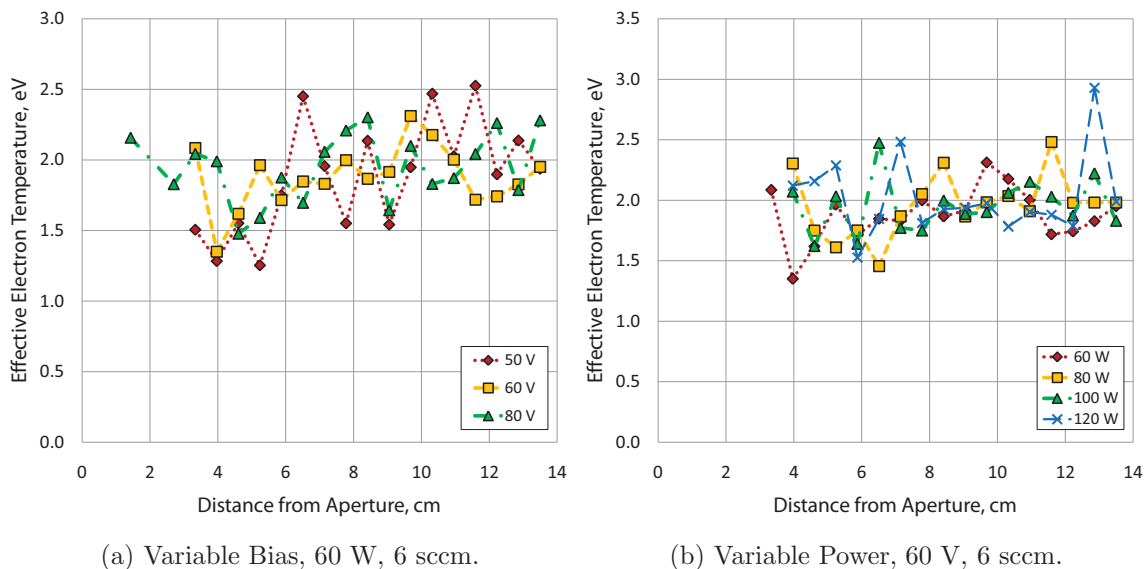
Figure 6.11: Electron temperature along krypton plume vs. microwave power, flow rate, and anode bias. Anode located at 14 cm.

the aperture, the flow rate was adjusted downward to approximate the same internal pressure with the unblocked orifice. The conductance scales linearly with the aperture area, so an effective area of the aperture area minus the probe cross-sectional area was used to calculate an effective conductance. This gave a scaling factor of 0.22; that is, to recreate the internal pressure established by an unblocked flow of X sccm, the actual flow rate through the blocked aperture was scaled to $0.22 \times X$. All probe maps here are shown in terms of "effective" flow rates, meaning that while the actual flow rate through the plasma cathode was lower, the internal pressure is the same as that in the unobstructed device at the "effective" flow rate.

The approach of using an "effective flow rate" was later verified by measuring the cold gas pressure in the plasma cathode with the pressure tapped endplate and 1 Torr capacitance manometer (Figure 5.9). With an unobstructed aperture, argon gas was flowed through the plasma cathode over the range of 1 to 9 sccm and the internal pressure was measured. An alumina rod (3.16 mm diameter, 170 mm long) was then inserted 50 mm into the plasma cathode, through the 4.0 mm diameter
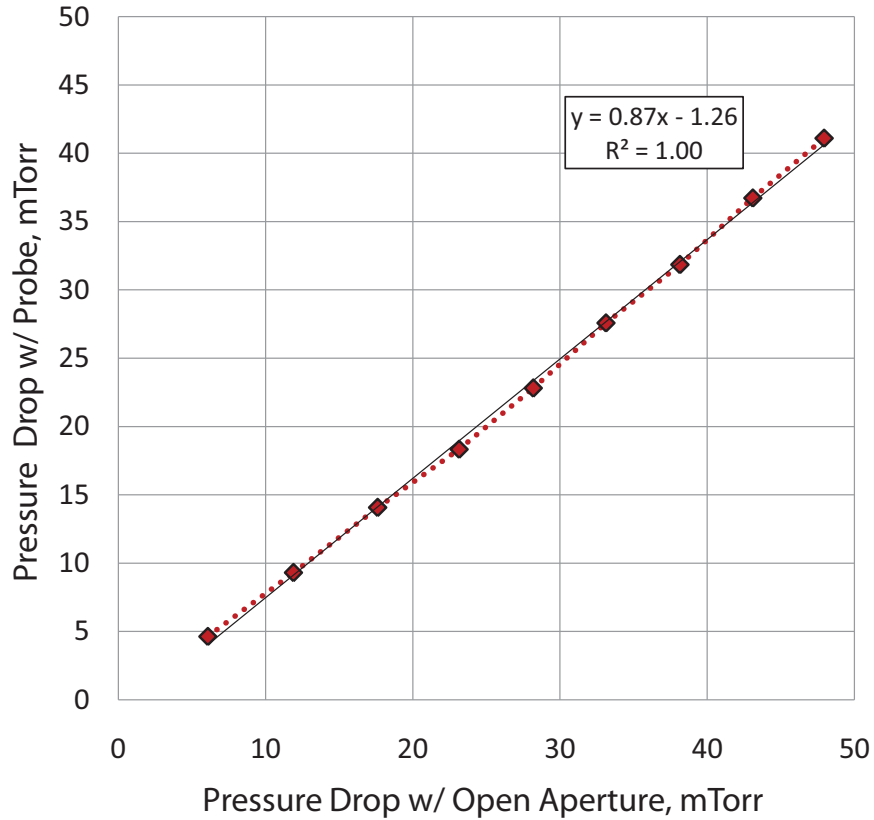
Figure 6.12: Internal pressure with obstruction and scaled flow rate vs. desired internal pressure.

aperture. This reduced the open area of the aperture by a factor of 0.37, and this area reduction was used as the scaling factor for the gas flow rate. The internal pressure was measured over the range of "effective" flow rates from 1 to 9 sccm (with actual impeded flow rates of 0.37 to 3.3 sccm). The pressure with the probe obstruction (using the effective flow rates) was plotted against the corresponding pressure in the unobstructed source (using the nominal flow rates), as shown in Figure 6.12. The pressure in the obstructed source agrees with the desired internal pressure to within 13 percent.

For each axial map, the probe was initially placed 0.6 cm from the quartz pressure window and an I-V characteristic was recorded with the automated probe system. The probe was then moved toward the aperture in 0.6 cm increments with a probe trace
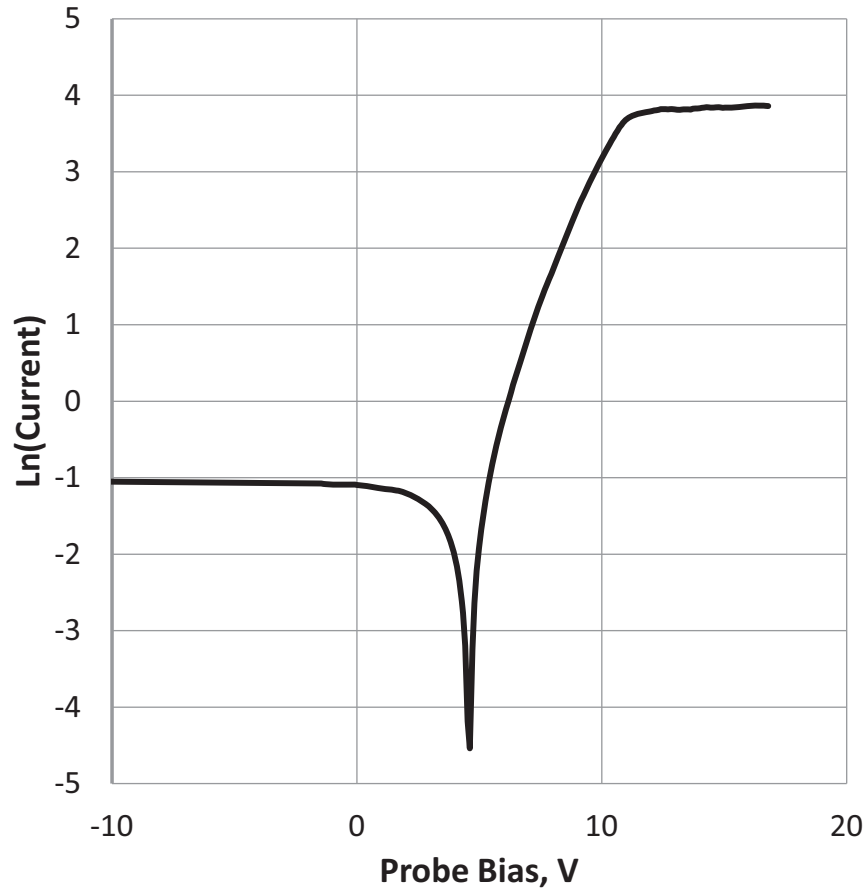
Figure 6.13: Sample Langmuir probe trace taken inside plasma cathode, 5 cm from the window ($\mathbf{B} = 875$ G), at 6 sccm xenon and 120 W.

taken at each step, along the entire length of the plasma cathode. The probe traces taken within the ECR discharge were much closer to the theoretical characteristic shape described in Chapter 4, when compared with probe traces in the plume. An example is shown in Figure 6.13, taken in the region of peak density near the ECR zone. The knee in these curves are more clearly defined than those taken in the plume, giving a well-defined plasma potential. However, it will be shown that the knee in the curve is shifted negative of the actual potential value, due to magnetic field effects. Again, the natural logarithm of the absolute value of ion saturation current is shown on the left-hand end of the plot.

6.2.1 Influence of Magnetic Field on Probe Measurements

It is well known that the presence of a magnetic field can disrupt the shape of a Langmuir probe I-V characteristic. Such distortions must be considered here, particularly in those regions where the Larmor radii are small relative to the probe dimensions.[11, 32] To assess this, the magnetic field profile along the axis of the source was measured using a Hall probe mounted on a positioning system. The $\hat{z}$ component of the magnetic field on axis is shown in Figure 6.14. (The radial component there was negligible.) The peak magnetic field on axis is 750 Gauss, occurring 2.3 cm from the window. This is slightly weaker than the magnetic field calculated by the Maxwell 2D model, which predicted a field strength of roughly 875 Gauss on axis. The discrepancy is due to the fact that the magnet ring consists of discrete blocks rather than a continuous ring. The field does reach a strength of 875 Gauss near the peak location, but shifted roughly 1 cm off axis.

At 750 Gauss, the electron and ion Larmor radii are $r_e = 5.4 \times 10^{-3}$ and $r_i = 0.14$ cm, respectively. This calculation assumes an electron temperature of 3 eV and room temperature ions (0.026 eV). Room temperature ions provide a conservative estimate the effect of the magnetic field on ion collection, though T_i can be a few times room temperature.[44] Near the ECR heating zone it is reasonable to assume electron densities at cutoff, 7.4×10^{10} cm^{-3}, or above, giving a Debye length of 4.9×10^{-3} cm. When the probe is biased in the ion or electron saturation regimes, the difference between the plasma potential and probe bias is several times the electron temperature (at a minimum), so a high voltage Child-Langmuir sheath forms at the probe surface with thickness $s = \lambda_D(\sqrt{2}/3)(2eV/k_BT_e)^{3/4}$.[45] For a ratio of the probe bias to kT_e/e equal to 10, the probe sheath thickness is $s = 2.2 \times 10^{-2}$ cm. The sheath thickness is then in a regime where $r_e \ll s \ll r_i$. In this case, electron orbits within the probe sheath should be taken into account, while the magnetic field does not affect ion collection.
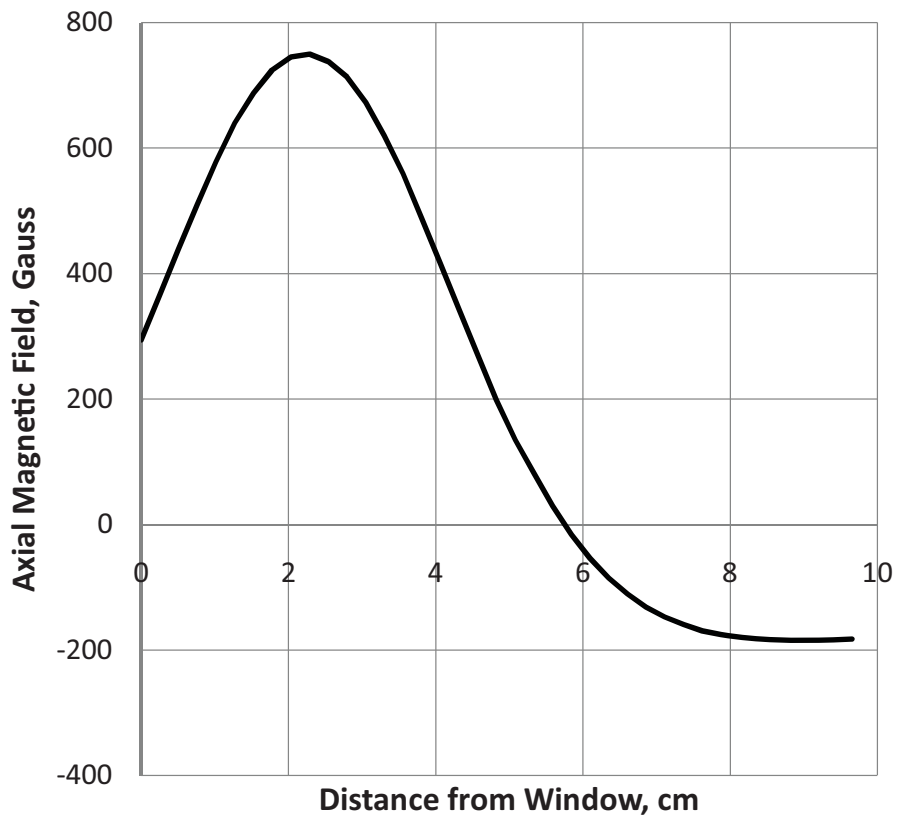
Figure 6.14: Measured magnetic field profile on axis, in Gauss. Positive B points downstream, negative B points upstream.

Since a static magnetic field cannot do work on charged particles, the electron retardation region of a Langmuir probe current-voltage characteristic is unaffected by the presence of the magnetic field. The electron temperature can therefore be obtained by analyzing the electron retardation region using standard Langmuir probe techniques.[11, 66] If the radius of a planar probe, r_0 is sufficiently large, a probe biased in the electron saturation regime can deplete the local electron population faster than it can be replenished by diffusion in a magnetized plasma. The magnetic field suppresses the electron saturation current collected by the probe. An experimentally verified model was developed by Sugawara to determine the unmagnetized electron saturation current from the magnetic field strength and measured electron saturation current.[69] Sugawara determined the electron current collection perpendicular to the magnetic field and parallel to the magnetic field. The effect on the perpendicular current collection is intuitive; for magnetized electrons ($\omega_{ce}/\nu_m >> 1$), electron diffusion across magnetic field lines to the probe sheath is suppressed. When the probe is oriented to collect current parallel to the field lines, magnetized electrons can freely diffuse to the probe, but for continuity, must be replaced by electron diffusion across field lines. In this work, the latter was the case, because the probe surface was always oriented perpendicular to the magnetic field on axis. The unsuppressed electron saturation current J_{e0} found by Sugawara was:

$$\frac{J_{e\parallel}}{J_{e0}} = \left[\left(1 + \frac{32}{3} \frac{\lambda_e}{\pi r_0} \right) \alpha^{\frac{1}{2}} \right] \times \left[1 + \frac{32}{3} \frac{\lambda_e}{\pi r_0} \alpha^{\frac{1}{2}} \right]^{-1} \tag{6.2}$$

where $J_{e\parallel}$ is the magnetized saturation current, λ_e is the electron mean free path, r_0 is the planar probe radius and,

$$\alpha = \frac{1}{1 + \left(\frac{\omega_{ce}}{\nu_m} \right)^2} \tag{6.3}$$

Because the electron temperature is unperturbed, the suppression of electron

saturation current will give an apparent decrease in the plasma potential, given by,

$$\Delta V_p = -\frac{kT_e}{e} \ln \left\{ \left[\left(1 + \frac{32}{3} \frac{\lambda_e}{\pi r_0} \right) \alpha^{\frac{1}{2}} \right] \times \left[1 + \frac{32}{3} \frac{\lambda_e}{\pi r_0} \alpha^{\frac{1}{2}} \right]^{-1} \right\} \qquad (6.4)$$

Pressures inside the plasma cathode were as low as 25 mTorr (on argon at 4 sccm effective) during the internal probe measurements. Assuming an elastic scattering rate constant of 10^{-7} cm^3/s for argon,[45] this gives a mean free path of $\lambda_e = 1.4$ cm and average collision frequency of 81 MHz. The cyclotron frequency at 750 Gauss is 13×10^9 rad/s, giving a value of $\alpha = 3.9 \times 10^{-5}$. The plasma potential given these conditions would be suppressed by 1.8 $k_B T_e$. This is not an insignificant effect, so for each of the plasma potential profiles, the value of V_p was corrected using the internal pressure and magnetic field strength at that each location.

The unmagnetized ion saturation current can be used to calculate the internal plasma density without any magnetic field correction. The ion larmor radius is large relative to the probe sheath width, so orbital effects in the sheath can be neglected. At the 25 mTorr, the ion-neutral mean free path is 0.12 cm, so ions are collected by the probe collisionlessly. Ion transport to the probe sheath is not severely limited by the magnetic field. A similar treatment to that described above, but applied to ion current, gives a value of $\alpha = 0.73$ at 750 Gauss. This translates to a magnetized ion current within 5 percent of the theoretical unmagnetized value. Therefore, it is a reasonable approximation to assume that ion current is collected at the probe surface with a current density $I_{i,\text{sat}}$ given by Equation (4.2).

6.2.2 Density Profiles

The axial plasma density profiles on xenon feed gas are shown in Figure 6.15, at effective flow rates of 2, 4, and 6 sccm. High plasma densities were achieved in the source at all flow rates, with peak values several times the cutoff density observed at all conditions. The maximum density is generally seen in the region just downstream

of the peak magnetic field, which is centered at 2.3 cm from the window. At the axial position of the peak field, the ECR zone is closest to centerline, resulting in the maximum overlap between microwave electric field and the resonant magnetic field strength. Further downstream from this region, the ECR zone expands away from the centerline as the magnetic field on axis decreases. ECR heating downstream of the peak magnetic field contributes to the electron density on axis as well. The electron temperature profiles from these probe measurements will show that electron heating occurs over a range of several centimeters downstream of the peak magnetic field.

As the magnetic field decreases further from the peak of the ECR zone, the density decays via diffusion along the magnetic field lines. The minimum density is seen near the aperture, and is on the order of 1 to 2×10^{10} cm^{-3}, depending on the microwave power and flow rate. In general, the plasma density along the axis of the plasma cathode increases with both flow rate and microwave power, as predicted in Chapter 5. The internal pressures in the range of 25 to 80 mTorr are far below that required for collisional disruption of ECR heating,[3] because $\nu_m = \omega_{ce}$ for 875 Gauss at a pressure of ~ 5 Torr. Ionization fractions are quite low, in the range of 2 to 3×10^{-4} at 120 W. Therefore, as both the neutral density and input power are increased, additional ionization occurs in the ECR zone and the density increases in kind. The higher peak density then translates to higher densities downstream with diffusion out of the heating zone.

An interesting effect appears at the location ~ 5.8 cm downstream of the window, where a peak in plasma density is sometimes observed. This location corresponds to the null in the axial magnetic field. As shown in Figure 6.14, the magnetic field is in the $+z$ direction on the upstream side of this point, and in the $-z$ direction on the downstream side. Electrons can become trapped at this point via the mirror and minimum B effect, because a positive magnetic field gradient is seen in all directions. As the pressure is increased, additional cross-field diffusion will free electrons from
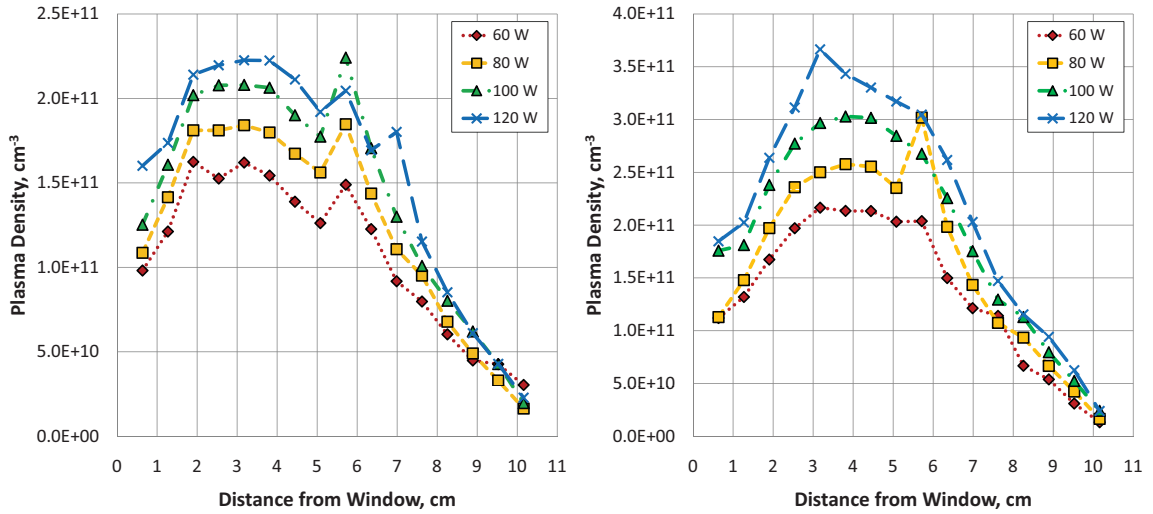
(a) 2 sccm Effective.
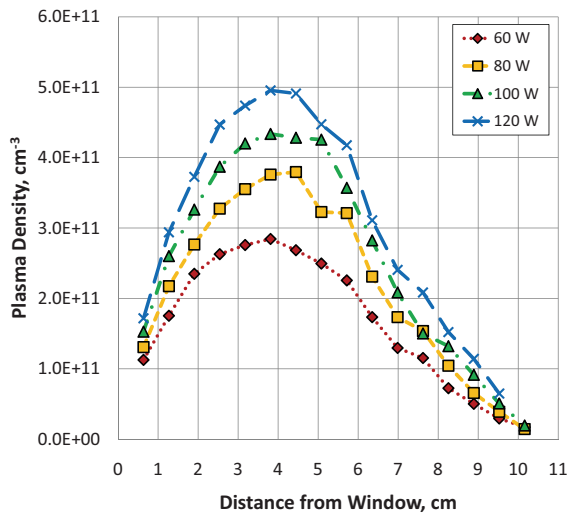
(b) 4 sccm Effective.

(c) 6 sccm Effective.

Figure 6.15: Plasma density along plasma cathode centerline, on xenon. Aperture located at 10 cm.

the field "trap," and the peak is smoothed out. This is observed as the flow rate is increased from 2 to 6 sccm.

To summarize the dependencies of the xenon plasma density distribution on flow rate and microwave power, the density profiles are plotted at low and high power conditions in Figure 6.16. Again, the peak densities monotonically increase with flow rate and power level, ruling out the possibility that decreased extractable current at high flow is due to electron cooling or neutral burnout.[46] The secondary peak at the magnetic trap occurs at lower flow, but is several centimeters from the aperture, so it should not contribute directly to the extracted current. Plasma densities at the aperture were in the range of 1.5 to 3×10^{10} cm^{-3} over all of the traces here. Though the profiles at 2 sccm have lower peak densities than those at 6 sccm, they are more uniform. That is, highly peaked profiles do not necessarily translate to significantly higher plasma densities at the aperture. The difference is described by enhanced electron transport from the ECR heating zone to the aperture at low flow rates. In the axial direction, the diffusion coefficient scales inversely with pressure, while in the radial direction it is proportional to pressure due to the strong magnetic field. Over the length of the device, additional gains in ionization at higher pressure appear to be offset by a more peaked density profile at those pressures.

The density profiles on krypton and argon are included in Figures 6.17 and 6.18, respectively. The dependence of plasma density in the ECR zone on the flow rate was less pronounced relative to the behavior on xenon. For krypton, densities on the order of 2×10^{11} cm^{-3} were achieved, while on argon the peak density was around 1.2 to 1.4×10^{11} cm^{-3}, still overdense by a factor of two. On both gases, the peak densities occur at the peak magnetic field, and the secondary peak at the "trap" location is observed. At high power levels, the density at the heating zone drops off more rapidly than on xenon, especially at low flow rates. On argon in particular, the density profile is slightly double-peaked, with the region at the ECR zone and
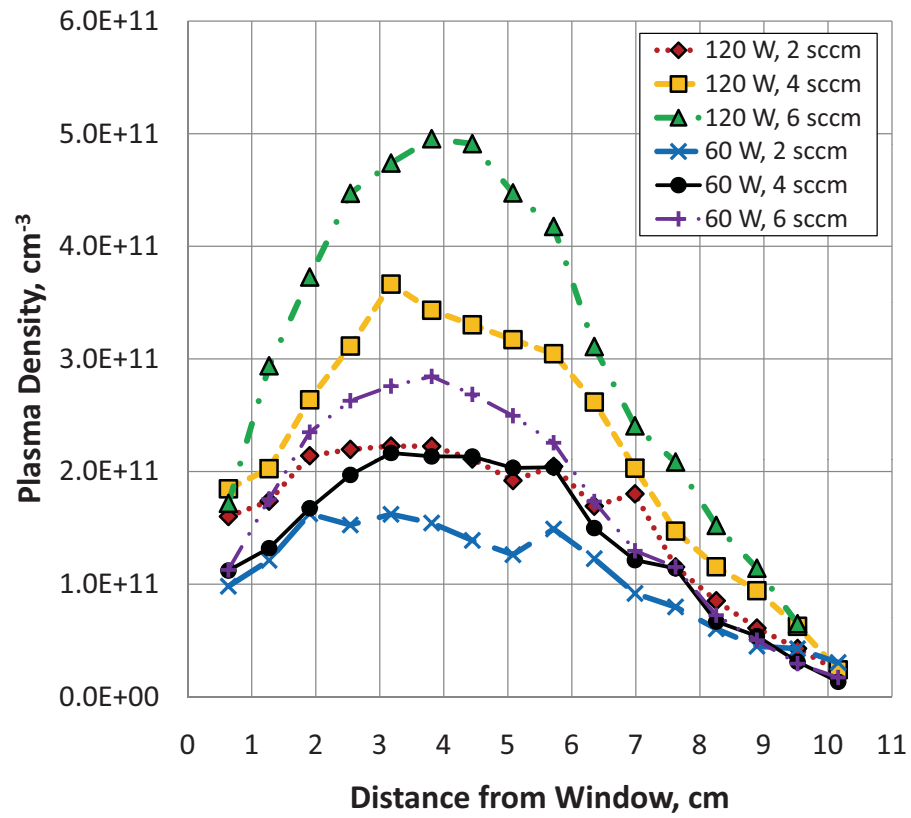
Figure 6.16: Summary of internal density profiles on xenon.

the other at the null in the magnetic field having comparable densities. Because of the lower residence time of argon in the plasma cathode, the internal pressure on argon varied from 25 to 48 mTorr over the gas flow range of 4 to 8 sccm, while on krypton the pressure varied from 36 to 69 mTorr. For this reason, the double-peaked behavior at the null magnetic field is more pronounced on argon than on krypton. Lower internal pressures correspond to lower collision frequencies, which decreases the rate at which electrons can escape from the magnetic trap.

6.2.3 Temperature Profiles

The internal electron temperature profiles on xenon are shown in Figure 6.19. At all flow rates, the trends in electron temperature can be broken down into three distinct regions. Within the first 2 cm of the window, the temperature drops rapidly until the peak magnetic field is reached at 2.3 cm. In the downstream region of decreasing magnetic field, the electron temperature drops by a factor of two again, in a linear fashion, between the peak magnetic field region and the downstream null in the field at 5.7 cm. Then along the length between the null field and the aperture, the temperature is uniform to within 10 percent at all three flow rates.

The high temperature region near the window is explained by the trapping of hot electrons in the region between the ECR zone and the window itself. Near the window, electrons are accelerated by the microwave electric field, and are magnetized ($B > 475$ Gauss). As a result, electrons cannot diffuse radially to the plasma cathode wall in this region. Electrons are not lost to the quartz window, and those traveling downstream from the window encounter an increasing magnetic field and are reflected. This cycle can repeat itself, forming a high temperature region between the window and ECR zone.

In the linear region between the peak magnetic field and the null, the temperature profile becomes dominated by resonant absorption of the incident microwaves. The

146
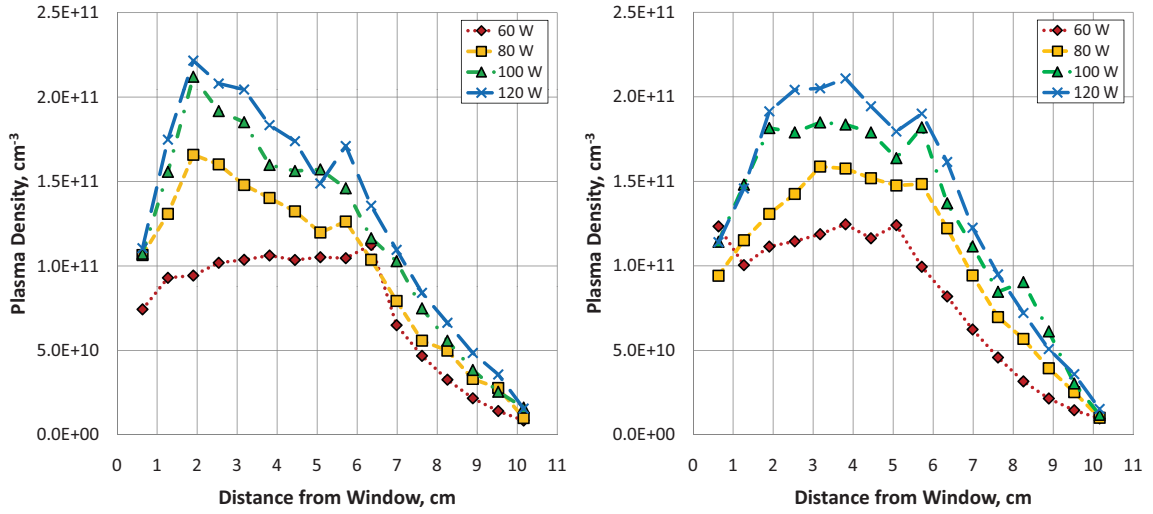
(a) 4 sccm Effective.
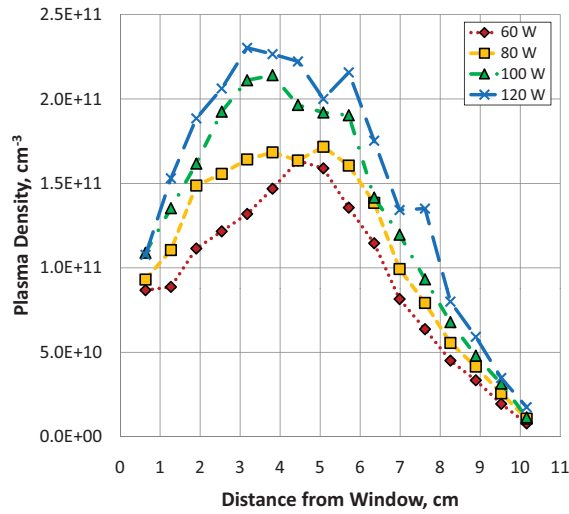
(b) 6 sccm Effective.

(c) 8 sccm Effective.

Figure 6.17: Plasma density along plasma cathode centerline, on krypton. Aperture located at 10 cm.

(a) 4 sccm Effective.
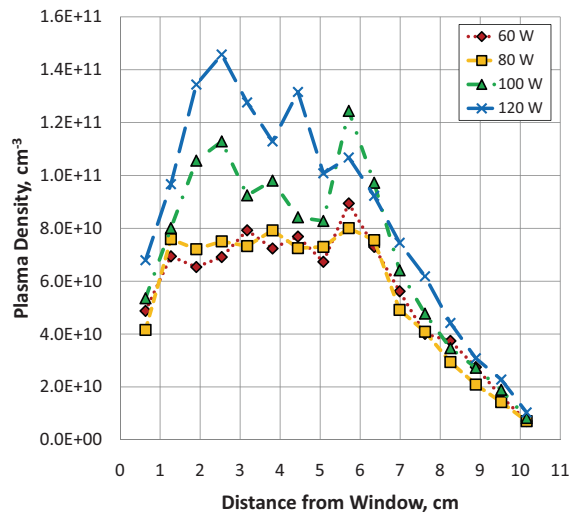
(b) 6 sccm Effective.

(c) 8 sccm Effective.

Figure 6.18: Plasma density along plasma cathode centerline, on argon. Aperture located at 10 cm.

monotonic decrease in temperature in this region arises from the fact that the peak magnetic field is at 2.3 cm, and decreases further downstream. As the magnetic field decreases, the resonance zone expands outward toward the wall. The maximum overlap of the electric field and the static magnetic field where the magnetic field peaks on axis. The microwave field strength decreases along the axis as energy is absorbed by the plasma, but ECR heating also takes place off-axis in the downstream region to an extent. Electrons that are heated off-axis can diffuse toward the centerline via cross-field diffusion, and lose energy in the process. Simultaneously, hot electrons diffusing along field lines from the peak ECR zone will also lose energy via collisions. Thus, at regions further from the ECR zone, the temperature decreases.

In the uniform region, the temperature varies by less than 10 percent with microwave power at a given flow rate. As the flow rate is increased, the temperature in this region drops, from 1.4 eV at 2 sccm to 1.1 eV at 6 sccm. Here, the microwave electric field no longer influences the electron temperature, and the electrons in this region originate from diffusive transport along field lines from the ECR zone and bulk ionization interactions in the downstream region. The magnetic field in this region is nearly uniform in the radial direction, varying by less than 10 percent at the exit plane. Here, the electron temperature is predominately determined by electron and ion loss rates to the walls and surrounding regions, which is determined by the geometry of the source. On krypton and argon, the temperature profiles have the same general features as the xenon temperature profiles; they are included in Appendix A for completeness.

6.2.4 Plasma Potential Profile

The internal plasma potential profiles on xenon feed gas are shown in Figure 6.20 for flow rates of 2, 4, and 6 sccm. These measurements were corrected for magnetic field effects using the aforementioned analysis by Sugawara. In all cases, the plasma

(a) 2 sccm Effective.
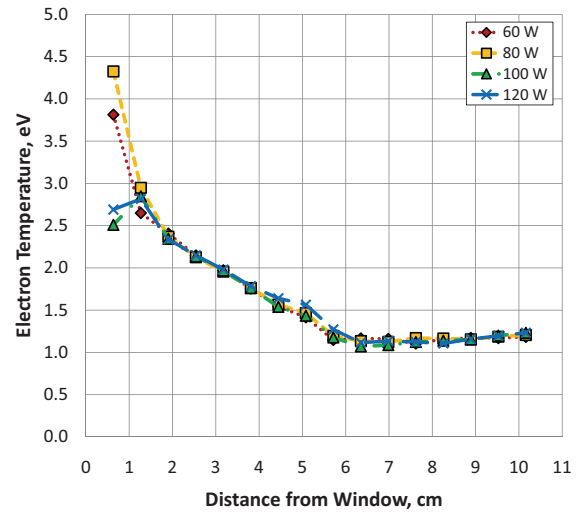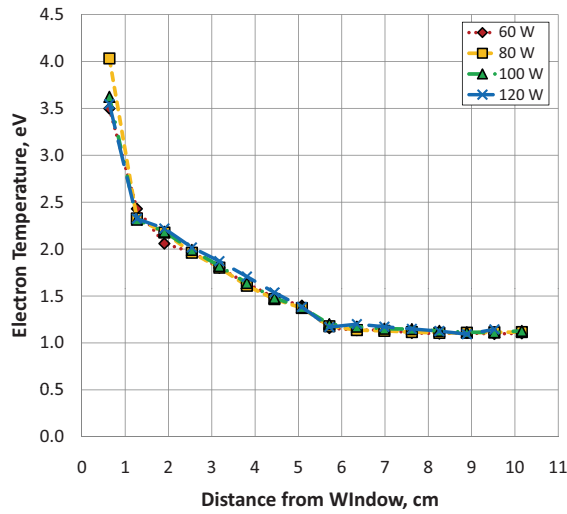
(b) 4 sccm Effective.

(c) 6 sccm Effective.

Figure 6.19: Electron temperature along plasma cathode centerline, on xenon. Aperture located at 10 cm.

potential varies within ~ 10 Volts across the length of the device. The peak potential generally occurs in the region of maximum density and decreases further downstream. The downstream magnetic "trap" at 5.7 cm influences the plasma potential as well: near this location, there is a negative potential gradient pointing toward the null field location. This is again explained by the increase in magnetic field on either side of the null field. As the null is approached from either direction, the magnetic field lines expand radially outward (*i.e.*, the field is decreasing). As the plasma expands along the magnetic field lines, the density on axis decreases and a distributed potential drop forms from the high to low magnetic field region.[45] This acts to accelerate ions from the high to low magnetic field region, contributing to the trapped peak in plasma density seen in Figure 6.15. Similar potential profiles were observed on argon and krypton feed gases; those plots are also included in Appendix A.

6.2.5 Comparison of Gases

A comparison between the density profiles for each gas is shown in Figure 6.21, at 120 W of microwave power and flow rates of 4 and 6 sccm. In both plots, the density profiles have the same general shape for all three gases: with the maximum density at the ECR zone, a secondary small peak or shoulder at the null field location, and a decreasing density in the far upstream and downstream regions. The maximum density scales as expected from variations in ionization potential between the three gases, with xenon achieving the highest peak density and argon the lowest density. Overdense plasma is achieved with all three gases. At the furthest downstream point (at the aperture), the plasma density is roughly a factor of 10 lower than the peak density; indicating that the plasma cathode may be optimized further by increasing plasma uniformity with additional confining magnets.

The temperature profiles of the three gases, shown in Figure 6.22, are similar as well. In all cases, the trapped population of high energy electrons between the window
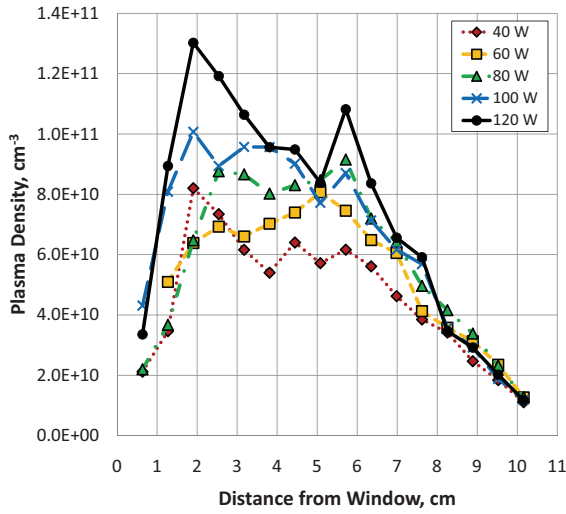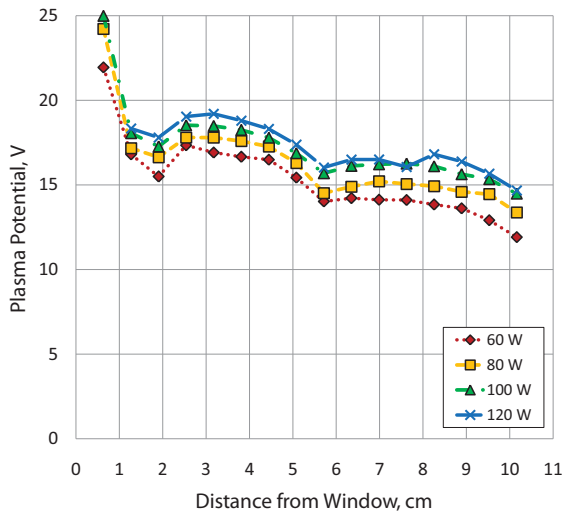
(a) 2 sccm Effective.
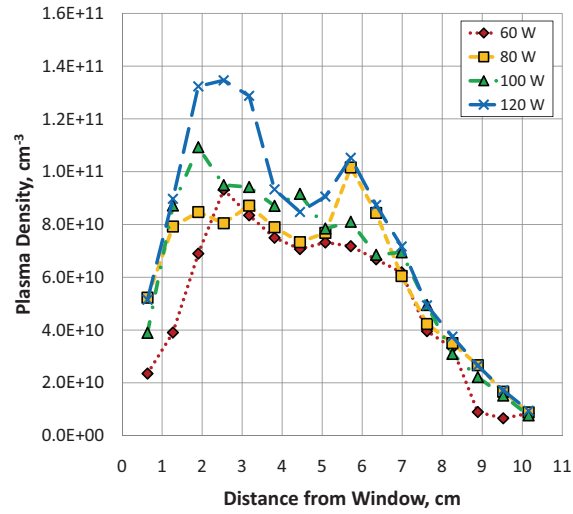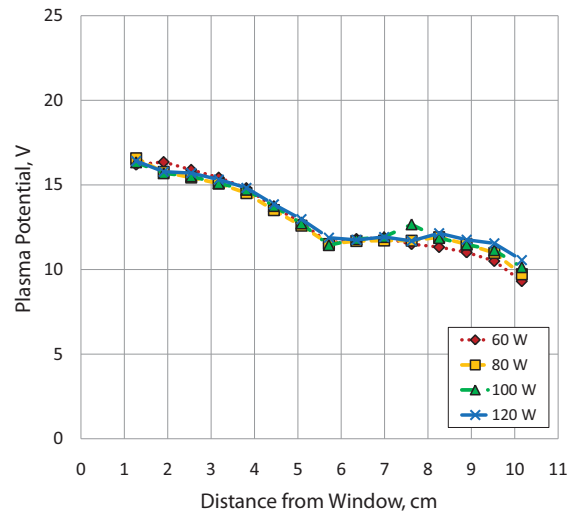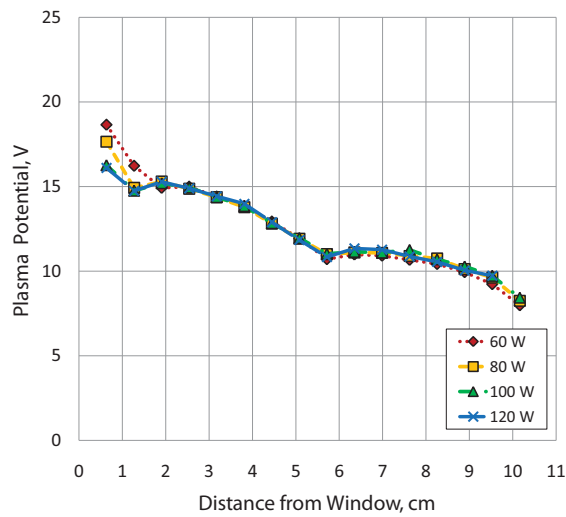

(b) 4 sccm Effective.

(c) 6 sccm Effective.

Figure 6.20: Plasma potential along plasma cathode centerline, on xenon. Aperture located at 10 cm.
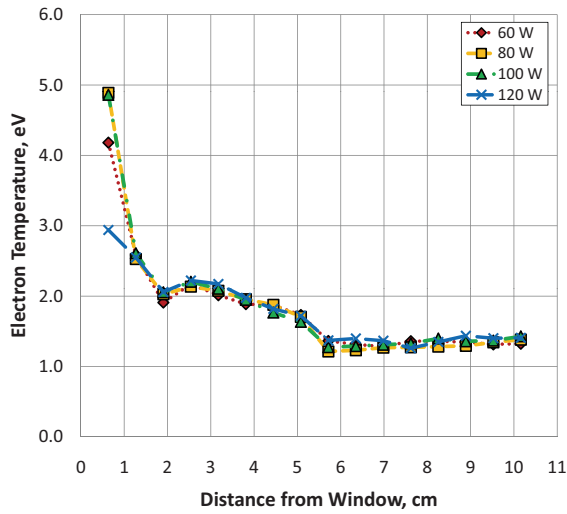
(a) 4 sccm Effective.

(b) 6 sccm Effective.
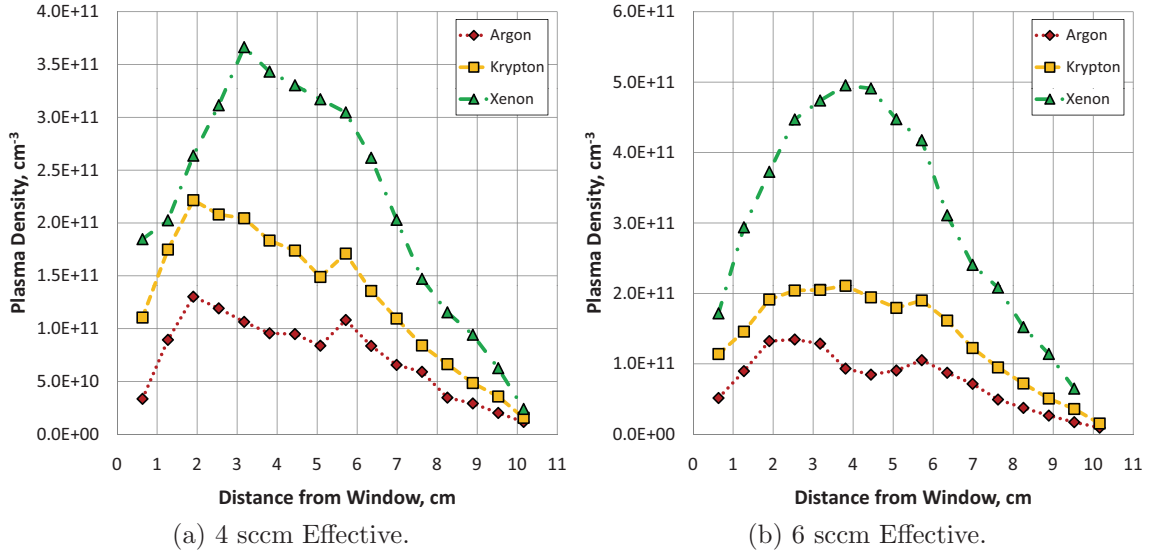
Figure 6.21: Comparison between density profiles on Ar, Kr, and Xe, at 120 W. Aperture located at 10 cm.

and peak magnetic field are observed. In the resonance zone, the electron temperature decreases from the upstream to downstream regions. In the nearly uniform magnetic field region downstream from the null (5.7 cm), the electron temperature is uniform on all three gases. Along the entire profile, electron temperature decreases as the feed gas is varied from xenon to krypton to argon. The reason for this is twofold. 1) the internal pressure at a fixed flow scales as $\sqrt{M_i}$, so the more massive the feed gas, the higher the collision frequency and 2) in the range of 1-3 eV, the rate constants for inelastic processes decrease from Xe to Kr to Ar. For a given population of electrons, at a fixed gas pressure, more energy is lost through inelastic processes with xenon than with argon. The electron temperature in the downstream region of the plasma cathode remains in the range of 1 to 2.5 eV between all three gases.

The plasma potential profiles are also compared, as shown in Figure 6.23. Again, the profiles are similar with a long-range potential drop of $\sim$ 10 Volts across the length of the plasma cathode. The dip in plasma potential at the null is observed on all three gases. The plasma potential is expected to scale proportionally with the

(a) 4 sccm Effective. (b) 6 sccm Effective.
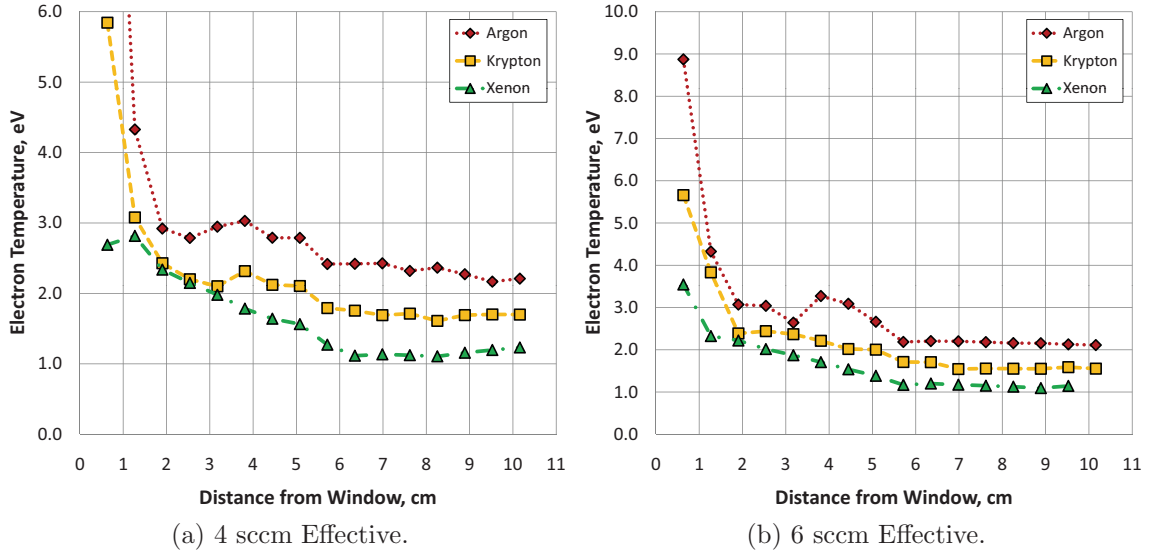
Figure 6.22: Comparison between temperature profiles on Ar, Kr, and Xe, at 120 W. Aperture located at 10 cm.

electron temperature and $\ln\sqrt{M_i/(2\pi m)}$. The latter term varies from 4.7 on argon to 5.3 on xenon, while the electron temperature varies up to a factor of two between the two gases (Figure 6.22). The lower plasma potential on xenon relative to that on argon is explained by the lower electron temperature when operating on xenon, with the dependence on M_i having a smaller effect.

6.3   Summary of Probe Results

A summary of basic plasma quantities calculated for the internal source plasma is shown in Figure 6.24 for argon. The neutral argon pressure inside the source varied from 20 to 60 mTorr over the tested range of flow rates. The Langmuir probe measurements suggest that 2.5 eV can be used as an estimate of average electron temperature within the source, so this is assumed in the calculation of the rate constants. For the calculation of ionization and excitation path lengths, the maximum cross sections for each are used. Room temperature ions and neutral atoms ($T = 0.026$ eV) are assumed. For pressure-dependent quantities, a range of values is shown,

(a) 4 sccm Effective.

(b) 6 sccm Effective.
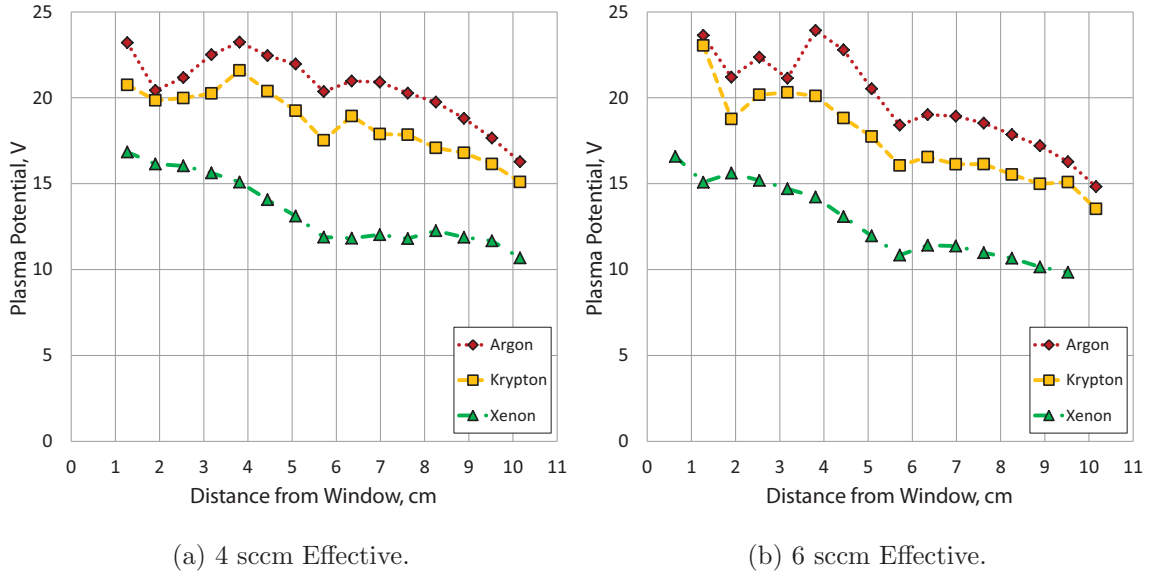
Figure 6.23: Comparison between plasma potential profiles on Ar, Kr, and Xe, at 120 W. Aperture located at 10 cm.

corresponding to 20–60 mTorr. The ionization and excitation rates were calculated by multiplying the neutral gas density by the applicable rate constant.[45] The argon ionization rate constant in m^3/s is calculated from,

$$K_{iz} \approx 2.34 \times 10^{-14} T_e^{0.59} \exp(-17.44/T_e), \tag{6.5}$$

where T_e is in eV. Similarly, the excitation rate constant in m^3/s is:

$$K_{ex} \approx 2.48 \times 10^{-14} T_e^{0.33} \exp(-12.78/T_e). \tag{6.6}$$

The "ECR Zone" values correspond to a magnetic field of 875 Gauss, while the "Downstream" values correspond to the downstream field strength of 150 Gauss.

6.3.1   Internal Plasma and Extracted Current

One proposed explanation for the peaked behavior in the current vs. flow rate plots (from Chapter 5) was that plasma production via ECR heating may have been

Quantity	Value
Pressure Range, mTorr	20 - 60
e- Mean Speed (2.5 eV), cm/s	1.1×10^{8}
e- Elastic Scattering Rate Constant (2.5 eV), cm³/s	9.8×10^{-8}
Argon Ionization Rate Constant (2.5 eV), cm³/s	3.8×10^{-11}
Argon Excitation Rate Constant (2.5 eV), cm³/s	2.0×10^{-10}
e- Elastic Scattering Frequency, MHz	64 - 192
Mean e- Elastic Scattering Pathlength, cm	0.4 - 1.2
Argon Ionization Rate, kHz	24.4 - 73.2
Argon Excitation Rate, kHz	131 - 394
Minimum Argon Ionization Pathlength, cm	1.3 - 3.9
Minimum Argon Excitation Pathlength, cm	4.3 - 13
Ion Mean Free Path, cm	0.05 - 0.15
Electron Larmor Radius (ECR zone), cm	0.004
Ion Larmor Radius (ECR zone), cm	0.12
Electron Larmor Radius (Downstream), cm	0.03
Ion Larmor Radius (Downstream), cm	0.7
Debye Length (Cutoff Density), cm	0.004

Figure 6.24: Summary of basic plasma quantities. Electron temperature of 2.5 eV is assumed, unless otherwise noted.

disrupted under some conditions. For example, if the internal pressure reached a point where the collision frequency became comparable to the ECR frequency, the efficiency of the ECR will drop because the total acceleration of electrons between collisions is reduced. Depending on the plasma density upstream of the ECR region, additional microwave absorption may also be disrupted though cutoff effects at some conditions.

The data show that variations in plasma production in the ECR zone is not responsible for the trends in extracted current. The peak plasma density (taken at the 2.3 cm location) is plotted in Figure 6.25 as a function of flow rate and microwave power on xenon. Over the range of operating conditions, the peak density increases monotonically with both flow rate and absorbed power. If the extractable current were limited by the plasma production rate, these plots should eventually saturate as the microwave power is increased or start to decrease at higher flow rates. The internal probe traces indicate that the optimal conditions for current extraction are dictated in large part by the applied bias, by influencing the plume conditions or the efficiency of electron extraction from the source plasma.

6.3.2   Plume Plasma and Extracted Current

As a check on the collected current with respect to the plume conditions, the electron current density at the anode was calculated from the xenon plume Langmuir probe data. The electric field near the anode was found from a linear fit to each plasma potential profile in the region of 8 to 14 cm downstream of the plume (c.f. Figure 6.6) and calculating the slope of the fit. The average electron density in this region was calculated as well. The neutral pressure in the plume was assumed to be equal to the background chamber pressure, and was used to calculate the DC conductivity of the plume region σ_{dc}. The current density J was then calculated by $J = \sigma_{dc}E$, where E is the average electric field. In the xenon plume, the electric
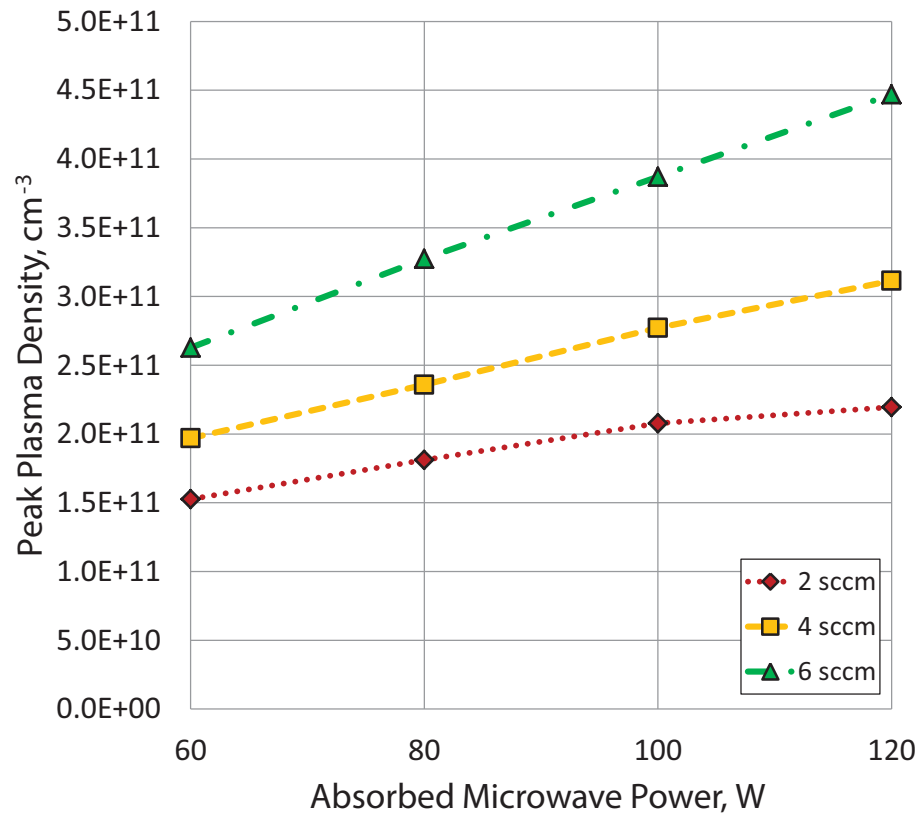
Figure 6.25: Plasma density at the ECR zone ($z = 2.3$ cm) versus microwave power and flow rate.

field varied between 30 to 50 V/m, and the background pressure varied in the range of 1.5 to 4.0×10^{-5} Torr. The calculation gives current densities in the range of 5 to 12 A/cm^2 depending on the operating conditions. For extracted currents on the order of a couple of Amperes, this corresponds to beam sizes on the order of 0.1 to 0.3 cm^2. This is likely an underestimate, because the neutral density in the plume is likely higher than in the chamber as a whole, but these beam sizes are reasonably close to those observed, as an order-of-magnitude estimate.

CHAPTER VII

Electron Extraction Mechanism

7.1 Background: Study of Electron Extraction Mechanism

While the demonstration of a feasible electrodeless ECR plasma cathode is an interesting problem in itself, the endeavor has uncovered questions regarding the operation of the device. Most interesting was the dramatic change in plasma density within the extraction aperture during current extraction. One of the initial tests of the waveguide plasma cathode operating on argon feed gas involved the insertion of a Langmuir probe in the extraction aperture. The extraction electrode was fixed at 14 cm downstream from the aperture. The Langmuir probe was used to measure the plasma density in the aperture, both with and without an applied bias. The absorbed microwave power was varied at fixed flow rate (6 sccm). The resulting changes in the plasma density are shown in Figure 7.1. The measurements show that during current extraction, the density jumps by nearly a factor of 100 in the aperture, with the current scaling with this corresponding density. Plasma densities of up to 7×10^{11} cm^{-3} were observed, a factor of ten above the cutoff density at the 2.45 GHz microwave frequency (7.4×10^{10} cm^{-3}).

Langmuir traces were also taken inside the bulk plasma, at the downstream end of the plasma cathode (from Chapter 5, Probe "B" in Figure 5.11). The resulting densities and temperatures (typically ~ 3 eV) were used to calculate the available
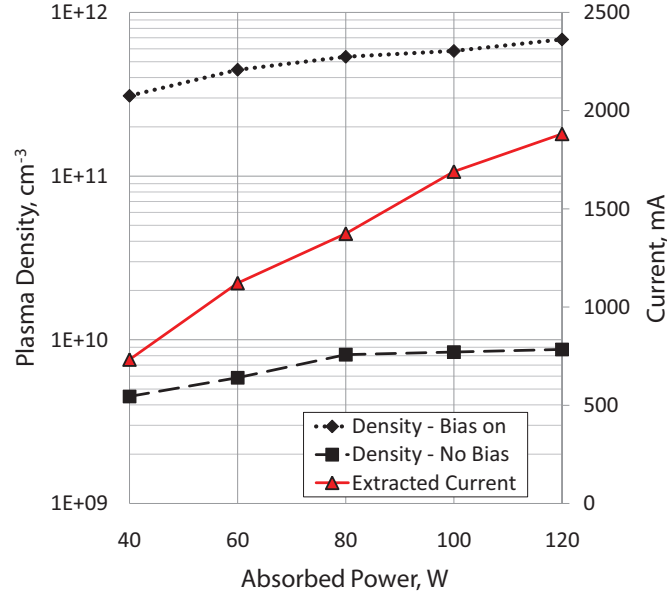
Figure 7.1: Variation in plasma density within aperture, with and without 80 V bias, on 6 sccm argon.

electron current through the extraction aperture. Assuming a Maxwellian electron energy distribution, the maximum current density through the aperture would simply be $\frac{1}{4}en\bar{c}$, with $\bar{c} = \sqrt{8k_BT_e/\pi m}$, as described in Chapter 3. The extraction area is assumed to be equal to the aperture area. When plotted against the measured extracted current, as shown in Figure 7.2, the measured current was several (~ 8) times greater than the calculated result. Significant amounts of plume ionization were ruled out as the cause, from the discussion in Chapter 5. If the assumption of a Maxwellian plasma upstream of the aperture were invalid, and the extracted electrons had a directed "beam" velocity, then the discrepancy between extracted and measured currents could be resolved. If the electrons had undergone a potential drop of ΔV upstream of the probe, then the electron flux through the aperture is given by, $en\sqrt{2e\Delta V/m}$. By taking the ratio of this "beam" electron flux to the Maxwellian electron flux, we find that the factor of 8 could be accounted for by an upstream potential drop of ~ 15 Volts.

The dependence of density on applied bias and the unexpectedly high extracted
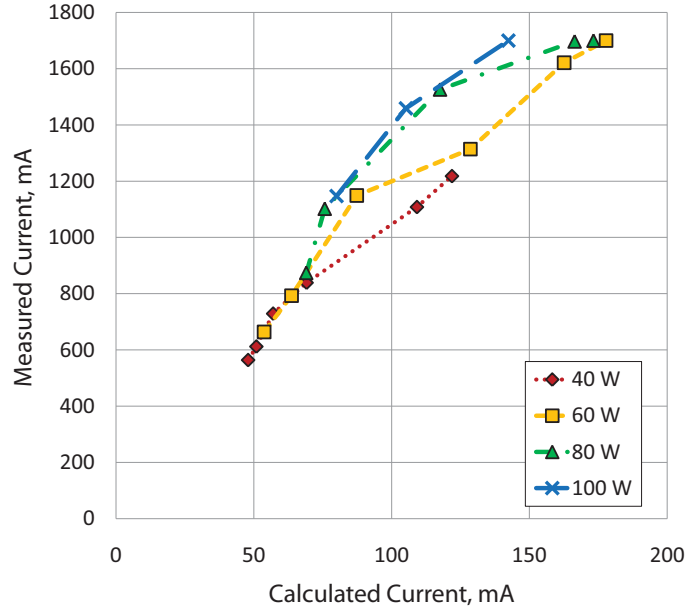
Figure 7.2: Extracted current vs. expected current from bulk plasma density at 80 V, on 6 sccm argon.

current both conflicted with the theory behind plasma cathode operation. The discussion in Chapter 3 presented this theory, which generally assumes that the maximum available current from a plasma cathode is the Maxwellian electron saturation current through the aperture. In some cases, where the internal collection area for ions at the plasma cathode walls is too small, that may be the limiting factor on extractable current. But with sufficient wall area, the extractable current is not assumed to be any different than that by a Langmuir probe in the electron saturation regime. Current extraction is not usually assumed to have any effect on the local plasma density in the device, up to the electron saturation condition. Instead, with an increasing anode bias, the global plasma potential is expected to increase, and electron acceleration from the plasma cathode aperture can take place when the anode potential exceeds the plasma potential.

Three explanations for the electron extraction characteristics of the device are proposed. The increase in plasma density may be an effect of focusing electrons from the bulk plasma into a small cross-sectional area. Also, a degree of electric field

leakage through the aperture could establish an additional mobility term, and since the magnetic field is axial between the ECR heating zone and the aperture, this may significantly increase electron transport to the aperture. Since ECR plasma sources have been shown to produce overdense discharges, enhanced electron transport from the heating zone to the aperture may explain the increased density. It is also possible that electron acceleration could produce additional ionization. A collaborative effort between the U-M PSTL and Sandia National Laboratories was established to study these possibilities, using laser collision-induced fluorescence (LCIF). LCIF is a technique for generating two-dimensional images of electron densities and effective electron temperatures, in a non-intrusive fashion. The measurement is not sensitive to strong magnetic fields, in contrast to Langmuir probe measurements. This diagnostic method is well-suited for the study of a magnetized ECR plasma cathode.

7.2 Summary of LCIF Diagnostic Technique

LCIF is a powerful, non-invasive tool that can spatially resolve electron density and temperature profiles. The use of LCIF for generating two-dimensional images is relatively recent. An overview of this method is covered in detail in Barnat and Frederickson.[6] The formulism for LCIF used here was developed for helium plasmas. One can use a 389 nm laser beam to pump the $2^3\text{S} \rightarrow 3^3\text{P}$ helium transition. Because the 2^3S state is metastable, a reservoir of helium in that state is formed via collisions with electrons. The beam then pumps a fraction of the metastables to the 3^3P state. As electrons collide with the pumped neutral species, they will redistribute the population to nearby states, and the distribution of those states depends on the electron density and EEDF. The pumping scheme is shown in Figure 7.3 along with the relevant helium states and transitions for this work. Using a collisional radiative model (CRM), it is possible to calculate the expected time evolution of spontaneous emission rates as a function of the plasma properties. This implies

163
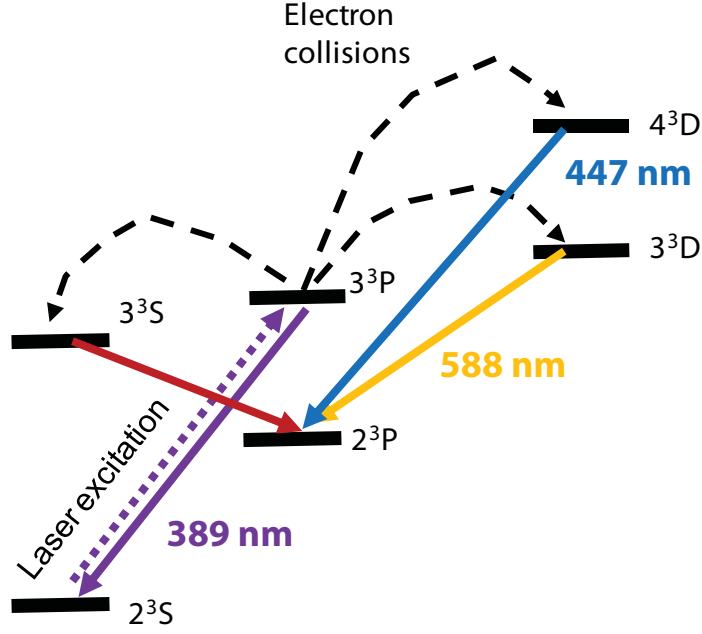
Figure 7.3: Illustration of the LCIF technique, adapted from [6].

that the transition rate constants and cross-sections related to spontaneous, electron-electron, and electron-atom processes must be well understood. A CRM including the helium triplet states up to the $n = 5$ levels was used in this study, and was solved over a density range of 10^9 to 10^{13} cm^{-3} and temperature range of 0.5 to 6 eV.[6] This CRM is described in detail below.

7.2.1 Collisional Radiative Model

The generalized CRM takes the form of,

$$\frac{dN_j}{dt} = \left[\sum_{i \neq j} K_{ij}^e N_i - \sum_{i \neq j} K_{ji}^e N_j \right] n_e$$

$$+ \left[\sum_{i > j} A_{ij} N_i - \sum_{i < j} A_{ji}^j N_j \right]$$

$$+ \sum_k \left[\sum_{i \neq j} K_{ikj}^a N_i - \sum_{i \neq j} K_{jki}^a N_j \right] N_k \qquad (7.1)$$

where N_x is the density of any given atomic state and x is specified by subscripts i, j, and k, n_e is the electron density, and $K_{xy}^{a,e}$ is the rate constant for a given transition. The first and second terms on the right hand side of Equation (7.1) represent the population rate of state j via electron collisional processes: they correspond respectively to collisional excitation into state j and collisional de-excitation out of state j. The third and fourth terms are the spontaneous radiative transitions into and out of state j, respectively. The final two terms are the source and loss rates due to atomic mixing, wherein collisions between excited neutrals either populate (fifth term) or depopulate (sixth term) state j. In Equation (7.1), a denotes an atom-atom interaction and e denotes an electron-atom interaction from initial state x to final state y. Coefficients A_{xy} are the Einstein spontaneous emission coefficients from x to y. Three body interactions are neglected.

In order to account for the time dependence of the incident laser pulse and the radiative coupling between the laser-pumped 3^3P state and 3^3S state, "effective" values of the A coefficients were developed for the 3^3P $\rightarrow$ 2^3S and 3^3P $\rightarrow$ 3^3S transitions,

$$A_{\text{Eff}} = A_{\text{Nom}} \left[1 + \left(\frac{\lambda^2}{8\pi} \right) g(\nu) \left(1 - \frac{g_i N_j}{g_j N_i} \right) \frac{I(\nu, t)}{h\nu} \right] \tag{7.2}$$

where A_{Eff} is the effective spontaneous emission coefficient, A_{Nom} is the nominal spontaneous emission coefficient, λ is the wavelength and ν is the frequency of the transition, $g(\nu)$ is the absorption profile of the transition, $g_{i,j}$ is the statistical weight of each level, and $I(\nu, t)$ is the incident photon intensity associated with the transition. The effective emission coefficient takes into account the dependence of absorption and stimulated emission of the pumped transition on the incident photon intensity and relative populations of states i and j, which vary in time during the laser pulse. At low photon intensities or when there is no population inversion, the effective coefficient becomes equal to the nominal value. All values of A_{Nom} in the CRM were compiled

165

by NSRDS-NBS (NIST).[75]

The rate constants for electronic excitation from a lower to higher energy state are achieved by integrating the relevant cross-section over an assumed Maxwellian distribution, according to,

$$K_{ij}^e = \langle \sigma_{ij} v_e \rangle = \left(\frac{m_e}{2\pi k_B T_e} \right)^{3/2} \times \int_0^\infty \sigma_{ij}(v) v \exp \left(\frac{-m_e v^2}{2k_B T_e} \right) 4\pi v^2 \, dv \qquad (7.3)$$

where σ_{ij} is the energy-dependent cross-section, v_e is the electron speed, m_e is the electron mass, k_B is the Boltzmann constant, and T_e is the assumed electron temperature. For electronic de-excitation from a higher to lower energy level, the rate constant is evaluated to include detailed balance,

$$K_{ij}^e = \langle \sigma_{ij} v_e \rangle = \left(\frac{m_e}{2\pi k_B T_e} \right)^{3/2} \times \int_0^\infty \sigma_{ij}(v) v \exp \left(\frac{-m_e v^2}{2k_B T_e} \right) 4\pi v^2 \, dv$$
$$\times \left[\frac{g_j}{g_i} \exp \left(\frac{(E_j - E_i)}{k_B T_e} \right) \right] \qquad (7.4)$$

where E is the energy of the states. All values for σ_{ij} used in these calculations were from analytic expressions published by Ralchenko *et.al.*[61] In general, the values of the rate coefficients for each transition were within a factor of two agreement of experimentally determined values reported in the literature at moderate (≥ 1 eV) electron temperatures. Transitions resulting from atom-atom collisions were limited to nearest-neighbor processes ($\Delta n = 0, \Delta l = \pm 1$) in the CRM, with rate constants determined from Denkelmann *et.al.*[13] Rate constants for these interactions were typically a factor of 10^6 lower than those associated with electronic processes, so atomic mixing should be a significant factor only when the ionization fraction in the plasma is less than 10^{-6}.

The CRM results for a 1 eV helium plasma at 25 mTorr is shown in Figure 7.4.

166
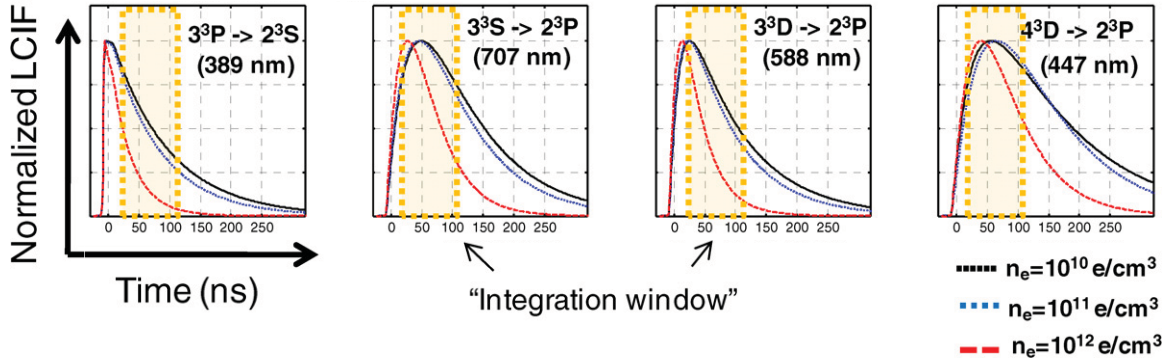
Figure 7.4: Time evolution (in ns) of the LCIF intensities (in arbitrary units) after the laser pulse. Calculated at 1 eV electron temperature, at 25 mTorr.

The figure shows the normalized intensity of the LCIF emission as a function of time after the laser pulse, for four transitions. The 389 nm pumped state generally reaches its peak immediately following the laser pulse, with the 588 and 447 nm transitions peaking a few tens of nanoseconds afterward. When the electron density is sufficiently high, collisional de-excitation of the upper energy states contributes significantly to the time decay of each transition. This manifests in Figure 7.4 as the steeper dropoff in intensity with time, in the 10^{12} cm^{-3} case. In some cases, it is possible to measure the evolution of these transition intensities over time, and fit the results to the time-resolved CRM model to determine the electron density. However, this requires a minimum plasma density in order to capture the effect of electronic processes on the transition decay time (in contrast with spontaneous emission dominating the process). The time-resolved intensity curves show that this minimum density occurs near 10^{11} cm^{-3}, where the curves begin to separate. At lower densities, spontaneous emission overwhelms collisional de-excitation, and the time-resolved intensity profiles become nearly independent of electron density. The plasma densities in this study were near the 10^{11} cm^{-3} threshold, so the time-resolved CRM fitting procedure could not be used to determine the density.

If one integrates the LCIF-driven emission of the 389, 588, and 447 nm transitions over a range of time after the laser pulse and determines the ratios of these time-

integrated transitions, one can uniquely determine the plasma properties using the CRM results. For example, one might use a 100 ns integration window after the laser pulse, as shown by the yellow box in Figure 7.4. For helium in particular, the ratio of the 3^3D $\rightarrow$ 2^3P (588 nm) to the 3^3P $\rightarrow$ 2^3S (389 nm) transitions is linearly related to the electron density in this range, and generally independent of electron temperature. This is due to the small difference in energy between the 3^3D and states 3^3P states ($\sim$ 0.07 eV). Nearly any electron can populate the 3^3D state from the 3^3P state regardless of energy, so the population of the 3^3D state to that of the 3^3P state (driven by LCIF alone) depends linearly on density. Once the density is known, the ratio of the 4^3D $\rightarrow$ 2^3P (447 nm) transition to the 588 nm transition can be used in conjunction with the electron density to determine the electron temperature. The difference in energy between the 4^3D state and the pumped state is much larger ($\sim$ 0.7 eV), so the population of this state is sensitive to both electron density and temperature. By taking the ratio of the LCIF intensity from the temperature-sensitive 4^3D state to that from the insensitive 3^3D state, one can uniquely relate the intensity ratio to the electron temperature at a given density. A plot showing the relationship between time-integrated LCIF intensity ratios and the plasma properties (calculated from the CRM) is shown in Figure 7.5, and similar tabulated results were used to analyze each LCIF measurement. The ratio the 588 nm to the 389 nm transition is used first to uniquely determine the electron density. Then, the density and the ratio of the 447 nm to 589 nm intensity is used to uniquely determine the electron temperature from the bottom plot in Figure 7.5. The densities measured with the LCIF technique in this experiment were later compared against Langmuir probe measurements at the same plasma conditions; in all cases, the two measurements agreed to within a factor of three. For example, with the 6.35 mm aperture, at the operating conditions of 130 mTorr and 50 mA, the aperture plasma density measured by the probe was 2×10^{11} cm^{-3} while LCIF predicted 0.8×10^{11} cm^{-3}. Given the uncertainty in the cross
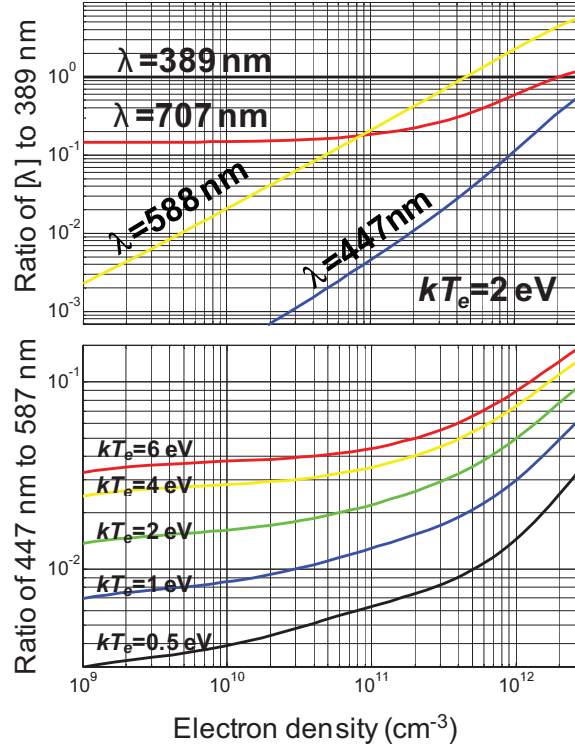
Figure 7.5: Integrated ratios of helium LCIF transitions as they relate to electron density and temperature.

sections used in the CRM and the uncertainty in density measurements in Langmuir probe analysis, the two techniques reasonably agree.

7.2.2 LCIF Experimental Procedure

A simplified schematic of the optical setup is shown in Figure 7.6. A pulsed Nd:YAG laser (3rd harmonic) with a spectral linewidth of < 0.01 nm and pulse width of 10 ns was used to pump a tunable optical parametric oscillator (OPO) system with ~ 300 mJ of 355 nm laser light, at a pulse rate of 20 Hz. The OPO was tuned to generate a 777 nm idler beam, which was then doubled in frequency, resulting in a 388.5 nm laser light output. The signal beam was detected by a fast photodiode. Interchangeable neutral density filters were used to attenuate the output beam, which passed through a series of beam-shaping optics to produce a planar beam. The sheet beam passed through the centerline of an optically accessible plasma cathode
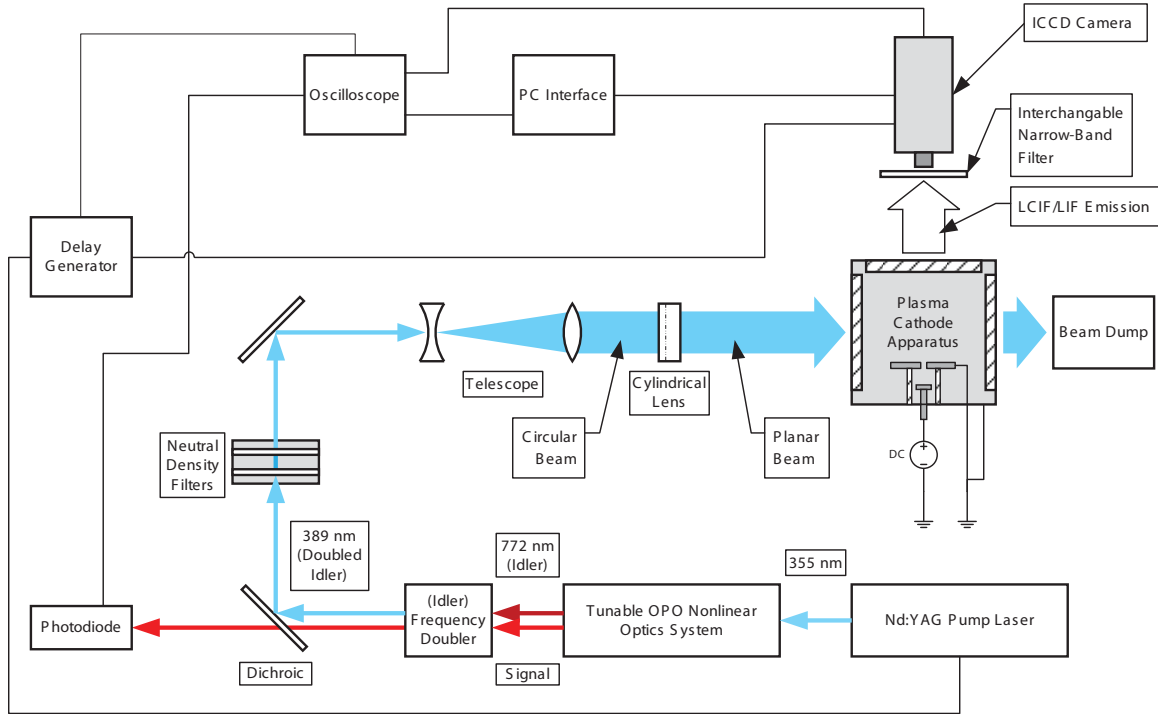
Figure 7.6: Optical setup of LCIF experiment.

setup, illuminating the imaging area of interest, and was ultimately collected by a beam dump. Oriented perpendicular to the sheet laser beam, an intensified charge-coupled device (ICCD) camera was mounted and focused on the region of interest. An interchangeable narrow-band filter was placed between the chamber and the ICCD. A delay generator was used to trigger the laser pulse and oscilloscope, and to control the delay of the ICCD gate width, total image accumulation time, and gate start time relative to the laser pulse. The delay generator and ICCD parameters such as gain and imaging region of interest were controlled by computer interface. The photodiode pulse and ICCD gate pulse were monitored by a digital oscilloscope. The optical setup of the LCIF diagnostic is shown in Figure 7.6.

The procedure for generating a set of density and temperature maps is as follows. The ICCD gain and gate width are fixed for each set of measurements, with the gate width chosen to capture the rapid decay in transition intensities after the laser pulse (c.f. Figure 7.4). A 389 nm narrow-band filter is placed in front of the ICCD, and the

170

camera takes a series of images. First, an image is taken 10 ns after the laser pulse passes through the chamber, capturing the time-integrated intensity due to LCIF and optical emission together. Then, a second image is taken 1 ms after the laser pulse, capturing optical emission alone. This is repeated over a total accumulation time that is varied to get a good signal-to-noise ratio for each transition, and the two series of images are saved. The accumulation time controls the total number of individual images that are taken in a series. It was chosen for each measurement so that the ICCD pixel with the highest number of counts was kept just under the maximum for the ICCD processing ability (50000 counts / pixel). The process is repeated with the 588 nm and 447 nm narrow-band filters in place as well. When analyzing the data, the optical emission intensities are subtracted from the total emission intensities, giving the emission due only to LCIF. They are then normalized to the accumulation times and filter efficiencies for each transition. The ratio of the 588 nm to 389 nm LCIF intensities are calculated at each pixel, and the density at each pixel is then found from the ratio using the CRM results. Then, the ratio of the 447 nm intensity to the 588 nm intensity is calculated at each pixel, and along with the electron density, the electron temperature is calculated using the CRM. In situations where a pixel implied an electron density or temperature beyond the range of the CRM solutions, the value was obtained by linear extrapolation.

7.3   LCIF Diagnostics of an ECR Plasma Cathode Setup

The first plasma cathode investigated with LCIF was based on the U-M waveguide plasma cathode. The apparatus was designed to function as a plasma cathode while still allowing for optical access to the internal plasma, as shown in Figure 7.7. The vacuum chamber used in this setup was 150 mm cube with ConFlat mounts on each side. The source plasma was a 2.45 GHz ECR plasma, though in this case, the ECR plasma was established in a rectangular waveguide. Samarium cobalt magnets were

used to establish an axial magnetic field, with the ECR zone near the centerline. The magnets were placed as close to the waveguide exit as possible so that the effects of the static magnetic field on the plasma could be captured. The ECR plasma source was mounted to the top flange, and quartz windows were mounted to three of the sides. The fourth side held the turbomolecular pump and throttling valve. On the bottom flange, a 70 mm diameter, 6 mm thick stainless steel disc was mounted, with a through bore of roughly 25 mm in diameter. The bore accepted a thinner disc with a 6.4 mm diameter by 1 mm aperture through the center. An extraction electrode, 13 mm in diameter, was mounted 25 mm below the aperture disc and surrounded by a 25 mm glass tube. The tube isolated the extraction electrode from the bulk plasma that filled the rest of the chamber, with the exception of the plasma which passed through the aperture. In this sense, the setup functioned like a plasma cathode, where electrons flow through the aperture, while the chamber walls act as the ion loss area. The extraction anode was connected to a DC power supply. The extracted current was measured by the voltage drop across a 1 Ohm resistor. The spacing between the downstream end of the ECR source and the aperture disc was roughly 40 mm. A photograph of the setup is shown in Figure 7.8.

An interesting phenomenon was observed when the collector electrode was biased positively. As in the U-M waveguide plasma cathode, the current did not gradually increase with the applied bias. Instead, less than a milli-Ampere of current was extracted over a range from zero to tens of Volts. Then, above a threshold voltage, the extracted current increased dramatically. At the same time, a bright plasma structure was observed on the upstream side of the extraction aperture, as shown in Figure 7.9. The structure appeared to be a necessary for any appreciable amount of current extraction. Though the structure was first observed at 130 mTorr, it was later observed for a range of pressures (75 to 200 mTorr), appearing at varying voltages. The initial conclusion was that this aperture plasma structure may explain
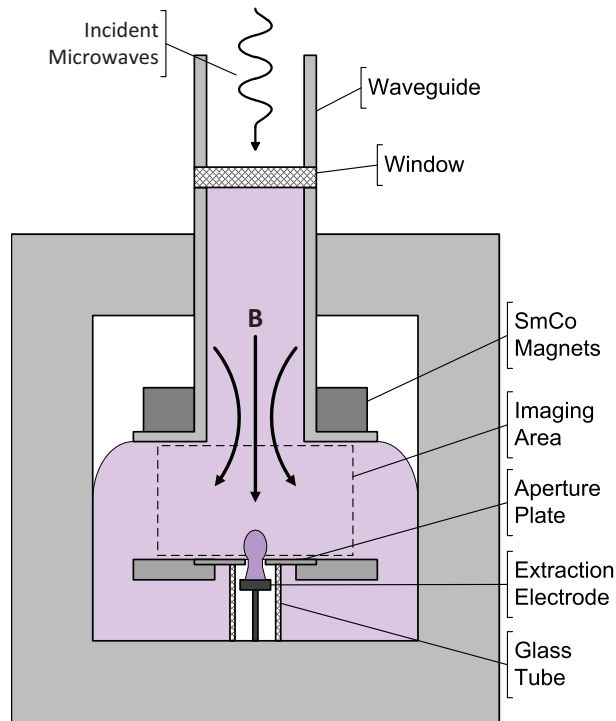
Figure 7.7: Schematic of Plasma Cathode Setup.
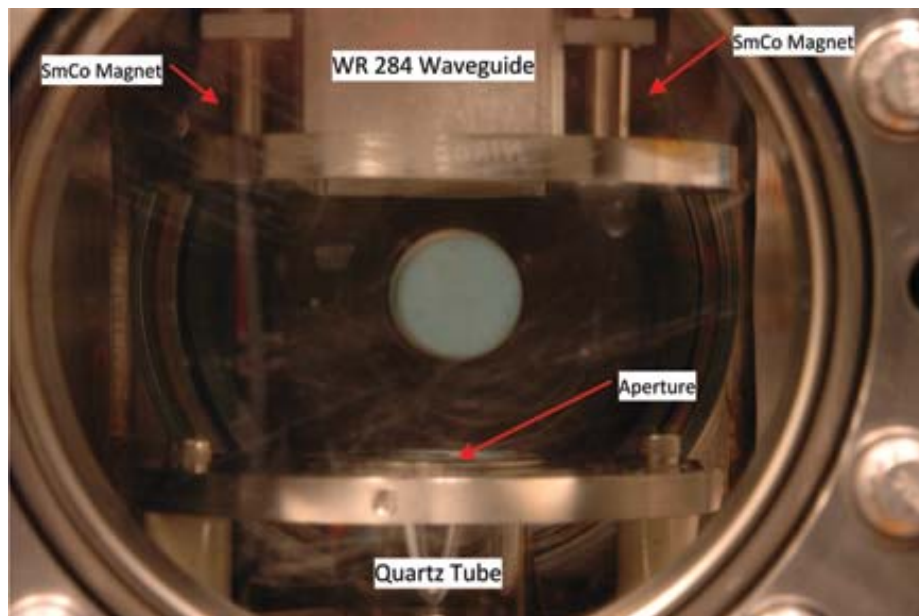
Figure 7.8: Photograph of the LCIF / ECR plasma cathode setup.

Figure 7.9: Photograph of an aperture plasma structure. Figure from [74].

the enhanced electron current and plasma densities seen in the U-M source and in other similar devices.

7.3.1 Density and Temperature Maps - ECR Setup

The LCIF density maps taken of the ECR plasma cathode are shown in Figure 7.10, at 130 mTorr and variable extracted current. Clearly shown at the upper portion of the figures is the dense ECR plasma with two lobes positioned at the location of the ECR heating zones. At the lower end of the images, the aperture plasma structure is seen. At low currents ($\sim$ 50 mA), the structure is small and spherical within the aperture. As the current is increased, the structure within the aperture increases in diameter, and a second structure appears to form on the upstream side of the aperture. The additional lobe was not stable, as it was observed to flicker and behave chaotically. Though it is not shown in the LCIF images, the upstream structure was oriented out of the page at an angle, and appeared to point toward one of the ECR heating zones at any given time. The structure jumped between the four symmetric heating zones, which were established by virtue of using two finite bar magnets oriented parallel to establish the static B-field.

174

(a) No Bias   (b) 50 mA   (c) 100 mA

(d) 150 mA   (e) 200 mA
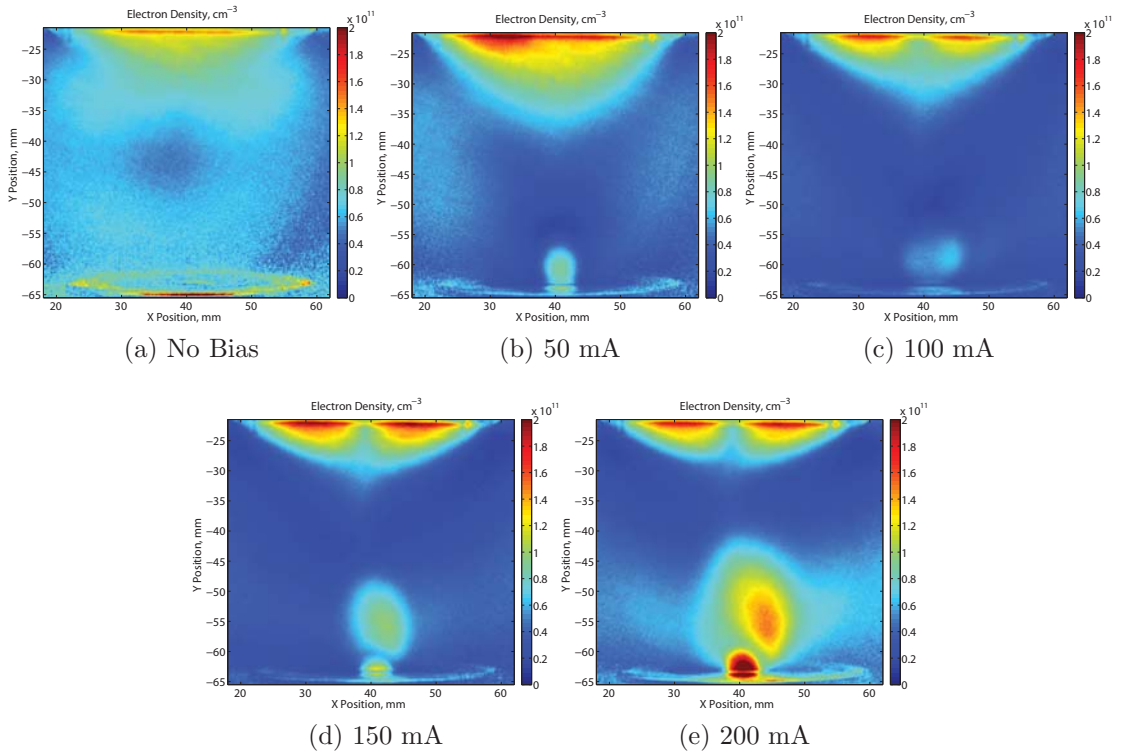
Figure 7.10: Maps of electron density in ECR plasma cathode, 130 mTorr and 100 W. Axis labels denote position in mm.

The images of electron temperature provide a great deal of insight into the aperture plasma structure as well. A series of temperature maps corresponding to the same conditions in Figure 7.10 is shown in Figure 7.11. At the top of the image, there are clear bands of high temperature electrons near the ECR heating zones, and these are clear regardless of extracted current. When the aperture plasma structure is formed, a clearly visible "halo" of high energy electrons is seen around the outside of the high-density region. This, along with the sharp dropoff in electron density at the boundary of the structure suggest the presence of a double layer sheath at the surface of the aperture plasma. This sheath focuses electrons toward the aperture, producing a high concentration of electrons, and a high-energy electron region near the sheath. The CRM gives temperatures of order 10 eV in this hot region, however, this is based on the assumption of a Maxwellian plasma. The formation of a double layer would cause electrons to gain at several eV as they pass through it, so this "temperature" is best characterized as an "effective temperature." Although these are not actual temperatures in the formal sense, the images gave the first clues about the formation and mechanism behind the aperture plasma structure. The presence of a high density region surrounded by a potential double layer sheath suggested that the structure is similar in nature to anode spots found near the surface of positively biased electrodes in plasmas.[52].

7.4 LCIF Diagnostics of an RF Plasma Cathode

The spatial and temporal variations of the aperture plasma structure in the ECR apparatus made it difficult to make repeatable measurements. The LCIF diagnostic often required image averaging over several minutes, but the shape of the plasma structure would sometimes change over this time period. In related studies of anode spots at low pressures, the presence of a magnetic field on the order of tens of Gauss was shown to cause spatially non-uniform regions. To avoid magnetic field effects

(a) No Bias (b) 50 mA (c) 100 mA

(d) 150 mA (e) 200 mA
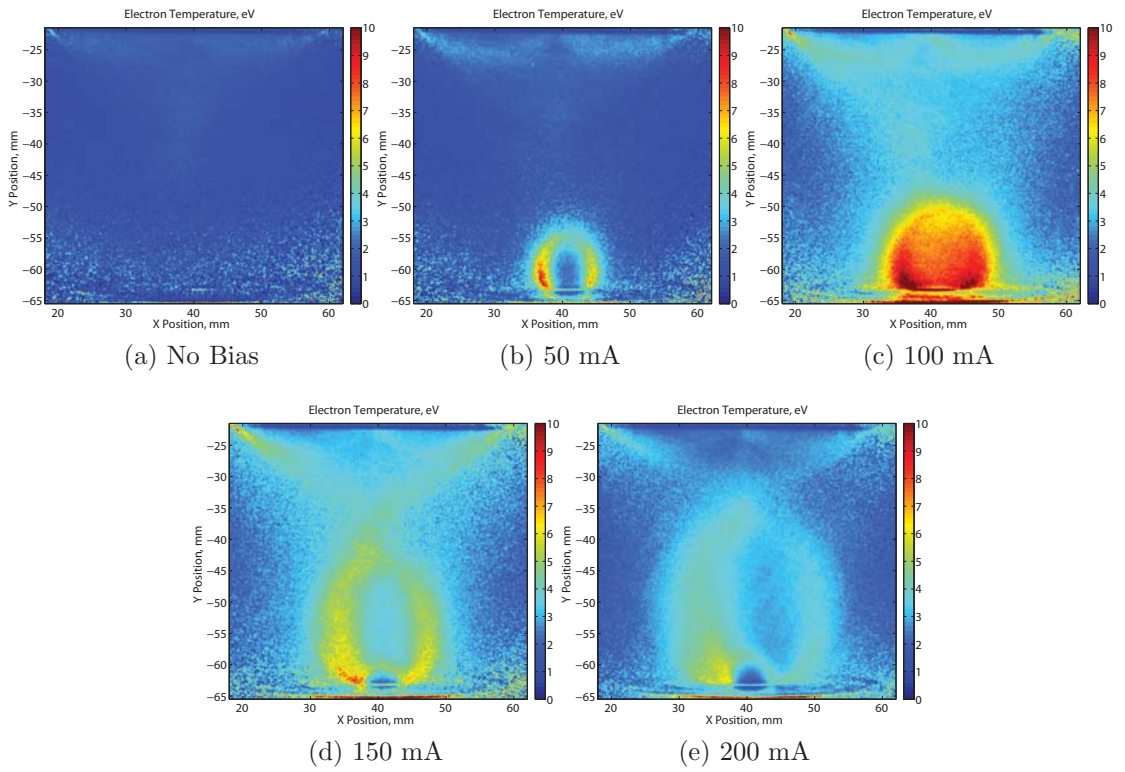
Figure 7.11: Maps of electron density in ECR plasma cathode, 130 mTorr and 100 W. Axis labels denote position in mm.
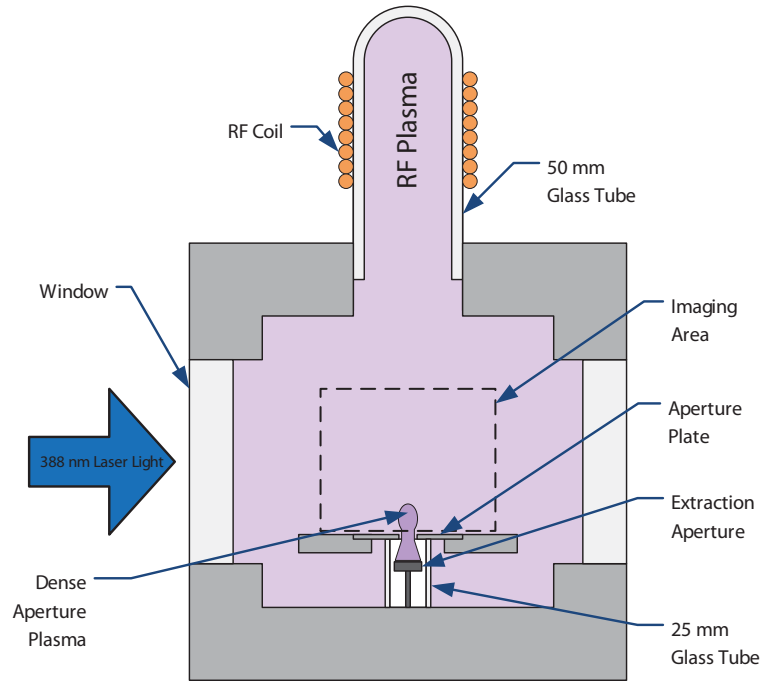
Figure 7.12: Schematic of Plasma Cathode Setup.

on the aperture plasma, the physics of the aperture plasma was studied with an inductively coupled plasma, implemented as shown in Figure 7.12.

The RF source consisted of a 50 mm glass tube surrounded by a helical copper coil, excited with a variable frequency RF amplifier driven by an external function generator. The exit plane of the RF source was located 100 mm upstream from aperture plate. The internal pressure was controlled with a throttling valve over a range of 75 to 200 mTorr. Forward and reflected power levels were monitored by analog directional wattmeters. Load matching was achieved by varying the frequency of the RF bias, and the best match at all pressures was found near 22 MHz. In all cases, the absorbed (forward minus reflected) RF power was held at 40 W, with forward power levels in the range of 50 to 55 W.

7.4.1   Density and Temperature Maps - RF Setup

The LCIF-generated electron density images with the RF plasma cathode apparatus are shown in Figure 7.13 (130 mTorr) and Figure 7.14 (200 mTorr). Both sets of images were taken with a 6.4 mm extraction aperture diameter. In all images, the center of the aperture is located at coordinates (x = 40.3 mm, y = -38.3 mm). In Figure 7.13a, the plasma density is shown without any applied bias to the extraction electrode; that is, it shows the plasma density generated by the RF source. The electron density in this "source" plasma is near 2×10^{10} cm^{-3}, and uniform across the image. The irregular secondary plasma structure is no longer seen at high extraction currents, and was likely due to magnetic field effects, as suspected. When the aperture plasma is present, the density consistently peaks a few mm upstream of the aperture. For example, at an extracted current of 100 mA, the peak plasma density was 1.1×10^{11} cm^{-3} 3 mm upstream of the aperture. As the extracted current was increased, the boundary of the plasma structure expands away from the aperture while the location of the peak density remained mostly fixed. As the structure expands, the surface area in contact with the bulk plasma increases, allowing the structure to collect more electron flux from the bulk.

Similar behavior is seen in the series of images at 200 mTorr. Again, the boundary of the structure is symmetric and appeared to be stable. The peak density again occurred roughly 2 mm upstream from the aperture, but peak electron densities were about 30 percent higher at the elevated pressure. Additionally the electron density in the bulk plasma (25 mA upstream of the aperture plasma structure) slightly increased with extracted current, from 2×10^{10} cm^{-3} at 0 mA to 5×10^{10} cm^{-3} at 200 mA. A more detailed discussion of the dependence of plasma density and shape on current extraction is presented in later sections of this chapter.

The electron temperature maps of the RF plasma cathode apparatus again show the presence of the high energy electron "halo" around the aperture plasma core.

179
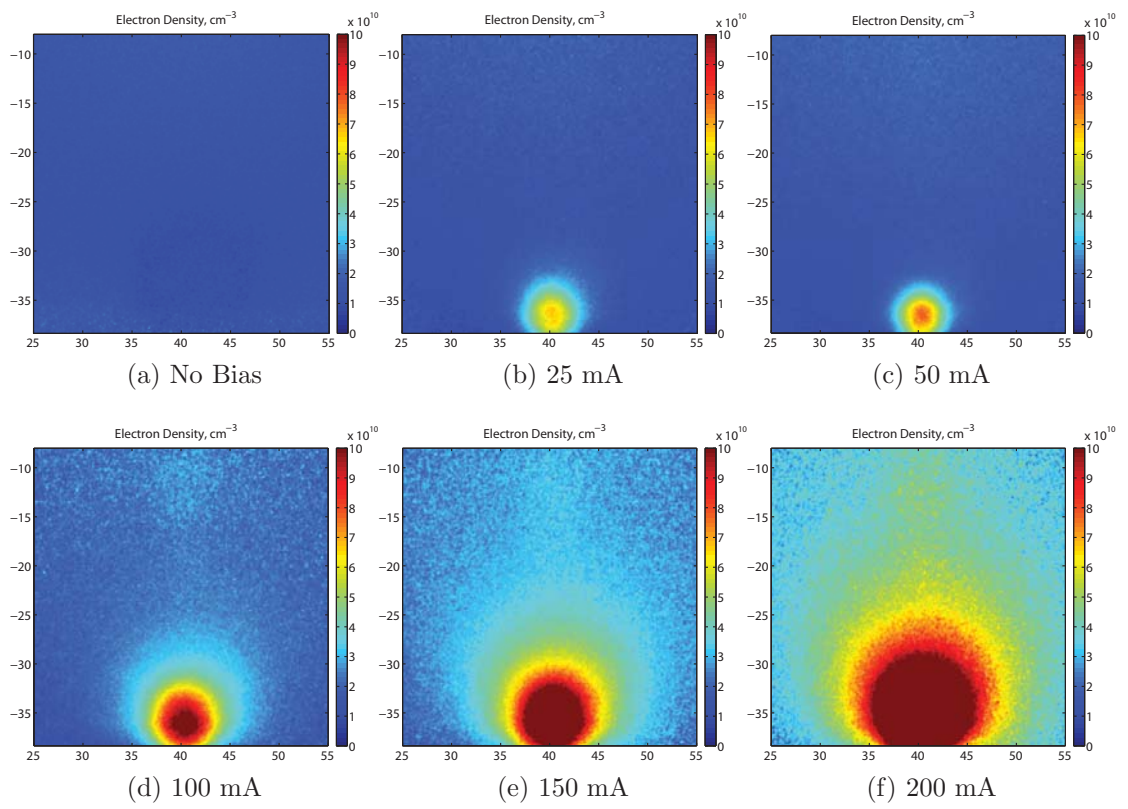
Figure 7.13: Maps of electron density with 6.4 mm aperture, 130 mTorr. Axis labels denote position in mm.
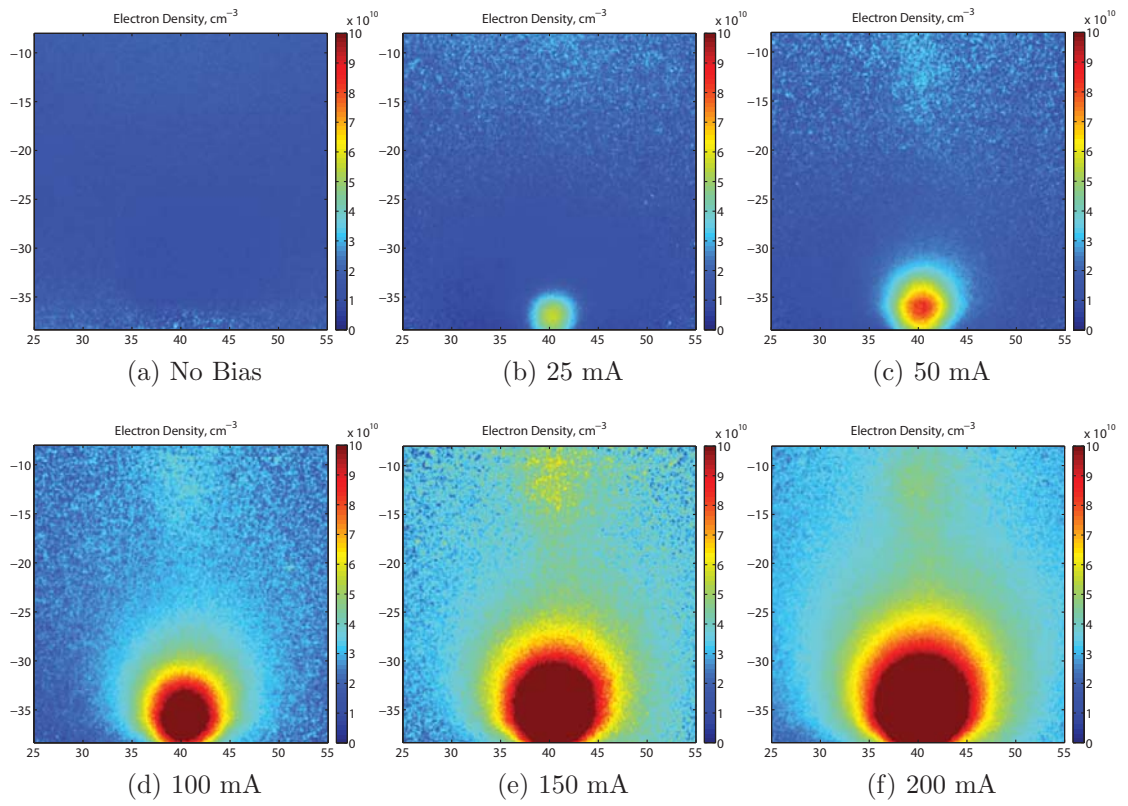
Figure 7.14: Maps of electron density with 6.4 mm aperture, 200 mTorr. Axis labels denote position in mm.

Interestingly, the halo does not appear to expand spatially outward as rapidly with increasing current as is observed with the electron density. Instead, the layer grows in thickness and the peak temperature is lowered. The effect of current extraction on the bulk plasma temperature is difficult to resolve, because of the low signal-to-noise ratio of the 447 nm counts in that region (which is used to calculate T_e). When the intensity of 447 nm light driven by LCIF is low relative to that from plasma induced emission, there is a high uncertainty in the electron temperature at each pixel. This effect manifests in the electron temperature maps as high and low temperature pixels adjacent to one another, as is seen in the upstream region of Figure 7.14b. The trends in the "effective temperatures" illustrate the existence of the double layer regardless of the upstream plasma source, along with qualitative trends in the average electron energy as a function of extracted current.

7.5 Analysis of Aperture Plasma Structure

As previously mentioned, the plasma structure observed near the aperture suggests a mechanism similar to what has been documented in low pressure anode spots. Key characteristics of these spots are a hysteresis effect in the I-V characteristic, the critical onset voltage to initiate the spot, the variation in spot size with applied voltage or current, and the presence of a double layer sheath between the spot and the bulk plasma.[52, 70, 68, 5, 12] All of these features are present in the aperture plasma structure, with the key difference in this work being that the aperture plasma is far removed (35 mm) from the surface of the electrode.

7.5.1 Current-Voltage Hysteresis

To record the current-voltage characteristic of the aperture plasma, the DC voltage between the electrode and chamber was gradually increased from zero to the "critical voltage" for ignition of the aperture plasma and beyond, while the extracted current

(a) No Bias   (b) 25 mA   (c) 50 mA

(d) 100 mA   (e) 150 mA
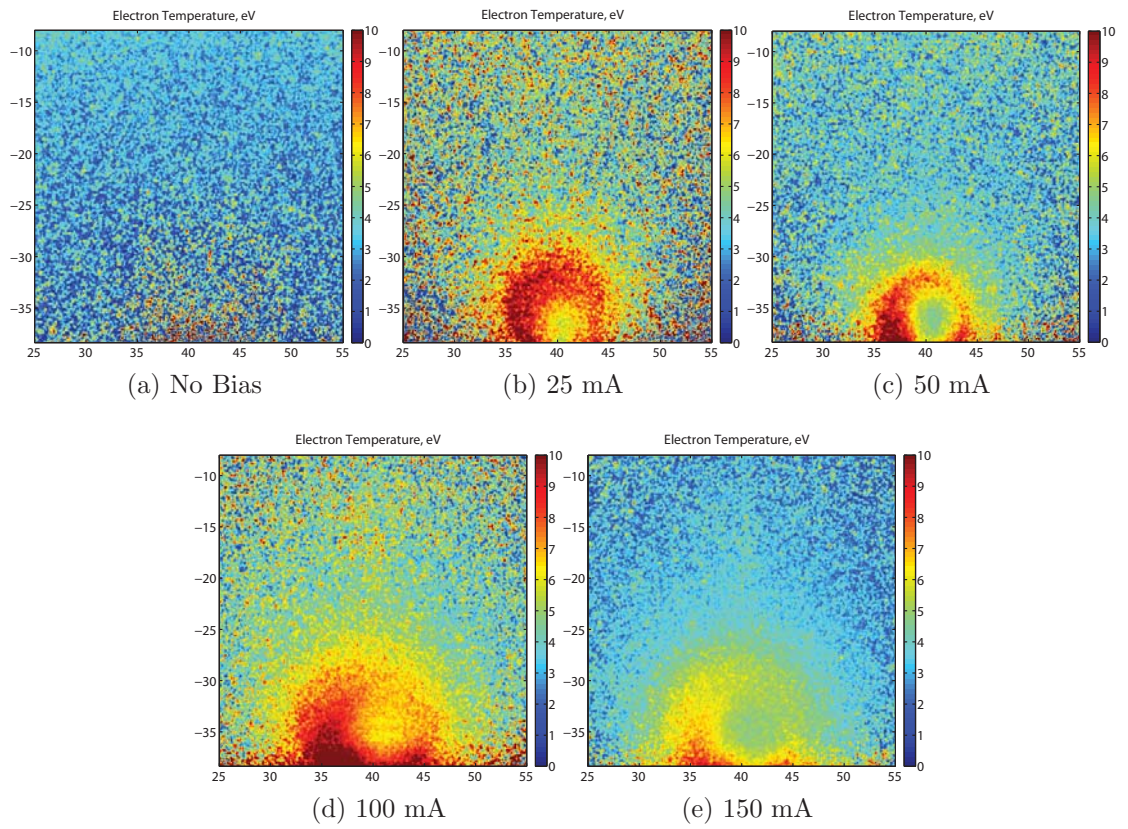
Figure 7.15: Maps of effective electron temperature with 6.4 mm aperture, 130 mTorr. Axis labels denote position, in mm.
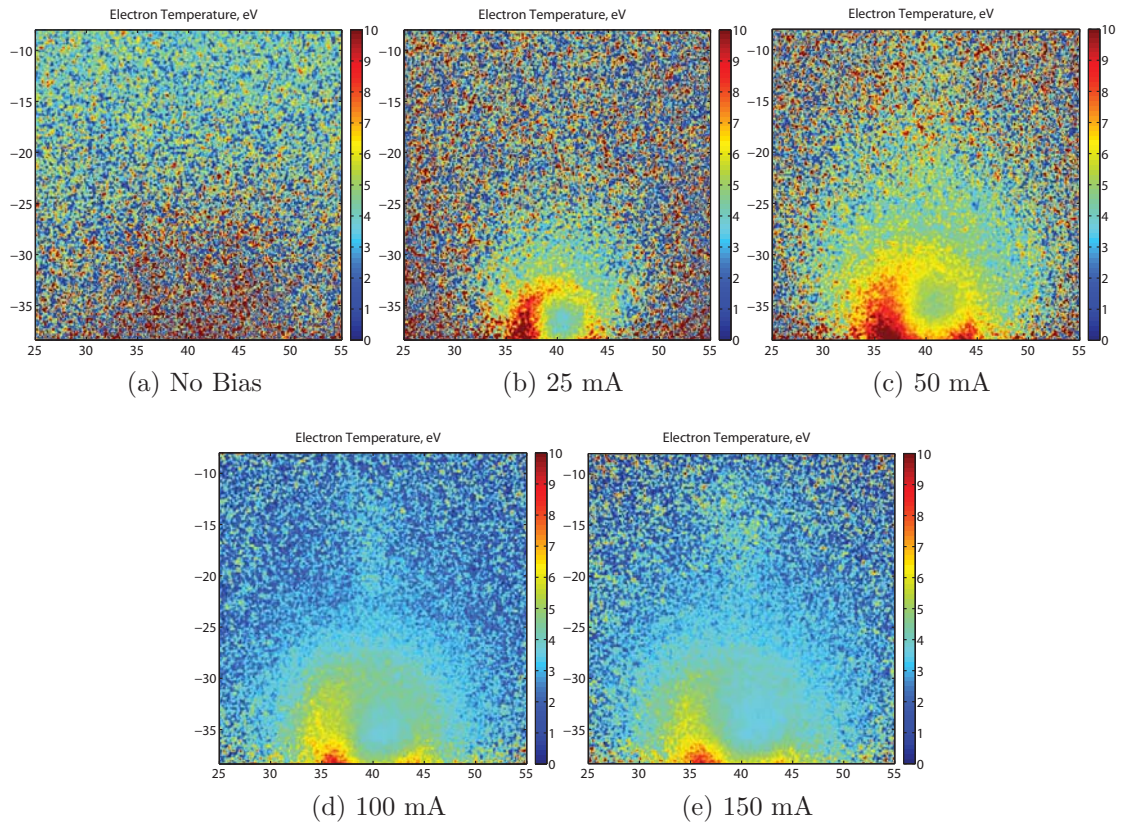
Figure 7.16: Maps of effective electron temperature with 6.4 mm aperture, 200 mTorr. Axis labels denote position, in mm.
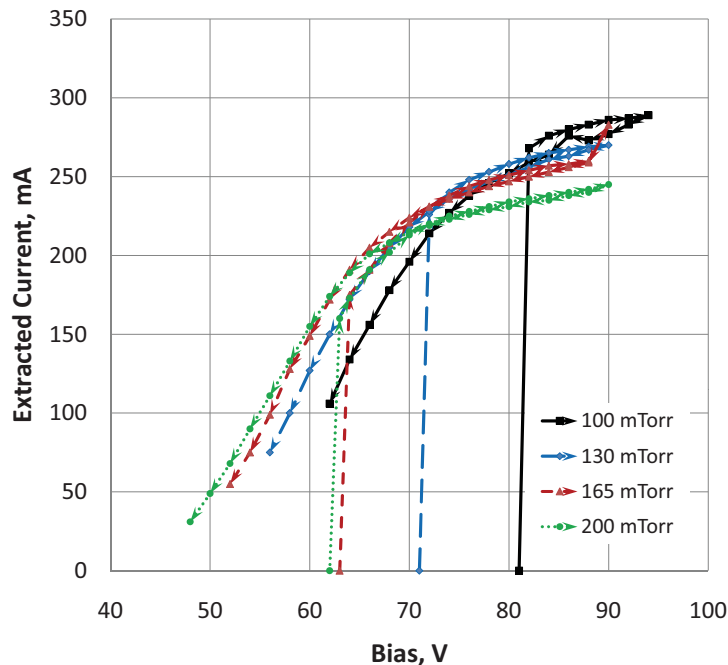
Figure 7.17: Extracted current vs. voltage characteristic, with 6.4 mm aperture.

was recorded. The resulting curves at 130 mTorr are shown in Figure 7.17. Below the critical voltage, with no aperture plasma present, extracted current was on the order of a few milliamperes. This regime is not shown in Figure 7.17 for clarity. At the critical voltage, the structure appears and extracted current increases dramatically to hundreds of milliamperes. This critical voltage is marked in Figure 7.17 by the intercept on the horizontal axis for each curve. After the structure is initiated, it can be sustained at a lower voltage than was required to produce it. The direction of the hysteresis in Figure 7.17 is shown with arrows on each trace. Above the critical bias, the I-V characteristic differs by 10 mA at most between the voltage upswing and downswing regions. On the voltage downswing, spots can be sustained at currents as low as tens of milliamperes, as seen in the 200 mTorr case. This behavior is similar to that observed anode spots, although those studies were done at much lower pressures.[5, 70, 68]

In anode spots, the formation and hysteresis mechanisms are described as follows.

In the anode glow regime, with the anode bias less than the critical bias, an electron sheath forms at the surface of a positively biased electrode. Electron acceleration by this sheath will increase the amount of ionization near the surface, though the total electron current produced within the sheath is negligible when compared to the incident electron flux. As liberated electrons are lost to the electrode faster than the newly created ions, depletion of electrons near the electrode leads to an adjacent thin, ion-rich region. The thin ion region shields out the electron sheath produced at the electron surface, driving the formation of a double layer further from the surface.[12] One explanation for the hysteresis in the I-V characteristic was presented by Baalrud, Longmier, and Hershkowitz.[5] They propose that the anode spot is initiated when the ion density due to this trapping of positive charge near the electrode increases to a point where the ion and electron densities in a Debye cube become roughly equal. At this point, a quasineutral plasma is formed. The ions within the plasma see a double layer between the spot and bulk plasma which is similar to an ion sheath. But for the sheath to be stable, ions must enter the double layer at a speed of at least $k_B T_e / M_i$, so a presheath is formed with a thickness of several Debye lengths. The double layer sheath is pushed out from the electrode surface, and an anode spot is born.

The hysteresis effect is explained by that same mechanism for spot formation. Even after the spot is formed, a minimum amount of ionization is needed to flatten out the potential profile near the electrode surface. Below the critical voltage, the only area where this ionization can take place is within the electron sheath itself. After the spot is ignited, there is an additional source of ionization within the spot itself, and the thin ion region near the electron sheath is no longer the only source of ions. Then, the voltage can be reduced below the critical value, and relying on both sources of ionization, the quasineutrality condition is still met. It appears that this behavior still holds true with the aperture plasma. Electron sheaths have been

observed in the aperture of plasma cathode sources.[47] In that case, the presence of the electrode itself should not be necessary to initiate an anode spot, since the electron sheath will still deplete electrons and leave behind the residual ions needed to form the spot. That is, *the aperture acts as a "virtual anode" when an external electric field is applied.* To the author's knowledge, the theory of spot formation near electron sheaths has not yet been extended to plasma cathode apertures, but it should provide a great deal of insight into their operation.

LCIF images were also recorded at several points on the I-V hysteresis curve, as shown in Figure 7.18. The expansion and contraction of the aperture plasma structure is clearly seen as the voltage (and consequently, current) is varied up and then back down past the critical bias. Again, the ionization rate in the aperture itself is not sufficiently high to contribute to the extracted current, relative to the electron flux incident on the double layer. Instead, the structure should vary in size to collect the required current from the bulk plasma, as seen here. The critical voltage in this series of images was 65 Volts, and on the downswing the spot was extinguished at 54 Volts. In the last image of Figure 7.18, when the spot is on the verge of extinction, the spot had contracted to roughly the size of the aperture itself.

7.5.2 Critical Voltage for Structure Formation

The critical required voltage for aperture plasma formation is shown in Figure 7.19, as a function of aperture size and pressure. At all pressures, it is clear that smaller aperture sizes require a higher applied bias for initiation of the spot. This may be expected because with a smaller aperture, a higher plasma density in the aperture plasma structure may be required to support a given extracted current. As shown in Figure 7.18, as the voltage is increased, the spot expands, increasing the total electron current from the bulk and the current density in the aperture. The dependence of plasma formation on pressure is another trend that is consistent with anode spot

187
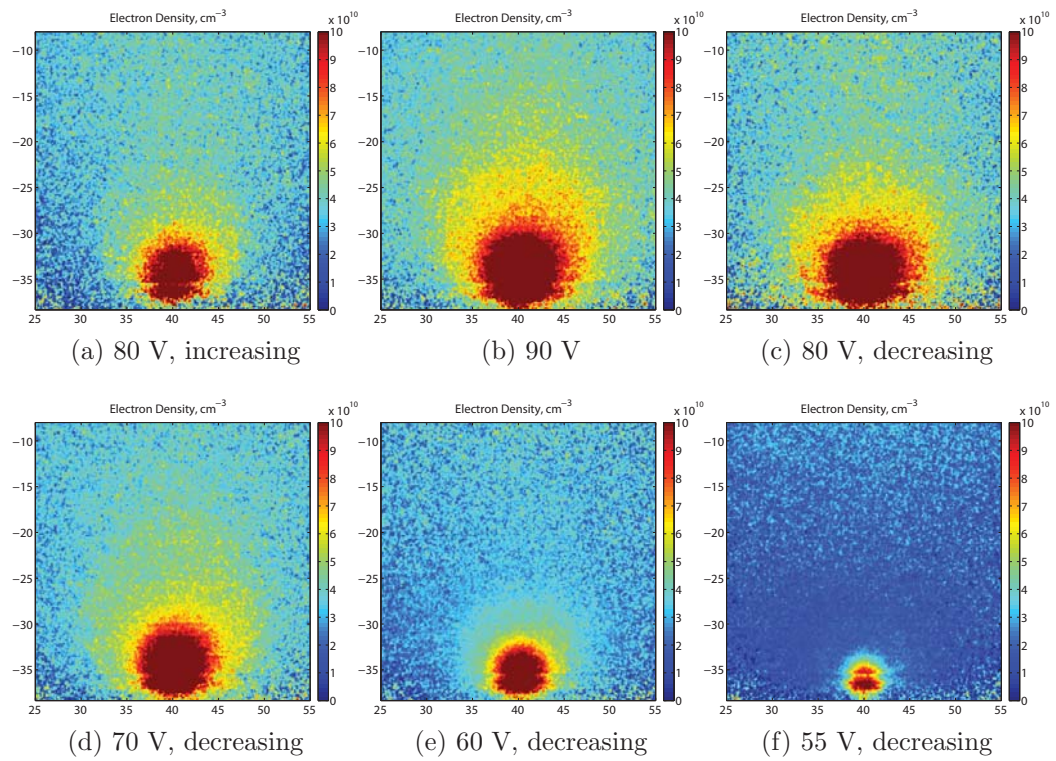
Figure 7.18: Maps of electron density during voltage sweep, with 6.4 mm aperture, at 130 mTorr. Axis labels denote position, in mm.

behavior. At reduced pressure (on the order of a few mTorr, rather than tens of mTorr), the critical bias of anode spots shows a linear scaling with $1/P$, where P is the neutral pressure.[5, 70] Because a threshold amount of ionization near the aperture is necessary to sustain the plasma spot, this $1/P$ scaling is expected, since the ionization pathlength decreases with P. With the RF plasma cathode, in the low pressure limit, this appears to be the case. In addition, in the limit of the "no aperture" case, where the anode is basically exposed to the upstream plasma, the $1/P$ scaling holds under all pressures, and this is the most similar configuration to the cited anode spot studies. For the small 4.8 mm aperture at high pressures, however, the scaling appears to saturate at a required bias of around 100 Volts. It may be the case that at these high pressures, the bulk plasma is sufficiently dense so that the limiting factor on current extraction is not the available electron current upstream from the aperture, but rather the amount of current that can be extracted through the smaller aperture by the external anode. That is to say, the condition may be limited by the electric field penetration through the constricted aperture.

7.5.3   Aperture Plasma Size

The dependence of the aperture plasma size on the internal pressure was investigated. The LCIF measurements of the electron density at 80 Volts and 130 mTorr are shown as a function of pressure in Figure 7.20. In general, there is a slight variation in the structure as pressure is increased. From 100 to 130 mTorr, the spot does not change appreciably, with only a slight decrease in the upstream bulk plasma density. As the pressure is increased further, however, the upstream bulk plasma density increases while the spot expands slightly. Presumably the increase in upstream density is due to a slight increase in ionization frequency as the pressure is increased. In this range of pressures, the overall the dependence on pressure is much less pronounced than the dependence on current, voltage, or aperture dimensions. A
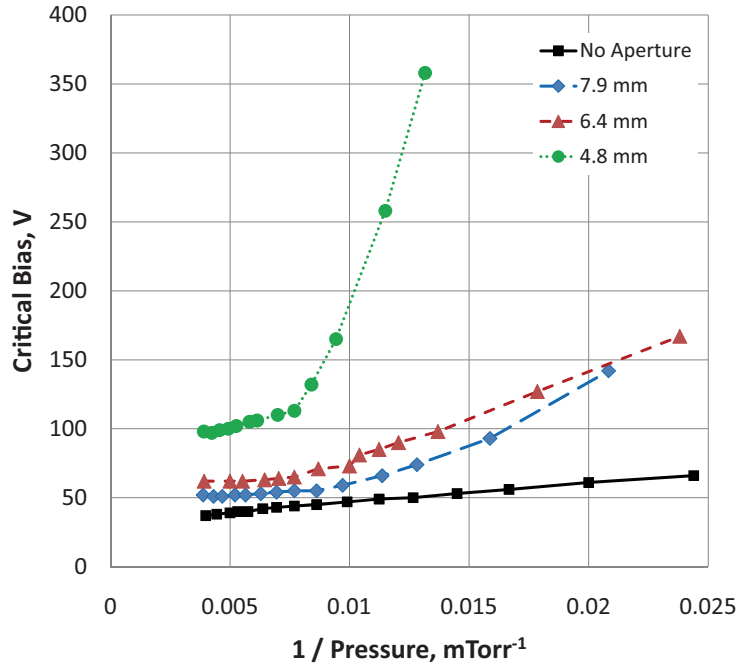
Figure 7.19: Critical bias for aperture plasma initiation, with 6.4 mm aperture.

series of images in Figure 7.21 shows the aperture plasma structure at fixed current, with all three aperture diameters along with the "open" configuration where the anode is exposed to the plasma. In the open configuration, there is a slight increase in plasma density observed during current extraction, but this is clearly much less pronounced than in the presence of the aperture. This is additional evidence in support of the idea that the observed spot requires a constricted aperture to form, most likely by the formation of an electron sheath at the aperture. That is, the structure is not simply a large anode spot at the surface of the external anode, which is then "necked" by the presence of the aperture.

The size and shape of the structure displays a clear dependence on the aperture diameter. The smallest diameter aperture produced the largest aperture plasma spot, almost 2 cm in diameter. To collect a given electron current at the anode, a higher current density is required at the aperture, so the required electric field at the aperture is higher as well. The higher anode bias with the smaller aperture forces

(a) 100 mTorr (b) 130 mTorr (c) 165 mTorr (d) 200 mTorr
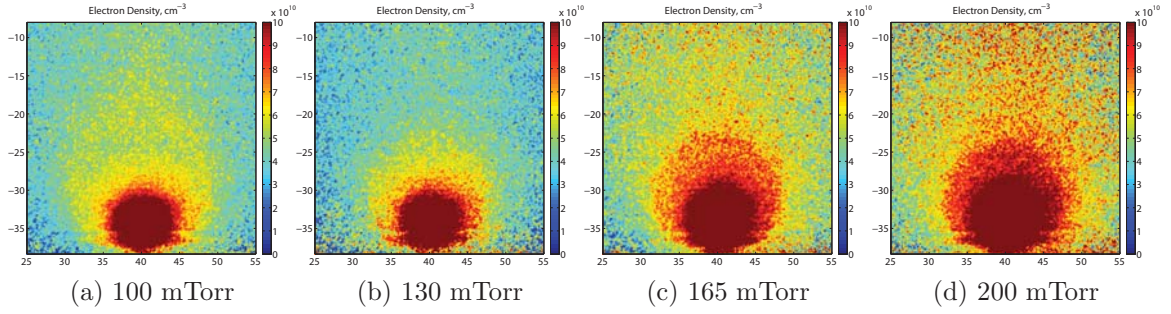
Figure 7.20: Maps of electron density with pressure; 6.4 mm aperture, at 80 V and 130 mTorr. Axis labels denote position, in mm.

(a) 4.8 mm (b) 6.4 mm (c) 7.9 mm (d) Open
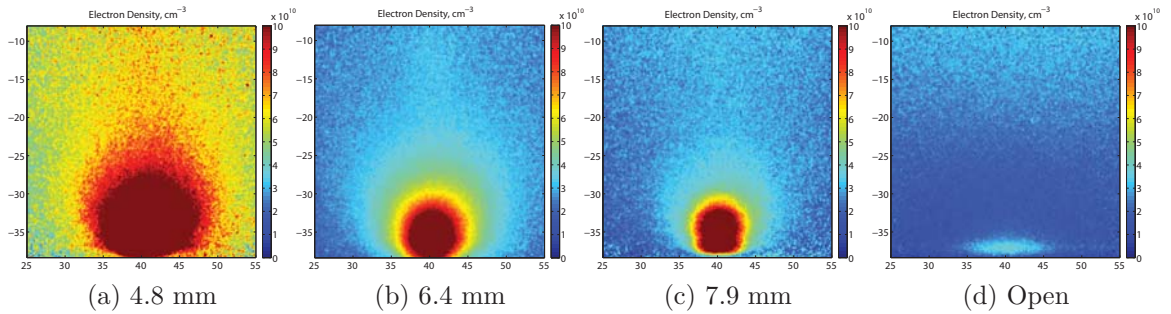
Figure 7.21: Maps of electron density with variable aperture size, at 150 mA and 130 mTorr. Axis labels denote position, in mm.

the aperture plasma structure to expand outward, producing a larger spot. With the large aperture, the smallest structure is seen because of similar reasoning, and the shape is more cylindrical than spherical. Cylindrical anode spots, known as "fire rods" in the literature, have been observed in configurations with large anode surfaces. The formation of a double layer arises from the balance of electron and ion current losses from the bulk plasma. In cases where the electron loss area is sufficiently large, elongated structures will form in order to reduce the loss area for electrons while still maintaining a monotonically decreasing potential across the boundary of the spot.

The electron density profile along the vertical axis was extracted from the images, with the 6.4 mm aperture, at 130 and 200 mTorr. The results are shown in Figures 7.22 and 7.23, respectively. The peak electron density generally varied linearly with extracted current, as expected. In every case, the electron density

191

reached its peak value a few millimeters upstream and decays to the bulk plasma density further from the aperture. This type of density profile has been observed experimentally [23, 37] and computationally [49] in HCAs, and in other plasma cathode devices as well.[15] All of the profiles converge to the same bulk plasma densities at a few centimeters from the aperture, so the aperture plasma structure does not appear to affect the plasma density globally. Particularly at low current levels, there is a slight dip below the bulk plasma density between the "peak" and "bulk" regions, which may be due to rarefaction of the incident electron flux as it traverses the double layer. Additionally, especially at 200 mTorr, there is a pronounced bump or shoulder in the electron density profile at roughly 2 cm upstream of the density peak. This separation is on the order of the charge exchange pathlength between the peak density and the shoulder. Ions born within the aperture plasma will are accelerated toward the bulk by the double layer potential drop, and can accumulate in the shoulder region via charge exchange. This would lead to a buildup of positive space charge in an otherwise quasineutral plasma, which would attract surrounding electrons. The small peak in plasma density here could be a product of the influx of these ions balancing ambipolar diffusion losses.

7.5.4 Double Layer Potential Drop

In order to confirm the presence of a double layer sheath at the aperture plasma boundary, a Langmuir probe was used to determine the plasma potential in the bulk and aperture plasma regions. During data acquisition, the probe I-V traces were sampled every 1.5 Volts. The data were then smoothed using a moving average over five data points, and the plasma potential was determined by finding the knee in the trace using the second derivative of the I-V trace. Measurements were taken at variable current, with two different aperture sizes (4.8 mm and 6.4 mm) and at two pressures (130 mTorr and 200 mTorr). The anode voltage, the plasma potential at

192
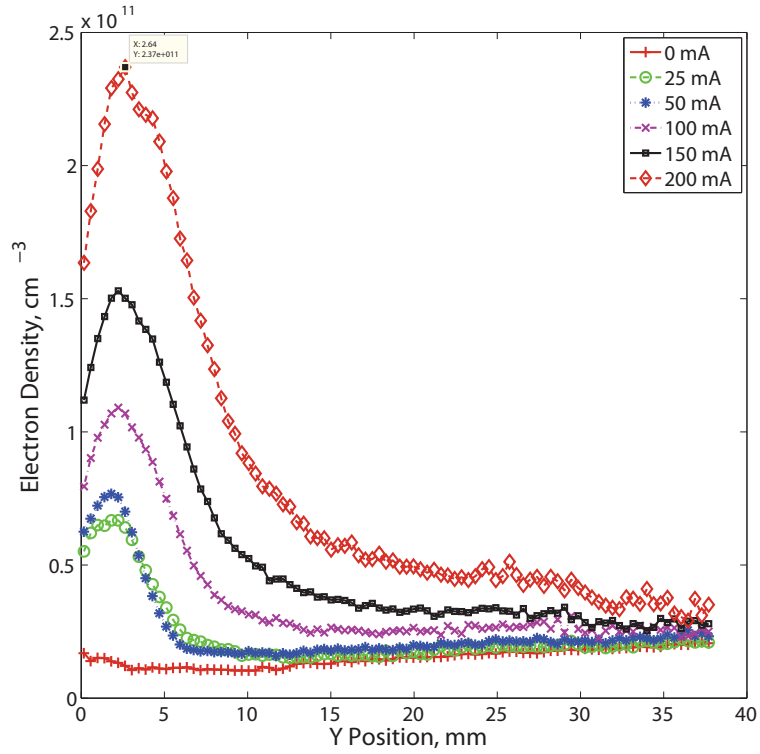
Figure 7.22: Electron density along Y axis, with 6.4 mm aperture, at 130 mTorr. The aperture is located at 0 mm, and $+y$ is upstream.
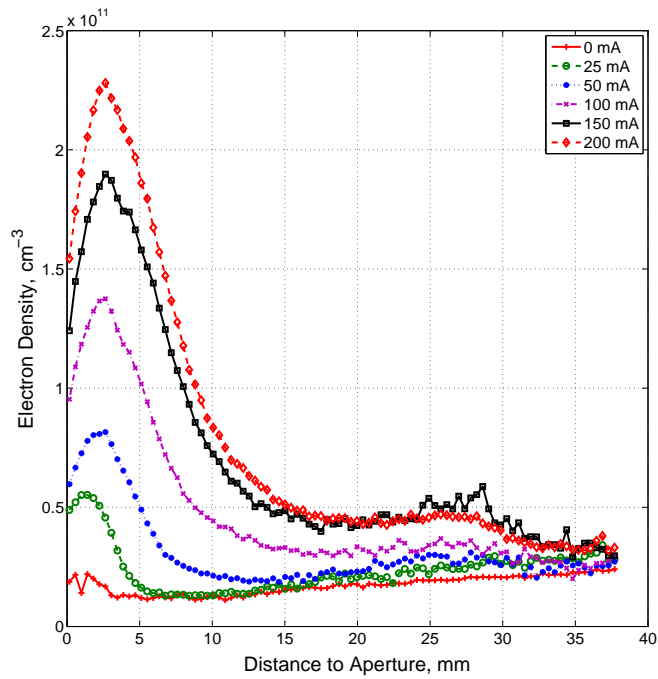
Figure 7.23: Electron density along Y axis, with 6.4 mm aperture, at 200 mTorr. The aperture is located at 0 mm, and $+y$ is upstream.

the aperture and that within the bulk are shown, for the 6.4 mm aperture at 200 mTorr, in Figure 7.24. The same quantities are plotted for the 4.8 mm aperture in Figure 7.25.

In both figures, without any applied bias, the potential in the aperture region is the same as in the bulk plasma as expected. As the anode bias is increased, both the aperture plasma and bulk plasma potentials increase correspondingly. With the larger aperture, the aperture plasma potential follows the anode bias, but is generally 5-15 Volts below the anode bias. With the smaller aperture, the trends are similar, but with a potential difference of 10-20 Volts. However, in both cases, the aperture plasma potential is on the order of 50 Volts or higher, while the bulk plasma potential varies from 20-40 Volts, depending on the conditions. The potential drop between the anode and aperture plasma suggest the presence of a long-range potential drop similar to that seen in the plume of the U-M plasma cathode. The potential difference between the aperture and bulk plasmas, that is, the potential across the double layer, is shown in Figure 7.26. At all conditions, the double layer potential drop is at or above the ionization potential of helium at 24.5 eV. This is a minimum requirement for anode spot formation, as shown in the literature.[5, 52, 12] At 200 mTorr, this condition is just barely satisfied, while at lower pressures, the potential drop increases to 35 Volts or more. At these lower pressures and with the smaller aperture, an increase in the double layer potential increases the electron loss area, in order to extract a sufficient amount of current. The "locking" of the aperture plasma potential to the anode bias is expected as a consequence of nonambipolar flow in anode spots.[4] Additionally, the locking of the bulk plasma potential is predicted from earlier plasma cathode theories as a result of a global balance of electron and ion losses.[54]
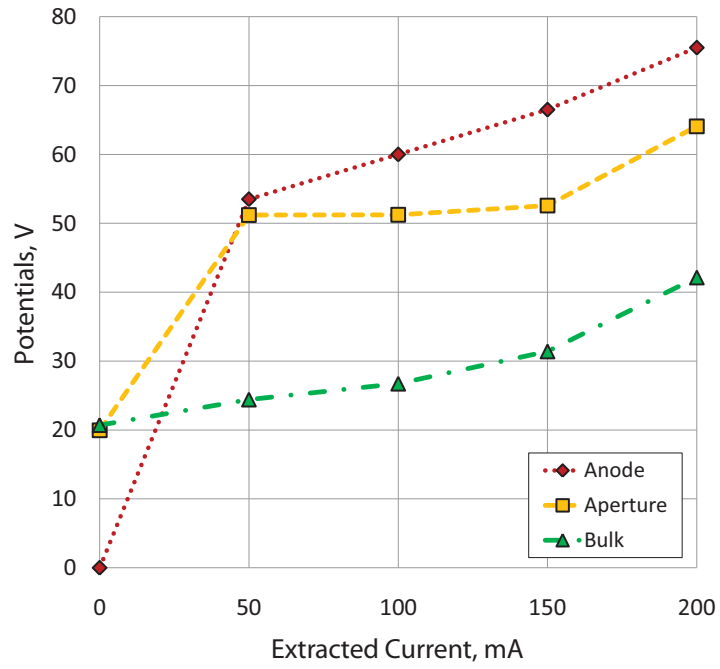
Figure 7.24: Anode bias, aperture plasma potential, and bulk plasma potential at 200 mTorr, with 6.4 mm aperture.
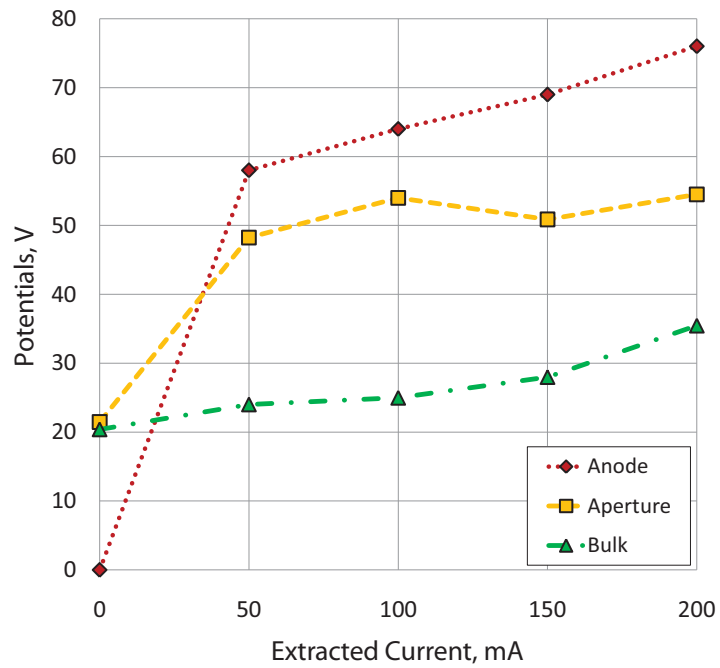
Figure 7.25: Anode bias, aperture plasma potential, and bulk plasma potential at 200 mTorr, with 4.8 mm aperture.
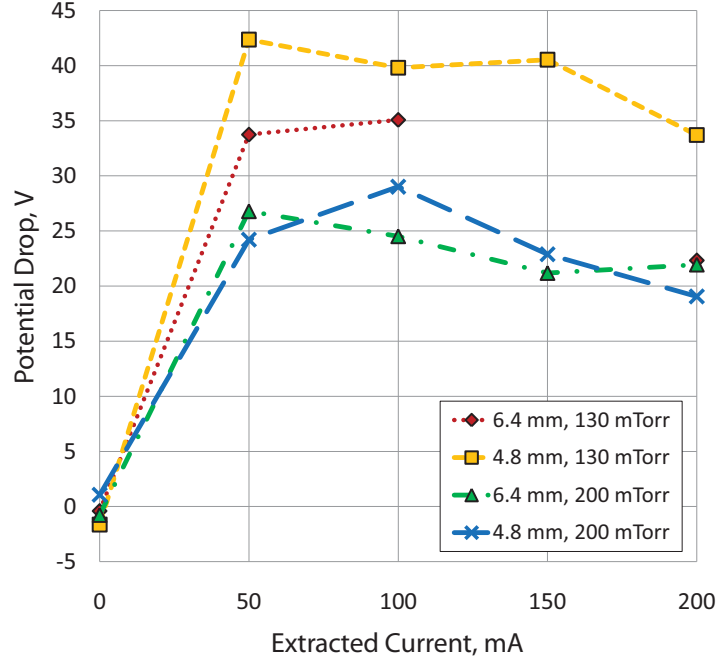
Figure 7.26: Difference in plasma potential between the bulk and aperture plasmas.

7.5.5 Extracted Current vs. Available Current From Bulk

To check the theory of the expanding electron loss area established by the aperture plasma, the images were analyzed to calculate the expected Maxwellian electron flux from the bulk plasma. This was then compared to the measured current to determine whether ionization within the spot itself contributes to the extracted current. The electron saturation current, J_{sat}, is given by,

$$J_{\mathrm{sat}} = \frac{e n_e}{4} \sqrt{\frac{8 k_B T_e}{\pi m}} \qquad (7.5)$$

where e is the elementary charge. The aperture plasma boundary was assumed to be an ellipsoid, with axes equal to the full width at half-maximum (FWHM) relative to the peak density in the aperture plasma structure, in the horizontal and vertical directions. An electron temperature of 3 eV was assumed (roughly the bulk plasma electron temperature), and the value of J_{sat} was calculated at every pixel along the boundary. The current density was then integrated on the part of the ellipsoid

196

boundary above the aperture disc, A, according to,

$$I_{\text{bulk}} = \iint\limits_A \mathbf{J}_{\text{sat}} \bullet \mathbf{dA} \tag{7.6}$$

where I_{bulk} is the total current from the bulk and $\mathbf{A}$ is the area of the collecting surface. The calculated bulk current was plotted against the measured current, as shown in Figure 7.27. The calculated current from Equations (7.5) and (7.6) was consistently several times higher than the extracted current. The measured and calculated values of current do have a strong linear correlation, however, and the ratio of calculated to measured current gets closer to unity as the aperture size is increased. Some of the disagreement between the two values can likely be attributed to the uncertainty in the LCIF measurement, which relies on a myriad of cross-sections known to within a factor of two. Another possible contributing factor to this discrepancy is the difference in elastic scattering and ionization pathlengths in helium. If a scattering cross-section of 5×10^{-15} cm^{-3} is assumed, then the elastic scattering mean free path is 0.05 cm at 130 mTorr. By contrast, if an incident electron energy of 35 eV is assumed (from the potential drop in Figure 7.26), then the helium total ionization cross-section is 1.29×10^{-17} cm^2 and the ionization pathlength is 38 cm.[43] Because the elastic scattering cross-section is much smaller than the aperture plasma dimensions, it is feasible that many electrons traversing the double layer are not actually lost through the aperture. Instead, many can be elastically scattered back into the bulk plasma without passing through the aperture or losing energy through an inelastic event. The available electron current at the aperture plasma boundary may not be completely utilized. The exceptions would be electrons that are born within the aperture plasma, or those that are scattered through the aperture. The electrons produced via ionization in the aperture plasma can only be lost if they are counterbalanced by ion current lost to the bulk plasma. Because the ion flux to the
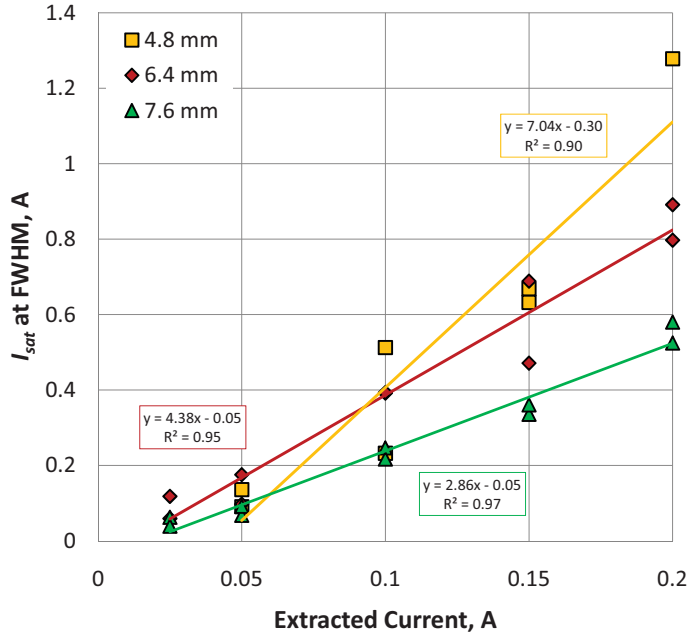
Figure 7.27: Electron saturation current at aperture plasma boundary versus extracted current, at 130 mTorr.

bulk plasma is less than the electron flux at the aperture by a factor of $\sqrt{2\pi m/M_i}$, the contribution of ionization to the extracted current is only a few percent of the total extracted current.

One important thing to note is that the bulk plasma itself is not high enough density to provide the measured currents shown in Figure 7.17. If one were to assume that the extractable current is just the electron saturation current through the aperture, then using the typical bulk plasma density of 2×10^{10} cm^{-3}, a bulk temperature of 3 eV, and Equation 7.5, then this current density is 90 mA/cm^2. For the 6.4 mm aperture, this translates to 30 mA, nearly a factor of 10 below the 260 mA of measured current at 130 mTorr. For the 4.8 mm aperture, the corresponding value is 16 mA, while up to 200 mA of current was extracted in that case. The data in this LCIF study of the aperture region clearly demonstrate that it is the aperture plasma structure, influenced by the aperture size, applied bias, and internal pressure, which regulates the extractable current from the plasma through the expansion of the

spot boundary.

7.6 Uniform Plasma Model

A computational model of the helium aperture plasma structure was developed for comparison with the LCIF experimental results. The model assumes a uniform density within the aperture plasma structure and a Maxwellian EEDF. Given these assumptions, the global electropositive plasma model can be used to calculate the plasma density and electron temperature in the structure as a function of neutral gas pressure, absorbed power, and effective boundary area of the structure.[45] The electron temperature is calculated from a global particle balance:

$$n_0 u_B A_{\text{eff}} = K_{iz} n_g n_0 V, \tag{7.7}$$

where n_0 is the plasma density, $u_B = (k_B T_e / M_i)^{0.5}$ is the Bohm speed, A_{eff} is the effective ion loss area, K_{iz} is the ionization rate coefficient, n_g is the neutral gas density, and V is the volume of the structure. The left hand side of equation 7.7 is the loss rate of ions from the structure through the boundary, and the right hand side is the ionization rate within the structure. Assuming a spherical boundary with radius R, the effective loss area is $A_{\text{eff}} = 4\pi R^2$ while the effective volume is $V = 4\pi R^3/3$. Equation 7.7 is independent of plasma density and absorbed power, and can be arranged with one side purely dependent on electron temperature:

$$\frac{K_{iz}(T_e)}{u_B(T_e)} = \frac{3}{n_g R} \tag{7.8}$$

Equation 7.8 can be solved numerically to determine the electron temperature as a function of n_g and R. The plasma density is determined from a global power balance:

$$P_{in} = e n_0 u_B A_{\text{eff}} E_T, \tag{7.9}$$

199

where P_{in} is the absorbed power in the system and E_T is the total energy loss per electron-ion pair created in the system. Thus, the absorbed power is balanced by the energy loss for each electron-ion pair leaving the system. The value of E_T is calculated from,

$$E_T = E_e + E_i + E_c, \tag{7.10}$$

$E_e = 2k_B T_e$ is the electron kinetic energy loss to the boundary, $E_i = 0.5k_B T_e + V_s$ is the ion energy lost at the boundary via presheath acceleration and the sheath potential drop V_s, and E_c is the total energy lost through collisional processes. E_c is found from,

$$E_c = \frac{K_{iz}E_{iz} + K_{ex}E_{ex} + K_{el}\frac{3m}{M}k_B T_e}{K_{iz}} \tag{7.11}$$

where E_{iz} is the ionization energy, K_{ex} is the excitation rate constant, E_{ex} is the excitation energy, and K_{el} is the elastic scattering rate constant. K_{el} has constant value of $\sim 10^{-7}$ cm^3/s, independent of electron temperature.[45] For helium, E_{iz} and E_{ex} have values of 24.49 eV and 21.22 eV, respectively. K_{iz} and K_{ex} are functions of electron temperature, which are determined by integrating the ionization and total excitation cross sections over the Maxwellian distribution for a given temperature. The electron-impact ionization and excitation cross-section data used here can be found in References [43] and [67], respectively. The excitation rate constant was estimated by adding the individual rate constants for 1s→2p, 1s→3p, and 1s→4p transitions. The sheath potential drop across the aperture plasma boundary V_s is assumed to be equal to the ionization energy E_{iz}, as supported by the plasma potential measurements in the aperture and bulk plasmas. The absorbed power P_{in} is dominated by Ohmic power deposition, so $P_{in} \approx IE_{iz}$, where I is the extracted current through the aperture.

The particle balance was used to calculate the electron temperature over a helium pressure range of 100 mTorr to 200 mTorr, and effective radii of 0.4 to 2 cm. The electron temperature at each condition was then used to calculate u_B and E_T, and the plasma density was calculated using Equation 7.12:

$$n_0 = \frac{P_{in}}{eu_B 4\pi R^2 E_T}. \qquad (7.12)$$

The resulting electron temperatures are shown in Figure 7.28. The model predicts that the electron temperature should increase as both the pressure and radius decrease. Qualitatively, these trends agree with the peak temperatures observed in the "halo" region of the electron temperature images measured with LCIF. The images in Figure 7.15 showed the aperture plasma structure with an approximate radius of 5 mm in the 25 mA case, increasing to 10 mm in the 150 mA case. The temperature is expected to be independent of the deposited power, and therefore independent of the extracted current for a given pressure and radius. The decrease in peak temperature observed as the current is increased from 25 to 150 mA is likely due to the expanding aperture plasma boundary, in agreement with the model. Quantitatively, the electron temperatures predicted by the model are large – up to 14 eV in the 200 mTorr case, and 23 eV in the 100 mTorr case. While peak effective temperatures of at least 10 eV were observed in the LCIF measurements, the model predicts even higher temperatures which are likely unphysical. In practice, the aperture plasma structure is surrounded by a double layer sheath of 20 to 30 Volts, which accelerates electrons inward toward the aperture. The potential drop should shift the EEDF in the aperture plasma to a more "beam-like" distribution, accelerating more electrons to energies above the ionization potential. To support a plasma structure radius on the order of 1 cm, high temperatures are required to support the necessary volume ionization rate if a Maxwellian distribution is assumed. Because of this assumption, unusually high temperatures are calculated in place of the incident electron "beam" from the bulk
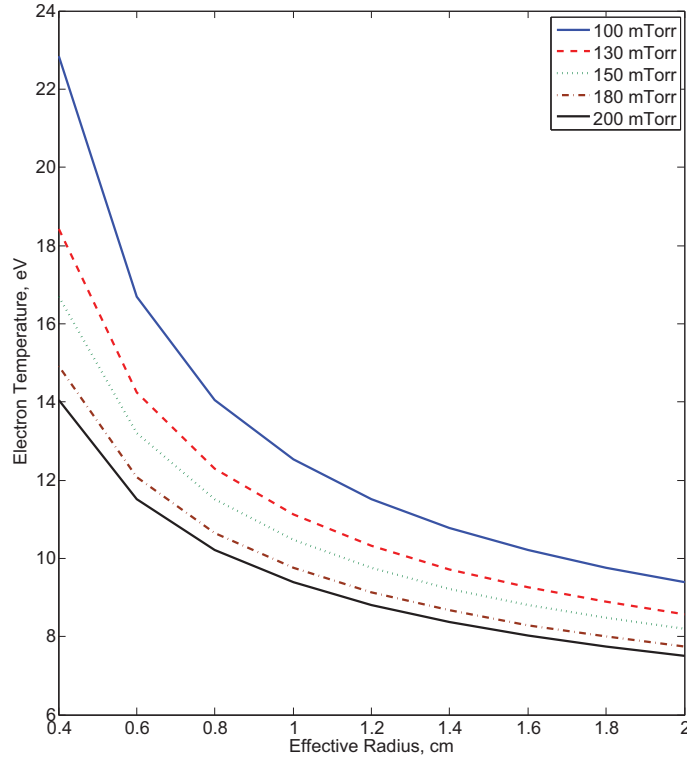
Figure 7.28: Electron temperatures, calculated from the uniform helium plasma model, as a function of pressure and effective radius.

plasma.

The plasma densities calculated from the model are shown in Figure 7.29, for the case of 200 mA of extracted current. Here, the qualitative trends agree with the LCIF images, with respect to the dependence of density on pressure. The density maps showed that the peak density increased as the neutral pressure was increased from 130 to 200 mTorr. At a given current level, the density is predicted to decrease as the aperture plasma boundary expands. However, in the LCIF measurements, the larger plasma structures correspond to the highest peak densities. This is because the the boundary radius of the aperture plasma is coupled to the absorbed power; as the current is increased, the radius increases as well, and the contribution from the increased power dominates over the increase in radius. The assumption of a spatially
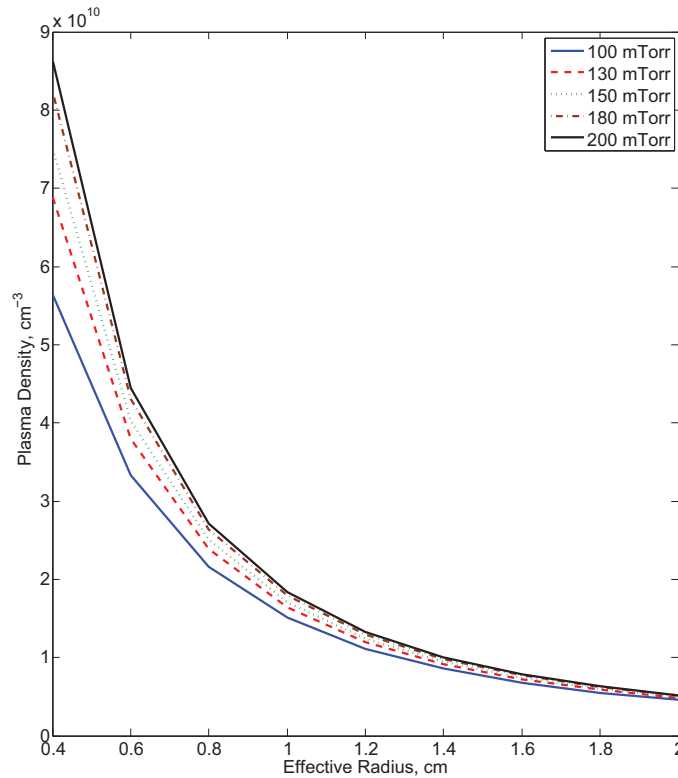
Figure 7.29: Plasma density, calculated from the uniform helium plasma model, as a function of pressure and effective radius at 200 mA.

uniform aperture plasma does not hold in practice, and the model could be extended to account for the peaked nature of the density profile. Nonetheless, the trends in density support the trends in the LCIF measurements, and the calculated densities are within a factor of 2 to 3 of the measured peak densities at similar conditions.

7.7 Summary of LCIF Results

A bright plasma structure was observed on the upstream end of plasma cathode apertures, in both an ECR and an RF plasma cathode setup. LCIF diagnostics were used to generate two-dimensional maps of electron density and temperature in this region, at various pressures and extracted current levels, as well as with different aperture sizes. The results were insightful, in that the structure appears to have a

high density core, surrounded by a region of hot electrons. This suggests the presence of a double layer sheath between the aperture plasma and bulk plasma, similar to those seen in anode spots. The double layer functions as a loss area for electrons, which expands away from the aperture as needed to drain electrons from the bulk plasma. The current-voltage characteristic displayed hysteresis, in that the structure could be sustained at a lower voltage than that initially required to form the structure. The critical voltage was measured at various pressures and aperture sizes; in most cases, the critical voltage scaled with $1/P$, although with the smallest aperture, this dependence disappeared at the high pressure limit. The size and shape of the structure depends strongly on the aperture size for a given current, with smaller apertures creating larger, spherical structures and larger apertures creating smaller, elongated structures. Both the peak electron density and the available electron current at the aperture/bulk plasma boundary scale linearly with the measured extracted current. Plasma potential locking was observed between the anode bias, aperture plasma, and bulk plasma potentials, with significant potential drops between all three. All of these trends are consistent with anode spot behavior near positively biased electrodes, though in this case, the aperture itself appears to act as the virtual electron loss area.

The aperture plasma structures that were observed in this experiment *could be universal features of plasma cathode sources.* Because of the need for a large internal ion collecting surface area, plasma cathodes generally are not optically accessible, so these features have not previously been observed. At most, there has been evidence of high density plasmas at the aperture from Langmuir probe measurements, [23, 15] and evidence of an electron sheath at the aperture via emissive probe measurements.[47] However, it has not yet been suggested that these two features are related to one another. From an engineering standpoint, understanding the aperture plasma has important consequences. In EP applications, there can be strict requirements on the power supply or amount of feed gas for a given mission. This study suggests that

by carefully designing the extraction aperture (and maybe the extraction electrode design), one can tailor the cathode performance to meet these requirements. In particular, smaller apertures may allow for lower gas flow rates, but require a higher voltage to sustain comparable extracted current values. Additional studies on aperture plasma structures may prove useful in clarifying these tradeoffs, so that the structures can be accounted for in plasma cathode models.

CHAPTER VIII

Conclusions and Future Work

8.1 Conclusions

The work presented in this dissertation was centered around two major goals. The first goal was to test the hypothesis that a 2.45 GHz waveguide-style ECR plasma cathode, using permanent magnets and based on a hollow cathode geometry, could deliver sufficient electron current for low to medium power applications in electric propulsion, particularly beam neutralization (0.5 to 5 A range). Long life inherent in electrodeless plasma production approaches, along with high ionization and gas utilization efficiency comprise the second criteria of the first goal. The second goal of this work was to study the proof-of-concept device to develop an understanding of the underlying physics. The internal "source" plasma properties were studied as a function of operating condition, as were the properties of the luminous, external extraction plume generated during operation. The electron extraction mechanism was investigated using a novel optical diagnostic, laser collision-induced fluorescence, giving two-dimensional images of electron density and temperature near a plasma cathode aperture. The LCIF experiments demonstrated the existence of an aperture plasma structure that determines the effective loss area for extracted electrons. This structure may be a common feature of plasma cathodes, and should perhaps be included in future models of these devices.

During the development phase, the waveguide plasma cathode design was tested in two iterations. The first was based on a large area ECR source previously tested at U-M, ([35]) but situated in a hollow geometry to allow for a larger ion collection surface at the interior walls of the device. This "ridged" waveguide plasma cathode used permanent magnets situated near the centerline of the device to establish the ECR heating zone. The device had two sharp field-enhancing ridges to maximize the overlap of the microwave electric field at the ECR zone. The maximum extracted current from this design was 131 mA, far too low for high power electric propulsion systems. It was determined that the strong radial magnetic fields in the device suppressed electron extraction and provided insufficient plasma confinement, leading to an unstable discharge. However, the results of these tests suggested that a waveguide plasma cathode based on a symmetric, axial magnetic field with the ECR heating zone established near the microwave window may provide better performance.

These findings eventually led to the development of the cylindrical waveguide plasma cathode design. This device used a ring of 24 axially oriented permanent magnets to establish an ECR heating zone near the microwave window. As in the ridged waveguide device, the magnetic circuit was designed so that the ECR zone occurs on centerline, where the microwave electric field is strongest. However, in the cylindrical design the electrons generated in the high density ECR discharge can freely diffuse along magnetic field lines to the exit plane of the source, while ions are collected at a large internal wall area to maintain current continuity during electron extraction.

The cylindrical plasma cathode was benchmarked in a variety of configurations. Without any endplate on the device, electron currents on the order of 500 mA were achieved, but the deliverable current continued to increase monotonically with the gas flow rate through the device. To increase the internal pressure at moderate flow rates and decouple the source plasma potential from the anode bias, an endplate with an

aperture was mounted on the exit plane of the device. The plasma cathode performed best with a 4 mm diameter aperture, delivering up to 4.2 Amperes of current on argon and xenon, exceeding the required neutralizer current for several flight-qualified thrusters. Electron production costs as low as 89 W/A and gas utilization factors up to 35.2 were achieved on xenon, which compares favorably to other plasma cathodes in the literature.

The trends in extracted electron current provided some useful insights. The current was found to follow the Child-Langmuir scaling at some conditions, suggesting a high voltage sheath at the extraction aperture. At higher extraction voltages, however, the current deviated from this scaling and became independent of the bias, suggesting that the extractable current was likely limited by the available ion current collected at the internal wall area. Langmuir probe measurements downstream of the device indicated that electron continuity was satisfied in the plume without significant external ionization. The observed trends in extractable current also raised some interesting questions regarding the underlying physics. At a given microwave power level and anode bias, as the gas flow rate was increased, the extracted current would tend to peak and then drop off at higher flow rates. The flow rate corresponding to this peak current decreased with increasing applied bias. Also, while operating on argon, the extractable current depended on the background pressure in the anode-cathode gap, but only up to a certain "critical" pressure - at chamber pressures less than 5×10^{-5} Torr, the argon plume could not be established. On xenon and krypton, the pressure due to gas flow through the source was sufficient to support the plume. Finally, Langmuir probe measurements taken in the extraction aperture showed a factor of 100 increase in the plasma density (relative to the unbiased case) when a +80 V bias was applied to the extraction anode. This contradicted some models of plasma cathode operation, wherein the internal plasma density is assumed to remain independent of the extraction bias.

To clarify some of these trends, Langmuir probe measurements were taken along the centerline of the plasma cathode and in the external plume. The plasma density in the plume could be divided into regions, one near the aperture and one near the extraction anode. The plasma density in the region near the aperture dropped off rapidly with axial downstream distance, as the extracted beam expanded outward from the aperture. In the region near the anode, the plasma density was more uniform. Plasma potential profiles in the plume showed the existence of a weak electric field along the plume, similar to that in a positive column of a glow discharge, which facilitates electron current transport across the gap. The nearly flat potential profile shows that the plume is nearly quasineutral, so a minimum amount of ionization is needed in the gap to establish the plume. However, electrons that are liberated from ionization collisions in the plume should not significantly amplify the collected current directly. Only a few percent of electrons leaving the plasma cathode undergo these collisions and collected current from external ionization is limited by ion transport to the plasma cathode walls. The critical background pressure to establish the argon plume was due to the minimum amount of ionization in the gap to prevent the buildup of space charge in the gap.

Probe measurements inside the source were carried out at variable flow rate and microwave power, with no current being extracted. Overdense plasmas ($> 7.4 \times 10^{10}$ cm^{-3}) were observed with all three gases. The peak plasma density occurred just downstream of the peak magnetic field on centerline, and decayed by nearly an order of magnitude between the peak density and that at the extraction aperture. A second downstream peak in the plasma density occurred at the null in the magnetic field. This peak is attributed to electron confinement via the mirror effect. The second peak was observed to be more pronounced at lower internal pressures. The electron temperature in the device was highest near the microwave window, where hot electrons are trapped between the quartz window and an increasing magnetic field.

In the region downstream of the primary heating zone, the temperature decreased linearly along the axis. Such decreases are due to cooling associated with collisions in the absence of additional, compensating heating. In the far downstream region, the electron temperature was generally uniform. The plasma potential profiles in the source were also influenced by the magnetic field profile. In regions of expanding magnetic field, the potential decreased along with the magnetic field strength.

The probe data provided insight into the relationship between plasma properties and the extracted current. In all cases, the plasma density within the source increased monotonically with both power and flow rate, suggesting that limitations on electron current are not due to limitations on the density achieved by the ECR source. The plasma density and electric field in the downstream plume were used to estimate electron current densities to the anode; these rough calculations predicted a beam size on the order of half of a centimeter, which is consistent with observations as an order of magnitude estimate.

The increase in plasma density in the aperture with an applied bias was unexpected from basic plasma cathode models. To study this effect in more detail, LCIF diagnostics were used to generate images of plasma density and electron temperature on the upstream side of the aperture in ECR and RF plasma cathodes, on helium feed gas. When the external plume was established and electron current was extracted, a bright plasma structure with sharp boundaries was observed at the aperture. The LCIF measurements indicated that this structure had a core density an order of magnitude higher than that seen in the bulk "source" plasma, and was surrounded by a high energy electron layer. This suggested the existence of a double layer sheath between the aperture plasma structure and the source plasma.

The behavior of the aperture plasma with respect to the I-V characteristic and the critical bias for spot formation was consistent with that seen in low-pressure anode spots. The aperture plasma expanded outward as more current was collected (via

increasing voltage) to establish a larger loss area for electrons from the bulk plasma. The critical bias to initiate the spot scaled with the inverse of pressure, suggesting that as in anode spots, a minimum ion density is required (through ionization in the electron sheath) to initiate the spot. As the aperture size was decreased, it was found that the size of the aperture plasma increased for a given extracted current, which may be a result of the higher voltage requirements to sustain the spot with smaller apertures. Langmuir probe measurements verified a potential drop between the bulk plasma and the aperture plasma structure, which was at least as large as the ionization potential for helium; this was expected from the literature on anode spots. The available electron current (from the bulk plasma) was calculated at the aperture plasma boundary, and it was found to scale linearly with total extracted current. This study showed that the extractable current from a plasma cathode is determined by the size of the electron loss area, which in turn depends on the internal pressure, applied bias, and aperture size.

In anode spots, as electrons are accelerated to the anode, they cause some trace ionization. The newly born ions are less mobile than the liberated electrons, which are quickly lost to the extraction anode. This results in a buildup of positive space charge until the point where the plasma locally satisfies quasineutrality. During electron extraction, the ions in this plasma must be lost through a boundary with the "source" plasma, across a sheath near the aperture. Because the plasma is quasineutral, a spot forms to establish a long-range presheath and accelerate ions to the Bohm speed before reaching the double layer. In the case of the plasma cathode, it appears that the aperture acts as the functional electron loss area, with trace ionization near the aperture driving the spot formation on the upstream side of the aperture. In order to develop and optimize a prototype plasma cathode design, it would be prudent optimize the aperture plasma structure by maximizing the plasma density and the size of the plasma boundary, while minimizing the power consumed by beam extraction

and generation of the internal source discharge.

8.2 Future Work

The results of the experiments in this thesis present several avenues for continued work, ranging from engineering-oriented problems to more fundamental plasma physics questions. Some of these possibilities are suggested as follows:

- Optimize Magnetic Confinement:

  The internal plasma density profiles suggest that the addition of downstream magnets in the plasma cathode could increase electron confinement, and correspondingly increase the uniformity of the plasma in the source. This would increase the fraction of the peak density that is available at the extraction aperture.

- Optimize Source with a Keeper/Triode Electrode Configuration:

  The dominant power loss mechanism in the plasma cathode is that which goes into extraction of the electron beam. By optimizing the geometry of the extraction anode, or possibly with the addition of a third "keeper" electrode, the required voltage for electron extraction may be decreased.

- Optimization of Microwave Launching Mechanism:

  One limitation of the waveguide plasma cathode is the possibility of sputter coating the microwave window via ion bombardment of the plasma cathode walls. By developing a more novel microwave circuit (possibly including bends, twists, custom transitions, etc.) it may be possible to shield the window from coating.

- Study Scalability of Device with Frequency:

  By increasing the microwave frequency, it is possible to develop a similar

device using smaller waveguide. Higher frequencies have the additional benefit of generating higher plasma densities. However, they also require stronger magnetic fields to establish the ECR condition, which may hinder electron extraction. Finding an optimal condition in this tradeoff would be useful when building a prototype.

- Emissive Probe Measurements in Aperture Plasma:

  The plasma potential measurements taken in the aperture plasma setup consisted of two representative points: one in the bulk and one at the aperture. By recording spatial profiles of plasma potential near the aperture plasma and in the plume using a small emissive probe, one would gain insight into whether there is just one potential drop at the aperture plasma double layer, or a second at the aperture itself.

- Radial Mapping of Internal and Plume Plasma Profiles:

  Additional mapping of the plasma properties inside the source and in the plume would provide insight into how much the plasma expands in each region, and allow for more accurate estimates of the expected current from each operating condition.

- Internal Probe Maps During Current Extraction:

  Internal probe maps taken while electron current is extracted would show what effect, if any, electron extraction has on the plasma properties in the ECR zone.

- Optical Emission Spectroscopy of Internal and External Plasma:

  Optical measurements of the plasma in both regions would give some hints into the contribution of processes like double ionization to the extracted current.

- Study of Aperture Plasma Structure in Higher Current Plasma Cathodes:

  A more optically accessible high current (Amperes instead of mA) plasma

cathode prototype should be developed and run on argon or xenon, to verify that the aperture plasma structure does indeed occur under various conditions. Optical emission can be used to roughly estimate the aperture plasma boundary and correlate the properties of the spot to the performance at high current conditions. This may be achieved with the development of an advanced LCIF model for argon plasmas.
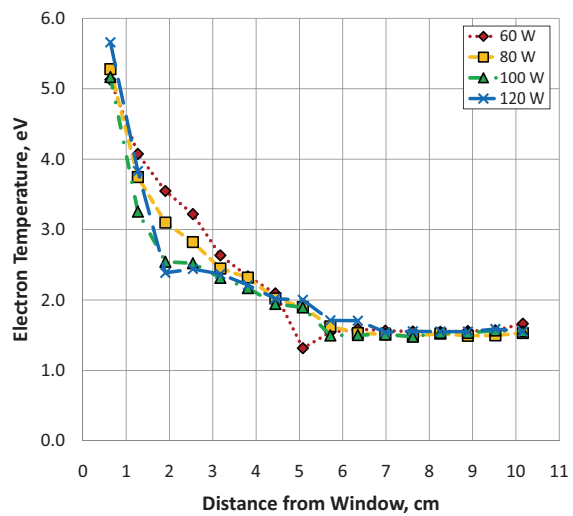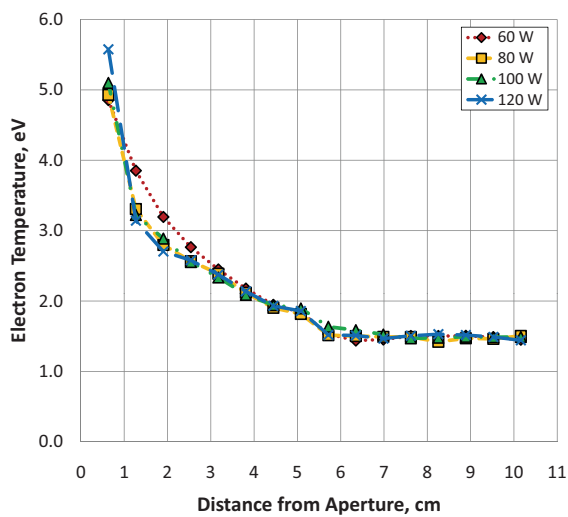
APPENDICES

APPENDIX A

Additional Langmuir Probe Data - Ar and Kr
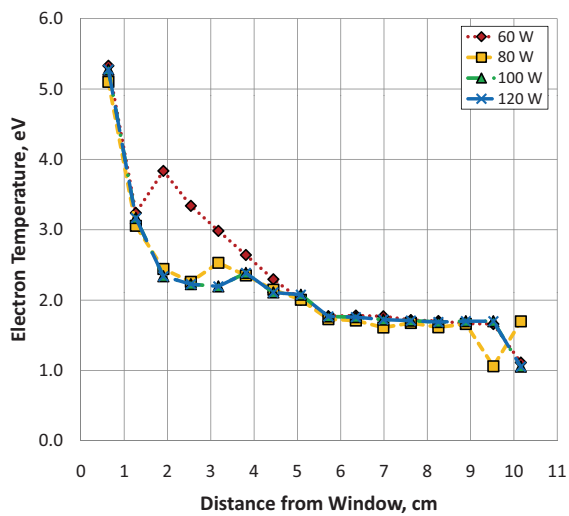
(a) 4 sccm Effective.

(b) 6 sccm Effective.

(c) 8 sccm Effective.

Figure A.1: Electron temperature along plasma cathode centerline, on krypton. Aperture located at 10 cm.

217

(a) 4 sccm Effective.
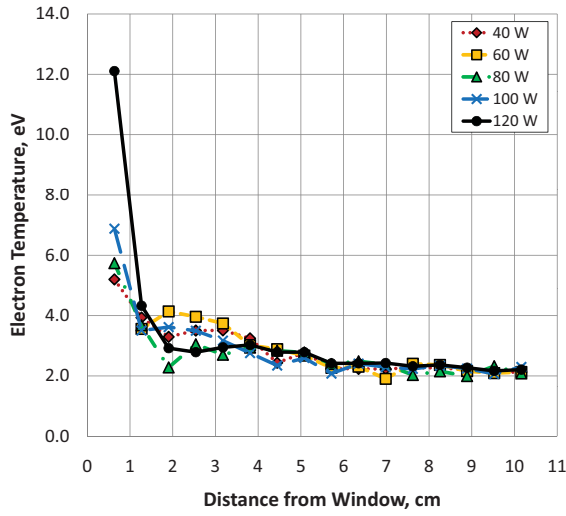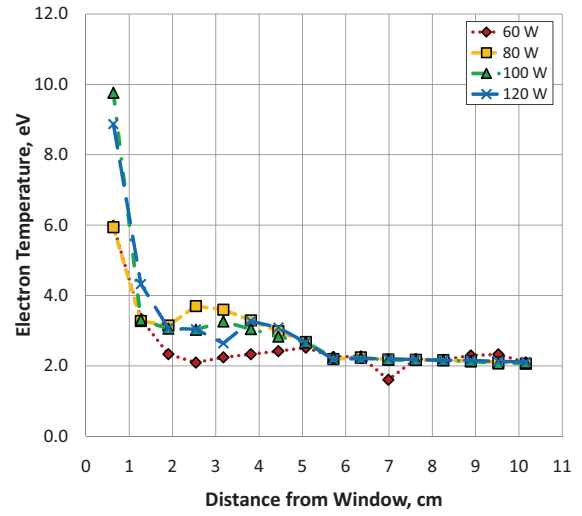

(b) 6 sccm Effective.

(c) 8 sccm Effective.

Figure A.2: Electron temperature along plasma cathode centerline, on argon. Aperture located at 10 cm.

(a) 4 sccm Effective.
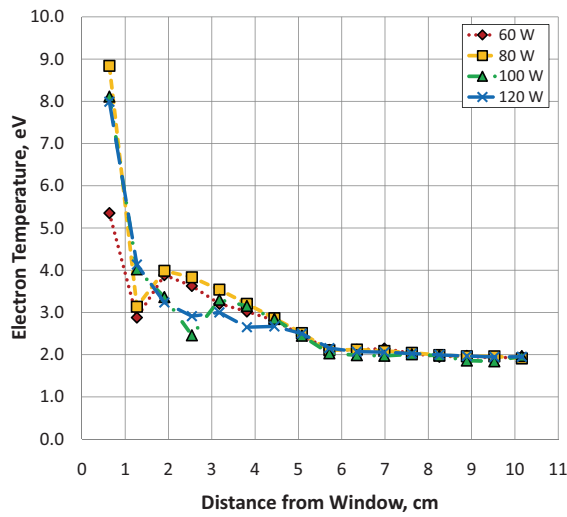

(b) 6 sccm Effective.

(c) 8 sccm Effective.

Figure A.3: Plasma potential along plasma cathode centerline, on krypton. Aperture located at 10 cm.
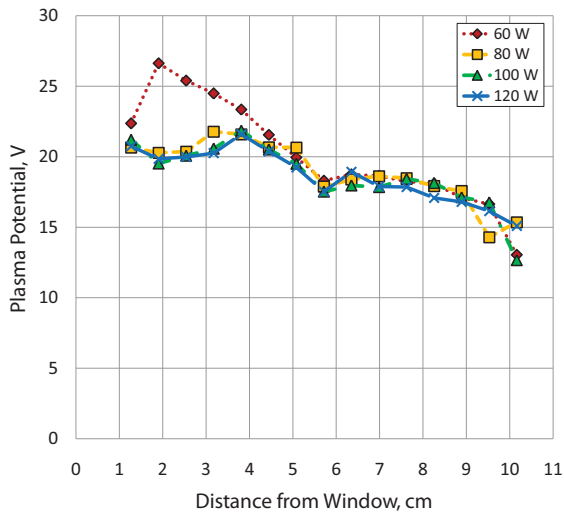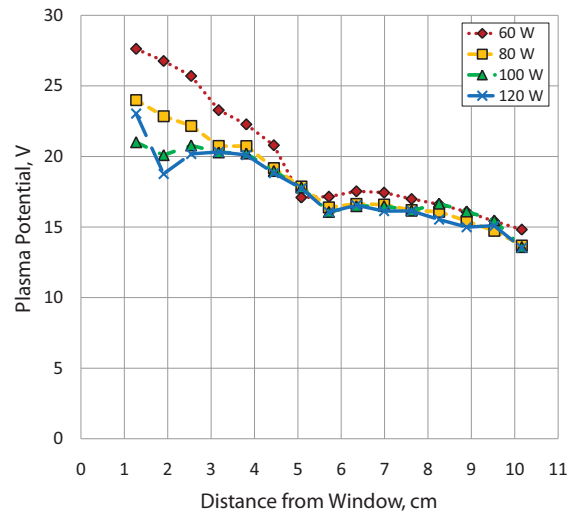
(a) 4 sccm Effective.
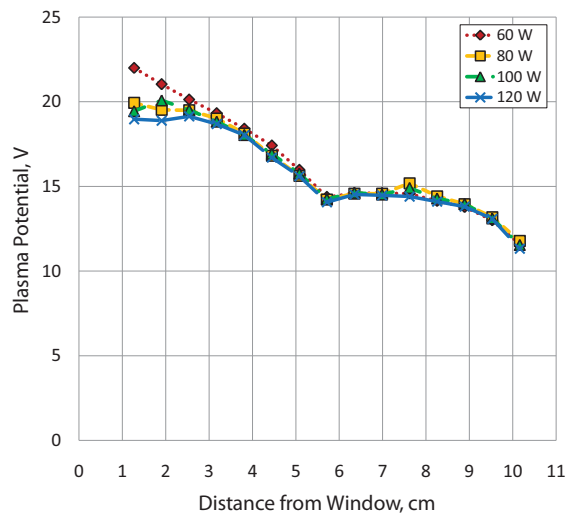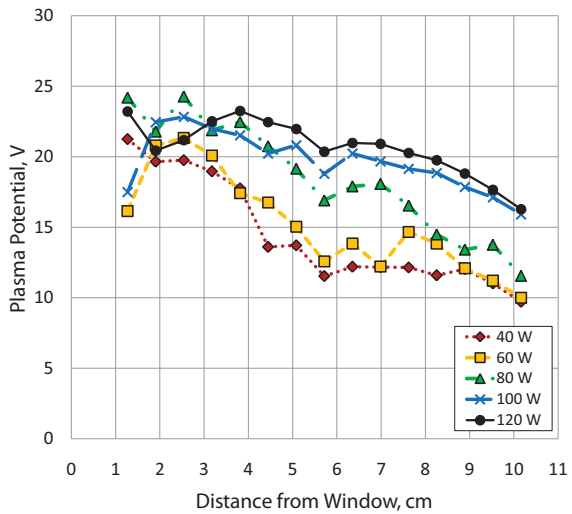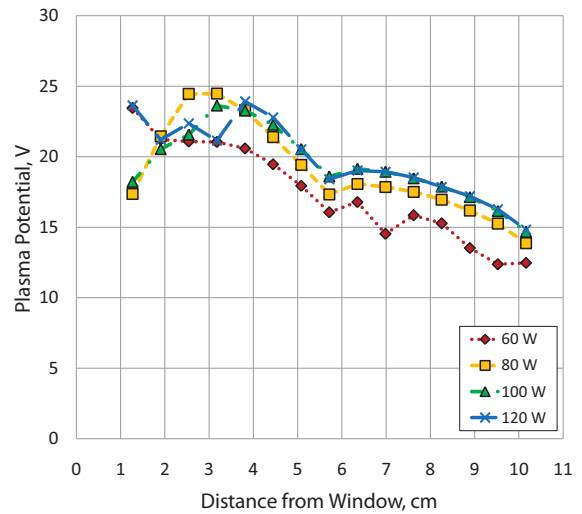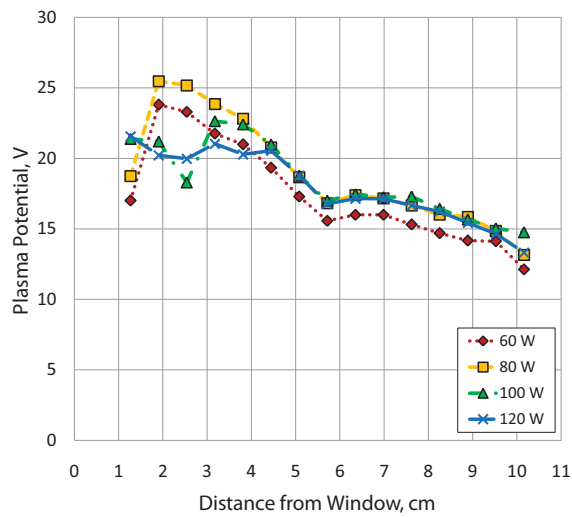

(b) 6 sccm Effective.

(c) 8 sccm Effective.

Figure A.4: Plasma potential along plasma cathode centerline, on argon. Aperture located at 10 cm.

BIBLIOGRAPHY

BIBLIOGRAPHY

[1] W. P. Allis, S. J. Buchsbaum, and A. Bers. *Waves in Anisotropic Plasmas*. MIT Press, Cambridge, MA, 1963.

[2] B. A. Arkhipov and K. N. Kozubsky. The development of the cathode-compensators for Stationary Plasma Thrusters (SPT) in USSR. In *Proc. 22nd International Electric Propulsion Conference*, Viareggio, Italy, October 1991. IEPC Paper 1991-023.

[3] J. Asmussen. Electron cyclotron resonance microwave discharges for etching and thin film deposition. In S. M. Rossnagel, J. J. Cuomo, and W. D. Westwood, editors, *Handbook of Plasma Processing Technology*. Noyes Publishing, New Jersey, 1990.

[4] S. D. Baalrud, N. Hershkowitz, and B. Longmier. Global nonambipolar flow: Plasma confinement where all electrons are lost to one boundary and all positive ions to another boundary. *Phys. Plasmas*, 14:042109, 2007.

[5] S. D. Baalrud, B. Longmier, and N. Hershkowitz. Equilibrium states of anodic double layers. *Plasma Sources Sci. Tech.*, 18:035002, 2009.

[6] E. V. Barnat and K. Frederickson. Two-dimensional mapping of electron densities and temperatures using laser-collisional induced fluorescence. *Plasma Sources Sci. Tech.*, page 055015, 2010.

[7] J. R. Beattie, J. D. Williams, and R. R. Robson. Flight qualification of an 18-mn xenon ion thruster. In *Proc. 23rd International Electric Propulsion Conference*, Seattle, WA, September 1993. IEPC Paper No. 93-106.

[8] D. Bohm. *The Characteristics of Electric Discharges in Magnetic Fields*. McGraw-Hill, New York, 1949. ed. by A. Guthrie and R. K. Wakering.

[9] J. R. Brophy, M. A. Etters, J. Gates, C. E. Garner, M. Klatte, C. J. Lo, M. G. Marcucci, S. Mikes, G. Pixler, and B. Nakazono. Development and testing of the Dawn ion propulsion system. In *Proc. 42nd AIAA/ASME/SAE/ASEE Joint Propulsion Conference & Exhibit*, Sacramento, CA, July 2006. AIAA Paper 2006-4319.

[10] J. R. Brophy, R. Y. Kakuda, J. E. Polk, J. R. Anderson, M. G. Marcucci, D. Brinza, M. D. Henry, K. K. Fujii, K. R. Mantha, J. F. Stocky, J. Sovey,

M. Patterson, V. Rawlin, J. Hamley, T. Bond, J. Christensen, H. Cardwell, G. Benson, J. Gallagher, M. Matranga, and D. Bushway. Ion propulsion system (NSTAR) DS1 technology validation report. Technical report, JPL Publication 00–10, October 2000.

[11] F. F. Chen. Electric probes. In R. H. Huddlestone and S. L. Leonard, editors, *Plasma Diagnostic Techniques*, pages 113 – 200. Academic Press, New York, 1965.

[12] L. Conde, C. Ferro Fontán, and J. Lambás. The transition from an ionizing electron collecting plasma sheath into an anodic double layer as a bifurcation. *Physics of Plasmas*, 13:113504, 2006.

[13] R. Denkelmann, S. Freund, and S. Maurmann. Measurement of rate coefficients or atom-atom collisions in a pulsed helium discharge by laser-induced fluorescence. *Contributions to Plasma Physics*, 40:91–95, 2000.

[14] K. D. Diamant. Resonant cavity hollow cathode. In *Proc. 41st AIAA/ASME/SAE/ASEE Joint Propulsion Conference & Exhibit*, Tuscon, AZ, July 2005. AIAA Paper 2005-3662.

[15] K. D. Diamant. Microwave cathode for air breathing electric propulsion. In *Proc. 31st International Electric Propulsion Conference*, Ann Arbor, MI, September 2009. IEPC Paper 2009-015.

[16] K. D. Diamant. Resonant cavity plasma electron source. *IEEE Transactions on Plasma Science*, 37(8):1558–1562, August 2009.

[17] M. J. Druyvesteyn. Der niedervoltbogen. *Z. Phys.*, 64:781 –798, September 1930.

[18] J. E. Foster, T. Haag, H. Kamhawi, M. Patterson, S. Malone, F. Elliot, G. J. Williams, Jr., J. S. Sovey, and C. Carpenter. The High Power Electric Propulsion (HiPEP) ion thruster. In *Proc. 40th AIAA/ASME/SAE/ASEE Joint Propulsion Conference and Exhibit*, Fort Lauderdale, FL, July 2004. AIAA Paper 2004-3812.

[19] I. Funaki, H. Kuninaka, and K. Toki. Plasma characterization of a 10-cm diameter microwave discharge ion thruster. *Journal of Propulsion and Power*, 20(4):718–727, July–August 2004.

[20] C. E. Garner, M. D. Rayman, and J. R. Brophy. In-flight operation of the Dawn ion propulsion system through start of the Vesta cruise phase. In *Proc. 45th AIAA/ASME/SAE/ASEE Joint Propulsion Conference & Exhibit*, Denver, CO, August 2009. AIAA Paper 2009-5091.

[21] F. N. Gesto, B. D. Blackwell, C. Charles, and R. W. Boswell. Ion detachment in the helicon double-layer thruster exhaust beam. *Journal of Propulsion and Power*, 22(1):24–30, 2006.

[22] V. Godyak, Y. Raitses, and N. J. Fisch. RF plasma cathode-neutralizer for space applications. In *Proc. 30th International Electric Propulsion Conference*, Florence, Italy, September 2007. IEPC-2007-266.

[23] D. M. Goebel, K. K. Jameson, R. M. Watkins, I. Katz, and I. G. Mikellides. Hollow cathode theory and experiment. i. plasma characterization using fast miniature scanning probes. *J. Appl. Phys.*, page 113302, 2005.

[24] D. M. Goebel and I. Katz. *Fundamentals of Electric Propulsion*. John Wiley & Sons, Hoboken, NJ, 2008.

[25] D. M. Goebel and I. Katz. *Fundamentals of Electric Propulsion: Ion and Hall Thrusters*, page 247. John Wiley & Sons, Inc., Hoboken, NJ, 2008.

[26] D. M. Goebel, R. M. Watkins, and K. K. Jameson. LaB_6 hollow cathodes for ion and hall thrusters. *Journal of Propulsion and Power*, 23(3):552–558, May–June 2007.

[27] J. A. Gudmundson and N. Hershkowitz. Performance characteristics of the Nonambipolar Electron Source using permanent magnets. In *Poster Presentation at: IEEE International Conference on Plasma Science, 2009*, june 2009.

[28] T. Haag and G. C. Soulas. Performance and vibration of 30 cm pyrolytic ion thruster optics. In *Proc. 39th AIAA/ASME/SAE/ASEE Joint Propulsion Conference and Exhibit*, Huntsville, AL, July 2003. AIAA Paper 2003-4557.

[29] D. Herman, G. Soulas, and M. Patterson. Status of the NEXT ion thruster long-duration test after 10,100 h and 207 kg demonstrated. In *Proc. 43rd AIAA/ASME/SAE/ASEE Joint Propulsion Conference & Exhibit*, Cincinnati, OH, July 2007. AIAA Paper 2007-5272.

[30] D. A. Herman. Status of the NASAs Evolutionary Xenon Thruster (NEXT) long-duration test after 30,352 hours of operation. In *Proc. 46th AIAA/ASME/SAE/ASEE Joint Propulsion Conference & Exhibit*, Nashville, TN, July 2010. AIAA Paper 2010-7112.

[31] G. Herrmann and S. Wagener. *The Oxide-Coated Cathode*, volume 1–2. Chapman & Hall, London, 1951.

[32] N. Hershkowitz. How langmuir probes work. In O. Auciello and D. L. Flamm, editors, *Plasma Diagnostics*, volume 1. Academic Press, Boston, 1989.

[33] N. Hershkowitz. How does the potential get from A to B in a plasma? *IEEE Transactions on Plasma Science*, 22(1):11–21, February 1994.

[34] N. Hershkowitz. Sheaths: More complicated than you think. *Physics of Plasmas*, 12:055502, May 2005.

[35] Y. Hidaka, J. E. Foster, W. D. Getty, R. M. Gilgenbach, and Y. Y. Lau. Performance and analysis of an electron cyclotron resonance plasma cathode. *Journal of Vacuum Science and Technology A*, 25(4):781–790, 2007.

[36] W. A. Hoskins, F. C. Wilson, J. Polaha, L. Talerico, M. J. Patterson, G. C. Soulas, and J. Sovey. Development of a prototype model ion thruster for the NEXT system. In *Proc. 40th AIAA/ASME/SAE/ASEE Joint Propulsion Conference & Exhibit*, Fort Lauderdale, FL, July 2004. AIAA Paper 2004-4111.

[37] K. Jameson, D. Goebel, and R. Watkins. Hollow cathode and keeper-region plasma measurements. In *Proc. 41st AIAA/ASME/SAE/ASEE Joint Propulsion Conference & Exhibit*, Tucson, AZ, July 2005. AIAA Paper 2005-3667.

[38] H. Kamhawi. Development of a hollow cathode assembly for the High Voltage Hall Accelerator. In *Proc. 43rd AIAA/ASME/SAE/ASEE Joint Propulsion Conference & Exhibit*, Cincinnati, OH, July 2007. AIAA Paper 2007-5172.

[39] H. Kamhawi, J. E. Foster, and M. J. Patterson. Operation of a microwave ECR cathode. In *Proc. 40th AIAA/ASME/SAE/ASEE Joint Propulsion Conference and Exhibit*, Fort Lauderdale, FL, July 2004. AIAA Paper 2004-3819.

[40] H. Kamhawi, M. J. Patterson, P. J. Dalton, and R. A. Borders. Update on the operational status of the International Space Station plasma contactor hollow cathode assemblies. In *Proc. 45th AIAA/ASME/SAE/ASEE Joint Propulsion Conference & Exhibit*, Denver, CO, August 2009. AIAA Paper 2009-5092.

[41] W. R. Kerslake. Oxide-cathode durability in mercury electron-bombardment ion thrustor. Technical report, NASA TN D-3818, February 1967.

[42] S-W. Kim, Y. Itoh, H. Okamoto, T. M. Sugiki, T. Kizaki, and M-R. Nam. Endurance test of microwave engine. In *Proc. 40th AIAA/ASME/SAE/ASEE Joint Propulsion Conference & Exhibit*, Fort Lauderdale, FL, July 2004. AIAA Paper 2004-4126.

[43] Y-K. Kim and M. E. Rudd. Binary-encounter-dipole model for electron-impact ionization. *Phys. Rev. A*, 50(5):3954, November 1994.

[44] M. A. Lieberman and R. A. Gottscho. Design of high density plasma sources for materials processing. In *Physics of Thin Films*, volume 18. Academic, New York, 1994.

[45] M. A. Lieberman and A. J. Lichtenburg. *Principles of Plasma Discharges and Materials Processing*. John Wiley & Sons, second edition, 2005.

[46] M. Liu, X. Hu, G. Yu, Q. Wu, and Y. Pan. Two-dimensional simulation of an electron cyclotron resonance plasma source with power deposition and neutral gas depletion. *Plasma Sources Science and Technology*, 11:260 –265, 2002.

[47] B. Longmier, S. Baalrud, and N. Hershkowitz. Nonambipolar Electron Source. *Review of Scientific Instruments*, 77:113504, 2006.

[48] B. Longmier and N. Hershkowitz. Improved operation of the Nonambipolar Electron Source. *Review of Scientific Instruments*, 79:093506, 2008.

[49] I. G. Mikellides, I. Katz, D. M. Goebel, and J. E. Polk. Hollow cathode theory and experiment. ii. a two-dimensional theoretical model of the emitter region. *J. Appl. Phys.*, page 113303, 2005.

[50] N. L. Milder and W. R. Kerslake. Evaluation of filament deterioration in electron-bombardment ion sources. Technical report, NASA TN D-2173, May 1964.

[51] H. Mott-Smith and I. Langmuir. Theory of collectors in gaseous discharges. *Phys. Rev.*, 28:727 – 763, 1926.

[52] M. A. Mujawar, S. K. Karkari, and M. M. Turner. Properties of a differentially pumped constricted flow hollow anode plasma source. *Plasma Sources Sci. Tech.*, 20:015024, 2010.

[53] K. Nishiyama, S. Hosoda, H. Koizumi, Y. Shimizu, I. Funaki, H. Kuninaka, M. Bodendorfer, and J. Kawaguchi. Hayabusa's way back to earth by microwave discharge ion engines. In *Proc. 46th AIAA/ASME/SAE/ASEE Joint Propulsion Conference & Exhibit*, Nashville, TN, July 2010. AIAA Paper 2010-6862.

[54] E. Oks. *Plasma Cathode Electron Sources*, pages 26 – 33. Wiley-VCH, 2006.

[55] E. M. Oks. Physics and technique of plasma electron sources. *Plasma Sources Science and Technology*, 1:249–255, 1992.

[56] S. R. Oleson. Electric propulsion technology development for the Jupiter Icy Moons Orbiter project. In *Proc. 40th AIAA/ASME/SAE/ASEE Joint Propulsion Conference and Exhibit*, Fort Lauderdale, FL, July 2004. AIAA Paper 2004-3449.

[57] S. R. Oleson and J. M. Sankovic. Advanced hall electric propulsion for future in-space transportation. Technical report, NASA/TM–2001-210676, April 2001.

[58] M. J. Patterson, J. A. Hamley, T. Sarver-Verhey, G. C. Soulas, J. Parkes, W. L. Ohlinger, M. S. Schaffner, and A. Nelson. Plasma contactor technology for Space Station Freedom. In *Proc. 29th AIAA/SAE/ASME/ASEE Joint Propulsion Conference and Exhibit*, Monterey, CA, June 1993. AIAA Paper 1993-2228.

[59] D. M. Pozar. *Microwave Engineering.* John Wiley & Sons, 2005.

[60] Y. Raitses, J. K. Hendryx, and N. J. Fisch. A parametric study of electron extraction from a low frequency inductively coupled RF-plasma source. In *Proc. 31st International Electric Propulsion Conference*, Ann Arbor, MI, September 2009. IEPC Paper 2007-024.

[61] Y. Ralchenko, R. K. Janev, T. Kato, D. V. Fursa, I. Bray, and F. J. De Heer. Electron-impact excitation and ionization cross sections for ground state and excited helium atoms. *A. Data Nucl. Data Tables*, 94:603–622, 2008.

[62] V. K. Rawlin and W. R. Kerslake. Sert ii: Durability of the hollow cathode and future applications of hollow cathodes. *J. Spacecraft*, 7(1), 1970.

[63] L. Schott. Electrical probes. In W. Lochte-Holtgreven, editor, *Plasma Diagnostics*. John Wiley, New York, 1968.

[64] A. Sengupta, J. A. Anderson, C. Garner, J. R. Brophy, K. K. de Groh, B. A. Banks, and T. A. Karniotis Thomas. Deep Space 1 flight spare ion thruster 30,000-hour life test. *Journal of Propulsion and Power*, 24(1):105–117, Jan. – Feb. 2009.

[65] G. C. Soulas and M. J. Patterson. NEXT ion thruster performance dispersion analyses. In *Proc. 43rd AIAA/SAE/ASME/ASEE Joint Propulsion Conference and Exhibit*, Cincinnati, OH, July 2007. AIAA Paper 2007-5213.

[66] M. Stanojevic, M. Cercek, T. Gyergyek, and N. Jelic. Interpretation of a planar langmuir probe current-voltage characteristic in a strong magnetic field. *Contrib. Plasma Phys.*, 34:607 – 633, 1994.

[67] P. M. Stone, Y.-K. Kim, and J. P. Desclaux. Electron-impact cross sections for dipole- and spin-allowed excitations of hydrogen, helium, and lithium. *J. Research of the National Institute of Standards and Technology*, 107(4):327–337, 2002.

[68] M. Strat, G. Strat, and S. Gurlui. Basic processes in discharge plasma double layers. *J. Phys. D: Appl. Phys.*, 32:34–40, 1999.

[69] M. Sugawara. Electron probe current in a magnetized plasma. *Phys. Fluids*, 9(1):797 – 800, 1966.

[70] D. Tang and P. K. Chu. Anode double layer in magnetized radio frequency inductively coupled hydrogen plasma. *J. Appl. Physics*, 94(3):1390–1395, 2003.

[71] W. G. Tighe, K.-R. Chien, E. Solis, P. Rebello, D. M. Goebel, and J. S. Snyder. Performance evaluation of the XIPS 25-cm thruster for application to NASA discovery missions. In *Proc. 42nd AIAA/ASME/SAE/ASEE Joint Propulsion Conference & Exhibit*, Sacramento, CA, July 2006. AIAA Paper No. 2006-4666.

[72] R. J. Umstattd. Advanced electron beam sources. In R. J. Barker, J. H. Booske, N. C. Luhmann Jr., and G. S. Nusinovich, editors, *Modern Microwave and Millimeter-Wave Power Electronics*, pages 401–402. Institute of Electrical and Electronics Engineers, 2005.

[73] G. Vannaroni, M. Dobrowolny, E. Melchioni, F. De Venuto, and R. Giovi. Characterization of the interaction between a hollow cathode source and an ambient plasma. *Journal of Applied Physics*, 71(10):4709–4717, May 1992.

[74] B. R. Weatherford, E. V. Barnat, and J. E. Foster. Two-dimensional LCIF images of electron density and temperature within an ECR plasma cathode. *IEEE Trans. Plasma Sci., 6th Triennial Special Issue, "Images in Plasma Science"*, 2011. Accepted for Publication.

[75] W. L. Wiese, M. W. Smith, and B. M. Glennon. *Atomic Transition Probabilities 4/V1 (National Standard Reference Data Series)*. U.S. Govt. Printing Office, Washington, DC, 1966.